

University of Alberta

Image registration in adaptive radiation therapy

by

Ryan Chad Rivest

A thesis submitted to the Faculty of Graduate Studies and Research
in partial fulfillment of the requirements for the degree of

Doctor of Philosophy

in

Medical Physics

Department of Physics

©Ryan Chad Rivest

Spring 2010

Edmonton, Alberta

Permission is hereby granted to the University of Alberta Libraries to reproduce single copies of this thesis and to lend or sell such copies for private, scholarly or scientific research purposes only. Where the thesis is converted to, or otherwise made available in digital form, the University of Alberta will advise potential users of the thesis of these terms.

The author reserves all other publication and other rights in association with the copyright in the thesis and, except as herein before provided, neither the thesis nor any substantial portion thereof may be printed or otherwise reproduced in any material form whatsoever without the author's prior written permission.

Examining Committee

Dr. B. Gino Fallone, Physics/Oncology, University of Alberta

Dr. Terence A. Riauka, Oncology, University of Alberta

Dr. Ron S. Sloboda, Oncology, University of Alberta

Dr. Don Robinson, Oncology, University of Alberta

Dr. Richard Marchand, Physics, University of Alberta

Dr. Sharon Morsink, Physics, University of Alberta

Dr. Piotr Slomka, Medicine, University of California-Los Angeles

Abstract

This thesis focuses on the development, validation and application of image registration software in adaptive radiation therapy. The contents can be divided into three components: deformable image registration validation, rigid registration based daily patient positioning and deformable image registration for dose accumulation. In the first component, a protocol was developed for the validation of commercial deformable registration systems, applicable to a wide range of applications. The protocol was used to assess the capabilities of a commercial system and results suggest that deformable registration could potentially be optimized by treating applications separately instead of using one algorithm for all applications.

The use of rigid registration for daily positioning of helical tomotherapy prostate patients was investigated in the second component. We quantified alignment discrepancies between daily treatment MVCT images and their corresponding planning CT images resulting from different automated rigid registration schemes. Based on alignments, errors in prostate positioning that would occur if patient repositioning was based on mutual information optimization of entire images or simply bony anatomy were evaluated, with the latter having a 20% decreased average prostate misplacement. The dosimetric implications of performing patient positioning based on either bony anatomy matching or prostate matching in treatment and planning images were also investigated. Prostate doses were fairly insensitive, however, doses to the

radiation sensitive bladder and rectum varied with not only positioning strategy, but also the direction of daily prostate motion.

The third component of this thesis involves the use of deformable registration and dose accumulation in the comparison of treatment and planning doses. Using correlation coefficient optimization and assuming B-spline parameterized deformations, we demonstrated that deformable registration can be improved by performing separate registrations over each clinically relevant region on interest. Our deformable model was incorporated into a dose accumulation framework and cumulative treatment doses were compared to those that were planned. In addition, cumulative doses that would have been delivered had patient positioning been based on bone matching and prostate matching were also evaluated. These studies may suggest that daily anatomical variations play a greater role in treatment dosimetry than does the selection of registration based image guidance procedure.

Table of Contents

Chapter 1: Introduction	1
1.1 Cells and Cancer	1
1.2 Treatment of Cancer.....	2
1.3 Medical Image Registration	3
1.4 Thesis Outline	4
1.5 References.....	5
Chapter 2: Concepts in image registration and adaptive radiation therapy ..	6
2.1 Three-dimensional Imaging for Radiation Therapy	6
2.1.1 Computed Tomography	7
2.1.2 Magnetic Resonance Imaging.....	10
2.1.3 Positron Emission Tomography.....	13
2.2 Image Registration Overview	14
2.2.1 Notation.....	14
2.2.2 Types of Registration Algorithms.....	15
2.2.3 Image Registration Framework.....	16
2.3 Components of an Image Registration Algorithm	17
2.3.1 Image Pre-processing.....	17
2.3.2 Transformations	18
2.3.3 Cost Functions	21
2.3.4 Interpolation	24
2.3.5 Optimization	25
2.4 Image Registration Software.....	26

2.4.1	Reveal-MVS	26
2.4.2	Insight Toolkit (ITK)	27
2.5	Radiation Therapy Preparation	27
2.5.1	Immobilization and Simulation.....	27
2.5.2	Target Definition and Nomenclature	28
2.5.3	Treatment Planning	29
2.6	Radiation Therapy Delivery	30
2.6.1	Linear Accelerator - C - Gantry Type.....	30
2.6.2	Helical Tomotherapy	31
2.7	Advanced Radiation Therapy Protocols	33
2.7.1	Image Guided Radiation Therapy	33
2.7.2	Adaptive Radiation Therapy	34
2.8	Thesis Objectives	35
2.9	References	38

Chapter 3: Assessment of a commercially available automatic deformable registration system	47	
3.1	Introduction.....	47
3.2	Methods and Materials.....	51
3.2.1	Registration Software.....	51
3.2.2	Phantom Study	53
3.2.3	Relative Patient Study.....	55
3.2.4	Intra-modality Registration.....	59
3.2.5	Inter-modality Registration.....	62

3.3	Results.....	65
3.3.1	Phantom Study	65
3.3.2	Relative Patient Study.....	67
3.3.3	Intra-modality Registration.....	67
3.3.4	Inter-modality Registration.....	72
3.4	Discussion	73
3.5	Conclusions.....	84
3.6	References.....	86

Chapter 4: Prostate positioning errors associated with two automatic registration based image guidance strategies 93

4.1	Introduction.....	93
4.2	Methods and Materials.....	95
4.2.1	Patient Images.....	95
4.2.2	Automatic Registration	96
4.2.3	Automatic Prostate Localization.....	97
4.2.4	Multi-start Procedure	99
4.3	Results.....	100
4.3.1	Prostate Localization Validation.....	100
4.3.2	Dependence on Planning CT Contour Delineation.....	103
4.3.3	Prostate Positioning Errors	104
4.3.4	Inter-fraction Prostate Motion.....	108
4.4	Discussion	110
4.5	Conclusions.....	114

4.6	References.....	115
Chapter 5: Dosimetric implications of two registration based patient positioning methods in image guided radiation therapy.....		
		119
5.1	Introduction.....	119
5.2	Methods and Materials.....	122
5.3	Results.....	125
5.3.1	Daily Prostate Motion.....	125
5.3.2	Dose Volume Histogram Analysis.....	125
5.3.3	Image Guidance Comparison.....	126
5.3.4	Contour Dependence.....	133
5.4	Discussion.....	133
5.5	Conclusions.....	139
5.6	References.....	139
Chapter 6: Incorporation of planning contour data into a voxel based deformable registration algorithm for prostate adaptive radiation therapy.....		
		146
6.1	Introduction.....	146
6.2	Methods and Materials.....	151
6.2.1	Rigid Transformation.....	153
6.2.2	Deformable Transformation.....	153
6.2.3	Prostate Motion.....	155
6.2.4	Image Correspondence.....	155
6.2.5	Registration Framework.....	158

6.2.6	Validation.....	160
6.3	Results.....	162
6.3.1	Dependence on Registration Settings	162
6.3.2	Cohort Analysis	164
6.3.3	Comparison to Standard B-spline Registration.....	168
6.4	Discussion	171
6.5	Conclusions.....	175
6.6	References.....	176
Chapter 7: Accounting for daily anatomical variations in the evaluation of		
cumulative dosimetry.....		
7.1	Introduction.....	182
7.2	Methods and Materials.....	186
7.2.1	Dose Accumulation.....	187
7.2.1.1	Deformable Registration.....	187
7.2.1.2	Dose Accumulation Software	189
7.2.2	Uncertainty in Accumulated Dose Distributions	190
7.2.2.1	Recalculation.....	192
7.2.2.2	Interpolation.....	192
7.2.2.3	Deformation	193
7.2.3	Landmark Based Assessment of Dose Warping	193
7.2.4	Comparison of Planned and Delivered Doses	195
7.2.5	Dosimetric Evaluation of Image Guidance Strategies	196
7.3	Results.....	197

7.3.1	Landmark Based Dose Warping Assessment	197
7.3.2	Comparison of Planned and Delivered Doses	197
7.3.3	Comparison of Bone and Prostate Matching Image Guidance Strategies	202
7.4	Discussion	205
7.5	Conclusions	211
7.6	References	212
Chapter 8: Conclusions and future work		219
8.1	Deformable Image Registration Validation	219
8.2	Rigid Registration Based Daily Patient Positioning	220
8.3	Deformable Registration and Dose Accumulation	221
8.4	References	223
Appendix A: Optimization algorithms.....		224
A.1	Nelder-Mead simplex.....	225
A.2	Limited memory Broyden-Fletcher-Goldfarb-Shanno with simple bounds	226
A.3	References	229
Appendix B: Relative evaluation of Reveal-MVS deformable registration settings.....		230
Appendix C: Interpolation based dose warping errors in prostate MVCT studies.....		257
C.1	References	260

List of Tables

Table 2-1. Approximate Hounsfield units or CT numbers for various tissues. 9

Table 3-1. Summary of the validation protocol procedure, including the analysis performed and images evaluated for each of the protocol's four components. 65

Table 3-2. Prostate DSC, TC, and mean separation (MS) values for each of the five patients. MS values are in mm. Initial values are given for rigid alignment and after deformable registration of pelvic MRI and planning CT images, using two different settings on Reveal-MVS. 74

Table 4-1. Comparison of actual prostate motion as determined from the positions of implanted localization seeds and measured prostate motion established with the automatic prostate localization algorithm. 103

Table 4-2. Statistics for prostate positioning errors based on bone matching (BM) and image matching (IM). 105

Table 4-3. Percentage of registrations that resulted in a prostate positioning error ≥ 3 mm in each of the translational directions. 108

Table 4-4. Percentage of registrations that resulted in a prostate positioning error ≥ 5 mm in each of the translational directions. 108

Table 4-5. Inter-fraction prostate motion statistics for entire cohort. Negative values correspond to motion superiorly, anteriorly and to the left. 110

Table 5-1. Prostate motion statistics for each individual patient. Negative values correspond to motion superiorly, anteriorly and to the left..... 127

Table 5-2. Per fraction mean \pm standard deviation prostate D95, bladder D45 and rectum D30 values for all ninety-nine fractions for each matching method. Inverse planning constraints are given in brackets. 128

Table 5-3. Percent of fractions in which the bladder and rectum inverse planning constraints were dosimetrically exceeded, exceeded by 10% and exceeded by 25% for each matching method..... 128

Table 5-4. Individual patient statistics for prostate Δ D95, bladder Δ D45 and rectum Δ D30. Δ denotes prostate matching minus bone matching. The combined patient values are also normalized to the inverse planning constraints (i.e. prostate: 2.72 Gy, bladder: 2.00 Gy and rectum: 1.80 Gy)..... 131

Table 6-1. Mean bladder DSC and \bar{d} metrics for the first 16 image pairs. 163

Table 6-2. Mean prostate DSC and \bar{d} metrics for the first 16 image pairs..... 163

Table 6-3. Mean rectum DSC and \bar{d} metrics for the first 16 image pairs.	164
Table 6-4. Statistics for the bladder, prostate and rectum DSC measures (n=49).	165
Table 6-5. Statistics for the bladder, prostate and rectum \bar{d} measures (n=49)..	165
Table 6-6. Mean \bar{d} for two registration strategies (n=10).	171
Table 7-1. Summary of the functions provided in each of the eleven tabs in the dose accumulation graphical user interface (GUI).	191
Table 7-2. Statistics for the landmark based method of determining dose warping errors. Errors were evaluated at each landmark in twenty treatment fractions and values are normalized to the fractionated prescription dose.	198
Table 7-3. Differences between treatment and planning prostate D95 values after completion of five, ten, fifteen, twenty, and twenty-five fractions. Dose differences are expressed in percent and normalized to planned D95 values, which are also included for reference (N_F = number of fractions).	201
Table 7-4. Differences between treatment and planning bladder D50 and D15 values after completion of five, ten, fifteen, twenty, and twenty-five fractions.	

Dose differences are expressed in percent and normalized to planned values, which are also included for reference. 201

Table 7-5. Differences between treatment and planning rectum D50 and D15 values after completion of five, ten, fifteen, twenty, and twenty-five fractions. Dose differences are expressed in percent and normalized to planned values, which are also included for reference. 202

Table 7-6. Prostate $\Delta D95$ (expressed in percent and normalized to planned D95 values) at five fraction intervals..... 203

Table 7-7. Bladder $\Delta D50$ (expressed in percent and normalized to planned D50 values) and $\Delta D15$ (expressed in percent and normalized to planned D15 values) at five fractions intervals..... 204

Table 7-8. Rectum $\Delta D50$ (expressed in percent and normalized to planned D50 values) and $\Delta D15$ (expressed in percent and normalized to planned D15 values) at five fractions intervals..... 205

Table 7-9. Comparison of mean fractionated bone matching (BM) and prostate matching (PM) bladder D45 values determined previously and the cumulative bladder D45 values determined in this study. Cumulative values are divided by

twenty-five to account for differences in scale. All dose values are in units of Gy..... 208

Table 7-10. Comparison of mean fractionated bone matching (BM) and prostate matching (PM) rectum D30 values determined previously and the cumulative rectum D30 values determined in this study. Cumulative values are divided by twenty-five to account for differences in scale. All dose values are in units of Gy..... 210

Table B-1. Rankings of the deformable registration setting combinations used on Reveal-MVS when registering PET/CT images. Rankings are based on post-registration normalized mutual information (NMI) values for each patient (P) as well as the mean value for all five patients. Also listed are the mean NMI values for each setting..... 231

Table B-2. Rankings of the deformable registration setting combinations used on Reveal-MVS when registering PET/CT images. Rankings are based on post-registration symmetric correlation ratio (SCR) values for each patient (P) as well as the mean value for all five patients. Also listed are the mean SCR values for each setting..... 233

Table B-3. Rankings of the deformable registration setting combinations used on Reveal-MVS when registering longitudinal PET images. Rankings are based on

post-registration normalized mutual information (NMI) values for each patient (P) as well as the mean value for all five patients. Also listed are the mean NMI values for each setting..... 235

Table B-4. Rankings of the deformable registration setting combinations used on Reveal-MVS when registering longitudinal PET images. Rankings are based on post-registration symmetric correlation ratio (SCR) values for each patient (P) as well as the mean value for all five patients. Also listed are the mean SCR values for each setting..... 237

Table B-5. Rankings of the deformable registration setting combinations used on Reveal-MVS when registering longitudinal PET images. Rankings are based on post-registration correlation coefficient (CC) values for each patient (P) as well as the mean value for all five patients. Also listed are the mean CC values for each setting..... 239

Table B-6. Rankings of the deformable registration setting combinations used on Reveal-MVS when registering longitudinal thoracic CT images. Rankings are based on post-registration normalized mutual information (NMI) values for each patient (P) as well as the mean value for all five patients. Also listed are the mean NMI values for each setting. 241

Table B-7. Rankings of the deformable registration setting combinations used on Reveal-MVS when registering longitudinal thoracic CT images. Rankings are based on post-registration symmetric correlation ratio (SCR) values for each patient (P) as well as the mean value for all five patients. Also listed are the mean SCR values for each setting. 243

Table B-8. Rankings of the deformable registration setting combinations used on Reveal-MVS when registering longitudinal thoracic CT images. Rankings are based on post-registration correlation coefficient (CC) values for each patient (P) as well as the mean value for all five patients. Also listed are the mean CC values for each setting..... 245

Table B-9. Rankings of the deformable registration setting combinations used on Reveal-MVS when registering male pelvic MRI images to planning CT images. Rankings are based on post-registration normalized mutual information (NMI) values for each patient (P) as well as the mean value for all five patients. Also listed are the mean NMI values for each setting 247

Table B-10. Rankings of the deformable registration setting combinations used on Reveal-MVS when registering male pelvic MRI images to planning CT images. Rankings are based on post-registration symmetric correlation ratio (SCR) values for each patient (P) as well as the mean value for all five patients. Also listed are the mean SCR values for each setting..... 249

Table B-11. Rankings of the deformable registration setting combinations used on Reveal-MVS when registering male pelvic MVCT images to planning CT images. Rankings are based on post-registration normalized mutual information (NMI) values for each patient (P) as well as the mean value for all five patients. Also listed are the mean NMI values for each setting 251

Table B-12. Rankings of the deformable registration setting combinations used on Reveal-MVS when registering male pelvic MVCT images to planning CT images. Rankings are based on post-registration symmetric correlation ratio (SCR) values for each patient (P) as well as the mean value for all five patients. Also listed are the mean SCR values for each setting..... 253

Table B-13. Rankings of the deformable registration setting combinations used on Reveal-MVS when registering male pelvic MVCT images to planning CT images. Rankings are based on post-registration correlation coefficient (CC) values for each patient (P) as well as the mean value for all five patients. Also listed are the mean CC values for each setting 255

Table C-1. Interpolation based dose warping error ($\delta d_i(\mathbf{x}_0(\mu))$) when adjacent treatment image voxels $\mathbf{x}_i(\mu)$ and $\mathbf{x}_i(\nu)$ deform into one planning CT voxel. A 10% dose gradient is assumed. The unit for dose values is percentage of prescription dose. 260

List of Figures

Figure 2-1. Sample (a) axial, (b) coronal and (c) sagittal slices of a 3D male pelvic CT image. Higher x-ray attenuating objects such as bone appear white, while lower attenuating objects such as air are dark..... 9

Figure 2-2. Sample (a) axial, (b) coronal and (c) sagittal slices of a 3D T1-weighted male pelvic MRI. Note the significant improvement in soft tissue contrast as compared to the CT image in figure 2-1..... 12

Figure 2-3. Coronal slice of a sample 3D FDG-PET image. The dark region of high FDG uptake at the top of the image is a malignancy. FDG is eliminated biologically through the renal system; hence the bladder at the bottom of the image also contains large concentrations of FDG. 14

Figure 2-4. Flowchart illustrating the steps involved in a typical image registration algorithm. 17

Figure 2-5. (a) Varian Silhouette (Varian Medical Systems, Inc., Palo Alto, CA) linear accelerator with C-type gantry and (b) Hi*Art II (TomoTherapy, Inc., Madison, WI) helical tomotherapy system. 32

Figure 2-6. Simple schematic demonstrating the process of dose accumulation. Suppose a region of interest (ROI) has changed shape between planning, fraction

1 and fraction 2 CT acquisition. Each anatomical point on the planned ROI (example shown in red) will be in a different location during each fraction. Deformable registration of fraction 1 CT to the planning CT yields the transformation T_1 that maps the position of each anatomical point in the treatment CT to the planning CT. Similarly, deformable registration of the fraction 2 CT to the planning CT yields transformation T_2 . If the dose is reconstructed on each treatment CT, the transformations can be used to map the dose delivered to each anatomical point during each fraction back to the planning CT geometry. This allows for cumulative dose calculation..... 37

Figure 2-7. Ideal ART framework that provides the basis for this thesis. After patient imaging and optimized planning, a treatment CT is acquired before each daily fraction. Based on the rigid registration of treatment and planning CT images, the patient is repositioned and radiation is delivered. After each fraction, the treatment dose is reconstructed and the accumulated dose is evaluated with the aid of deformable image registration. If at any point, treatment doses are unacceptable, the treatment plan can be re-optimized..... 38

Figure 3-1. (a) Side view photographic image of the phantom showing the seven solid spheres attached to plastic rods screwed into the phantom base. (b) Axial slice of target CT image. (c) Axial slice of target MRI image. (d) Axial slice of target PET image..... 55

Figure 3-2. Flowchart showing the steps and images involved in the synthetic transformation based intra-modality validation study. Rectangles represent steps or actions while images are denoted by ellipses. 62

Figure 3-3. Flowchart showing the steps and images involved in the contour based inter-modality validation study. Rectangles represent steps or actions while images are denoted by ellipses..... 64

Figure 3-4. Axial slices of coloured source images overlaid on greyscale target phantom images for two selected registrations. (a) Rigid alignment of CT images in which a single target has been translated 8 mm. (b) CT images after deformable registration (None-Fast-Coarse) on Reveal-MVS demonstrating that the system does not move the sphere back to its original location. (c) Rigid alignment of MRI and CT images in which a sphere in the MRI has approximately doubled in volume. (d) MRI and CT images after deformable registration (None-Fast-Medium)..... 66

Figure 3-5. (a) Plot of displacement error (DE) values measured by our grid based method versus true DE values for various magnitudes of B-spline warping. Either 500, 1000, 3000, or 5000 randomly located grid points were used. The solid dark line depicts correct measurement of true values. (b) Similar plot for axial components of DE..... 69

Figure 3-6. Scatter plot of post- versus pre-deformable registration (a) DE and (b) axial DE values for baseline and synthetically transformed thoracic CT images. Ten B-spline warped images were registered to their respective original unwarped images on Reveal-MVS for each of the five patients (denoted by separate coloured symbols). A reference line with unity slope is shown in black. 70

Figure 3-7. Sample coloured warped images overlaid on greyscale baseline images depicting the range of magnitudes of synthetic B-spline warped images used for validation of thoracic CT registrations. The images are also shown upon completion of deformable registration on Reveal-MVS. (a) Axial and (b) coronal views of images that differ by a displacement error of 4.6 mm and an axial displacement error of 3.4 mm. Corresponding (c) axial and (d) coronal views of images after registration. (e) Axial and (f) coronal views of images that differ by a displacement error of 9.4 mm and an axial displacement error of 7.1 mm. Corresponding (g) axial and (h) coronal views of images after registration. 71

Figure 3-8. Relationship between image similarity measures and absolute prostate contour based metrics for twelve different settings in the registration of pelvic MRI to planning CT images. (a) Normalized mutual information (NMI) versus Dice similarity coefficient (DSC), (b) NMI versus mean contour separation, (c) Symmetric correlation ratio (SCR) versus DSC, (d) SCR versus mean separation. Each patient is represented with a different coloured symbol. 75

Figure 3-9. Axial slices of prostate patient whose MRI and CT images were acquired on different shaped couches. (a) CT with both the prostate and patient body outlined. (b) MRI after rigid alignment showing the MRI prostate and the CT patient contours. Anatomical variation caused by the different couches is present in the bottom left hand corner. (c) CT prostate and patient contours overlaid on the MRI after deformable registration. Warping on Reveal-MVS accounted for couch based anatomical variations but completely ignored the prostate motion..... 84

Figure 4-1. Number of passes as a function of the contour border used in the registration cost function calculation for the two test patient image pairs with implanted prostate localization seeds, with and without use of a median filter (MF). Each multi-start procedure consisted of 20 starts and a registration was considered a pass if the prostate motion was within half a planning CT voxel of the true motion in each of the three lateral directions..... 102

Figure 4-2. Prostate motion as measured by the automatic prostate localization software using two different input planning CT contours. Analysis was performed for ten randomly selected fractions from a single patient. (a) Left-right (LR) motion. (b) Anterior-posterior (AP) motion. (c) Superior-inferior (SI) motion. 106

Figure 4-3. Frequency histograms for 3D prostate positioning errors when daily patient repositioning is based on (a) bone matching (BM) and (b) image matching (IM). 107

Figure 4-4. Inter-fraction prostate motion histograms for 175 treatment fractions. (a) Left-right (LR) motion. (b) Anterior-posterior (AP) motion. (c) Superior-inferior (SI) motion. 109

Figure 5-1. Simplified schematic demonstrating the potential increased dose to a critical structure as a result of target matching. A gap is present between the target and critical structure in the planning CT, but the target has moved towards the critical structure when the patient is treated. With appropriate margins, bone matching results in complete coverage of the target without having any of the critical structure situated in the high dose region. On the other hand, part of the critical structure receives the target dose if target matching is used for patient positioning. It should be noted that although the depicted scenario may be interpreted as the target being the prostate and the critical structure representing the rectum, this is not the intent. The diagram depicts a general scenario where the target has moved in the direction of a critical structure. 121

Figure 5-2. DVH comparison of prostate matching (PM) and bone matching (BM) for patient 1 odd numbered fractions (i.e. fraction 1, 3, ..., 23, 25). (a) Prostate, (b) bladder, (c) rectum. 129

Figure 5-3. Frequency histograms of the dosimetric differences between prostate and bone matching. (a) Prostate ΔD_{95} , (b) bladder ΔD_{45} , and (c) rectum ΔD_{30} values for all ninety-nine fractions. 130

Figure 5-4. Scatter plot of per fraction (a) bladder ΔD_{45} and (b) rectum ΔD_{30} values (Gy) for all ninety-nine fractions as a function of prostate motion in the superior/inferior and anterior/posterior directions. 132

Figure 6-1. Histogram plots of 49 DSC values for (a) bladder, (b) prostate and (c) rectum. 166

Figure 6-2. Histogram plots of 49 \bar{d} values for (a) bladder, (b) prostate and (c) rectum. 167

Figure 6-3. Axial slices from a selected treatment fraction demonstrating the algorithm's bladder deformation capabilities. (a) Planning CT with the bladder contoured in red. (b) Corresponding axial MVCT slice with the planning bladder overlaid. The bladder's size is clearly reduced during treatment as compared to planning. (c) After deformable registration, the MVCT bladder wall shows excellent alignment with the planning contour ($DSC = 0.92$, $\bar{d} = 1.2$ mm)..... 168

Figure 6-4. Demonstration of prostate registration in our deformable algorithm. (a) Axial slice of planning CT with planning prostate contour overlaid. An

interface between the posterior border of the prostate and the anterior rectum surface is clearly visible. (b) The corresponding axial MVCT slice for a selected treatment fraction with the same planning contour shown. The prostate has shifted anteriorly with respect to its planning position to the point where its planning contour is now on top of the MVCT rectum. (c) The same axial MVCT slice after prostate translation and deformation ($DSC = 0.82$, $\bar{d} = 1.9$ mm). The borders of the prostate are not as discernible as in the planning image, but a distinct interface between the prostate contour and the rectum is visible as is the case in the planning CT..... 169

Figure 6-5. Sample rectum deformation. (a) Axial slice of the planning CT showing the rectum contoured in red. (b) After bony alignment, it is apparent in the MVCT that the rectum has changed in size and shape prior to treatment. (c) The deformed MVCT image in which the MVCT rectal volume agrees well with the planning volume ($DSC = 0.76$, $\bar{d} = 1.6$ mm)..... 170

Figure 6-6. Axial slices depicting examples of mediocre bladder ($DSC = 0.63$, $\bar{d} = 3.8$ mm), prostate ($DSC = 0.73$, $\bar{d} = 2.5$ mm) and rectum ($DSC = 0.64$, $\bar{d} = 2.7$ mm) deformable registrations. Respective planning contours are overlaid on each of the deformed (a) bladder, (b) prostate and (c) rectum MVCT images... 170

Figure 7-1. Cumulative treatment doses minus planned doses (in percent, normalized to prescription dose) for patient 2 after (a) five, (b) ten, (c) fifteen, (d) twenty and (e) twenty-five fractions. 199

Figure 7-2. Comparison of patient 4 planned (solid) and treatment (dashed) dose volume histograms after (a) five, (b) ten, (c) fifteen and (d) twenty fractions. .. 200

Figure 7-3. Comparison of patient 4 bone matching (solid) and prostate matching (dashed) dose volume histograms after (a) five, (b) ten, (c) fifteen and (d) twenty fractions..... 203

List of Abbreviations

2D	two dimensional
3D	three dimensional
3DCRT	three dimensional conformal radiation therapy
4D	four dimensional
AP	anterior-posterior
ART	adaptive radiation therapy
BFGS	Broyden-Fletcher-Goldfarb-Shanno
BM	bone matching
CBCT	cone beam computed tomography
CC	correlation coefficient
cm	centimeter
COG	centre of gravity
CR	correlation ratio
CT	computed tomography
CTV	clinical target volume
DAD	direct aperture deformation
DE	displacement error
DICOM	Digital Imaging and Communications in Medicine
DOF	degrees of freedom
DRR	digitally reconstructed radiograph
DSC	Dice similarity coefficient
DVH	dose volume histogram

EPI	electronic portal image
F-18	fluorine-18
FDG	fluorodeoxyglucose
FEM	finite element method
FFD	free form deformable
FOV	field of view
GB	giga-bytes
GHz	giga-Hertz
GTV	gross tumour volume
GUI	graphical user interface
Gy	Gray
HDR	high dose rate
ICRU	International Commission on Radiation Units and Measurements
IGRT	image guided radiation therapy
IM	image matching
IMRT	intensity modulation radiation therapy
ITK	Insight ToolKit
J	Joules
keV	kilo electron volts
kg	kilogram
kV	kilovolt
kVCT	kilovoltage computed tomography

L-BFGS-B	limited memory Broyden-Fletcher-Goldfarb-Shanno with simple bounds
LOR	line of response
LR	left-right
MAD	mean absolute intensity difference
MF	median filter
MI	mutual information
mm	millimeter
MRI	magnetic resonance imaging
MRSI	magnetic resonance spectroscopic imaging
MSD	mean square intensity difference
MV	megavolt
MVCT	megavoltage computed tomography
NMI	normalized mutual information
NMR	nuclear magnetic resonance
NSCLC	non-small cell lung carcinoma
OAR	organ at risk
OBI	on-board imager
P	patient
PC	personal computer
PDE	partial differential equation
PET	positron emission tomography
PM	prostate matching

PTV	planning target volume
RAM	random access memory
RF	radio frequency
ROI	region of interest
RT	radiation therapy
RTOG	radiation therapy oncology group
SCR	symmetric correlation ratio
SI	superior-inferior
SSD	sum of square intensity differences
TC	Tanimoto coefficient
TBI	total body irradiation
TPS	thin plate spline

List of Symbols

\mathbf{A}	Hessian matrix
a	general target image voxel intensity
a_{\min}	minimum voxel intensity in target image
a_{\max}	maximum voxel intensity in target image
b	general source image voxel intensity
b_{\min}	minimum voxel intensity in source image
b_{\max}	maximum voxel intensity in source image
B_l	l -th basis function of the B-spline
\mathbf{B}_0	magnetic field strength of MRI
b_0^{ROI}	uniform border surrounding ROI in planning image
C_0^{ROI}	ROI contour in planning image delineated during planning
$C_0^{ROI, r}$	ROI contour in planning image delineated by radiation oncologist
C_i^{ROI}	ROI contour in treatment image i
$C_i^{ROI-deform}$	deformed ROI contour in treatment image i
D15	dose delivered to 15% of the volume
D25	dose delivered to 25% of the volume
D30	dose delivered to 30% of the volume
D35	dose delivered to 35% of the volume
D45	dose delivered to 45% of the volume
D50	dose delivered to 50% of the volume

D95	dose delivered to 95% of the volume
\bar{d}	mean surface distance
$d_0(\mathbf{x}_0)$	planning dose distribution
$d_i(\mathbf{x}_0)$	deformed treatment i dose distribution
$d_i(\mathbf{x}_0(\mu))$	deformed treatment i dose to single voxel μ in planning image
$d_i(x_0, y_0, z_0)$	dose at position (x_0, y_0, z_0) in deformed treatment i dose distribution
$d_i(\mathbf{x}_i)$	treatment i dose distribution
$d_i(\mathbf{x}_i(\mu))$	treatment dose to single voxel μ in treatment i image
$d_i(x_i, y_i, z_i)$	dose at position (x_i, y_i, z_i) in treatment i dose distribution
$d_i^{True}(\mathbf{x}_0(\mu))$	true treatment i dose to single voxel μ in planning image
$d_{total}(\mathbf{x}_0)$	cumulative deformed treatment dose distribution
$dtol$	simplex diameter tolerance for algorithm completion
$E(\mathbf{x}_i(\mu))$	energy absorbed in single voxel μ in treatment i image
f	a general function
f^*	value of function at simplex vertex P^*
f_{actr}	function tolerance for L-BFGS-B algorithm termination
f_h	largest function value amongst simplex vertices
f_i	value of function f at simplex vertex i
f_l	smallest function value amongst simplex vertices
$ftol$	function tolerance for simplex algorithm termination

H	approximation of the inverse Hessian
H_k	approximation of the inverse Hessian after iteration <i>k</i>
<i>I</i>	MVCT voxel intensity
<i>I</i> ₀	intercept of physical intensity versus MVCT voxel intensity curve
\bar{I}_0	mean target image intensity
<i>I</i> ₀ (x ₀)	planning image intensity map
\bar{I}_1	mean source image intensity
<i>I</i> _{<i>i</i>} (x _{<i>i</i>})	treatment image <i>i</i> intensity map
<i>I</i> (x ₁)	source image intensity map
<i>I</i> (x ₀)	target image intensity map
<i>I</i> (x _{<i>i</i>} (μ))	intensity of voxel μ in treatment <i>i</i> image
K	constant relating linear attenuation to CT number
l	lower bounds on variables z in L-BFGS-B optimizer
<i>m</i>	number of correction pairs stored by L-BFGS-B optimizer
M	net magnetization vector
<i>M</i> (x _{<i>i</i>} (μ))	mass of contents in single voxel μ in treatment <i>i</i> image
<i>N</i>	number of variables <i>f</i> is dependent upon
<i>N</i> ₀	number of gas voxels in a slice of planning image
<i>N</i> _F	number of fractions
<i>N</i> _{<i>i</i>}	number of gas voxels in a slice of treatment image <i>i</i>

N_t	threshold for number of gas voxels that determines whether rectum intensity modification is performed
N_V	number of image voxels
n_x	number of B-spline control points in x-direction
n_y	number of B-spline control points in y-direction
n_z	number of B-spline control points in z-direction
P^*	simplex vertex after reflection of P_h
$p(a,b)$	joint probability histogram
$p(a)$	marginal target image probability histogram
$p(b)$	marginal source image probability histogram
$pgtol$	gradient tolerance for L-BFGS-B algorithm termination
P_h	simplex vertex with largest function value
P_i	vertex i in a simplex
R	rotation matrix
s	slope of physical intensity versus MVCT voxel intensity curve
t	translation vector
T	general transformation
T₀	known synthetic transformation
T1	longitudinal relaxation time
T2	transverse relaxation time
T^{Bspline}	general B-spline transform

\mathbf{T}_i	transformation that maps treatment image i to planning image
\mathbf{T}_i^{Bone}	transformation that maps bony anatomy in treatment image i to planning image
\mathbf{T}_i^{ROI}	transformation that maps a general ROI in treatment image i to planning image
$\mathbf{T}_i^{ROI-deform}$	deformable component of transformation that maps a general ROI in treatment image i to planning image
$\mathbf{T}_i^{ROI-rigid}$	rigid component of transformation that maps a general ROI in treatment image i to planning image
$\mathbf{T}_i^{ROI-trans}$	translation component of transformation that maps a general ROI in treatment image i to planning image
\mathbf{T}^{euler}	general Euler transform
\mathbf{T}_{Reveal}	transformation output by Reveal-MVS
\mathbf{T}^{trans}	general translation transform
t_x	x-axis component of translation vector
t_y	y-axis component of translation vector
t_z	z-axis component of translation vector
\mathbf{u}	upper bounds on variables \mathbf{z} in L-BFGS-B optimizer
V30	percentage of volume that receives 30 Gy
V40	percentage of volume that receives 40 Gy
V50	percentage of volume that receives 50 Gy

V_{60}	percentage of volume that receives 60 Gy
V_{70}	percentage of volume that receives 70 Gy
V_{CT}	volume of ROI in CT image
V_{MRI}	volume of ROI in MRI image
x	x-coordinate of voxel
x_0	x-coordinate of voxel in planning image
\mathbf{x}_0	target image/planning image
$\mathbf{x}_0(\mu)$	single voxel μ in planning image
\mathbf{x}_1	source image
x_i	x-coordinate of voxel in treatment image i
\mathbf{x}_i	treatment image for fraction i
$\mathbf{x}_i(\mu)$	single voxel μ in treatment image i
x_{\min}	minimum x-coordinate that defines B-spline region
x_{\max}	maximum x-coordinate that defines B-spline region
y	y-coordinate of voxel
y_0	y-coordinate of voxel in planning image
y_i	y-coordinate of voxel in treatment image i
y_{\min}	minimum y-coordinate that defines B-spline region
y_{\max}	maximum y-coordinate that defines B-spline region
z	z-coordinate of voxel
z_0	z-coordinate of voxel in planning image

z_i	z-coordinate of voxel in treatment image i
z_{\min}	minimum z-coordinate that defines B-spline region
z_{\max}	maximum z-coordinate that defines B-spline region
\mathbf{z}	set of N variables upon which f is dependent upon
\mathbf{z}_k	\mathbf{z} after iteration k
$\Delta D15$	D15 for prostate matching minus D15 for bone matching
$\Delta D30$	D30 for prostate matching minus D30 for bone matching
$\Delta D45$	D45 for prostate matching minus D45 for bone matching
$\Delta D50$	D50 for prostate matching minus D50 for bone matching
$\Delta D95$	D95 for prostate matching minus D95 for bone matching
$\delta l_i(\mathbf{x}_0(\mu))$	error in deformed treatment i dose to single voxel μ in planning image
δ_x	spacing of B-spline control points in x-direction
δ_y	spacing of B-spline control points in y-direction
δ_z	spacing of B-spline control points in z-direction
ε_i	voxel error for voxel i
$\phi_{i,j,k}$	B-spline control point
Φ	3D mesh of B-spline control points
μ_t	linear attenuation coefficient of a tissue
μ_w	linear attenuation coefficient of water
ρ	physical density

Ω_0	registration domain in target image
Ω_0^{Bone}	domain in planning image containing only bony anatomy
$\Omega_0^{Pelvis-deform}$	domain in planning image in which the deformable transformation for the pelvic region is defined
Ω_0^{ROI}	domain in planning image containing only a general ROI and its border b_0^{ROI}
$\Omega_0^{ROI-deform}$	domain in planning image in which the deformable transformation for a general ROI is defined
Ω_1	registration domain in source image
σ	standard deviation
∇f	gradient of function f
∇f_k	gradient of function f after iteration k

Chapter 1: Introduction

1.1 Cells and Cancer

Cells are the smallest living functional unit in all known forms of life. In fact, humans are comprised of trillions of cells that together form the various tissues and organs in our bodies. Over the course of a cell's life, it undergoes repeated multiplications and eventually dies a programmed death. All organ functions and life itself rely on a delicate balance between cell reproduction and cell death. Cancer is a disease in which cells experience uncontrolled reproduction and eventually invade surrounding tissue. After invasion, cancerous or malignant cells may also spread to other parts of the body. This is referred to as metastasis.

According to Canadian Cancer Society¹ estimates, 171,000 new cases of cancer were diagnosed in Canada and over 75,000 Canadians died of the disease

in 2009 alone. Based on current incidence rates, approximately 40% of women and 45% of men in Canada will develop cancer over the course of their lives and approximately one in four Canadians will succumb to the disease. The most common form of cancer in men is prostate, while breast cancer is most prevalent amongst women.

1.2 Treatment of Cancer

The three primary methods of cancer treatment are surgery, chemotherapy and radiation therapy (RT). The choice of treatment depends on a number of factors including the location, grade and progression of the disease, but treatment often involves a combination of therapeutic methods.² Surgery is a localized therapy that involves incision and the removal of the diseased tissue or organ. It is not practical for cancers that have metastasized. Examples of surgical procedures include mastectomy for breast cancer and prostatectomy for prostate cancer. Chemotherapy is the treatment of cancer with cytotoxic drugs that are intended to kill cancerous cells by interfering with cell division. Unlike localized surgery, chemotherapy is systemic in that it affects the entire body, including healthy tissue.

Radiation therapy is the treatment of cancer with ionizing radiation. Although generally a localized treatment, it may be administered systemically as in the case of total body irradiation (TBI). The most commonly used forms of ionizing radiation are photons and electrons, however, neutrons and heavy ions may also be used. As ionizing radiation travels through a material it imparts

energy through a series of interactions. Radiation dose is defined as the energy imparted per unit mass. The standard unit for quantifying dose is Joules per kilogram (J/kg) or the Gray (Gy). The goal of radiation therapy is the delivery of a lethal or tumoricidal dose to malignant tissue while minimizing the dose to surrounding healthy tissues. Radiotherapy treatment modalities and methods as well as advanced treatment protocols such as image guided radiation therapy (IGRT) and adaptive radiation therapy (ART) will be discussed in the next chapter.

1.3 Medical Image Registration

Medical imaging plays an important role in the diagnosis, treatment, and follow-up of cancer patients, in particular, those treated with radiation. Imaging modalities such as computed tomography (CT), magnetic resonance imaging (MRI) and positron emission tomography (PET) provide an invaluable tool utilized throughout the entire radiation therapy process, however sometimes individual images do not provide all the necessary information required by clinicians. In some instances, it may be necessary to extract the combined medical information in multiple images acquired at different times. This is where image registration and image fusion play an important role in radiation therapy. Although the two terms are often used interchangeably, they are inherently different concepts. Image registration is the process of establishing mathematical correspondence between identical points in two or more images, while image fusion is the combined display of the registered images.

Medical image registration is used for a number of different applications in radiation therapy, a selection of which provide the basis for this thesis. It is often classified based on the type of images being registered. For example, inter-modality is the term used to describe registration in which images from different modalities such as CT and MRI are registered. On the other hand, intra-modality registration describes the registration of images acquired from the same imaging modality. Image registration may also be classified as either rigid or deformable. Rigid registration involves only translations and rotations. In deformable or non-rigid image registration, images are deformed to account for anatomical or biological changes that have occurred between imaging studies. A thorough review of image registration theory will be provided in the next chapter.

1.4 Thesis Outline

This thesis provides a thorough investigation encompassing the development, validation and application of image registration in adaptive radiation therapy. In the next chapter, the basic concepts of image registration, radiation therapy and adaptive radiation therapy will be introduced. In chapter 3, we develop a protocol for the validation of commercial deformable registration systems and as a test study, implement it on a system purchased by our clinic. Next, in chapter 4, prostate positioning errors associated with two common registration-based patient positioning strategies used in the treatment of prostate cancer are quantified. This is followed by an investigation of the dosimetric implications of two registration based positioning methods in chapter 5. In

chapter 6, a deformable registration algorithm specifically designed and optimized for use in prostate adaptive radiation therapy is presented. This algorithm is used to account for anatomically-based variations in the comparison of planned and delivered prostate treatment doses in chapter 7. Chapter 8 summarizes the main conclusions of this work and describes avenues of further research. It should be noted that all patient images and associated data were retrospectively anonymized and incorporated into this thesis with local research ethics board consent (ETH 21309, Cross Cancer Institute, Image fusion for cancer, Principal Investigator: B. G. Fallone; ETH 24115, Cross Cancer Institute, Deformable dose registration for tomotherapy prostate patients, Principal Investigator: B. G. Fallone). Finally, all analysis in this thesis was performed using three-dimensional (3D) image sets.

1.5 References

1. Canadian Cancer Society's Steering Committee. Canadian cancer statistics 2009. Toronto (ON): Canadian Cancer Society; 2009.
2. Washington CM, Leaver DT, editors. Principles and practice in radiation therapy, volume 1: introduction to radiation therapy. St. Louis (MO): Mosby-Year Book, Incorporated; 1996.

Chapter 2: Concepts in image registration and adaptive radiation therapy

2.1 Three-dimensional Imaging for Radiation Therapy

Medical imaging plays an important role in the diagnosis, treatment, and follow-up of cancer patients, in particular, those treated with radiation. Typically, 3D medical images used in radiation therapy are digitized and stored in the Digital Imaging and COmmunications in Medicine (DICOM) format¹. They consist of a 3D array of rectangular volume elements or voxels that have pre-defined dimensions and varying intensities that together make up the image. They are often displayed by taking orthogonal cuts or two dimensional (2D) slices in selected image planes. In principle, cross-sectional cuts in any planes may be used, but based on convention; the most common are the sagittal, coronal and axial planes². The sagittal plane is a vertical plane that passes through the erect body, dividing it into left and right portions. Coronal, another vertical plane,

divides the body into anterior and posterior portions. Finally, the axial plane passes through the body horizontally and divides it into superior and inferior portions. Although not a complete list, commonly used imaging modalities in radiation therapy are computed tomography (CT), magnetic resonance imaging (MRI), positron emission tomography (PET), nuclear medicine and ultrasound. Each modality yields different information about the state of the patient and the disease. Resources permitting, each modality that provides clinically useful information necessary to optimize the treatment of each individual patient should be used. Basic concepts in CT, MRI and PET will be discussed briefly. General nuclear medicine and ultrasound are not directly relevant to this thesis and will be excluded from further discussion.

2.1.1 Computed Tomography

Conventional radiography or x-ray imaging is based on the physical principle that materials of varying densities will attenuate x-ray photons by differing amounts. For example, high density bone will attenuate x-rays more than low density lung, resulting in observable contrast between the two tissue types on an x-ray film. Computed tomography relies on the acquisition of multiple radiographic images or projections at different angles. In 1917, Radon³ demonstrated mathematically that the interior of an object could be reconstructed using an infinite number of projections of the object. In other words, if a series of x-ray images are taken at different angles around a patient, the interior of that patient can be reconstructed. The first clinical CT scanner, developed by

Hounsfield,⁴ consisted of one x-ray source and one detector and was capable of producing one 2D slice in approximately five minutes. Since then, CT technology has progressed and scanners today consist of a rotating x-ray source and multiple arrays of detectors that completely surround the patient. They can simultaneously acquire upwards of 64 slices per source rotation and can reconstruct full 3D images in a matter of seconds. CT systems are often classified based on the shape and energy of the x-ray beam. The x-ray beam can either be fan or cone shaped and will have energies in either the kilovoltage (kVCT) or the megavoltage range (MVCT). The unit for the intensity for each voxel in a CT image, often referred to as a CT number, is called a Hounsfield unit and is based on the attenuation properties of the materials comprising each voxel.

For each tissue type:

$$\text{CT \#} = K \frac{\mu_t - \mu_w}{\mu_w}, \quad 2.1$$

where μ_t is the linear attenuation coefficient of the tissue, μ_w is the linear attenuation coefficient of water and K is a constant, which equals 1000 for Hounsfield units. By definition, the value of water is zero, while less attenuating materials such as lung have lower values and greater attenuating materials such as bone have larger values. Sample pelvic kVCT images are depicted in figure 2-1 and approximate Hounsfield units for various tissues⁵ are listed in table 2-1.

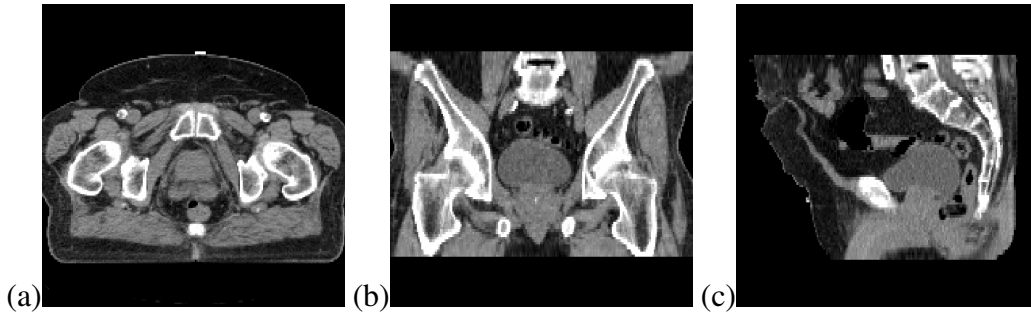


Figure 2-1. Sample (a) axial, (b) coronal and (c) sagittal slices of a 3D male pelvic CT image. Higher x-ray attenuating objects such as bone appear white, while lower attenuating objects such as air are dark.

Table 2-1. Approximate Hounsfield units or CT numbers for various tissues.

Tissue	CT Number
Dense bone	1000
Muscle	50
Blood	20
Water	0
Fat	-100
Lungs	-200
Air	-1000

CT is the primary imaging modality utilized in radiation therapy because Hounsfield units are strongly dependent on electron density, a physical parameter required for radiation dose calculation. The source of this dependence can be explained with an understanding of the photoelectric effect and the Compton effect, the two predominant physical processes by which CT x-rays are attenuated

in a patient. In the photoelectric interaction, an x-ray is completely absorbed and transfers all of its energy to an atomic electron, whereas in the Compton effect, the x-ray deflects from its original path as it transfers only some of its energy to an electron. For the energies used in CT systems, the Compton effect is the dominant interaction in human tissue and Compton cross-sections are dependent on electron density. Unfortunately, the electron densities of different soft tissue types have little variability meaning that CT images suffer from limited soft tissue contrast, sometimes making it difficult for clinicians to accurately delineate tumours and other anatomic structures. The soft tissue contrast that is present in CT images is due to small variability in photoelectric interaction cross-sections amongst different soft tissues. In addition, the contribution of the photoelectric effect to x-ray attenuation reduces as energies are increased from the kV to MV range, as such; MVCT images have less soft tissue contrast than images acquired on a kVCT system.

2.1.2 Magnetic Resonance Imaging

MRI is based on the concept of nuclear magnetic resonance (NMR). The nucleus of hydrogen and some other atoms in the human body have a physical property referred to as magnetic spin. They can be thought of as being tiny magnets and in the absence of any external interactions, the magnets all point in random directions. Now, suppose a strong, uniform and static magnetic field denoted by \mathbf{B}_0 is applied to these atomic nuclei. The little magnets will align in the direction of \mathbf{B}_0 producing what is known as a net magnetization vector \mathbf{M} . By

repeatedly applying a specific radiofrequency (RF) pulse, the net magnetization vector can be made to slowly tip away from its original direction until the pulses are turned off. After turning off the RF pulses, the net magnetization vector will slowly decay and the rate of decay is dependent on two physical quantities referred to as the longitudinal relaxation time (T1) and the transverse relaxation time (T2). Transverse relaxation is due to the dephasing of \mathbf{M} as a result of micromagnetic inhomogeneities, while longitudinal relaxation represents the decay of \mathbf{M} back to its original direction. The exact values of T1 and T2 are dependent on the local electronic environments of the excited nuclei and are different for each type of tissue in the human body. Generating purely T1 or T2 parameter images is technically challenging and time consuming, however, using a complex series of magnetic fields and RF pulse sequences, 3D MRI images can be generated that depend on these two quantities. An image whose intensities are mainly dependent on T1 values is referred to as a T1-weighted image, while an image predominantly dependent on T2 values is a T2-weighted image. The choice of acquiring T1-weighted or T2-weighted images often depends on which part of the patient anatomy is being imaged.

Unlike CT images, MRI images have excellent soft tissue contrast and for many tumours, significant contrast between normal and malignant tissue. This is due to the large differences in T1 and T2 values amongst different tissue types as well as healthy and cancerous tissue. Factors affecting the values of T1 and T2 relaxation times include the motion, size and interactions of the molecules containing the excited nuclei and for our discussion the most important of those

are molecular interactions. The dominant source of tissue contrast in MRI is from variations in water molecule relaxation times within different tissue types. Free water molecules that are not bound to surrounding macromolecules are less susceptible to disruptions in their local magnetic field environments and tend to have large T1 and T2 values. A common characteristic of cancerous tissue is increased water content, and with increased concentrations of water molecules relative to the number of surrounding organic molecules, the ratio of free to bound water molecules is greater in malignant than in healthy tissue. As a result, most tumours have a longer T1 and T2 relaxation times than surrounding healthy tissue. Sample T1-weighted pelvic MRI images are shown in figure 2-2. MR imagers are often classified by their B_0 magnetic field strength in units of Tesla (T). Most clinical systems and those used in this project have B_0 values of either 1.5 T or 3 T. In general, the stronger the magnetic field, the better the image quality.

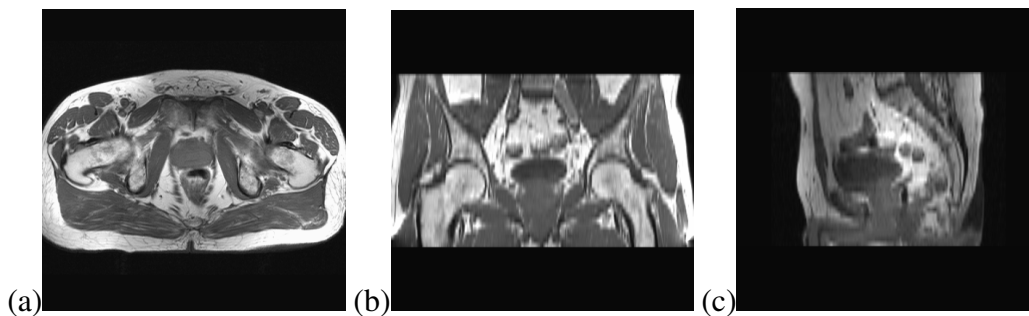


Figure 2-2. Sample (a) axial, (b) coronal and (c) sagittal slices of a 3D T1-weighted male pelvic MRI. Note the significant improvement in soft tissue contrast as compared to the CT image in figure 2-1.

2.1.3 Positron Emission Tomography

PET imaging is based on the differential uptake of radiopharmaceuticals in the body. Radiopharmaceuticals are produced by attaching a radioactive atom to a useful pharmaceutical or chemical. The most commonly used in oncologic imaging is fluorodeoxyglucose (FDG), which is labelled with a radioactive fluorine atom (F-18). When F-18 undergoes radioactive decay, it emits an extremely reactive sub-atomic particle called a positron. When a positron encounters an electron, the two particles are transformed into two 511 kilo-electron Volt (keV) photons that are emitted in nearly opposite directions in a process called annihilation. A patient, after being injected with an FDG solution is placed in the PET scanner which consists of a number of rings of detectors. When a positron annihilates, the two 511 keV photons may be detected by detectors, defining a line of response (LOR) for the two detectors. The positron annihilation is assumed to have occurred somewhere along the LOR. After millions of LOR's are collected, vendor specific image reconstruction methods are employed to produce a representation of the 3D distribution of activity within the field of view (FOV) of the scanner. Since different human organs and tissues take up differing amounts of FDG, by detecting millions of annihilation events, an image can be produced that depicts the differential FDG uptake. FDG uptake reflects levels of glucose metabolism in tissue and due to the uncontrolled reproduction of malignant cells; cancerous cells take up considerably more FDG than surrounding healthy cells. It should be noted that although the physics of the annihilation process limits image resolution, these systems have very high

sensitivity. The high sensitivity of PET imaging is useful for detecting cancerous spread or metastases that are not easily visualized by other imaging modalities. A sample lung FDG-PET image is shown in figure 2-3.

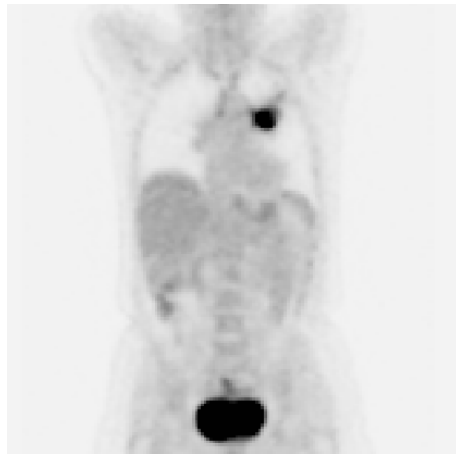


Figure 2-3. Coronal slice of a sample 3D FDG-PET image. The dark region of high FDG uptake at the top of the image is a malignancy. FDG is eliminated biologically through the renal system; hence the bladder at the bottom of the image also contains large concentrations of FDG.

2.2 Image Registration Overview

2.2.1 Notation

Image registration is the process of aligning images so that corresponding features overlap.^{6,7} Medical images used in radiation therapy are predominantly digital and the registration of medical images is a computational problem. In its simplest form, image registration requires two images and a set of instructions for solving the problem, often referred to as an algorithm. Mathematically, the two images can be denoted by their spatial supports, \mathbf{x}_1 and \mathbf{x}_0 , each of which are a

3D array of voxel locations (x, y, z) , and by their corresponding intensities $I(\mathbf{x}_1)$ and $I(\mathbf{x}_0)$. Throughout this thesis, the terms source and target will be used to refer to the two images involved in registration.⁸ The goal of registration is to determine the transformation \mathbf{T} that maps points from the source image \mathbf{x}_1 to homologous points in the target image \mathbf{x}_0 . This relationship can be expressed by the equation:

$$\mathbf{x}_0 = \mathbf{T}(\mathbf{x}_1). \quad 2.2$$

The transformation \mathbf{T} is defined over a finite domain which can be comprised of entire images or a smaller section of one of the images, often referred to as a mask. We will denote the registration domains of the source and target images as Ω_1 and Ω_0 , respectively.

2.2.2 Types of Registration Algorithms

A wide range of image registration algorithms have been developed by many researchers, some of which have gone on to become clinically implemented. In general, image registration algorithms are often classified as either feature based or voxel based. Feature based algorithms are often divided into two groups depending on whether they utilize points or surfaces in achieving image correspondence. Point based registration involves the identification of corresponding point landmarks or fiducials upon which the algorithm determines the transformation \mathbf{T} that minimizes the distances between corresponding points on the images being registered. Landmarks may consist of identifiable anatomical points or objects either placed externally on the patient or surgically

implanted in the patient prior to imaging. Surface based algorithms operate in a similar manner, except that the distance between corresponding boundaries or surfaces is minimized when registering images. On the other hand, voxel based methods take an entirely different approach. Instead of using identifiable structures, voxel based registration relies on the intensity information contained in the images being registered.

2.2.3 Image Registration Framework

Considering the vast array of image registration strategies that have been developed, it is difficult, if not impossible, to summarize the methodologies into an all encompassing general framework. However, the flowchart in figure 2-4 is representative of a significant number of algorithms including those utilized in this thesis. Although not required by all algorithms, image pre-processing entails any processing to prepare or improve the images for registration and is the first step performed in image registration. Upon completion of any pre-processing steps, an iterative process to achieve correspondence will ensue as follows. An initial transformation is applied to the source image which is then interpolated to have the same resolution and geometry as the target image. The transformation can be assumed to be either rigid or deformable. Next, a cost function that provides a measure of correspondence is evaluated for the aligned images. Depending on the implementation, all voxels or a random sample of voxels within the registration domain can be used in cost function evaluation. An optimizer then determines if the value of the cost function is optimized and if it concludes

that the potential for improvement exists, the transformation is updated. This process continues until the optimal cost function is found, at which point the algorithm outputs the transformed source image.

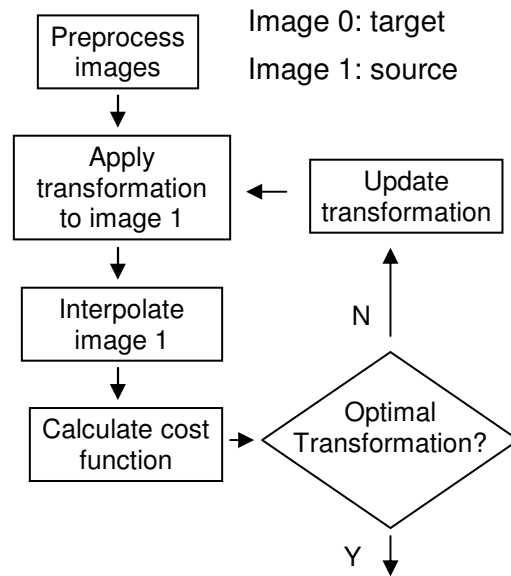


Figure 2-4. Flowchart illustrating the steps involved in a typical image registration algorithm.

2.3 Components of an Image Registration Algorithm

The image registration framework presented in figure 2-4 consists of five separate components (image pre-processing, transformations, cost functions, interpolation and optimization), each of which will be described in further detail.

2.3.1 Image Pre-processing

Examples of pre-processing steps include the manual or automatic delineation of points or surfaces in feature based algorithms,^{9,10} or the application

of a filter to reduce image noise.^{11,12} A common pre-processing step is the cropping or masking of relevant image regions such as the pelvic anatomy,^{13,14} bony anatomy¹⁵ or other regions of interest (ROI)¹⁶⁻¹⁸ in order to reduce the complexity of registration or ensure specific image regions are aligned after registration.

2.3.2 Transformations

Various transformations \mathbf{T} can be assumed to define the correspondence relationship between the source and target images. They can be either rigid or deformable and deformable transforms can be divided based on whether they are parametric or non-parametric. Parametric transformations are continuous functions while non-parametric transformations are defined by a set of discrete displacement vectors.

The simplest rigid transformation commonly used in medical image registration is the translation transform in which the location of each voxel in \mathbf{x}_1 is shifted by a translation \mathbf{t} :

$$\mathbf{T}^{trans}(\mathbf{x}_1) = \mathbf{x}_1 + \mathbf{t}. \quad 2.3$$

This transformation is described by three parameters or degrees of freedom (DOF) denoted by $\mathbf{t} = (t_x, t_y, t_z)$, where each DOF corresponds to a shift in each of the three directions (x, y, z) in the Cartesian coordinate system.

Instead of assuming simply translations, rigid transformations can also be described by a rotational component whereby rotations are allowed about each of

the three co-ordinate axes. This is referred to as the Euler transform and can be expressed mathematically by:

$$\mathbf{T}^{euler}(\mathbf{x}_1) = \mathbf{R}\mathbf{x}_1 + \mathbf{t}, \quad 2.4$$

where \mathbf{R} is the rotation matrix. Adding three rotational parameters in addition to the three translational parameters, the Euler transform is described by six DOF. Although useful in many medical applications, circumstances often dictate that the relationship between images cannot be sufficiently described by six DOF and warping of the source image is required to achieve the desired correspondence with the target image.

The most basic deformable transform is the affine transform in which the Euler transform is extended to allow for scaling and shearing. This twelve DOF transform is often referred to as a first order polynomial transformation. By adding additional DOF, the affine transform can be extended whereby the transform is defined by second (30 DOF), third (60 DOF), fourth (105 DOF) or higher order polynomials.⁸ Such higher order polynomials are limited in that they can model only global deformations and fail to accommodate smaller localized anatomical variations. This is also a limitation of the commonly used thin-plate spline (TPS) transformation.¹⁹ Thin-plate splines, which are defined by a series of control points, have infinite support, meaning that each control point has a global influence on the transformation.

The ability to account for local variations that occur independently of the surrounding patient anatomy is an important requirement in many deformable registration applications. A common approach is the use of freeform

deformations (FFD) based on locally controlled functions such as B-splines.²⁰

B-splines are defined by an $n_x \times n_y \times n_z$ mesh of control points $\phi_{i,j,k}$ with initial uniform spacing $\delta_x, \delta_y, \delta_z$. By modifying the location of each individual control point $\phi_{i,j,k}$, the source image is deformed by a displacement field given by:

$$\mathbf{T}^{B\text{spline}} = \sum_{l=0}^3 \sum_{m=0}^3 \sum_{n=0}^3 B_l(u) B_m(v) B_n(w) \phi_{i+l,j+m,k+n}, \quad 2.5$$

$$\text{where } i = \left\lfloor \frac{x}{\delta_x} \right\rfloor - 1, \quad j = \left\lfloor \frac{y}{\delta_y} \right\rfloor - 1, \quad k = \left\lfloor \frac{z}{\delta_z} \right\rfloor - 1, \quad u = \frac{x}{\delta_x} - \left\lfloor \frac{x}{\delta_x} \right\rfloor, \quad v = \frac{y}{\delta_y} - \left\lfloor \frac{y}{\delta_y} \right\rfloor,$$

$$w = \frac{z}{\delta_z} - \left\lfloor \frac{z}{\delta_z} \right\rfloor \text{ and } B_l \text{ represents the } l\text{-th basis function of the B-spline:}$$

$$B_0(u) = (1 - u)^3 / 6,$$

$$B_1(u) = (3u^3 - 6u^2 + 4) / 6,$$

$$B_2(u) = (-3u^3 + 3u^2 + 3u + 1) / 6,$$

$$B_3(u) = u^3 / 6.$$

B-spline basis functions have limited support, meaning that changing the location of one control point affects the transformation only in the local neighbourhood of that control point. Amongst their numerous applications, they have been used in the registration of breast,²¹ pelvic^{13,14} and thoracic²² images.

Another approach used in deformable registration is to assume a non-parametric transform in which the transformation is defined by a discrete set of displacement vectors instead of a continuous function. Warping an image using a

discrete function can be advantageous in that it provides considerable freedom to model large local deformations, but deformable registration algorithms that assume a non-parametric transformation are prone to generating physically unrealistic deformations. To overcome this, a regularization term or penalty function is often added to the cost function to limit physically unrealistic image warping. Regularization terms based on viscous fluid,^{23,24} optical flow^{25,26} and diffusion²⁷⁻²⁹ equations have been proposed.

2.3.3 Cost Functions

Computationally, image registration algorithms are designed to find the transformation that optimizes a cost function that in some way measures the correspondence between the images being registered. In feature based algorithms, this cost function is often the distance between the corresponding features whereas voxel based algorithms often use what is referred to as a similarity measure. A few common examples of similarity measure cost functions will be discussed.

Perhaps the simplest similarity measures are those based on the minimization of the differences in intensities between overlapping voxels. Consider the scenario where two identical images are being registered. If they are perfectly overlapped, the difference in voxel intensity between each overlapping voxel in the two images will be nil. On the other hand, if the images become misaligned, the intensity differences between each overlapping voxel will no longer be zero. This concept can be translated to the clinically relevant

situation where the patient images are no longer identical, but correct image overlap will still minimize the intensity differences. Commonly used cost functions include the mean square differences (MSD) and the mean absolute differences (MAD) similarity measures. Mathematically, they are described by:

$$\text{MSD}(\mathbf{x}_0, \mathbf{x}_1) = \frac{1}{N_V} \sum_{\Omega_0} (I(\mathbf{x}_0) - I(\mathbf{x}_1))^2 \quad 2.6$$

and:

$$\text{MAD}(\mathbf{x}_0, \mathbf{x}_1) = \frac{1}{N_V} \sum_{\Omega_0} |I(\mathbf{x}_0) - I(\mathbf{x}_1)|, \quad 2.7$$

where N_V is the number of voxels in Ω_0 . It has been demonstrated that these metrics are ideal when the images differ by only Gaussian noise, which will never be the case in inter-modality registration.⁸ As such; the use of metrics based on intensity differences is limited to intra-modality registration.

Another class of cost functions are those based on the correlation between images. Perhaps the most common is the correlation coefficient (CC) defined by:

$$\text{CC}(\mathbf{x}_0, \mathbf{x}_1) = \frac{\sum_{\Omega_0} (I(\mathbf{x}_0) - \bar{I}_0) \cdot (I(\mathbf{x}_1) - \bar{I}_1)}{\left[\sum_{\Omega_0} (I(\mathbf{x}_0) - \bar{I}_0)^2 \cdot \sum_{\Omega_0} (I(\mathbf{x}_1) - \bar{I}_1)^2 \right]^{1/2}}, \quad 2.8$$

where \bar{I}_0 and \bar{I}_1 are the mean voxel intensities in the region Ω_0 in images \mathbf{x}_0 and \mathbf{x}_1 , respectively. Like MSD and MAD, CC is based on voxel intensities and is only suitable for intra-modality registration. A slightly different approach is required for voxel based inter-modality registration.

A number of cost functions used in medical image registration are based on information theory³⁰ and the joint probability histogram. Assume the intensities $I(\mathbf{x}_0)$ of the voxels in Ω_0 , which for simplicity we will denote by a , range in value from a_{\min} to a_{\max} . Similarly, intensities $I(\mathbf{x}_1)$ range in value from b_{\min} to b_{\max} . The joint probability histogram is generated by plotting the number of overlapping voxels with intensities a in \mathbf{x}_0 and b in \mathbf{x}_1 as a function of the intensities themselves. The joint probability histogram, denoted by $p(a,b)$ is normalized by dividing by N_v , the number of voxels in Ω_0 . Registration algorithms based on information theory exploit the fact that mis-registration results in dispersion or blurring of the joint probability histogram.

The most common information theoretic cost function used in image registration is mutual information (MI),³¹⁻³³ which is expressed by:

$$\text{MI}(\mathbf{x}_0, \mathbf{x}_1) = \sum_a \sum_b p(a,b) \log \frac{p(a,b)}{p(a) \cdot p(b)}. \quad 2.9$$

The terms $p(a)$ and $p(b)$ are the marginal image probability histograms which are simply sums over $p(a,b)$ and given by:

$$p(a) = \sum_b p(a,b) \quad 2.10$$

and

$$p(b) = \sum_a p(a,b). \quad 2.11$$

Studholme³⁴ has proposed a modified version, normalized mutual information (NMI):

$$\text{NMI}(\mathbf{x}_0, \mathbf{x}_1) = \frac{\sum_a p(a) \log p(a) + \sum_b p(b) \log p(b)}{\sum_a \sum_b p(a, b) \log p(a, b)}, \quad 2.12$$

which has been demonstrated to be more robust than standard mutual information.

Another set of cost functions dependent on the joint probability histogram are those based on the correlation ratio. Like mutual information and normalized mutual information, these functions are also suitable for inter-modality registration. The correlation ratio is defined by:

$$\text{CR}(\mathbf{x}_0, \mathbf{x}_1) = 1 - \frac{1}{\sigma^2} \sum_a \sigma_a^2 p(a) \quad 2.13$$

where

$$\sigma^2 = \sum_b b^2 p(b) - \left[\sum_b b \cdot p(b) \right]^2$$

and

$$\sigma_a^2 = \frac{1}{p(a)} \sum_b b^2 p(a, b) - \left[\frac{1}{p(a)} \sum_b b \cdot p(a, b) \right]^2.$$

Unlike all the other metrics introduced in this section, the correlation ratio is not symmetric, meaning that $\text{CR}(\mathbf{x}_0, \mathbf{x}_1) \neq \text{CR}(\mathbf{x}_1, \mathbf{x}_0)$. A symmetric correlation ratio (SCR) was introduced by Lau *et al.*¹¹:

$$\text{SCR}(\mathbf{x}_0, \mathbf{x}_1) = \text{CR}(\mathbf{x}_0, \mathbf{x}_1) + \text{CR}(\mathbf{x}_1, \mathbf{x}_0). \quad 2.14$$

2.3.4 Interpolation

When a voxel in the source image \mathbf{x}_1 is mapped by transformation \mathbf{T} , its resultant position will generally not correspond to the centre of a voxel in the

target image \mathbf{x}_0 . As such, interpolation of source image intensity values is required after each application of transform \mathbf{T} . This occurs multiple times during image registration and when outputting the final transformed source image. As is the case with many computational procedures, interpolation requires a trade-off between accuracy and speed. The simplest interpolation scheme is nearest neighbour in which the voxel in the source image nearest to the voxel of interest in the target image is found and the intensity of that voxel is assigned. Perhaps the most popular technique in medical image registration is linear interpolation whereby the intensity of a voxel is determined by a weighted combination of the intensities of its adjacent neighbours. More sophisticated interpolators such as cubic spline, B-spline and sinc, although more accurate, include more neighbouring voxels when evaluating intensity values and consequently tend to be slower. Often a lower order interpolation kernel such as nearest neighbour or linear is used during registration, but a higher order interpolator is employed when outputting the final transformed source image after registration is complete.³³

2.3.5 Optimization

Image registration in its most common implementation is essentially a standard optimization problem that requires an optimizer to drive the procedure. The optimizer is the workhorse that strategically determines the transformation that optimizes the cost function during registration. Optimization algorithms are often classified as either gradient based or non-gradient based depending on whether the derivative of the cost function is evaluated.³⁵ In this project, we use

the non-gradient based Nelder-Mead simplex optimizer³⁶ for rigid registration and the gradient based limited memory Broyden-Fletcher-Goldfarb-Shanno with simple bounds (L-BFGS-B) optimization algorithm³⁷ for deformable registration. The finer details of these and other optimization algorithms are beyond the scope of this thesis, however, a brief outline of the techniques are given in Appendix A. In general, the selection of the optimizer used in image registration depends on a number of factors including the image characteristics, the number of DOF and the cost function.

2.4 Image Registration Software

Two software packages had instrumental roles in the research conducted throughout this thesis. One is a commercially available image registration system purchased by our laboratory, while the other is an open-source software toolkit. Both will be introduced in this section.

2.4.1 Reveal-MVS

Two Reveal-MVS (Ed. 6) Fusion Workstation (Mirada Solutions, Ltd, Oxford, UK) systems were acquired by the Cross Cancer Institute in the fall of 2003. Reveal-MVS is a stand alone software package operating on a PC – Windows (XP) platform. Each system has two Intel Xeon 2.8 GHz processors and 3 GB of RAM. The Reveal-MVS software has landmark based rigid, automatic rigid, landmark based deformable and automatic deformable

registration capabilities, as well as a separate PET/CT scanner automatic motion correction option.

2.4.2 Insight Toolkit (ITK)

The Insight Toolkit (ITK) is an open-source software toolkit for performing image processing, registration and segmentation.³⁸ It consists of a collection of cross-platform, objected-orientated C++ classes that can be implemented in user developed software. All in-house developed registration software referred to in this thesis was built with the aid of ITK.

2.5 Radiation Therapy Preparation

The biological effects of delivering radiation to human cells, both healthy and cancerous, play a fundamental role in how radiation therapy is administered. Radiobiology, the study of the biological effects of radiation, dictates that the prescription dose in curative radiation treatments should be delivered in small doses over multiple fractions instead of in one high dose treatment.³⁹ Typically, radiation therapy patients will receive twenty-five or more daily fractions over a period of five or more weeks. The steps carried out prior to treatment delivery will be discussed in this section.

2.5.1 Immobilization and Simulation

An important element of radiation therapy is daily patient positioning. To ensure proper treatment delivery, patients should be positioned identically during

each daily treatment fraction. Although a simple concept, it is very difficult to achieve in clinical practice. Reproducibility of patient positioning is often aided with the use of immobilization devices. They may be generic devices as simple as straps or knee rests or they may be more complex such as casts customized for each individual patient. The selection of immobilization devices for each patient often depends on the type of cancer and the treatment site. Once immobilization devices have been put in place, a 3D kVCT of the patient in treatment position is acquired. This process is often referred to as simulation as it simulates or mimics each daily treatment fraction. This image is called the patient planning CT and is required for calculation of the radiation dose delivered to each patient. Depending on the treatment, images acquired on other modalities, such as PET for lung patients^{22,40,41} and MRI for prostate patients^{9,42} may be registered to the planning CT to improve the identification of anatomical structures.

2.5.2 Target Definition and Nomenclature

The next step in treatment preparation is the contouring of regions of interest (ROI) on the planning CT. These ROI include both the tumour and any surrounding dose sensitive critical structures that should receive limited radiation, often referred to as organs at risk (OAR). A number of terms and a standard nomenclature recommended by the International Commission on Radiation Units and Measurements (ICRU) are used to define the target volumes.⁴³ The term gross tumour volume (GTV) is the “gross palpable or visible/demonstrable extent

and location of malignant tumour”. The clinical target volume (CTV) is the “tissue volume that contains a demonstrable GTV and/or subclinical microscopic malignant disease that must be eliminated”. The final target volume is the planning target volume (PTV). The PTV “is a geometrical concept, and it is defined to select appropriate beam sizes and beam arrangements, taking into consideration the net effect of all the possible geometrical variations and inaccuracies in order to ensure that the prescribed dose is actually absorbed in the CTV”.

2.5.3 Treatment Planning

After ROI delineation, a custom treatment plan is generated for each individual patient. Treatment plans are generated using a dedicated computer referred to as a treatment planning system. The majority of current clinical treatment planning systems use a process called inverse planning. In inverse planning, a radiation oncologist prescribes a radiation dose to the PTV and also sets constraints to limit the dose to the surrounding critical structures. Based on the prescribed constraints and the machine used to deliver the radiation, the treatment planning system determines a suitable combination of beam directions and shapes that best satisfies the constraints. The system also calculates the radiation dose delivered to each voxel in the planning CT, generating what is referred to as a 3D dose distribution. The planning process also involves determination of the number of treatment fractions and the dates they will be delivered. Finally, the completed treatment plan is approved by a radiation

oncologist, the numbers are double checked by a physicist and the patient commences treatment.

2.6 Radiation Therapy Delivery

Radiation is delivered to cancer patients through either radioimmunoglobulintherapy, brachytherapy, or teletherapy. In teletherapy, radiation is delivered externally, while in the former two methods, the source of radiation is injected or inserted inside the patient. The delivery method for the vast majority of radiation therapy patients and the primary focus of this project is teletherapy. The various machines used for teletherapy include orthovoltage units, cobalt-60 units and linear accelerators. Linear accelerators may be either the very common C-gantry type or helical tomotherapy. Both orthovoltage and cobalt-60 units are in use at our clinic, but the majority of teletherapy treatments are delivered on either C-gantry type linear accelerators⁴⁴ or helical tomotherapy⁴⁵ systems. These two systems, which will be discussed in further detail, are illustrated in figure 2-5.

2.6.1 Linear Accelerator –C – Gantry Type

The linear accelerator (linac) uses high-frequency electromagnetic waves to accelerate electrons to extremely high energies. Low energy electrons produced by an electron gun are accelerated in a waveguide by absorbing the energy from pulsed microwaves generated in either a magnetron or klystron.⁴⁴ After reaching megavoltage energies, a thin ~3 mm wide beam of electrons

emerges from the accelerating structure into the linac's treatment head. Depending on whether high energy x-rays or high energy electrons are used for treatment, the electron pencil beam strikes either an x-ray target or an electron scattering foil. For x-ray treatments, electrons incident on the target produce x-rays through a process known as bremsstrahlung. In electron treatments, the electron pencil beam is scattered by the scattering foil in order to spread the electron beam. The high energy x-rays or electrons then pass through a system of collimators that shape the radiation beam, which emerges from the gantry and treats the patient lying on the treatment couch. The treatment couch, collimation system, and the gantry are all designed to rotate 360 degrees in order to allow a wide range of potential treatment setups. C-gantry linacs are very versatile in terms of treatment accessories and delivery. They are capable of conventional radiation delivery as well as advanced intensity modulated radiation therapy (IMRT) where radiation dose is highly tailored for individual patients by controlling or modulating the radiation beam's intensity. In addition, many C-gantry linacs have CT imagers mounted on their gantries.

2.6.2 Helical Tomotherapy

The Hi*Art II (TomoTherapy, Inc., Madison WI) helical tomotherapy unit shown in figure 2-5 was specifically designed to deliver intensity modulated radiation therapy (IMRT) using image guidance. In addition to treatment delivery, the system includes its own dedicated thirty-two processor treatment planning system and is capable of acquiring megavoltage CT (MVCT) images of

a patient while in treatment position. It consists of a conventional accelerator waveguide and an array of detectors mounted opposite each other on a ring gantry. During treatment, the gantry continuously rotates and the treatment couch continuously translates through the gantry, delivering radiation in a helical manner. Treatments are delivered with a 6 MV fan shaped x-ray beam. An added feature of the Hi*Art II system is its inherent Planned Adaptive software which uses the planned beam delivery characteristics to recalculate the dose distribution on the 3D pre-treatment MVCT.

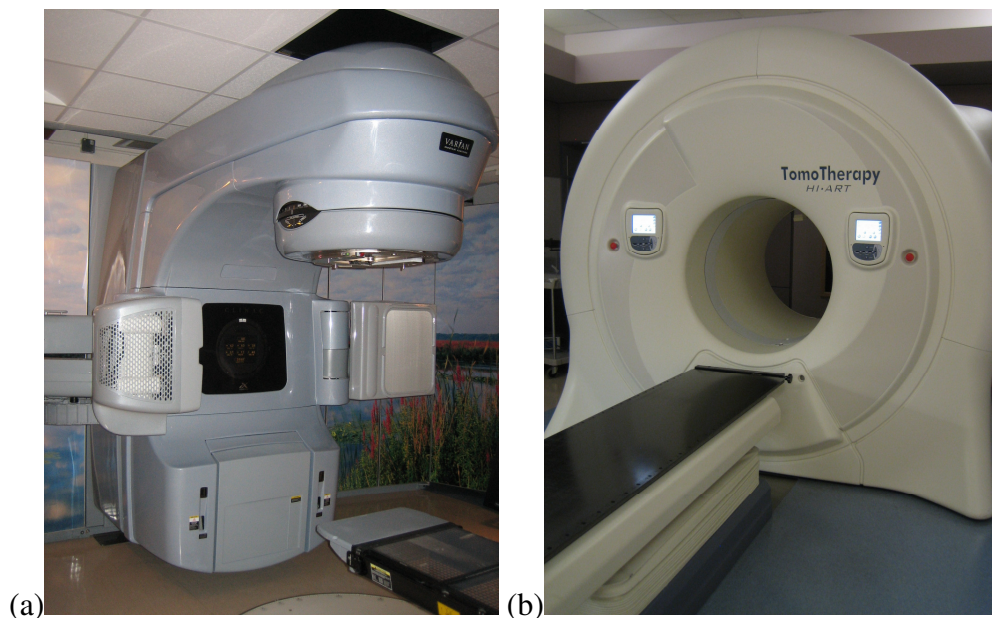


Figure 2-5. (a) Varian Silhouette (Varian Medical Systems, Inc., Palo Alto, CA) linear accelerator with C-type gantry and (b) Hi*Art II (TomoTherapy, Inc., Madison, WI) helical tomotherapy system.

2.7 Advanced Radiation Therapy Protocols

The major problem encountered in delivering fractionated radiation therapy has been alluded to a number of times in this thesis, but will now be discussed in more detail. Treatments are based on radiation doses calculated on a planning CT, which provides only one snapshot of the patient's anatomy. Over weeks of treatment, patients lose weight, tumours shrink, and internal organs move or change shape making it impossible to perfectly reproduce that one anatomical snapshot in time on a daily basis. As a result of anatomical variations and errors in daily patient positioning, the planned dose distribution will never be delivered exactly. External markers and laser localization systems aid in patient positioning, but they cannot address internal anatomical variations. A tremendous amount of monetary and human resources are expended annually towards the research and implementation of solutions to reduce this problem. As a result, two progressively developing concepts, image guided radiation therapy (IGRT) and adaptive radiation therapy (ART) have arisen.

2.7.1 Image Guided Radiation Therapy

Frequent daily imaging while the patient is positioned for treatment on the treatment machine, and making decisions based on the images is referred to as image guided radiation therapy.⁴⁶ Early IGRT protocols involved using the treatment x-ray beam to acquire 2D radiographic images of the patient in treatment position. Based on the films or digital versions called electronic portal images (EPI), patients could be repositioned based on anatomical markers such as

bony anatomy.⁴⁷⁻⁵² Although an improvement over external markers, these images provide very little soft tissue contrast and if the PTV has moved with respect to surrounding bony anatomy, there is a chance that the target will be missed. IGRT has changed dramatically in the past decade with the incorporation of CT imagers into radiation therapy treatment rooms.^{45,53-57} These include CT imagers mounted on linacs as well as the Hi*Art II helical tomotherapy system. By acquiring a 3D CT image with the patient in treatment position immediately prior to each fraction, image registration can be used to find anatomical correspondence between the treatment CT and the original planning CT. Based on the registration, the patient can be re-positioned to increase the effectiveness of treatment. IGRT significantly increases the probability that the target receives the prescription dose, but still fails to address any differences between planned and delivered doses to the target or surrounding critical structures. These problems provide the basis for adaptive radiation therapy.

2.7.2 Adaptive Radiation Therapy

The concept of adaptive radiation therapy was first suggested in 1997 when Yan *et al.*⁵⁸ proposed the idea of monitoring treatment variations and using them to modify treatment plans over the course of fractionated treatment. Although yet to be fully realized, for more than a decade many researchers have made significant contributions towards succeeding in making ART standard clinical practice. For the purpose of this project, the two most important advancements are the ability to calculate daily treatment dose distributions and

improvements in automatic image registration techniques. It has been demonstrated that by computationally applying the treatment plan to daily treatment CT images, the actual dose distribution delivered during each treatment fraction can accurately be calculated.^{59,60} By using deformable image registration, the dose delivered to each tiny voxel of tissue in the planning CT can be tracked and accumulated over the course of treatment. This concept, referred to as deformable dose registration or dose accumulation,^{10,24,28,61} is illustrated in figure 2-6 for a simplistic schema. Dose accumulation allows for the potential comparison of planned and cumulatively delivered doses to the target and surrounding critical structures after each treatment fraction. If at any point the delivered target dose is insufficient, or the dose delivered to a critical structure is unacceptably high, the treatment plan can be modified. A flowchart highlighting the steps involved in an ideal adaptive radiation therapy protocol is given in figure 2-7.

2.8 Thesis Objectives

At the onset of this project, deformable image registration was a relatively new concept in radiation therapy and it was deemed that prior to using any deformable registration program in IGRT or ART, its accuracy and capabilities must be fully understood. Unfortunately, a standard protocol for the validation of these programs did not and currently, does not exist. The first objective of this project was the development of a protocol to validate commercially available automatic deformable image registration systems and to apply the protocol to a

research system purchased by our laboratory.⁶² Based on the results, we concluded that instead of using one algorithm for all applications of deformable registration in radiation therapy, deformable image registration could potentially be optimized by focusing on one single application. As a result, we chose to concentrate on prostate adaptive radiation therapy on the Hi*Art II helical tomotherapy system. Instead of focusing solely on deformable registration, we opted to address all the image registration components in the ART framework presented in figure 2-7 that apply to prostate treatments on the Hi*Art II system. The next section of this project addresses the issue of registration based daily patient repositioning. We quantified the alignment discrepancies that occur between daily MVCT and planning CT images when using two different automatic rigid image registration schemes. Based on registration alignments, we calculated the errors in daily prostate positioning that would occur if patient repositioning was based on each of the different registration methods.⁶³ After quantifying alignment differences, we investigated the dosimetric implications to the target prostate and the radiation sensitive bladder and rectum for the different automatic registration based daily patient repositioning methods.⁶⁴ Focus then turned from patient positioning to dose accumulation in prostate ART on helical tomotherapy. We developed and validated a deformable registration algorithm specifically designed and optimized for prostate adaptive radiation therapy.⁶⁵ The final objective was the development and application of software that uses our deformable registration algorithm for the purpose of dose accumulation in the comparison of planned and treatment doses for prostate patients on the Hi* Art II

system. In addition, developed image warping software was incorporated into a framework for distortion correction in 3T MRI images proposed by a colleague at our centre.⁶⁶

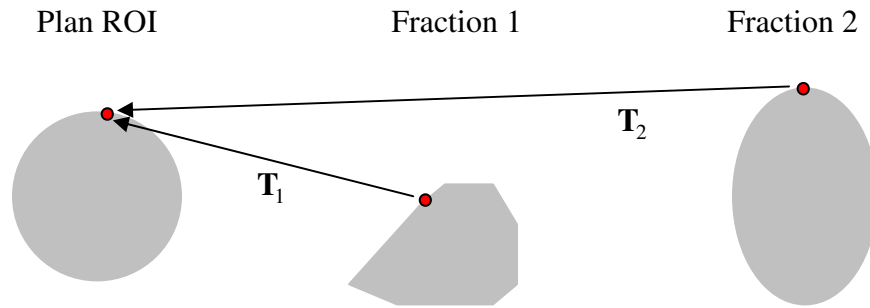


Figure 2-6. Simple schematic demonstrating the process of dose accumulation. Suppose a region of interest (ROI) has changed shape between planning, fraction 1 and fraction 2 CT acquisition. Each anatomical point on the planned ROI (example shown in red) will be in a different location during each fraction. Deformable registration of fraction 1 CT to the planning CT yields the transformation T_1 that maps the position of each anatomical point in the treatment CT to the planning CT. Similarly, deformable registration of the fraction 2 CT to the planning CT yields transformation T_2 . If the dose is reconstructed on each treatment CT, the transformations can be used to map the dose delivered to each anatomical point during each fraction back to the planning CT geometry. This allows for cumulative dose calculation.

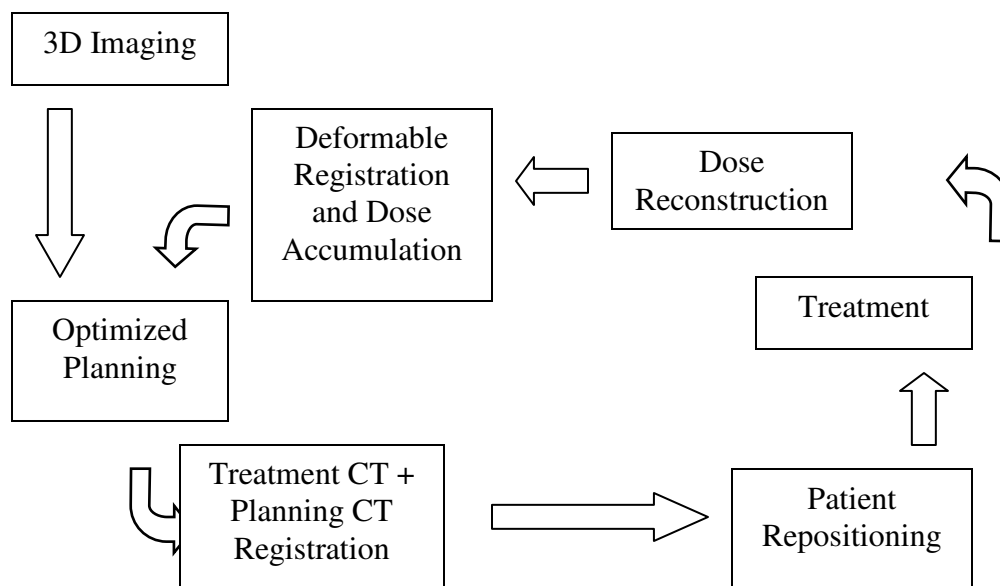


Figure 2-7. Ideal ART framework that provides the basis for this thesis. After patient imaging and optimized planning, a treatment CT is acquired before each daily fraction. Based on the rigid registration of treatment and planning CT images, the patient is repositioned and radiation is delivered. After each fraction, the treatment dose is reconstructed and the accumulated dose is evaluated with the aid of deformable image registration. If at any point, treatment doses are unacceptable, the treatment plan can be re-optimized.

2.9 References

1. DICOM Standards Committee. Digital imaging and communications in medicine (DICOM) part 1: introduction and overview. Rosslyn (VA): National Electrical Manufacturers Association; 2008.
2. Kelley LL, Petersen CM. Sectional anatomy for imaging professionals. 3rd ed. St. Louis (MO): Mosby, Inc; 2007.

3. Radon J. On the determination of functions from their integral values along certain manifolds. *IEEE Trans Med Imag.* 1986;5:170-176.
4. Hounsfield GN. Computerized transverse axial scanning (tomography): part 1. description of system. *British J Radiology.* 1973;46:1016-1022.
5. Bushong SC. Radiological science for technologists: physics, biology, and protection. 7th ed. St. Louis (MO): Mosby, Inc; 2001.
6. Hawkes DJ. Algorithms for radiological image registration and their clinical application. *J Anat.* 1998;193:347-361.
7. Hill DLG, Batchelor PG, Holden M, Hawkes DJ. Medical image registration. *Phys Med Biol.* 2001;46:R1-R45.
8. Hajnal JV, Hill DLG, Hawkes DJ, editors. Medical image registration. Boca Raton (FL): CRC Press LLC; 2001.
9. Kagawa K, Lee WR, Schultheiss TE, Hunt MA, Shaer AH, Hanks GE. Initial clinical assessment of CT-MRI image fusion software in localization of the prostate for 3D conformal radiation therapy. *Int J Radiat Oncol Biol Phys.* 1997;38:319-325.
10. Schaly B, Kempe JA, Bauman GS, Battista JJ, Van Dyk J. Tracking the dose distribution in radiation therapy by accounting for variable anatomy. *Phys Med Biol.* 2004;49:791-805.
11. Lau YH, Braun M, Hutton BF. Non-rigid image registration using a median-filtered coarse-to-fine displacement field and a symmetric correlation ratio. *Phys Med Biol.* 2001;46:1297-1319.

12. Yang D, Chaudhari SR, Goddu SM, Pratt D, Khullar D, Deasy JO, El Naqa I. Deformable registration of abdominal kilovoltage treatment planning CT and tomotherapy daily megavoltage CT for treatment adaptation. *Med Phys.* 2009;36:329-338.
13. Klein S, Staring M, Pluim JPW. Evaluation of optimization methods for nonrigid medical image registration using mutual information and B-splines. *IEEE Trans. Image Process.* 2007;16:2879-2890.
14. Murphy MJ, Wei Z, Fatyga M, Williamson, J, Anscher M, Wallace T, Weiss E. How does CT image noise affect 3D deformable image registration for image-guided radiotherapy planning? *Med Phys.* 2008;35:1145-1153.
15. Ruchala KJ, Olivera GH, Kapatoes JM. Limited-data image registration for radiotherapy positioning and verification. *Int J Radiat Oncol Biol Phys.* 2002;54:592-605.
16. Smitsmans MHP, Wolthaus JWH, Artignan X, de Bois J, Jaffray DA, Lebesque JV, van Herk M. Automatic localization of the prostate for on-line or off-line image-guided radiotherapy. *Int J Radiat Oncol Biol Phys.* 2004;60:623-635.
17. Smitsmans MHP, de Bois J, Sonke JJ, Betgen A, Zijp LJ, Jaffray DA, JV Lebesque, van Herk M. Automatic prostate localization on cone-beam CT scans for high precision image-guided radiotherapy. *Int J Radiat Oncol Biol Phys.* 2005;63:975-984.
18. Court LE, Dong L. Automatic registration of the prostate for computed-tomography-guided radiotherapy. *Med Phys.* 2003;30:2750-2757.

19. Bookstein FL. Principal warps: thin plate splines and the decomposition of deformations. *IEEE Trans Pattern Anal Mach Intell.* 1989;11:567-585.
20. Lee S, Wolberg G, Chwa KY, Shin SY. Image metamorphosis with scattered feature constraints. *IEEE Trans Vis Comp Graph.* 1996;2:337-354.
21. Rueckert D, Sonoda LI, Hayes C, Hill DLG, Leach MO, Hawkes DJ. Nonrigid registration using free-form deformations: application to breast MR images. *IEEE Trans Med Imag.* 1999;18:712-721.
22. Mattes D, Haynor DR, Vesselle H, Lewellen TK, Eubank W, PET-CT image registration in the chest using free-form deformations. *IEEE Trans Med Imag.* 2003;22:120-128.
23. Christensen GE, Rabbitt RD, Miller MI. Deformable templates using large deformation kinematics. *IEEE Trans Image Process.* 1996;5:1435-1447.
24. Foskey M, Davis B, Goyal L, Chang S, Chaney E, Strehl N, Tomei S, Rosenman J, Joshi S. Large deformation three-dimensional image registration in image-guided radiation therapy. *Phys Med Biol.* 2005;50:5869-5892.
25. Horn BPK, Schunck BG. Determining optical flow. *Artific Intell.* 1981;17:185-203.
26. Thirion JP. Image matching as a diffusion process: an analogy with Maxwell's demons. *Med Image Anal.* 1998;2:243-260.
27. Lu W, Chen ML, Olivera GH, Ruchala KJ, Mackie TR. Fast free-form deformable registration via calculus of variations. *Phys Med Biol.* 2004;49:3067-3087.

28. Lu W, Olivera GH, Chen Q, Ruchala KJ, Haimerl J, Meeks SL, Langen KM, Kupelian PA. Deformable registration of the planning image (kVCT) and the daily images (MVCT) for adaptive radiation therapy. *Phys Med Biol.* 2006;51:4357-4374.
29. Gao S, Zhang L, Wang H, de Crevoisier R, Kuban DD, Mohan R, Dong L. A deformable image registration method to handle distended rectums in prostate cancer radiotherapy. *Med Phys.* 2006;33:3304-3312.
30. Shannon CE. A mathematical theory of communication. *Bell System Technical Journal.* 1948;27:623-656.
31. Wells WM, Viola P, Atsumi H, Nakajima S, Kikinis R. Multi-modal volume registration by maximization of mutual information. *Med Imag Anal.* 1996;1:35-51.
32. Maes F, Collignon A, Vandermeulen D, Marchal G, Suetens P. Multimodality image registration by maximization of mutual information. *IEEE Trans Med Imag.* 1997;16:187-198.
33. Pluim JPW, Maintz JBA, Viergever MA. Mutual-information-based registration of medical images: a survey. *IEEE Trans Med Imag.* 2003;22:986-1004
34. Studholme C, Hill DLG, Hawkes DJ. An overlap invariant entropy measure of 3D medical image alignment. *Pattern Recognit.* 1998;32:71-86.
35. Press WH, Teukolsky SA, Vetterling WT, Flannery BP. Numerical recipes in C: the art of scientific computing. 2nd ed. Cambridge (UK): Cambridge University Press; 1992.

36. Nelder JA, Mead R. A simplex method for function minimization. *Computer Journal*. 1965;7:308-313.
37. Byrd RH, Lu P, Nocedal J, Zhu C. A limited memory algorithm for bound constrained optimization. *SIAM J Sci Comput*. 1995;16:1190-1208.
38. Ibanez L, Schroeder W, Ng L, Cates J. *The ITK software guide*. 2nd Ed. Clifton Park (NY): Kitware, Inc.; 2005.
39. Hall EJ. *Radiobiology for the radiologist*. 5th Ed. Philadelphia (PA): Lippincott Williams and Wilkins; 2000.
40. Slomka PJ, Dey D, Przetak C, Aladl UE, Baum RP. Automated 3-dimensional registration of stand-alone ¹⁸F-FDG whole-body PET with CT. *J Nucl Med*. 2003;44:1156-1167.
41. Yap JT, Carney JPJ, Hall NC, Townsend DW. Image-guided cancer therapy using PET/CT. *Cancer J*. 2004;10:221-233.
42. Lian J, Xing L, Hunjan S, Dumoulin C, Levin J, Lo A, Watkins R, Rohling K, Giaquinto R, Kim D, Spielman D, Daniel B. Mapping of the prostate in endorectal coil-based MRI/MRSI and CT: a deformable registration and validation study. *Med Phys*. 2004;31:3087-3094.
43. ICRU. ICRU report 62: prescribing, recording, and reporting photon beam therapy (supplement to ICRU report 50). Washington (DC): ICRU; 1999.
44. Greene D, Williams PC. *Linear accelerators for radiation therapy*. 2nd Ed. Bristol (UK): Institute of Physics Publishing, Ltd.; 1997.

45. Tome WA, Jaradat HA, Nelson IA, Ritter MA, Mehta MP. Helical tomotherapy: image guidance and adaptive dose guidance. *Front Radiat Ther Oncol.* 2007;40:162-178.
46. Dawson LA, Jaffray DA. Advances in image-guided radiation therapy. *J Clin Oncol.* 2007;25:938-946.
47. Cionini L, Bucciolini M. Role of portal imaging in clinical radiotherapy: Florence experience. *Radiother Oncol.* 1993;29:230-236.
48. Gilhuijs KG, el-Gayed AA, van Herk M, Vijlbrief RE. An algorithm for automatic analysis of portal images: clinical evaluation for prostate treatments. *Radiother Oncol.* 1993;29:261-268.
49. Althof VG, Hoekstra CJ, te Loo HJ. Variation in prostate position relative to adjacent bony anatomy. *Int J Radiat Oncol Biol Phys.* 1996;34:709-715.
50. Bieri S, Miralbell R, Nouet P, Delorme H, Rouzaud M. Reproducibility of conformal radiation therapy in localized carcinoma of the prostate without rigid immobilization. *Radiother Oncol.* 1996;38:223-230.
51. Mubata CD, Bidmead AM, Ellingham LM, Thompson V, Dearnaley DP. Portal imaging protocol for radical dose-escalated radiotherapy treatment of prostate cancer. *Int J Radiat Oncol Biol Phys.* 1998;40:221-231.
52. Greer PB, Mortensen TM, Jose CC. Comparison of two methods for anterior-posterior isocenter localization in pelvic radiotherapy using electronic portal imaging. *Int J Radiat Oncol Biol Phys.* 1998;41:1193-1199.

53. Jaffray DA, Siewerdsen JH, Wong JW, Martinez AA. Flat-panel cone-beam computed tomography for image-guided radiation therapy. *Int J Radiat Oncol Biol Phys.* 2002;53:1337-1349.
54. Cheng CW, Wong J, Grimm L, Chow M, Uematsu M, Fung A. Commissioning and clinical implementation of a sliding gantry CT scanner installed in an existing treatment room and early clinical experience for precise tumor localization. *Am J Clin Oncol.* 2003;26:e28-e36.
55. Wong JR, Grimm L, Uematsu M, Oren R, Cheng CW, Merrick S, Schiff P. Image-guided radiotherapy for prostate cancer by CT-linear accelerator combination: prostate movements and dosimetric considerations. *Int J Radiat Oncol Biol Phys.* 2005;61:561-569.
56. Sorcini B, Tilikidis A. Clinical application of image-guided radiotherapy, IGRT (on the Varian OBI platform). *Cancer Radiother.* 2006;10:252-257.
57. Lehmann J, Perks J, Semon S, Harse R, Purdy JA. Commissioning experience with cone-beam computed tomography for image-guided radiation therapy. *J Appl Clin Med Phys.* 2007;8:21-36.
58. Yan D, Vicini F, Wong J, Martinez A. Adaptive radiation therapy. *Phys Med Biol.* 1997;42:123-132.
59. Langen KM, Meeks SL, Poole DO, Wagner TH, Willoughby TR, Kupelian PA, Ruchala KJ, Haimerl J, Olivera GH. The use of megavoltage CT (MVCT) images for dose recomputations. *Phys Med Biol.* 2005;50:4259-4276.
60. Yang Y, Schreiber E, Li T, Wang C, Xing L. Evaluation of on-board kV cone beam CT (CBCT)-based dose calculation. *Phys Med Biol.* 2007;52:685-705.

61. Yan D, Jaffray DA, Wong JW. A model to accumulate fractionated dose in a deforming organ. *Int J Radiat Oncol Biol Phys.* 1999;44:665-675.
62. Rivest DRC, Riauka TA, Murtha AD, Fallone BG. Assessment of a commercially available automatic deformable registration system. *J Appl Clin Med Phys.* Submitted.
63. Rivest DRC, Riauka TA, Murtha AD, Fallone BG. Prostate positioning errors associated with two automatic registration based image guidance strategies. *J Appl Clin Med Phys.* 2009;10:165-176.
64. Rivest DRC, Riauka TA, Murtha AD, Fallone BG. Dosimetric implications of two registration based patient positioning methods in prostate image guided radiation therapy. *Radiol Oncol.* 2009;43:203-212.
65. Rivest DRC, Riauka TA, Murtha AD, Fallone BG. Incorporation of planning contour data into a voxel based deformable registration algorithm for prostate adaptive radiation therapy. *J Appl Clin Med Phys.* Submitted.
66. Baldwin LN, Wachowicz K, Thomas SD, Rivest R, Fallone BG. Characterization, prediction, and correction of geometric distortion in 3T MR images. *Med Phys.* 2007;34:388-399.

Chapter 3: Assessment of a commercially available automatic deformable registration system

A version of this chapter has been submitted for publication:

Rivest DRC, Riauka TA, Murtha AD, Fallone BG. Assessment of a commercially available automatic deformable registration system. *J Appl Clin Med Phys*. Submitted.

3.1 Introduction

In recent years, deformable image registration has become a very important component in a number of image guided radiation therapy (IGRT) and adaptive radiation therapy (ART) protocols. It has been applied to problems such as autosegmentation,^{1,2} four-dimensional (4D) treatment optimization,³⁻⁷ dose accumulation^{1,8} and tumour growth/regression analysis.⁹ When accurate, deformable image registration can be an extremely powerful tool in radiation therapy. However, erroneous deformable transformations can result in highly detrimental consequences when incorporated into clinical protocols. As such, deformable registration software must be validated prior to clinical use. Unfortunately, varied objectives in potential applications, compounded by the fact

that often the lack of a gold standard makes true assessment impossible,¹⁰ renders validation of deformable image registration algorithms very difficult.

A number of approaches have been applied to the problem of deformable registration validation. Although inherently limited, visual assessment has been used in combination with other methods to qualitatively validate registration results.¹¹⁻¹⁴ It has become common practice to compare algorithms by evaluating similarity measures such as the sum of square intensity differences (SSD), correlation coefficient (CC), and mutual information (MI) upon completion of image registration.^{13,15-17} It is assumed that there is a direct correlation between enhanced similarity values and registration accuracy. Although these methods may be sufficient for relative comparison, they provide limited information on the absolute accuracy of registration.

Various deformable thoracic¹⁸⁻²⁰ and pelvic^{14,21,22} phantoms with varying levels of design complexity have been manufactured and applied to deformable registration validation. Xiong *et al.*²³ used inflatable balloons with radio-opaque markers to assess their algorithm for bladder deformation in CT images acquired prior to high dose rate (HDR) vaginal cuff brachytherapy. A gel-balloon phantom containing plastic beads molded to the gel that propagate based on levels of balloon inflation was used by Lu *et al.*¹⁵ to validate their free-form deformable registration program. Although practical, authors have argued that phantoms have limited value in validating deformable registration algorithms because they cannot fully assess the impact of anatomical variations on the algorithm's performance.^{24,25}

A useful quantitative method of assessing registration is to apply a known simulated mathematical transformation to a patient image, generating a synthetic warped image. Registration of the original and warped images allows for direct comparison of the true displacement field with that generated by registration. Lu *et al.*¹⁵ applied a harmonic function to a 2D pelvic CT image, while Lau *et al.*²⁶ warped 2D T1-weighted MR brain images with five types of synthetic mathematical transformations. Intuitively, the closer the simulated transformation resembles clinical anatomical variations, the more relevant this method is for validation. As such, this procedure is enhanced by using a second independent deformable registration algorithm to generate the known transformation for validation of the algorithm in question. Fiducial based thin-plate spline²⁷ registration has been used to warp thoracic CT¹⁸ and abdominal CT¹⁴ images for synthetic transformation based deformable image registration assessment. The major downside of using simulated warped images for registration validation is that the method is not applicable for registration of images of differing modalities.

The most commonly employed and perhaps the most accurate method of quantitatively validating deformable registration is to compare the position of anatomical landmarks or the overlap of regions of interest (ROI) in registered images. Measuring distances between manually identified points such as vascular and bronchial bifurcations is a common approach to validating thoracic CT deformable registration.³⁻⁷ Brock *et al.*²⁸ also identified landmarks on thoracic and abdominal MR images when validating a finite element model

(FEM) based deformable registration system. Various measures of volume overlap evaluated using radiation oncologist delineated prostate contours have been used for validation of deformable registration of T2-weighted pelvic images with and without inflated endorectal coils.²⁹⁻³¹ Volumetric based methods have also been used when validating deformable registration of pelvic CT^{1,2} and head and neck CT¹⁶ images.

The majority of the aforementioned references share a commonality in that the authors develop a novel algorithm that requires some procedure to assess its capabilities. However, the problem of assessing a commercial black box deformable registration system prior to clinical implementation has not been addressed, in particular, a box with an automatic registration system in which the deformable transformation is not readily accessible. Proper quality assurance and acceptance testing of such systems is necessary to identify limitations for various clinical applications. Using a collection of novel and established methods, we have developed a comprehensive protocol for the validation of automatic deformable image registration systems over a range of IGRT and ART applications. The protocol consists of a qualitative phantom study to determine the system's general tendencies, a similarity measure based relative comparison of the system's registration settings, absolute intra-modality registration validation using synthetic transformations and finally, a contour based evaluation of the system's inter-modality registration accuracy. The protocol has been applied to the Reveal-MVS Fusion Workstation (Mirada Solutions, Ltd, Oxford, UK) as a test study.

3.2 Methods and Materials

As is the case for other technological advancements implemented in radiation therapy, the extent of the capabilities and limitations of a commercial system must be understood prior to its use in any deformable registration application. Given the wide range of anatomical variations across the population, different imaging modalities and scanning protocols and the number of potential applications of deformable registration in IGRT and ART, a single standardized algorithm is probably insufficient. As such, an automatic commercial deformable registration system would require multiple algorithms or at the very least, multiple registration settings in order for it to be relevant over a spectrum of applications. Our protocol consists of four separate components: a phantom study to determine the system's general tendencies, relative validation of different registration settings, absolute verification of the system's intra-modality and inter-modality deformable registration tools. In all deformable registrations on the Reveal-MVS system, images were initially aligned using the system's automatic rigid registration tools. It should be noted that where at all possible, all studies were designed and implemented with the goal of testing the system's inherent capabilities. As such, registration was not aided by external pre-processing such as the cropping or filtering of images prior to Reveal-MVS import.

3.2.1 Registration Software

As mentioned in the previous chapter, the Reveal-MVS system has automatic rigid and deformable registration capabilities, as well as a separate

PET/CT scanner automatic motion correction option specifically designed to account for the typically minor anatomical variations present between PET and CT scans on a combined or hybrid PET/CT system. The deformable registration algorithm is proprietary, thus severely limiting the authors' knowledge of its actions. However, the roots of the company Mirada Solutions, Ltd. (currently Mirada-Medical) can be traced to the Wolfson Medical Vision Laboratory at the University of Oxford. The automatic deformable registration and PET/CT motion correction tools have user defined settings for stiffness (None, Soft, Medium, Stiff), speed (Slow, Medium, Fast), and refinement (Coarse, Medium, Fine), giving rise to thirty-six permutations of setting combinations. Although the methods are not open source, some information about the settings is provided with the software's documentation. If stiffness is set to 'None', no constraints are set to the registration, whereas a stiffness of 'Stiff' typically limits displacements to less than ½ cm. 'Soft' and 'Medium' settings typically limit displacements to 5 cm and 2 cm, respectively. The speed setting sets the approximate registration time to less than a minute, 3-4 minutes or in excess of 10 minutes, for 'Fast', 'Medium' and 'Slow' settings, respectively. The refinement setting determines the level of localization at which the deformations are applied to images. For example, the 'Coarse' setting results in deformations applied at a resolution of approximately 5 cm. Resolutions of 2 cm and ½ cm are typical of the 'Medium' and 'Fine' settings, respectively. The deformation function generated after registration of the source and target images is not accessible, although it can be saved and subsequently loaded and reapplied to the original source or any other

image. The system allows for export of deformed images, features built-in contouring tools with exporting capabilities, but is unable to import ROI contours delineated on other systems. All import and export functions are based on the DICOM standard.

3.2.2 Phantom Study

A number of authors have argued that phantoms have limited value in quantitatively evaluating deformable registration software because they cannot fully assess the impact of anatomical variations on the algorithm's performance.^{24,25} In principle, we agree with this assertion, however, it was believed that a simple, site nonspecific, multi-modality phantom may yield pertinent information about an unknown deformable registration algorithm. As such, we included a phantom study in our protocol not for quantitative evaluation of Reveal-MVS, but as a qualitative assessment tool that was designed and implemented with two objectives. First, to determine if the system has any general tendencies that might influence the registration of patient images and second, to determine whether or not the system's actions when registering images were modality dependent.

We began with a commercial cylindrical water phantom and manufactured a circular water equivalent plastic slab with a 12 x 12 grid of ¼ inch threaded holes 8 mm apart and attached the slab to the inside base of the phantom. Seven solid plastic spheres of varying diameters attached to ¼ inch diameter rods were inserted in the base so as to be fairly evenly distributed throughout the phantom.

Reference target CT (dimensions: 512 x 512 x 62; spacing: 0.9375 mm x 0.9375 mm x 2.0 mm), T1-weighted MRI (dimensions: 512 x 512 x 21; spacing: 0.5859 mm x 0.5859 mm x 5.0 mm) and PET images (dimensions: 144 x 144 x 30; spacing: 4.0 mm x 4.0 mm x 4.0 mm) were acquired on the clinical imaging systems used for radiation therapy patients in our clinic at the time the phantom study was performed (Figure 3-1). CT images were acquired on a PQ5000 (Philips Medical Systems, Cleveland, OH) scanner, while a 1.5 T Gyroscan Intera (Philips Medical Systems, Cleveland, OH) was used for MRI image acquisition. An 82 MBq FDG solution was injected into the water phantom prior to imaging on an Allegro (Philips Medical Systems, Cleveland, OH) PET scanner. The size and location of individual plastic spheres was modified in various combinations of replacements or 8 mm translations. Source images of each of the different phantom set-ups were acquired with all three imaging modalities. Since we were predominantly interested in the system's treatment of the modified spheres, the plastic rods were digitally removed from all images using the method described by Crouch *et al.*²² in removing brachytherapy seeds from pelvic CT images. Intra-modality deformable registration of each source image to its respective target image was performed on the Reveal-MVS system. PET and MRI source images were also registered to the target CT image for inter-modality investigation. Analysis was limited to a qualitative visual inspection of the deformable registration results.

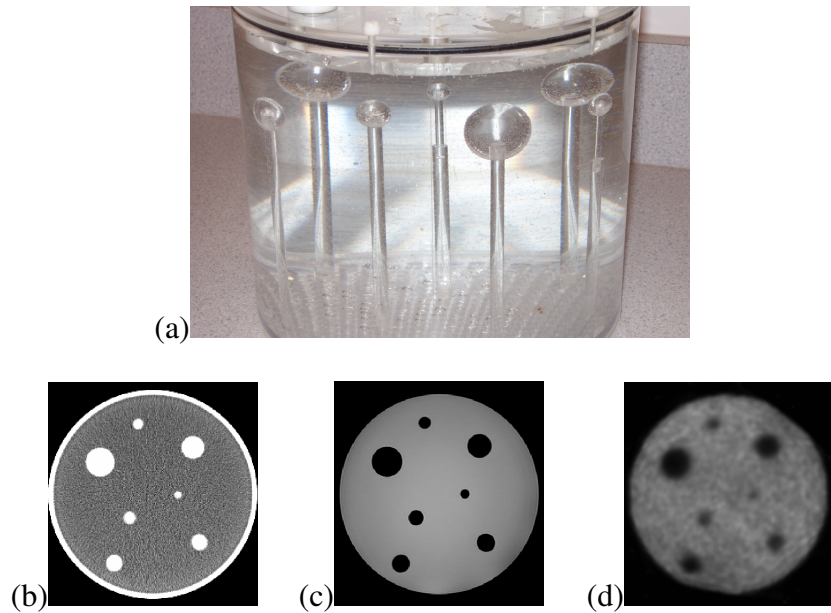


Figure 3-1. (a) Side view photographic image of the phantom showing the seven solid spheres attached to plastic rods screwed into the phantom base. (b) Axial slice of target CT image. (c) Axial slice of target MRI image. (d) Axial slice of target PET image.

3.2.3 Relative Patient Study

The objective of the second component of the protocol is to determine the optimal deformable registration settings for a collection of IGRT applications. It should be re-iterated that patient images were acquired retrospectively and unlike in the phantom study, the authors could not dictate which imaging systems were used. As such, different scanners were used for different applications; however, there were no variations amongst each individual application. The following five image combinations, selected based on availability and the desire to include multiple anatomical sites and imaging modalities, were investigated. The

applicability and prevalence of the applications range from standard clinical practice to untested and potential uses of deformable image registration.

PET/CT: Studies have demonstrated that staging detection with FDG PET leads to improved patient management and often impacts radiation therapy planning in non-small cell lung carcinoma (NSCLC) patients.^{32,33} Combining functional PET and anatomical CT information presents many challenges, but a number of them have been addressed with the advent of combined PET/CT scanners.³⁴ In a single imaging study, these systems consecutively acquire CT and PET images with the patient in a fixed position on a single imaging couch in a timeframe on the order of minutes. The design does not eliminate, but significantly reduces the level of anatomical variations between patient PET and CT images acquired on independent systems. PET (dimensions: 144 x 144 x varied; spacing: 4.0 mm x 4.0 mm x 4.0 mm) and CT (dimensions: 512 x 512 x varied; spacing: 1.1719 mm x 1.1719 mm x 5.0 mm) images used in this work were acquired on a Gemini EXP PET/CT unit (Philips Medical Systems, Cleveland, OH).

Longitudinal PET: Longitudinal or temporal imaging studies where a patient is successively imaged to monitor change in a disease state, or to assess the effectiveness of treatment is a common practice in radiation therapy. We address this particular application by registering post-treatment follow-up images to pre-treatment baseline images (dimensions: 144 x 144 x varied; spacing: 4.0 mm x 4.0 mm x 4.0 mm) acquired on an Allegro (Philips Medical Systems, Cleveland, OH) PET scanner.

Longitudinal thoracic CT: The utilization of deformable image registration in 4D radiotherapy of the lung has been well documented.³⁻⁷ Registration of thoracic CT images acquired during different respiratory phases allows for modeling of respiratory motion and improved delineation of target margins. For simplicity we register longitudinal thoracic CT (dimensions: 512 x 512 x varied; spacing: 0.7656 mm x 0.7656 mm x 7.5 mm) studies imaged on a diagnostic Mx8000 scanner (Philips Medical Systems, Cleveland, OH).

Pelvic MRI to planning CT: It has been reported that the positions of both the prostate apex and base are often misidentified on pelvic CT images and that manual rigid registration of MRI and CT based on bony landmark identification can improve target delineation during prostate treatment planning.³⁵ However, if the prostate has translated or slightly deformed with respect to surrounding anatomy between imaging studies, rigid registration of the entire image sets, whether by manual or automated methods, may not result in accurate overlap of the MRI and CT prostate volumes. Deformable registration may have the potential to further improve target delineation by accounting for internal prostate motion. Although the validity of this hypothesis has yet to be tested, nor has the method been compared to more established ROI overlap methods, it does not prevent the inclusion of these image sets in this study. T1-weighted MRI (dimensions: 512 x 512 x varied; spacing: 0.7813 mm x 0.7813 mm x 6.0 mm) and planning CT images (dimensions: 256 x 256 x varied; spacing: 1.875 mm x 1.875 mm x 3.0 mm) were acquired on an Intera 3T (Philips Medical Systems,

Cleveland, OH) magnet and a PQ5000 CT scanner (Philips Medical Systems, Cleveland, OH), respectively.

Pelvic megavoltage CT (MVCT) to planning CT: The protocol for patients treated on the Hi*Art II (TomoTherapy, Inc., Madison, WI) helical tomotherapy unit at our clinic calls for the acquisition of daily megavoltage CT (MVCT) images (dimensions: 512 x 512 x varied; spacing: 0.7540 mm x 0.7540 mm x 6.0 mm) with the patient in treatment position. Pre-treatment MVCT images are beneficial in that they provide daily image guidance³⁶ and allow for calculation of the daily delivered dose.³⁷ It has been demonstrated that accurate deformable registration of daily MVCT and planning CT images permits the evaluation of accumulated dose distributions delivered over the course of treatment.⁹ Planning CT images (dimensions: 256 x 256 x varied; spacing: 1.875 mm x 1.875 mm x 3.0 mm) were acquired on a PQ5000 (Philips Medical Systems, Cleveland, OH) system.

Five image pairs for each individual application were imported into the Reveal-MVS system for this study. After initial automatic normalized mutual information based rigid alignment, every source image was automatically registered to its respective target image using each of the possible thirty-six automatic deformable registration settings. The automatic motion correction tool was used for PET/CT registration in place of automatic deformable registration. Deformed images were exported and post-registration similarity measures were evaluated using in-house software developed in C++. Symmetric correlation ratio, mutual information, and correlation coefficient values were calculated for

each intra-modality image pair with the latter excluded from inter-modality analysis. A simple qualitative visual assessment of fused images was used to evaluate the generally accepted notion that similarity measure optimization corresponds to improved registration accuracy.

3.2.4 Intra-modality Registration

Two of the registration applications evaluated in the previous section, one intra-modality and the other inter-modality, were selected for analysis of absolute registration accuracy. For the intra-modality application, mathematically simulated deformations were used for absolute validation of longitudinal thoracic CT deformable registration. Unedited and synthetically deformed patient images that differed by a known transformation \mathbf{T}_0 were registered using Reveal-MVS. Absolute comparison of the true transformation \mathbf{T}_0 and that produced by the commercial system $\mathbf{T}_{\text{Reveal}}$ was achieved by calculation of the displacement error (DE),²⁶ which is defined as:

$$DE = \frac{1}{\sqrt{N_V}} \sqrt{\sum_{i=0}^{N_V-1} \varepsilon_i^2}, \quad 3.1$$

where N_V is the number of overlapping image voxels and for each voxel i , ε_i is the voxel error, the displacement between the true position of each deformed voxel and the position obtained by registration. In addition to full 3D analysis, axial components of DE values were also evaluated.

In order to best represent clinical reality, transformations were selected by registering baseline to follow-up patient images with a standard B-spline

parameterized 3D free form deformable (FFD) registration algorithm implemented in the Insight Segmentation and Registration Toolkit (ITK). The registration did not need to be perfect so long as the generated transformation and the synthetic deformed baseline image were clinically relevant and plausible. Synthetic images were then registered to the original baseline images on the Reveal-MVS system using the optimal settings determined by relative evaluation.

Upon conducting this procedure on each of the five image pairs analyzed in the previous section, we recognized that additional information could be extracted from the process in order to further enhance analysis of the commercial system's absolute capabilities. FFD registration is an iterative process and not only can the final iteration be considered a clinically relevant transformation, each preceding iteration can be viewed as representing clinical plausibility. As such, B-spline transformation parameters for nine additional iterations from each FFD registration were used to produce synthetic images. In all five FFD registrations, convergence required greater than ten iterations, so additional iterations were selected to obtain B-spline transformations representing varying magnitudes of deformation.

Calculation of the displacement error for Reveal-MVS registrations was hindered by the fact that transformations in Reveal-MVS cannot be accessed by the user. To overcome this problem, we developed a grid-based system in which baseline patient images were modified by initially setting the intensity of each voxel to zero. A set of randomly selected individual image voxels was then modified to have non-zero intensity values creating a non-uniform grid image. A

non-uniform grid was selected to allow sampling of both the local and global components of the deformable transformation. All image modification was performed with a Matlab (The MathWorks, Inc., Natick, MA) script. Grid images were then deformed using the same known B-spline transformation \mathbf{T}_0 applied to the original baseline image and deformed grid images were subsequently imported into Reveal-MVS. The Reveal-MVS registration derived transformation $\mathbf{T}_{\text{Reveal}}$ was applied to the deformed grid image, which was then exported for analysis. Perfect registration on Reveal-MVS would result in the exported image being equivalent to the original non-deformed, non-uniform grid image and a displacement error value of nil. Both grid images were imported into analysis software developed in C++ and the approximate displacement error was calculated using the locations of each of the grid points. A flowchart is used to summarize the intra-modality registration validation procedure in figure 3-2.

Recognizing that the accuracy of our proposed DE evaluation method was limited by a number of factors including statistics, and the potential merging or crossover of grid points, we felt that validation of its efficacy was required. A collection of known B-spline transformations defining varying magnitudes of deformation was applied to a randomly selected grid image. B-spline functions were extracted for all iterations during the registration of one of the longitudinal thoracic CT images pairs with our FFD registration program based on ITK. After setting the intensity of all image voxels in the baseline image to zero, either 500, 1000, 3000, or 5000 randomly selected voxels were set to non-zero values. The deformed and original grids were imported into our evaluation software for

calculation of approximate DE values, which were compared with true displacement error values extracted from the known B-spline functions.

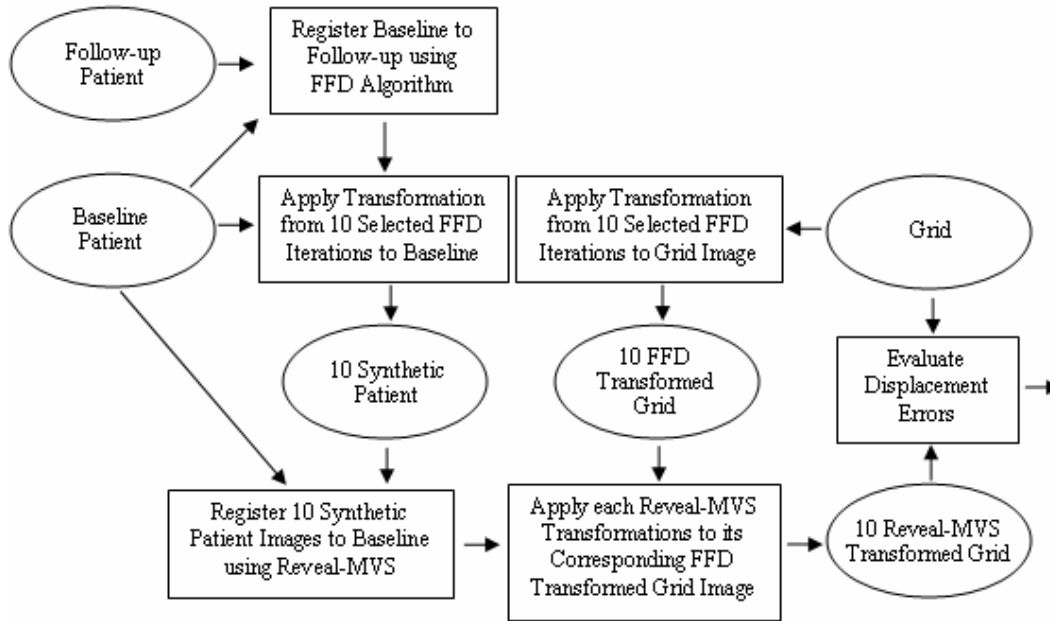


Figure 3-2. Flowchart showing the steps and images involved in the synthetic transformation based intra-modality validation study. Rectangles represent steps or actions while images are denoted by ellipses.

3.2.5 Inter-modality Registration

Finally, we evaluated the Reveal-MVS system’s ability to deform pelvic MRI images to planning CT images through analysis of radiation oncologist delineated prostate contours. However, an important factor must be considered when performing volumetric analysis of prostate contours drawn on CT and MRI images. It has been demonstrated through independent studies that contoured prostate volumes are greater in CT than in MRI images.^{35,38} Kagawa *et al.*³⁵

observed that CT contours often erroneously included sections of seminal vesicles, the base of the bladder, adjacent structures such as venous plexus and fibromuscular stroma, neurovascular bundles, and the anterior rectal wall. In fact, inter-modality variation has been demonstrated to exceed inter-observer variation³⁸ and its consequences should influence the procedural design of this study.

Each patient MRI image was registered to its respective planning CT using the optimal deformable registration setting determined through relative validation. Prostate volumes were contoured on each of the five CT and five unregistered MRI pelvic images by a single radiation oncologist on Reveal-MVS. Each patient's unregistered MRI image was displayed on a monitor adjacent to the registration system in an attempt to improve prostate CT delineation. Contours were exported and a C++ program was used to convert patient images into binary images in which voxels corresponding to prostate had intensity of one, while all other voxel intensities were set to zero. Binary MRI images were imported into Reveal-MVS and appropriate transformations were applied, generating deformed binary MRI images for comparison with each patient's binary CT image.

Volumetric analysis of binary CT and deformed binary MRI images consisted of evaluation of the mean surface distance between contours and the two most common measures of region overlap,²⁵ the Tanimoto Coefficient (TC) and Dice Similarity Coefficient (DSC). Given a CT contour volume V_{CT} and a MRI contour volume V_{MRI} , TC and DSC are defined by:

$$TC = \frac{V_{CT} \cap V_{MRI}}{V_{CT} \cup V_{MRI}}, \quad 3.2$$

and:

$$DSC = \frac{2(V_{CT} \cap V_{MRI})}{V_{CT} + V_{MRI}}. \quad 3.3$$

Both measures have possible values ranging from 0 for no overlap to 1 for perfect agreement between volumes. A flowchart is used to summarize the inter-modality registration validation procedure in figure 3-3. In addition, all four protocol components are summarized in table 3-1.

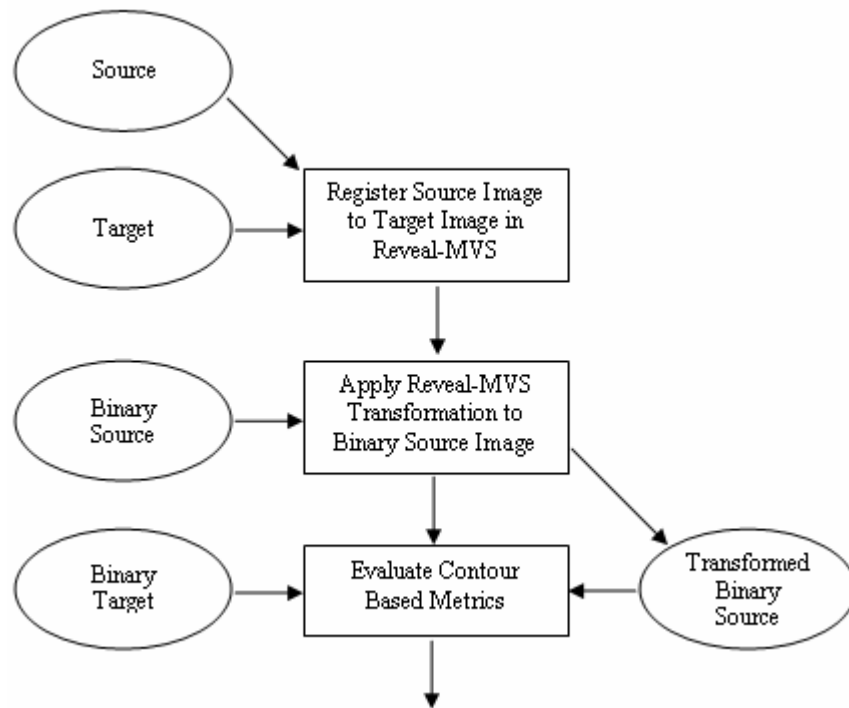


Figure 3-3. Flowchart showing the steps and images involved in the contour based inter-modality validation study. Rectangles represent steps or actions while images are denoted by ellipses.

Table 3-1. Summary of the validation protocol procedure, including the analysis performed and images evaluated for each of the protocol’s four components.

	Analysis	Images Registered
Phantom study	Qualitative visual analysis of registration	CT to CT; MRI to MRI; PET to PET; MRI to CT; PET to CT
Relative validation	Comparison of post-registration similarity measures	PET/CT; Longitudinal PET; Longitudinal thoracic CT; Male pelvic MRI to planning CT; Male pelvic MVCT to planning CT
Intra-modality	Evaluation of post-registration axial and 3D displacement errors (DE)	Synthetic thoracic CT to original thoracic CT
Inter-modality	Evaluation of post-registration contour metrics	Male pelvic MRI to planning CT

3.3 Results

3.3.1 Phantom Study

A very consistent trend was observed in all of the phantom image deformable registrations on the Reveal-MVS system regardless of phantom modification or image modality. Whether one of the plastic spheres was translated or replaced with a different sized sphere, the registration software

performs little or no image warping in the vicinity of the modified sphere. This is illustrated in figure 3-4 for a CT to CT registration in which a sphere was translated 8 mm and a MRI to CT registration where a sphere was approximately doubled in volume. The illustration for the second example contains an additional inset window in which a portion of the outside edge of the phantom is magnified with respect to the remainder of the phantom. Due to a lack of signal from the plastic phantom perimeter, the phantom diameter is smaller in the MRI image than in CT and as a result, the system attempts to deform the MRI phantom volume to that of the CT phantom volume. These and other observations suggest that the commercial system is more apt to account for global deformations than local variations when performing deformable image registration.

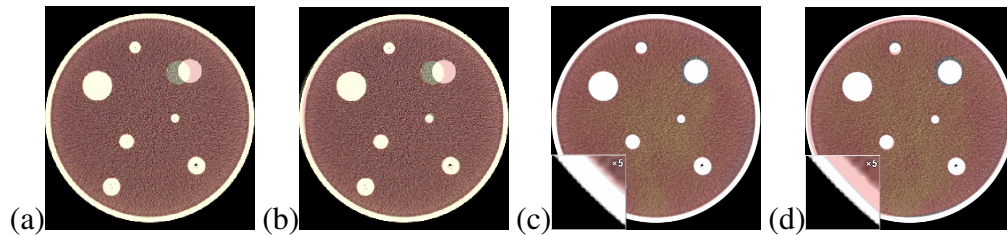


Figure 3-4. Axial slices of coloured source images overlaid on greyscale target phantom images for two selected registrations. (a) Rigid alignment of CT images in which a single target has been translated 8 mm. (b) CT images after deformable registration (None-Fast-Coarse) on Reveal-MVS demonstrating that the system does not move the sphere back to its original location. (c) Rigid alignment of MRI and CT images in which a sphere in the MRI has approximately doubled in volume. (d) MRI and CT images after deformable registration (None-Fast-Medium).

3.3.2 Relative Patient Study

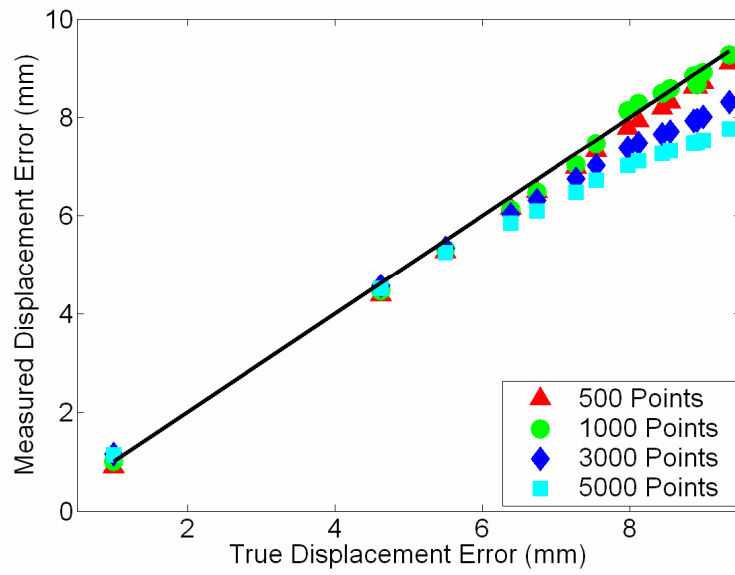
Results for the relative patient study are tabulated in Appendix B.

3.3.3 Intra-modality Registration

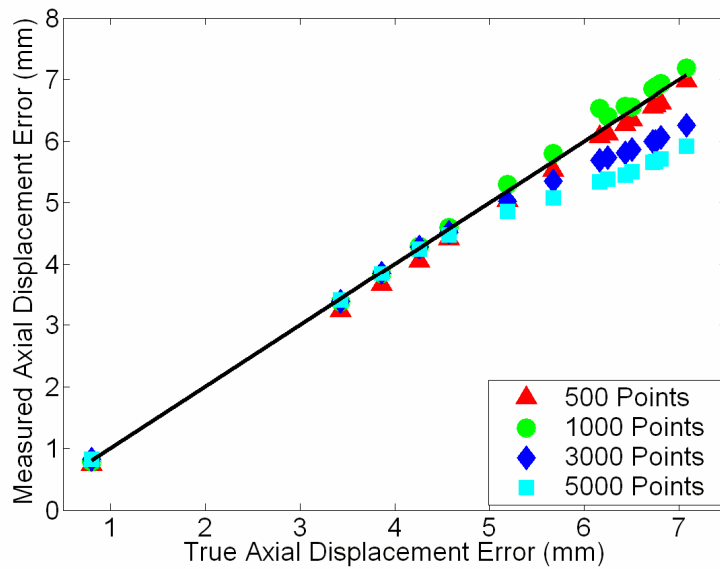
Our method for determining approximate displacement error values for images registered on systems that do not provide access to the transformation function was tested by applying known B-spline functions to a set of non-uniform grid images. True displacement error and true axial displacement error values are plotted against the approximate values calculated by our in-house software for each of the deformed grid images in figure 3-5. Measured and true displacement error values for all grid images show excellent agreement when true values are below 6 mm, at which point faults in the measured values begin to increase for the grid images containing 3000 and 5000 points. This divergence of approximate values measured using our technique from true values also occurs when evaluating axial displacement errors greater than 5mm. Presumably, for larger quantities of grid points and more complex deformations with greater displacement errors, the probability that the proximity of nearby grid points results in our software incorrectly determining corresponding grid points in original and deformed images increases. Considering this upper limit and the fact that statistics mandate a lower limit, we decided to use 1000 point grid images for intra-modality registration assessment. Based on data points in figure 3-5, for deformations with displacement errors less than 9.35 mm and axial displacement errors less than 7.08 mm, on average our technique correctly

measures these quantities within 0.13 mm and 0.11 mm, respectively. It requires mention that the reported accuracy of our grid based method of evaluating displacement errors is only applicable for the image matrix sizes, voxel dimensions and the registration application inherent to this particular section. Modification of any of these parameters may necessitate re-assessment of the method.

After generating synthetic images by applying mathematically known deformations to patient images followed by the registration of synthetic to original thoracic CT images on Reveal-MVS, post-registration axial and 3D displacement errors were evaluated. Registrations were performed with the Stiff-Slow-Fine setting on Reveal-MVS as mean NMI (Table B-6), SCR (Table B-7) and CC (Table B-8) values were all optimal for that particular setting in the relative longitudinal thoracic CT analysis. Resultant values are plotted against known pre-deformable registration values for all five patients in figure 3-6. If we assume the difference between pre and post-registration DE values is a measure of improvement in image correspondence achieved by registration, correspondence increases for images that differ by initial displacement errors greater than approximately 4 mm. For initial DE values less than 2 mm, deformable registration on the commercial system appears to have negative effects. For reference, varying magnitudes of B-spline warped images, before and after deformable registration on Reveal-MVS, are depicted in figure 3-7.



(a)



(b)

Figure 3-5. (a) Plot of displacement error (DE) values measured by our grid based method versus true DE values for various magnitudes of B-spline warping. Either 500, 1000, 3000, or 5000 randomly located grid points were used. The solid dark line depicts correct measurement of true values. (b) Similar plot for axial components of DE.

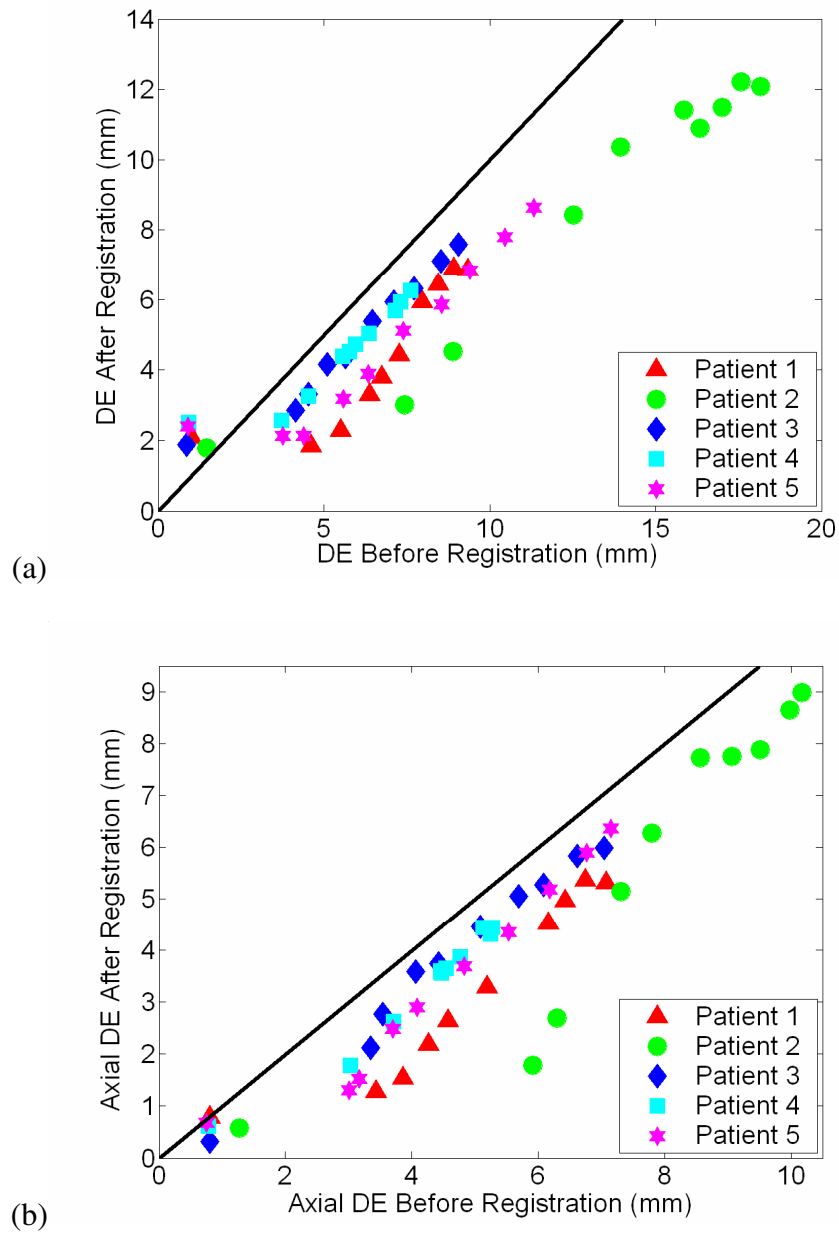
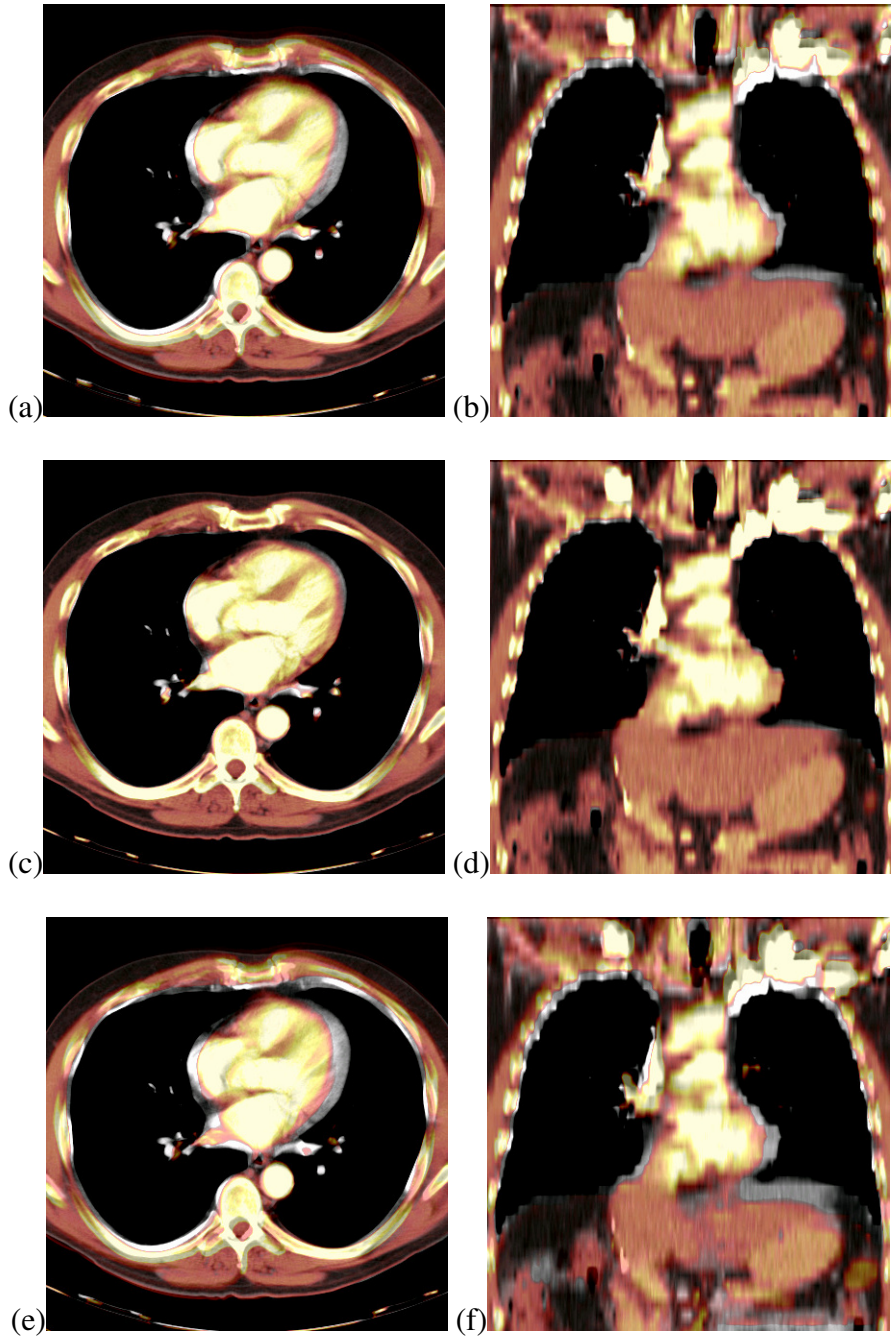


Figure 3-6. Scatter plot of post- versus pre-deformable registration (a) DE and (b) axial DE values for baseline and synthetically transformed thoracic CT images. Ten B-spline warped images were registered to their respective original unwarped images on Reveal-MVS for each of the five patients (denoted by separate coloured symbols). A reference line with unity slope is shown in black.



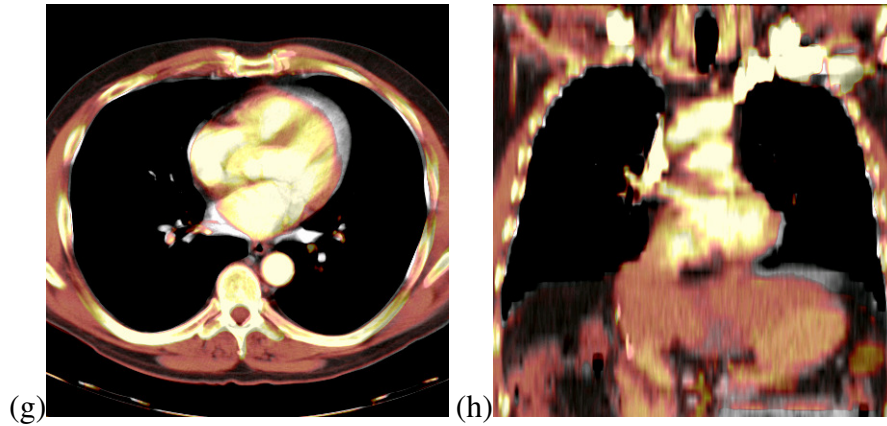


Figure 3-7. Sample coloured warped images overlaid on greyscale baseline images depicting the range of magnitudes of synthetic B-spline warped images used for validation of thoracic CT registrations. The images are also shown upon completion of deformable registration on Reveal-MVS. (a) Axial and (b) coronal views of images that differ by a displacement error of 4.6 mm and an axial displacement error of 3.4 mm. Corresponding (c) axial and (d) coronal views of images after registration. (e) Axial and (f) coronal views of images that differ by a displacement error of 9.4 mm and an axial displacement error of 7.1 mm. Corresponding (g) axial and (h) coronal views of images after registration.

3.3.4 Inter-modality Registration

Based on mean NMI (Table B-9) and SCR (Table B-10) values, the optimal registration settings for prostate MR to CT deformable registration are None-Fast-Medium and None-Slow-Medium, respectively. Pre- and post-registration prostate DSC, TC, and mean contour separation values for both settings are given in table 3-2. In addition, post-registration DSC and mean contour separation values were evaluated for ten additional setting combinations

and were plotted against similarity measures in order to establish the relationship between relative and absolute validation metrics. Setting combinations were selected with the goal of including a spread of post-registration NMI and SCR values for each patient. NMI versus DSC, NMI versus mean separation, SCR versus DSC, and SCR versus mean separation are plotted in figure 3-8 for all five patients. For the most part, increased SCR and NMI similarity measure values correspond to improvements in the evaluated absolute validation metrics; however this trend is clearly not universal. Results show that for Patient 1, a range of NMI and SCR values leads to little or no change in DSC or mean separation. Based on visual analysis of the original and deformed images, this apparent exception can be attributed to anatomical deviations between the original source and target images away from the prostate. This will be discussed in further detail in the following section.

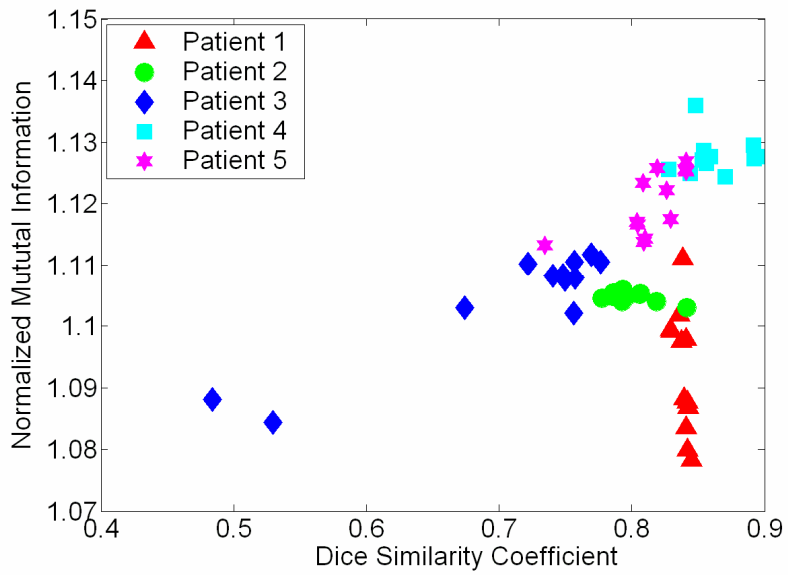
3.4 Discussion

The use of phantoms in deformable registration validation is an on-going area of discussion. Researchers continue to utilize them even though any phantom, no matter how complex the design, will not be able to simulate the range of anatomical variations that may occur in clinical imaging studies. We included a phantom study in our validation protocol not to quantify assessment, but with the intent that it may provide important insight on the tendencies of a black box commercial deformable image registration system. Based on phantom images, we established that the deformable registration algorithm in Reveal-MVS

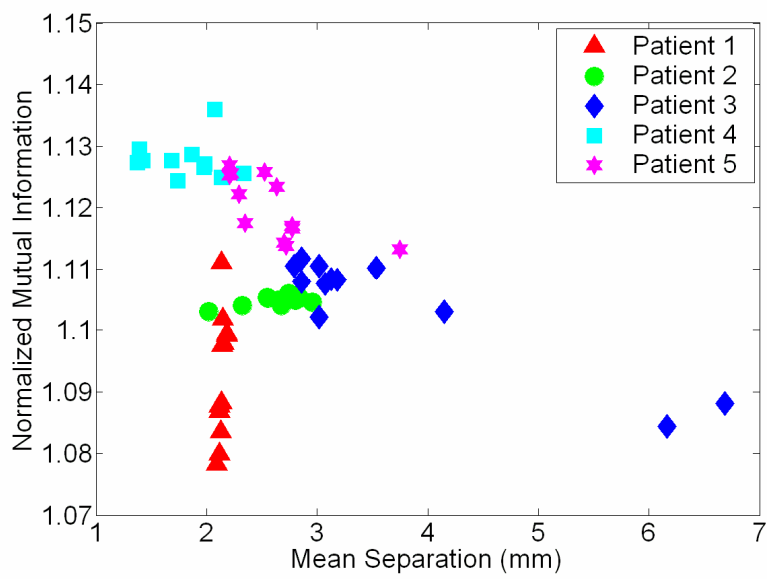
must have strict constraints on the amount of local deformation that may occur. In addition, various intra and inter-modality phantom registrations revealed little or no evidence that the commercial system’s apparent preference for global over local deformation is modality dependent. Although not quantifiable, these observations provide useful information that may be extrapolated to predict the system’s ability to perform clinical deformable image registration applications. For example, if many local image deformations are required, this system may not be up to the task.

Table 3-2. Prostate DSC, TC, and mean separation (MS) values for each of the five patients. MS values are in mm. Initial values are given for rigid alignment and after deformable registration of pelvic MRI and planning CT images, using two different settings on Reveal-MVS.

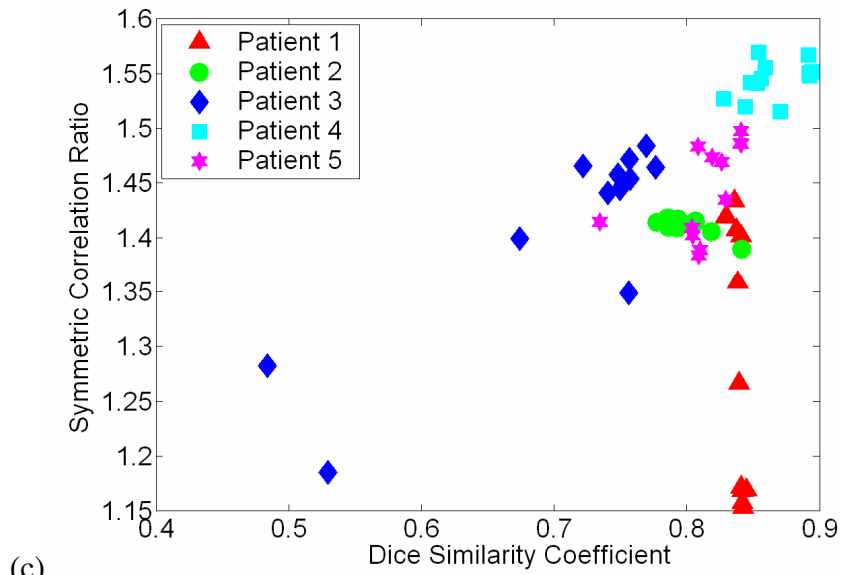
	Rigid			None-Fast-Medium			None-Slow-Medium		
	DSC	TC	MS	DSC	TC	MS	DSC	TC	MS
Patient 1	0.840	0.724	2.1	0.834	0.716	2.2	0.832	0.712	2.2
Patient 2	0.852	0.743	1.9	0.781	0.641	2.9	0.789	0.651	2.8
Patient 3	0.730	0.574	3.3	0.747	0.560	3.1	0.749	0.598	3.1
Patient 4	0.893	0.807	1.4	0.893	0.807	1.4	0.893	0.807	1.4
Patient 5	0.822	0.700	2.5	0.830	0.709	2.4	0.833	0.713	2.4



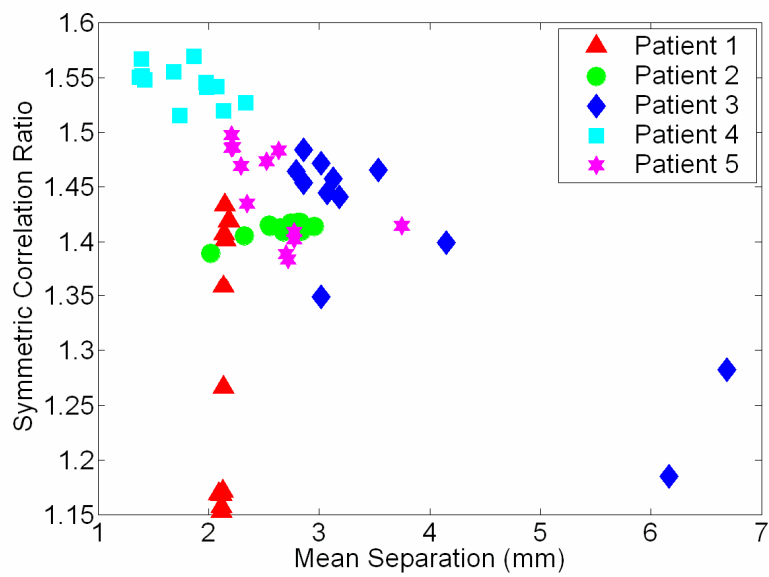
(a)



(b)



(c)



(d)

Figure 3-8. Relationship between image similarity measures and absolute prostate contour based metrics for twelve different settings in the registration of pelvic MRI to planning CT images. (a) Normalized mutual information (NMI) versus Dice similarity coefficient (DSC), (b) NMI versus mean contour separation, (c) Symmetric correlation ratio (SCR) versus DSC, (d) SCR versus mean separation. Each patient is represented with a different coloured symbol.

Upon completion of the phantom study, relative evaluation of each of the commercial system's thirty-six registration settings was performed for five potential deformable registration applications. Not only did this study yield the optimal settings for each application, it also provided an interesting insight into the system's application dependence. For example, None-Medium-Fine worked extremely well for longitudinal PET and PET/CT deformable registration, but performed extremely poorly in the registration of pelvic MVCT to CT images. However, trends were similar amongst the different patient images evaluated for each individual application, in particular, the thoracic CT patients. Whether each of the thirty-six settings performed poorly, admirably, or somewhere in between, they performed similarly for all thoracic CT patients investigated. Visual inspection of registration qualitatively reveals that a relationship exists between optimized similarity measure values and registration accuracy. It should be emphasized however that all five image pairs for each application were acquired with consistent imaging protocols. Which, if any, of the observed trends are transferable when images are pre-processed or acquired using different imaging protocols is not known. For example, the pelvic MVCT and T1-weighted MRI images were all acquired with 6.0 mm thick slices. It would be interesting to repeat the study prospectively with equivalent slice thicknesses to that of the planning CT images (i.e. 3.0 mm) for comparison with the presented results. It may be that relative analysis of commercial systems is required for not only each application, but also for each image processing and acquisition protocol.

After establishing the optimal registration settings for the five deformable registration applications through relative measures, absolute quantitative evaluation of an intra- and inter-modality registration was performed. Intra-modality deformable registration validation using known transformations is common in inter-subject brain studies,^{26,39-42} but has had limited use in applications directly relevant to radiation therapy. By registering multiple B-spline warped images to original thoracic CT images, we quantified the commercial system's performance over a range of potential initial clinical deformations. The resultant plot of post-registration versus pre-registration displacement errors in figure 3-6 demonstrates a dual component trend in Reveal-MVS's abilities. For the largest and progressively smaller initial DE values, correspondence is generally improved by deformable registration until a point is reached where post-registration DE values level off. Perhaps such plots or more specifically, the location of the pivot point can be used as a standard for absolute comparison of deformable registration methods. Of course, further research is required to determine if the trend observed for Reveal-MVS is consistent with other deformable registration algorithms.

The use of deformable registration instead of conventional rigid registration to improve structure delineation in the planning of prostate radiation therapy is an interesting concept. The predominant application of deformable registration of prostate MRI to CT images in the literature is to account for the deformation of the prostate caused by the insertion of an endorectal coil during magnetic resonance spectroscopic imaging (MRSI).^{21,30} Acquisition of

anatomical MRI images with surface or other non-invasive coils significantly reduces problems related to prostate deformation but daily prostate motion^{43,44} remains a major concern. As a result, any translational offset between prostate positions in the MRI and CT with respect to surrounding anatomy may lead to inaccurate overlap of the MRI and CT prostate volumes after rigid registration. Based on our analysis in table 3-2, Reveal-MVS does not accurately account for internal prostate motion as deformable registration has little effect on the absolute DSC, TC and mean separation validation metrics. Of course, the values of these absolute metrics are dependent on the contouring abilities of the radiation oncologist, however, even without perfect structure delineation, one would expect to observe differences in pre and post registration values if registration deformed or translated the MRI prostate volume in any meaningful way. Visual inspection of figure 3-9 confirms this result.

Although contour analysis was used for inter-modality registration validation in this study, point landmark based evaluation is also an option. Both methods have the potential to provide useful quantitative information on the capabilities of a deformable registration system, but ultimately, we selected volumetric analysis simply because radiation therapy planning and delivery is based on doses delivered to volumetric regions of interest (ROI). However, for larger regions of interest that are susceptible to internal local deformations or ROI whose borders cannot be visually delineated, point based validation may be required. Ultimately, there may be some application dependence involvement in absolute inter-modality deformable registration validation.

In addition to landmark based validation, two other validation methods excluded from our protocol have been the focus of recent research. The first is the consistency approach in which given three images (A, B, C), comparison of transformations produced by registering A to B, B to C, and C to A provide a measure of registration error, assuming that errors are random and distributed evenly between each transformation.⁴⁵ For the most part consistency methods have been used for rigid registration validation,¹⁰ but have recently been applied to deformable models by Malsch *et al.*⁴⁶ A novel registration assessment tool recently introduced is the concept of unbalanced energy⁴⁷ whereby instead of using gold standards, the physical fidelity of the deformation field is quantified through finite element models (FEM). It has been applied with success to deformable registration of truncated pelvic CT images that include only a small region surrounding the prostate gland. Although promising, its relevancy for full 3D images of sites prone to significant anatomical deformations must be established. Like consistency testing, unbalanced energy certainly requires further research and was excluded from our protocol mainly because they both rely heavily on the extensive knowledge of the deformation field, which as demonstrated by Reveal-MVS, may not necessarily be the case for commercial systems.

The primary intent of this particular research was the development of a protocol for the assessment of commercial deformable registration systems, but while applying our protocol, two additional matters were also investigated. First, we developed and validated a method to compare true displacement fields with

those produced by registration when the registration software does not allow access to the deformable transformation. We also tested the generally accepted notion that the quality of different deformable registration procedures can be ranked by comparing post-registration similarity measures. Whether the results of both investigations are specific to the deformable registration applications analyzed or are relevant to other applications requires further investigation.

In the known transformation study, we showed that by applying known B-splines to a blank image with one thousand randomly positioned grid points followed by locating the discernible deformed grid points, the calculated displacement error from the sample points is highly accurate for a range of displacement error values. However, based on figure 3-5, an upper limit is eventually reached due to our analysis software's reduced ability to correctly identify corresponding grid points in heavily deformed images. When registering images on the commercial system that differ by displacement error values greater than these upper limits, the accuracy of measured post-registration values may be questionable. Although an acceptable value for post-registration displacement errors has yet to be discussed, these upper limits certainly exceed any ideal acceptable quantity.

In using our random grid point method for DE evaluation of deformable registration on the Reveal-MVS system, we make two fundamental assumptions. First, we assume that the commercial system improves or at the very least does not significantly reduce correspondence between the synthetically deformed and original thoracic CT images during the deformable registration procedure. The

concern is that deformable registration may reduce correspondence to the point that post-registration displacement error values exceed the aforementioned threshold in which results can no longer be considered accurate and measured DE values may provide an erroneous picture of the system's capabilities. However, a problem such as this would be observable through visual inspection of registrations and this was certainly not the case. The second assumption is based on the accuracy of using a sample of voxels instead of the entire image to calculate displacement errors. We have demonstrated it to be acceptable for B-splines, but whether or not the same is true for deformable transformations on the Reveal-MVS system cannot be verified. Here the concern is that the commercial system performs significant local deformations whose contributions to the post-registration displacement error would not be picked up by sampling a limited number of voxels. Based on the observed global tendencies of Reveal-MVS in comparison to B-spline deformation, once again, we feel this is not a significant problem. In fact, part of the reason we chose to model synthetic transformations with B-splines is that they are well known for allowing tremendous local control of image warping in comparison to other deformable models.⁴⁸

The second investigation beyond the scope of the validation protocol was the establishment of a relationship between absolute measures of registration accuracy and post-registration similarity measure comparison. Figure 3-8 demonstrates that an increased SCR or NMI may not necessarily correspond to superior deformable registration of prostate MRI and CT images. For one patient in particular, registrations resulting in significantly different similarity measures

led to little change in absolute contour based metrics. Further exploration revealed the source of the anomaly. All five CT images and all but one MRI images were acquired with the patient positioned on a flat imaging couch, however, the patient in question was scanned with a slightly curved couch on the MRI unit. As a result, in addition to visible prostate motion, anatomical variations near the patient's posterior were present after rigid registration of the MRI and CT images. Deformable registration on Reveal-MVS focused on patient deformation attributed to the different couches and essentially ignored the clearly visible prostate motion that had occurred between imaging studies. This is demonstrated for the optimal NMI registration setting in Figure 3-9. In deforming the patient's backside, overall image similarity improved, but correspondence in the region of interest was compromised. Interestingly, an argument could be made that this result was predictable based on qualitative observations in the phantom study in which the system attempted to deform the MRI phantom volume to the CT phantom volume while essentially ignoring any modifications to the solid sphere. Regardless, although the problem will be reduced through cropping of image data, anatomical variations away from clinically important sites must be factored into the practice of comparing deformable registrations based on similarity measure evaluation.

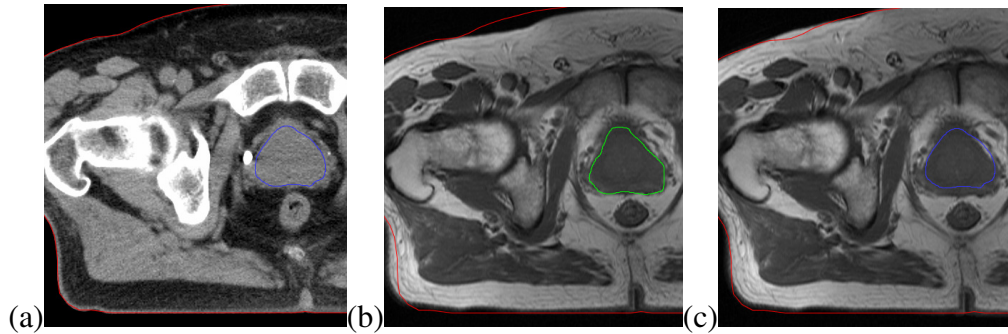


Figure 3-9. Axial slices of prostate patient whose MRI and CT images were acquired on different shaped couches. (a) CT with both the prostate and patient body outlined. (b) MRI after rigid alignment showing the MRI prostate and the CT patient contours. Anatomical variation caused by the different couches is present in the bottom left hand corner. (c) CT prostate and patient contours overlaid on the MRI after deformable registration. Warping on Reveal-MVS accounted for couch based anatomical variations but completely ignored the prostate motion.

3.5 Conclusions

We have presented a protocol for the validation of automatic commercial deformable image registration systems. Through a series of tests, the protocol provides a well-balanced general assessment of a commercial system's capabilities. It initially consists of a qualitative phantom study to determine the system's general tendencies followed by a relative comparison of the system's registration settings through similarity measure evaluation. The protocol also includes an assessment of the system's absolute intra-modality registration accuracy using synthetic transformations and finally, a contour based evaluation

of the system's inter-modality registration capabilities. Developed software and acquired images are readily available for assessment of other commercial systems that may be purchased for clinical or research objectives by our centre. Access to the registration displacement field is not required as long as it can be stored and later re-applied, which would probably be considered mandatory in a system approved for clinical use. The protocol is by no means static or definitive and can readily be expanded to investigate other potential deformable registration applications. Future work will include applying the protocol to additional deformable registration systems and the establishment of standard minimum benchmarks for the evaluated absolute measures. Standard minimum benchmarks for the evaluated absolute measures must be established; however, doing so based on the results of this work would be premature.

In applying the protocol to the commercial Reveal-MVS, we came to a number of conclusions particularly relevant to this research project. First, Reveal-MVS is not suitable for use in the ideal adaptive radiation therapy framework presented in figure 2-7 in chapter 2. Dose accumulation requires knowledge of the anatomical correspondence between individual voxels in images acquired over the course of treatment. The system's inability to correct for local anatomical variations such as prostate translation suggests that Reveal-MVS will not provide the required accurate correspondence. In addition, results also suggest that the goal of achieving anatomical correspondence through deformable registration may be simplified by focusing on individual applications. Even with thirty-six different registration settings, Reveal-MVS could not satisfy the

requirements of five different deformable registration applications. As such, we decided to develop deformable registration tools optimized for one single application: deformable registration of daily MVCT images to planning CT images for the purpose of dose accumulation in prostate adaptive radiation therapy on helical tomotherapy. However, for completion, we chose to investigate both elements of the adaptive radiation therapy framework in figure 2-7 involving image registration: daily patient positioning and dose accumulation.

3.6 References

1. Foskey M, Davis B, Goyal L, Chang S, Chaney E, Strehl N, Tomei S, Rosenman J, Joshi S. Large deformation three-dimensional image registration in image-guided radiation therapy. *Phys Med Biol.* 2005;50:5869-5892.
2. Gao S, Zhang L, Wang H, de Crevoisier R, Kuban DD, Mohan R, Dong L. A deformable image registration method to handle distended rectums in prostate cancer radiotherapy. *Med Phys.* 2006;33:3304-3312.
3. Rietzel E, Chen GTY. Deformable registration of 4D computed tomography data. *Med Phys.* 2006;33:4423-4430.
4. Pevsner A, Davis B, Joshi S, Hertanto A, Mechalakos J, Yorke E, Rosenzweig K, Nehmeh S, Erdi YE, Humm JL, Larson S, Ling CC, Mageras GS. Evaluation of an automated deformable image matching method for quantifying lung motion in respiration-correlated CT images. *Med Phys.* 2006;33:369-376.
5. Heath E, Collins DL, Keall PJ, Dong L, Seuntjens J. Quantification of accuracy of the automated nonlinear image matching and anatomical labeling (ANIMAL)

nonlinear registration algorithm for 4D CT images of lung. *Med Phys.* 2007;34:4409-4421.

6. Boldea V, Sharp GC, Jiang SB, Sarrut D. 4D-CT lung motion estimation with deformable registration: quantification of motion nonlinearity and hysteresis. *Med Phys.* 2008;35:1008-1017.

7. Wu Z, Rietzel E, Boldea V, Sarrut D, Sharp GC. Evaluation of deformable registration of patient lung 4DCT with subanatomical region segmentations. *Med Phys.* 2008;35:775-780.

8. Schaly B, Kempe JA, Bauman GS, Battista JJ, Van Dyk J. Tracking the dose distribution in radiation therapy by accounting for variable anatomy. *Phys Med Biol.* 2004;49:791-805.

9. Lu W, Olivera GH, Chen Q, Ruchala KJ, Haimerl J, Meeks SL, Langen KM, Kupelian PA. Deformable registration of the planning image (kVCT) and the daily images (MVCT) for adaptive radiation therapy. *Phys Med Biol.* 2006;51:4357-4374.

10. Hutton BF, Braun M. Software for image registration: algorithms, accuracy, efficacy. *Seminars in Nuclear Medicine.* 2003;33:180-192.

11. Rohlfing T, Maurer CR, O'Dell WG, Zhong J. Modeling liver motion and deformation during the respiratory cycle using intensity-based nonrigid registration of gated MR images. *Med Phys.* 2004;31:427-432.

12. Wu X, Dibiase SJ, Gullapalli R, Yu CX. Deformable image registration for the use of magnetic resonance spectroscopy in prostate treatment planning. *Int J Radiat Oncol Biol Phys.* 2004;58:1577-1583.

13. Rueckert D, Sonoda LI, Hayes C, Hill DLG, Leach MO, Hawkes DJ. Nonrigid registration using free-form deformations: application to breast MR images. *IEEE Trans Med Imag.* 1999;18:712-721.
14. Wang H, Dong L, O'Daniel J, Mohan R, Garden AS, Ang KK, Kuban QA, Bonnen M, Chang JY, Cheung R. Validation of an accelerated 'demons' algorithm for deformable image registration in radiation therapy. *Phys Med Biol.* 2005;50:2887-2905.
15. Lu W, Chen ML, Olivera GH, Ruchala KJ, Mackie TR. Fast free-form deformable registration via calculus of variations. *Phys Med Biol.* 2004;49:3067-3087.
16. Castadot P, Lee JA, Parrage A, Geets X, Macq B, Gregoire V. Comparison of 12 deformable registration strategies in adaptive radiation therapy for the treatment of head and neck tumors. *Radiother Oncol.* 2008;89:1-12.
17. Pekar V, Gladilin E, Rohr K. An adaptive irregular grid approach for 3D deformable image registration. *Phys Med Biol.* 2006;51:361-377.
18. Guerrero T, Zhang G, Huang TC, Lin KP. Intrathoracic tumour motion estimation from CT imaging using the 3D optical flow method. *Phys Med Biol.* 2004;49:4147-4161.
19. Kashani R, Hub M, Kessler ML, Balter JM. Technical note: a physical phantom for assessment of accuracy of deformable alignment algorithms. *Med Phys.* 2007;34:2785-2788.

20. Serban M, Heath E, Stroian G, Collins DL, Seuntjens J. A deformable phantom for 4D radiotherapy verification: design and image registration evaluation. *Med Phys*. 2008;35:1094-1102.
21. Lian J, Xing L, Hunjan S, Dumoulin C, Levin J, Lo A, Watkins R, Rohling K, Giaquinto R, Kim D, Spielman D, Daniel B. Mapping of the prostate in endorectal coil-based MRI/MRSI and CT: a deformable registration and validation study. *Med Phys*. 2004;31:3087-3094.
22. Crouch JR, Pizer SM, Chaney EL, Hu YC, Mageras GS, Zaider M. Automated finite-element analysis for deformable registration of prostate images. *IEEE Trans Med Imag*. 2007;26:1379-1390.
23. Xiong L, Viswanathan A, Stewart AJ, Haker S, Tempany CM, Chin LM, Cormack RA. Deformable structure registration of bladder through surface mapping. *Med Phys*. 2006;33:1848-1856.
24. Slomka PJ. Software approach to merging molecular with anatomic information. *J Nucl Med*. 2004;45:36S-45S.
25. Crum WR, Camara O, Hill DLG. Generalized overlap measures for evaluation and validation in medical image analysis. *IEEE Trans Med Imag*. 2006;25:1451-1460.
26. Lau YH, Braun M, Hutton BF. Non-rigid image registration using a median-filtered coarse-to-fine displacement field and a symmetric correlation ratio. *Phys Med Biol*. 2001;46:1297-1319.
27. Bookstein FL. Principal warps: thin plate splines and the decomposition of deformations. *IEEE Trans Pattern Anal Mach Intell*. 1989;11:567-585.

28. Brock KK, Sharpe MB, Dawson LA, Kim SM, Jaffray DA. Accuracy of finite element model-based multi-organ deformable image registration. *Med Phys.* 2005;32:1647-1659.
29. Alterovitz R, Goldberg K, Pouliot J, Hsu ICJ, Kim Y, Noworolski SM, Kurhanewicz J. Registration of MR prostate images with biomechanical modeling and nonlinear parameter estimation. *Med Phys.* 2006;33:446-454.
30. Venugopal N, McCurdy B, Hnatov A, Dubey A. A feasibility study to investigate the use of thin-plate splines to account for prostate deformation. *Phys Med Biol.* 2005;50:2871-2885.
31. Bharatha A, Hirose M, Hata N, Warfield SK, Ferrant M, Zou KH, Suarez-Santana E, Ruiz-Alzola J, D'Amico A, Cormack RA, Kikinis R, Jolesz FA, Tempany CMC. Evaluation of three-dimensional finite element-based deformable registration of pre- and intraoperative prostate imaging. *Med Phys.* 2001;28:2551-2560.
32. Vanuytsel LJ, Vansteenkiste JF, Stroobants SG, De Leyn PR, De Wever W, Verbeken EK, Gatti GG, Huyskens DP, Kutcher GJ. The impact of ^{18}F -fluoro-2-deoxy-D-glucose positron emission tomography (FDG-PET) lymph node staging on the radiation treatment volumes in patients with non-small cell lung cancer. *Radiother Oncol.* 2000;55:317-324.
33. MacManus MP, Hicks RJ, Ball DL, Kalff V, Matthews JP, Salminen E, Khaw P, Wirth A, Rischin D, McKenzie A. F-18 fluorodeoxyglucose positron emission tomography staging in radical radiotherapy candidates with nonsmall cell lung

carcinoma: powerful correlation with survival and high impact on treatment. *Cancer*. 2001;92:886-895.

34. Yap JT, Carney JPJ, Hall NC, Townsend DW. Image-guided cancer therapy using PET/CT. *Cancer J*. 2004;10:221-233.

35. Kagawa K, Lee WR, Schultheiss TE, Hunt MA, Shaer AH, Hanks GE. Initial clinical assessment of CT-MRI image fusion software in localization of the prostate for 3D conformal radiation therapy. *Int J Radiat Oncol Biol Phys*. 1997;38:319-325.

36. Langen KM, Zhang Y, Andrews RD, Hurley ME, Meeks SL, Poole DO, Willoughby TR, Kupelian PA. Initial experience with megavoltage (MV) CT guidance for daily prostate alignments. *Int J Radiat Oncol Biol Phys*. 2005;62:1517-1524.

37. Langen KM, Meeks SL, Poole DO, Wagner TH, Willoughby TR, Kupelian PA, Ruchala KJ, Haimerl J, Olivera GH. The use of megavoltage CT (MVCT) images for dose recomputations. *Phys Med Biol*. 2005;50:4259-4276.

38. Rasch C, Barillot I, Remeijer P, Touw A, van Herk M, Lebesque JV. Definition of the prostate in CT and MRI: a multi-observer study. *Int J Radiat Oncol Biol Phys*. 1999;43:57-66.

39. D'Agostino E, Maes F, Vandermeulen D, Seutens P. A viscous fluid model for multimodal non-rigid image registration using mutual information. *Med Image Anal*. 2003;7:565-575.

40. Kybic J, Thevenaz P, Nirkko A, Unser M. Unwarping of unidirectionally distorted EPI images. *IEEE Trans Med Imag*. 2000;19:80-93.

41. Xue Z, Shen D, Karacali B, Stern J, Rottenberg D, Davatzikos C. Simulating deformations of MR brain images for validation of atlas-based segmentation and registration algorithms. *Neuroimage*. 2006;33:855-866.
42. Schnabel JA, Tanner C, Castellano-Smith AD, Degenhard A, Leach MO, Hose DR, Hill DLG, Hawkes DJ. Validation of nonrigid image registration using finite-element methods: application to breast MR images. *IEEE Trans Med Imag*. 2003;22:238-247.
43. Langen KM, Jones DTL. Organ motion and its management. *Int J Radiat Oncol Biol Phys*. 2001;50:265-278.
44. Byrne TE. A review of prostate motion with considerations for the treatment of prostate cancer. *Medical Dosimetry*. 2005;30:155-161.
45. Woods RP, Grafton ST, Holmes CJ, Cherry SR, Mazziotta JC. Automated image registration: I. general methods and intrasubject, intramodality validation. *J Comput Assist Tomogr*. 1998;22:139-152.
46. Malsch U, Thieke C, Huber PE, Bendl R. An enhanced block matching algorithm for fast elastic registration in adaptive radiotherapy. *Phys Med Biol*. 2006;51:4789-4806.
47. Zhong H, Peters T, Siebers JV. FEM-based evaluation of deformable image registration for radiation therapy. *Phys Med Biol*. 2007;52:4721-4738.
48. Lee S, Wolberg G, Chwa KY, Shin SY. Image metamorphosis with scattered feature constraints. *IEEE Trans Vis Comp Graph*. 1996;2:337-354.

Chapter 4: Prostate positioning errors associated with two automatic registration based image guidance strategies

A version of this chapter has been published:

Rivest DRC, Riauka TA, Murtha AD, Fallone BG. Prostate positioning errors associated with two automatic registration based image guidance strategies. *J Appl Clin Med Phys.* 2009;10:165-176.

4.1 Introduction

Movement of the prostate gland throughout a course of radiation therapy occurs as a result of daily variations in bladder and rectal filling.¹⁻⁴ This movement can result in significant changes in the radiation dose received by the prostate and adjacent critical structures.^{5,6} As treatments evolve and use more aggressive or complex treatment approaches (i.e. dose escalation, hypofractionation margin reduction, or dominant nodule boost), the need to correct for daily setup errors of the prostate will take on greater importance. Daily image guidance on the Hi*Art II (TomoTherapy, Inc., Madison, WI) system provides a solution to correct for prostate motion.⁷ After positioning the patient on the treatment couch, a three-dimensional (3D) megavoltage CT (MVCT)

image of the patient in the treatment position is acquired. The image is subsequently registered to the patient's planning CT and, based on the translation-only registration, the patient is re-positioned and treated. In our clinic, the goal of registration, whether manual or automated, is an overlap of the prostate gland in the MVCT and planning CT images to ensure that after patient repositioning the target volume is in the same geometric position on a day to day basis. Otherwise, patient repositioning will result in prostate misplacement during treatment delivery and the efficacy of the treatment may be compromised.

The Hi*Art II system has both manual and automatic capabilities for registering daily MVCT and planning CT images. Automatic registration allows the user to select whether the registration is based on either the bony anatomy, bone plus tissue, or the entire image. The system does not have the ability to perform automatic registration based on the overlap of a particular region of interest (ROI) such as the prostate. Alignment of the prostate gland in MVCT images and planning CT images using anatomy based manual registration techniques has been demonstrated to result in inaccurate daily positioning of the prostate, presumably due to the inherent difficulties of identifying soft tissue structures in MVCT images.⁸

The objective of this work is to quantify and compare the daily prostate positioning errors associated with helical tomotherapy patient re-positioning based on the automatic registration of bony anatomy or the automatic registration of the entire image. In order to examine this question, accurate prostate localization in daily MVCT images is required. Traditionally, prostate

localization in treatment images has been performed through either contouring of the prostate⁹ or with the use of implanted fiducials.¹⁰ The inherent reduced contrast of MVCT images compared to kVCT images makes contouring difficult and subject to observer variability, while implantation of fiducials is invasive and not practical for all patients. Recently, a registration-based technique that uses contour information from an initial kVCT to automatically localize the prostate in subsequent CT images has been developed and validated.¹¹⁻¹³ We have produced our own software based on this technique that uses median filtration in order to accurately and automatically localize the prostate in patient MVCT images. The software was used to retrospectively localize the prostate in patient treatment images acquired on the Hi*Art II system. In addition, we used established automatic voxel based methods to register either the bony anatomy or all voxels in MVCT and planning CT images.^{14,15} By evaluating automatic registration and prostate localization results, we calculated the prostate misplacement that would have occurred if daily patient repositioning was based on automatic registration of bony anatomy or if it was based on automatic registration of the entire image.

4.2 Methods and Materials

4.2.1 Patient Images

Images from eight research patients undergoing prostate treatment on the Hi*Art II system were used for this retrospective study. The planning CT images (dimensions: 256 x 256 x varied; spacing: 1.875 mm x 1.875 mm x 3.0 mm) were acquired on a PQ5000 scanner (Philips Medical Systems, Cleveland, OH), while

daily MVCT images (dimensions: 637 x 637 x varied; spacing: 0.754 mm x 0.754 mm x 6.0 mm) were acquired prior to each treatment fraction on the TomoTherapy Hi*Art II unit. The sole requirement in the MVCT acquisition protocol mandated that the mid-plane of the prostate be captured; as such, the extent of the patient imaged in the superior/inferior direction varied from fraction to fraction, but was typically on the order of approximately 15 cm. Of the eight patients, six patients underwent 25 treatment fractions, one received 23, and the final patient had 31 fractions. Each of the 204 MVCT images was manually registered to their respective planning CT image on the Reveal-MVS Fusion System (Mirada Solutions Ltd., Oxford, UK) to account for any gross misalignments that may have occurred as a result of poor initial patient positioning. The manual registrations were performed by a single physicist with the objective of achieving sub-cm accuracy, well within the capture ranges of the automatic software used in the study.

4.2.2 Automatic Registration

Using the manual results as the initial alignment, each MVCT image was registered to its respective planning CT using two different automatic rigid algorithms integrated in our in-house registration software. One algorithm is designed to produce the best overall alignment of the registered images, while the other achieves alignment of just the bony anatomy. These registration methods will be referred to as image matching (IM) and bone matching (BM) throughout this thesis, respectively. Both voxel based algorithms use the Nelder-Mead

simplex optimizer¹⁶ to maximize different adaptations of the mutual information cost function proposed by Mattes *et al.*¹⁵ For IM, all planning CT image voxels were used in calculating the mutual information metric; for BM, only the planning CT voxels corresponding to bone were included.¹⁴ As such, the voxels used for BM which were segmented via thresholding represent a subset of the voxels used for IM.

4.2.3 Automatic Prostate Localization

Court and Dong¹¹ demonstrated that automatic localization of the prostate on treatment CT images could be achieved by registering treatment images to a planning CT image using only the voxels in the planning CT gross tumour volume (GTV) plus a 3-mm border or expansion margin when calculating the registration cost function. In their implementation, the mean absolute difference (MAD) between overlapping voxels was minimized. They assumed translations only, neglecting any rotation and changes in the size and shape of the prostate. Smitsmans *et al.*¹² incorporated prostate rotation into the algorithm's design and investigated its capabilities when other cost functions instead of MAD were used. More recently, they validated the technique for use on kV cone beam CT (CBCT) images as well.¹³ We propose using this registration based method for localizing the prostate in MVCT images acquired on the High*Art II system.

Our implementation uses the correlation coefficient metric and only radiation oncologist delineated prostate planning CT voxels plus a small border are used for calculation of the cost function. Voxels in the border region

corresponding to intestinal gas or bone are filtered out by thresholding in order to reduce their influence on registration. The increased noise and reduced contrast in MVCT images relative to conventional kVCT and kV CBCT images make application of the technique to our situation nontrivial. To reduce the complexity, we followed Court and Dong's model in that only prostate translation is assumed. In addition, a noise reducing median filter was applied to MVCT images as a pre-processing procedure prior to each registration. MVCT images were not cropped prior to registration nor were any limits placed on prostate translations.

Although the prostate localization technique has been thoroughly validated for other treatment CT modalities, it had not been applied to MVCT images. Therefore, we believed that verification of its efficacy was required. This task was carried out using images from two patients, separate from the eight patients described above, who had three localization seeds implanted in the prostate. An initial planning CT and a single MVCT were acquired for each patient and the prostate was contoured in the planning CT. The true motion of the prostate was determined by analyzing the centre of gravity (COG) of the seeds in each image. The seeds were subsequently digitally removed by editing the image intensity data¹⁷ prior to registration with the prostate localization software. The dependence of the software's performance on the border surrounding the contoured prostate was established by repeating the registrations with borders ranging in size from 0 to 10 mm in 1-mm intervals. The improvements achieved by incorporating median filtration into the technique were verified by repeating

the registrations without use of the filter. Registration results were compared to the known prostate motion as determined by the seed positions. We also investigated the algorithm's dependence on the radiation oncologist's delineation of the prostate. One patient was randomly selected and the radiation oncologist was asked to re-contour the planning CT prostate months after the original contour had been drawn. Ten MVCT images for that patient were chosen at random and automatic prostate localization was repeated using the new contour for segmentation of the planning CT voxels used in registration.

4.2.4 Multi-start Procedure

To reduce registration uncertainty and eliminate any gross mis-registrations, a multi-start optimization procedure was employed.¹⁸ Every registration was repeated ten times, each time with a different random initial image overlap. For bone and image matching, the MVCT image position was randomly offset from the manual alignment position by a maximum of 10 mm and 5 degrees in 3D Euclidean space. In the prostate localization procedure, the initial MVCT image position was randomly offset from the optimal bone matching alignment by a maximum of 5 mm. Of the ten starts, the registration that resulted in the optimal mutual information value for IM and BM and the optimal correlation coefficient value for prostate localization was chosen as the true result. A simple test was implemented to reduce the possibility that the optimal cost function value corresponded to a false minimum. If more than two of the other nine registrations differed from the optimal result by greater than a 1

mm translation or 1 degree rotation in 3D Euclidean space, the result was discarded and the entire multi-start optimization procedure was repeated. If the multi-start procedure failed a second time, that registration was not included in subsequent analysis. In addition, all results were visually inspected and any registration that failed visual inspection was also repeated. Although, this process may seem like a deliberate attempt to bury failures, it is demanded by the design and objective of the study. Evaluated errors in prostate positioning resulting from the two automatic registration based patient positioning methods are dependent on the translational differences in the image alignments corresponding to prostate overlap and cost function optimization, as well as errors in determining the optimized cost function alignment. By rejecting failures, we limit the latter contribution. The assumption is made that if a registration fails, the accuracy of the matching procedure may be in question. Our strategy reduces the possibility that an alignment produced by the multi-start procedure does not correspond to the desired cost function optimum. Of course, if the procedural design was different and we were validating the accuracy of each registration method, eliminating data would not be acceptable.

4.3 Results

4.3.1 Prostate Localization Validation

A simple pass/fail criterion was used to ensure the prostate localization algorithm validated for other treatment CT imaging modalities could also be used on MVCT images. The multi-start procedure described above was carried out for

each image pair that contained implanted fiducials using each of the different border dimensions, with and without median filtration. To improve statistics, twenty random starts were used instead of ten. Registrations that localized the prostate within half a planning CT voxel to its true position in each translational direction as determined by the implanted seeds were considered a pass. This corresponds to accuracy within 0.94 mm, 0.94 mm, and 1.50 mm in the lateral left/right (LR), anterior/posterior (AP), and superior/inferior (SI) directions, respectively. The number of passes for each multi-start procedure is plotted in figure 4-1. The improved efficacy of the algorithm when median filtration is used is evident by the data. Focusing on the median filtered results, a dependence on the prostate border can be established. Results suggest that having too large or too small a prostate border when calculating the correlation coefficient cost function can lead to erroneous results. These results can be explained if we consider the inherent information contained in the voxels used in the calculation of the correlation coefficient metric. The individual voxels in the prostate itself have a fairly uniform range of intensity values in CT images. This lack of information makes it very difficult for the registration algorithm to accurately converge when little or no border is used and when prostate voxels themselves contribute to the vast majority or all of the voxels used when calculating the registration cost function. On the other hand, as more and more surrounding voxels are included, the contribution of the prostate itself to the cost function becomes diminished and the registration result slowly diverges from the truth. The competing effects set both a lower and upper limit on the border size

and it was decided that a 6 mm border should be used throughout the remainder of this work. The true prostate motion between MVCT and planning CT images for the two test patients are compared with the values determined by registration in table 4-1. Deviations between registration and true values for motion in the LR, AP and SI directions are all within 0.6 mm and results for both patients are accurate within 1 mm in 3D Euclidean space. Based on these results and validation studies in the literature with other treatment CT imaging modalities, our implementation of the automatic prostate localization algorithm can accurately be applied to MVCT images.

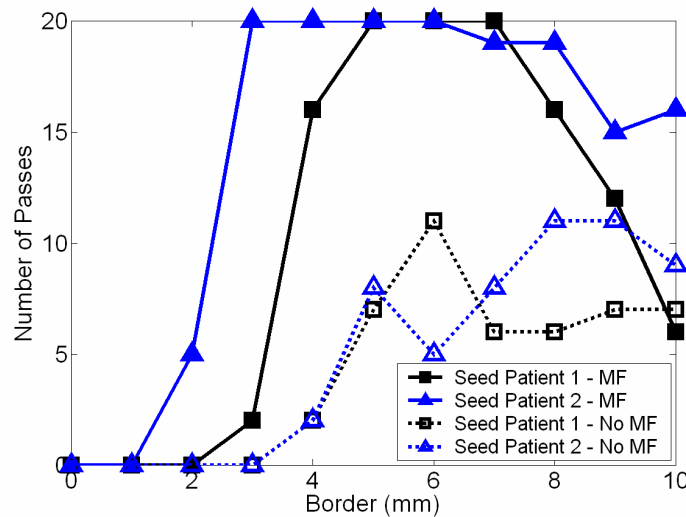


Figure 4-1. Number of passes as a function of the contour border used in the registration cost function calculation for the two test patient image pairs with implanted prostate localization seeds, with and without use of a median filter (MF). Each multi-start procedure consisted of 20 starts and a registration was considered a pass if the prostate motion was within half a planning CT voxel of the true motion in each of the three lateral directions.

Table 4-1. Comparison of actual prostate motion as determined from the positions of implanted localization seeds and measured prostate motion established with the automatic prostate localization algorithm.

	Actual (mm)	Measured (mm)	Difference (mm)
Patient 1			
LR	0.2	0.3	0.1
AP	-2.6	-2.0	0.6
SI	2.5	2.0	-0.5
Patient 2			
LR	-0.5	-0.7	-0.2
AP	-1.9	-1.9	0.0
SI	0.7	0.9	0.2

4.3.2 Dependence on Planning CT Contour Delineation

After re-drawing of the prostate contour on a single patient planning CT, the second radiation oncologist delineated contour was input into the automatic prostate localization software and the multi-start procedure was repeated for ten randomly selected MVCT images. Registration results from each planning CT contour were analyzed by calculating the absolute differences in prostate motion values produced by the two prostate localization procedures. The prostate motion values in the LR, AP, and SI directions for each input contour for all ten fractions are illustrated in figure 4-2. Average (\pm standard deviation) differences were 0.4

± 0.5 mm, 0.1 ± 0.1 mm, and 0.6 ± 0.2 mm in the LR, AP, and SI directions, respectively, demonstrating that the automatic prostate localization software has little dependence on intraobserver contouring discrepancies. For reference, the location of the centroid position in each contour differed by 0.8 mm in the LR direction, 0.5 mm in the AP direction, and 1.9 mm in the SI direction. Volumes were 36.7 cc and 37.3 cc, respectively.

4.3.3 Prostate Positioning Errors

Upon completion of the bone matching, image matching and prostate localization multi-start procedures for each image pair, the prostate positioning errors that would have occurred if daily patient repositioning was based on BM or IM were evaluated. Registrations that failed the multi-start procedure twice were excluded from analysis. For example, if image matching for a particular MVCT image failed, the IM prostate positioning error could not be calculated. Histograms for the BM and IM prostate positioning errors for all analyzed patient fractions are displayed in figure 4-3. In addition, mean and maximum 3D positioning errors for each individual patient are listed in table 4-2. Also included are standard deviation values which represent the range in positioning errors from fraction to fraction associated with each matching method. Results across the board demonstrate that daily prostate positioning using bone matching is superior to using image matching. For 157 treatment fractions, the mean prostate positioning error from image matching was 4.6 mm, with a standard deviation of 2.3 mm. The maximum value was 11.5 mm. In the 175 fractions

that the prostate positioning error from bone matching was calculated, the mean error was 3.7 mm, with a standard deviation of 2.1 mm. The maximum value was found to be 11.8 mm. Results were also analyzed in terms of each of the translational directions by calculating the percentage of fractions in which BM and IM would result in a prostate positioning error greater than 3 mm and greater than 5 mm in each direction. The 3 mm and 5 mm results are given in tables 4-3 and 4-4, respectively.

Table 4-2. Statistics for prostate positioning errors based on bone matching (BM) and image matching (IM).

P	Bone matching				Image matching			
	n	Mean (mm)	σ (mm)	Max (mm)	n	Mean (mm)	σ (mm)	Max (mm)
1	19	3.4	1.8	7.1	18	4.1	1.6	7.3
2	23	3.9	1.8	8.6	22	5.1	2.0	10.0
3	24	5.4	2.6	11.8	20	6.9	2.8	11.5
4	24	3.1	1.8	7.7	23	3.5	2.1	10.8
5	18	3.4	2.2	8.6	16	4.1	2.1	8.6
6	22	2.4	1.6	7.0	19	3.2	1.4	6.1
7	21	4.9	1.9	9.1	18	6.0	1.5	9.0
8	24	3.2	1.8	8.3	21	4.1	2.4	10.8

P = patient number; n = number of fractions analyzed

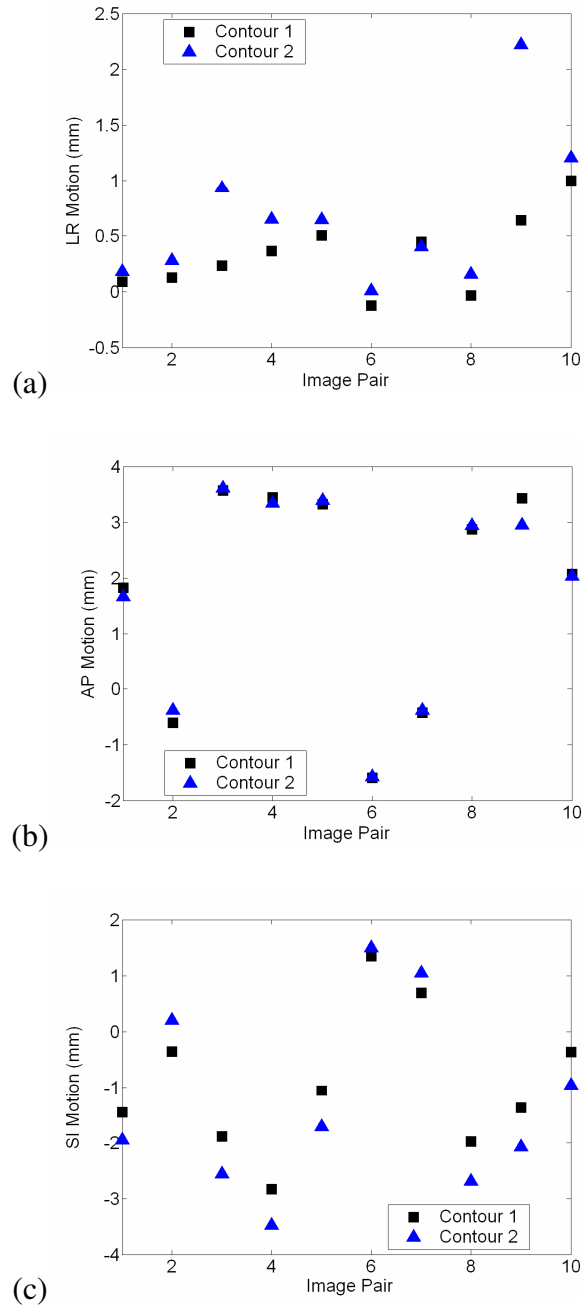
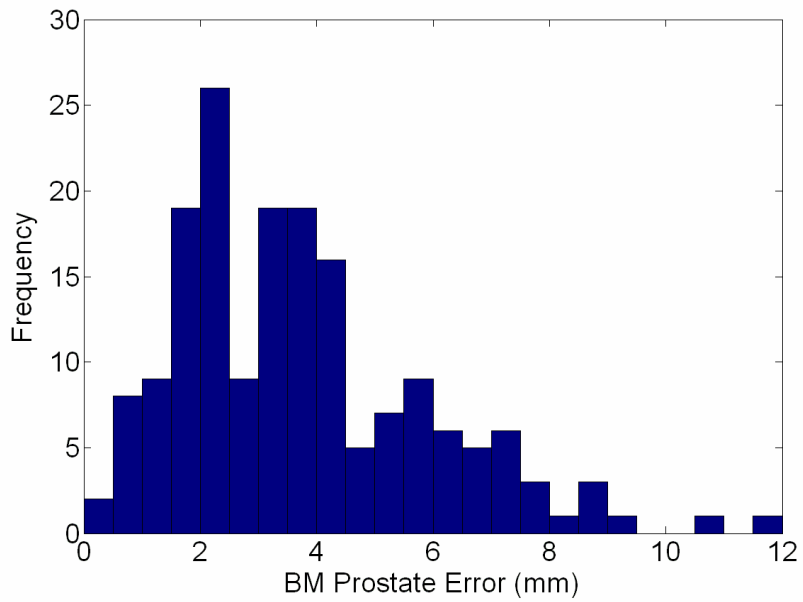
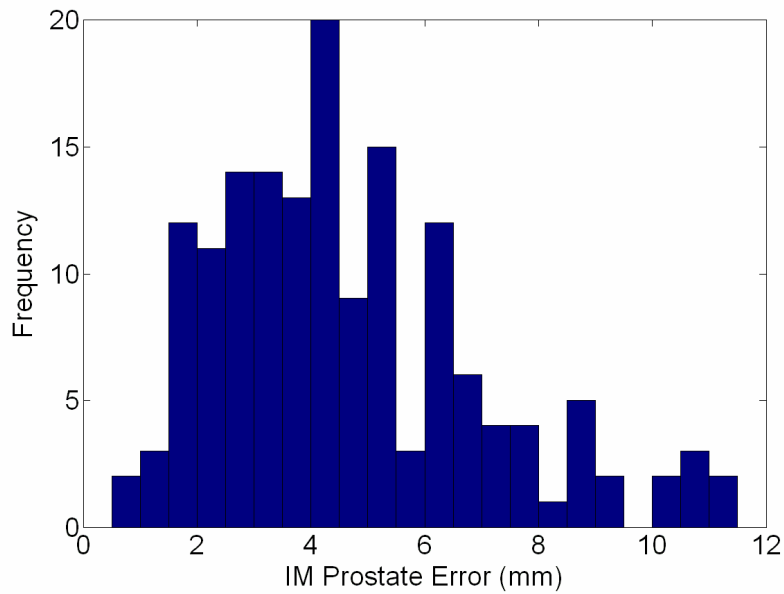


Figure 4-2. Prostate motion as measured by the automatic prostate localization software using two different input planning CT contours. Analysis was performed for ten randomly selected fractions from a single patient. (a) Left-right (LR) motion. (b) Anterior-posterior (AP) motion. (c) Superior-inferior (SI) motion.



(a)



(b)

Figure 4-3. Frequency histograms for 3D prostate positioning errors when daily patient repositioning is based on (a) bone matching (BM) and (b) image matching (IM).

Table 4-3. Percentage of registrations that resulted in a prostate positioning error ≥ 3 mm in each of the translational directions.

	LR	AP	SI
Bone matching (BM)	4%	37%	25%
Image matching (IM)	7%	39%	34%

Table 4-4. Percentage of registrations that resulted in a prostate positioning error ≥ 5 mm in each of the translational directions.

	LR	AP	SI
Bone matching (BM)	0%	11%	7%
Image matching (IM)	0%	17%	14%

4.3.4 Inter-fraction Prostate Motion

Once the multi-start procedures have been completed, evaluation of the offsets between prostate localization and bone matching in the LR, AP and SI directions provides a measure of the daily inter-fraction prostate motion. The distribution of values is shown in figure 4-4 and the inter-fraction prostate motion statistics are given in table 4-5. The observed standard deviations were 1.2 mm in the LR direction, 3.1 mm in the AP direction, and 2.6 mm in the superior-inferior direction. Mean values were sub-mm in each of the three directions, suggesting there are no systematic effects present for this patient population.

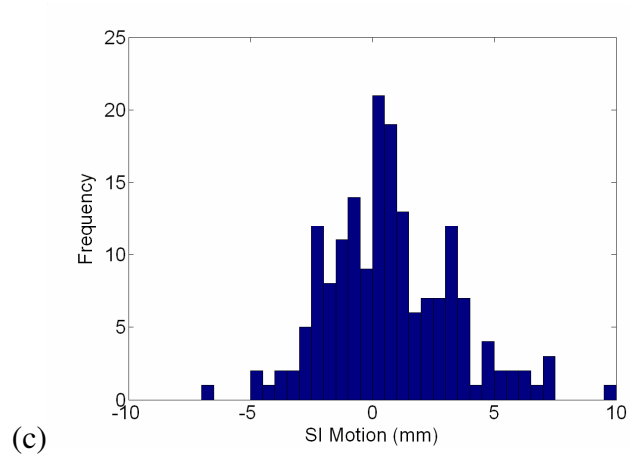
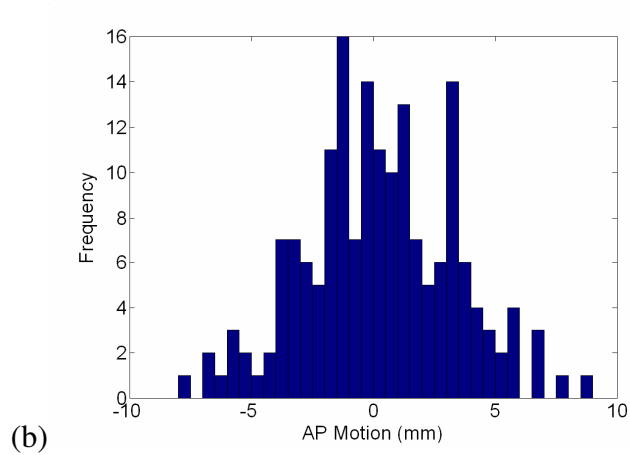
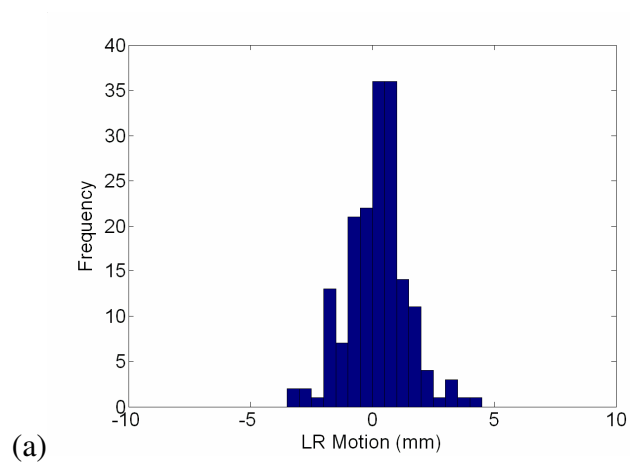


Figure 4-4. Inter-fraction prostate motion histograms for 175 treatment fractions. (a) Left-right (LR) motion. (b) Anterior-posterior (AP) motion. (c) Superior-inferior (SI) motion.

Table 4-5. Inter-fraction prostate motion statistics for entire cohort. Negative values correspond to motion superiorly, anteriorly and to the left.

Direction	Mean (mm)	σ (mm)	Range (mm)
Left/right (LR)	0.2	1.2	-3.3 to 4.2
Anterior/posterior (AP)	0.2	3.1	-7.6 to 8.7
Superior/inferior (SI)	0.7	2.6	-6.9 to 10.7

4.4 Discussion

Of the 204 multi-start procedures performed for BM, IM, and prostate localization the acceptance rates were 97%, 90%, and 89%, respectively. The acceptance rate for prostate localization requires further discussion. For temporal reasons and to reduce gonadal dose, care was taken to minimize the extent of daily MVCT image acquisition inferior to the prostate gland. As a result, numerous MVCT images used in this study did not contain the entire prostate. If only the multi-start prostate procedures in which the entire prostate is contained in the MVCT image are considered, the acceptance rate increases to 95%.

We have demonstrated that significant prostate positioning errors will occur when daily patient repositioning in the Hi*Art II system is performed based on bone matching and image matching. To put the results into perspective, consider that if during daily treatment, patients were repositioned based on the registration of MVCT and planning CT images using the standard automatic image matching algorithm used in this study, on average the prostate would be 4.6

mm away from where it should be during each treatment fraction. On the other hand, if repositioning the patient based on bone matching, the average daily prostate misplacement would be reduced to 3.7 mm. For reference, our values are slightly lower than the mean 3D distance of 5 mm between prostate overlap and bone matching alignments observed in the previously cited study by Ten Haken *et al.*¹ involving radiographs. In terms of the absolute translational directions, IM would lead to prostate positioning error ≥ 3 mm in any of the LR, AP or SI directions in 62% of treatment fractions. The corresponding value for BM is 51%. Analogous values for positioning errors ≥ 5 mm are 29% and 17% for IM and BM, respectively. These results suggest that location of the prostate is better correlated with pelvic bony anatomy as opposed to the pelvic anatomy as a whole. One possible explanation is that prostate positioning errors associated with bone matching are solely dependent on the motion of the prostate with respect to rigid anatomy, whereas in image matching, the overlap of amorphous structures such as the outer patient contour may also contribute to positioning errors.¹⁴ As such, given the choice of performing daily patient re-positioning based on automatic image matching or automatic bone matching, the latter should be chosen.

Results for all eight patients are consistent with the cohort data in that errors are greater for image matching than bone matching. In particular, there were three patients in which the mean value for image matching error was greater than 5 mm. The source of the large value is different for each patient; however, they can all be attributed to the fact that the prostate gland moves in response to

rectal and bladder filling.^{19,20} The standard treatment protocol for prostate patients at our clinic specifies a full bladder and empty rectum. Any deviation from this standard during planning CT image acquisition or during treatment can lead to the prostate being in a different location in MVCT images than in planning CT images. Patient 2, who had a mean image matching error of 5.1 mm had a significant amount of intestinal gas present during the planning CT that was not present in the majority of daily MVCT images. The treatment protocol was not fully satisfied for Patient 7, either, as the patient's bladder was not entirely full during planning CT acquisition and as a result, the bladder was significantly larger in the majority of MVCT images. The largest mean deviation occurred for Patient 3 and the explanation is slightly different. The patient had a full bladder and empty rectum during planning CT acquisition; however, the patient had large quantities of bowel gas during the majority of pre-treatment MVCT acquisitions, and presumably during treatment as well.

In the treatment of the patients investigated in this study, the prostate and seminal vesicles were taken to be the clinical target volume (CTV) and a margin of 7 mm posteriorly and 10 mm around the remainder of the CTV defined the planning target volume (PTV). Although observed offset values tend to be well within the extent of these margins, these offsets are clinically significant for a couple of reasons. Firstly, the entire PTV is planned to receive the prescription dose. If after patient repositioning based on IM, the prostate location is off by the mean value of 4.6 mm (although the entire CTV will still receive the prescription dose), there is a high probability that part of a surrounding critical structure will

also receive that prescription dose. In addition, studies have shown that increasing the prescription dose in prostate radiotherapy leads to improved cure rates²¹ and as doses continue to escalate, margins will need to be reduced accordingly in order to minimize dose to the surrounding critical structures. With reduced margins, prostate localization errors must be considered when performing automatic registration based daily positioning in order to prevent the CTV from being underdosed.

As mentioned previously, Langen *et al.*⁸ investigated manual registration techniques for daily prostate positioning on the Hi*Art II system and found that without the use of implanted fiducials, prostate errors greater than 3 mm in any one direction were common. We have shown that automatic registration methods based on bone matching and image matching also lead to daily prostate positioning errors. Although errors have been quantified for both manual and automatic methods, a statement advocating one technique over the other requires evaluation using the same cohort of image data. Regardless of the positioning method, prostate positioning errors are not dosimetrically acceptable in standard clinical practice. For example, Wong *et al.* investigated IMRT patients treated on a Primus (Siemens Medical Solutions, Concord, CA) linear accelerator and found that for a typical prostate case, failure to correct for a 10 mm posterior prostate shift results in a drop in CTV dose coverage from 95-107% to 71-100%.⁶ Further research is required to determine the extent of the dosimetric implications of prostate positioning errors for Hi*Art II patients. The only way to truly eliminate prostate positioning errors when performing daily patient repositioning based

image registration is to ensure that the daily registration results in accurate prostate overlap. One solution would be to have accurate automatic prostate localization tools incorporated into the Hi*Art II system. Further research is required before the algorithm used in this work can be implemented clinically on a daily basis. The multi-start procedure and the highly stringent convergence criterion used in our implementation resulted in registrations that took upwards of half an hour and would not permit for registration to be performed in clinically allowable times during treatments.

In 2001, a review of all the inter-fraction prostate motion studies in the literature was compiled by Langen and Jones.¹⁹ Standard deviations ranged from 0.7 mm to 1.9 mm for LR motion, 1.5 mm to 4.1 mm for AP motion, and 1.7 mm to 4.5 mm for SI motion. Not only does our data fit in the middle of the range of values in the reported literature, our results also follow the common trend that due to daily variations in bladder and rectal filling, inter-fraction prostate motion is greater in the AP and SI directions than in the LR direction. More importantly, we have shown that inter-fraction prostate motion can be measured in Hi*Art II prostate patients using automated registration techniques. This allows for a number of potential research opportunities.

4.5 Conclusion

We have quantified the prostate positioning errors that would occur if daily patient positioning of eight research patients treated on the Hi*Art II system was based on automatic image matching and automatic bone matching.

Clinically significant errors ranging up to 11.8 mm were observed. If the assumption is made that the prostate gland should be in the same location during each treatment fraction, automatic IM and automatic BM would have led to average prostate positioning errors of 4.6 mm and 3.7 mm, respectively. Further work is required to determine the dosimetric and biological consequences of these positioning errors, not only for the target volume, but also the surrounding dose sensitive structures. Ideally, an accurate automatic prostate localization algorithm should be implemented during daily treatment on the Hi*Art II system. The algorithm used in this work is a candidate; however, the code must be modified in order for it to operate quickly enough to be practical for clinical use. Whether or not such time saving modifications will compromise the algorithm's accuracy remains to be seen. As such, further research is required before the algorithm used in this work can be implemented clinically.

4.6 References

1. Ten Haken RK, Forman JD, Heimburger DK, Gerhardtsson A, McShan DL, Perez-Tamayo C, Schoepfel SL, Lichter AS. Treatment planning issues related to prostate movement in response to differential filling of the rectum and bladder. *Int J Radiat Oncol Biol Phys.* 1991;20:1317-1324.
2. Roeske JC, Forman JD, Mesina CF, He T, Pelizzari CA, Fontenla E, Vijayakumar S, Chen GTY. Evaluation of changes in the size and location of the prostate, seminal vesicles, bladder, and rectum during a course of external beam radiation therapy. *Int J Radiat Oncol Biol Phys.* 1995;33:1321-1329.

3. Melian E, Mageras GS, Fuks Z, Leibel SA, Niehaus A, Lorant H, Zelefsky M, Baldwin B, Kutcher GJ. Variation in prostate position quantitation and implications for three-dimensional conformal treatment planning. *Int J Radiat Oncol Biol Phys.* 1997;38:73-81.
4. van Herk M, Bruce A, Kroes APG, Shouman T, Touw A, Lebesque JV. Quantification of organ motion during conformal radiotherapy of the prostate by three dimensional image registration. *Int J Radiat Oncol Biol Phys.* 1995;33:1311-1320.
5. Schaly B, Bauman GS, Song W, Battista JJ, Van Dyk J. Dosimetric impact of image-guided 3D conformal radiation therapy of prostate cancer. *Phys Med Biol* 2005;50:3083-3101.
6. Wong JR, Grimm L, Uematsu M, Oren R, Cheng CW, Merrick S, Schiff P. Image-guided radiotherapy for prostate cancer by CT-linear accelerator combination: prostate movements and dosimetric considerations. *Int J Radiat Oncol Biol Phys.* 2005;61:561-569.
7. Tome WA, Jaradat HA, Nelson IA, Ritter MA, Mehta MP. Helical tomotherapy: image guidance and adaptive dose guidance. *Front Radiat Ther Oncol.* 2007;40:162-178.
8. Langen KM, Zhang Y, Andrews RD, Hurley ME, Meeks SL, Poole DO, Willoughby TR, Kupelian PA. Initial experience with megavoltage (MV) CT guidance for daily prostate alignments. *Int J Radiat Oncol Biol Phys.* 2005;62:1517-1524.

9. Kupelian PA, Langen KM, Zeidan OA, Meeks SL, Willoughby TR, Wagner TH, Jeswani S, Ruchala KJ, Haimerl J, Olivera GH. Daily variations in delivered doses in patients treated with radiotherapy for localized prostate cancer. *Int J Radiat Oncol Biol Phys.* 2006;66:876-882.
10. Balter JM, Sandler HM, Lam K, Bree RL, Lichter AS, Ten Haken RK. Measurement of prostate movement over the course of routine radiotherapy using implanted markers. *Int J Radiat Oncol Biol Phys.* 1995;31:113-118.
11. Court LE, Dong L. Automatic registration of the prostate for computed-tomography-guided radiotherapy. *Med Phys.* 2003;30:2750-2757.
12. Smitsmans MHP, Wolthaus JWH, Artignan X, de Bois J, Jaffray DA, Lebesque JV, van Herk M. Automatic localization of the prostate for on-line or off-line image-guided radiotherapy. *Int J Radiat Oncol Biol Phys.* 2004;60:623-635.
13. Smitsmans MHP, de Bois J, Sonke JJ, Betgen A, Zijp LJ, Jaffray DA, JV Lebesque, van Herk M. Automatic prostate localization on cone-beam CT scans for high precision image-guided radiotherapy. *Int J Radiat Oncol Biol Phys.* 2005;63:975-984.
14. Ruchala KJ, Olivera GH, Kapatoes JM. Limited-data image registration for radiotherapy positioning and verification. *Int J Radiat Oncol Biol Phys.* 2002;54:592-605.
15. Mattes D, Haynor DR, Vesselle H, Lewellen TK, Eubank W, PET-CT image registration in the chest using free-form deformations. *IEEE Trans Med Imag.* 2003;22:120-128.

16. Nelder JA, Mead R. A simplex method for function minimization. *Computer Journal*. 1965;7:308-313.
17. Crouch JR, Pizer SM, Chaney EL, Hu YC, Mageras GS, Zaider M. Automated finite-element analysis for deformable registration of prostate images. *IEEE Trans Med Imag*. 2007;26:1379-1390.
18. Popescu FC, Viceconti M, Traina F, Toni A. Evaluation of achievable registration accuracy of the femur during minimally invasive total hip replacement. *Med Biol Eng Comput*. 2005;43:421-430.
19. Langen KM, Jones DTL. Organ motion and its management. *Int J Radiat Oncol Biol Phys*. 2001;50:265-278.
20. Byrne TE. A review of prostate motion with considerations for the treatment of prostate cancer. *Medical Dosimetry*. 2005;30:155-161.
21. Pollack A, Zagars GK, Starkschall G, Antolak JA, Lee JJ, Huang E, von Eschenbach AC, Kuban DA, Rosen I. Prostate cancer radiation dose response: results of the M. D. Anderson phase III randomized trial. *Int J Radiat Oncol Biol Phys*. 2002;53:1097-1105.

Chapter 5: Dosimetric implications of two registration based patient positioning methods in image guided radiation therapy

A version of this chapter has been published:

Rivest DRC, Riauka TA, Murtha AD, Fallone BG. Dosimetric implications of two registration based patient positioning methods in prostate image guided radiation therapy. *Radiol Oncol.* 2009;43:203-212.

5.1 Introduction

The field of image-guided radiation therapy (IGRT) arose from the need to account for daily anatomically-based variations in the delivery of fractionated radiation therapy. This is particularly relevant to the treatment of prostate cancer as it has been repeatedly demonstrated that the position of the prostate gland varies as a result of bladder and rectal filling.^{1,2} A number of correctional strategies including implanted fiducials³⁻⁵ and on-line three-dimensional (3D) computed tomography (CT) imaging⁶⁻⁹ have been developed and clinically implemented. Although both methods provide daily image guidance, the latter is advantageous in that it allows for the evaluation of daily delivered doses.¹⁰

The principal modality for prostate IGRT at our clinic is the Hi*Art II helical tomotherapy unit (TomoTherapy, Inc. Madison, WI). Prior to each fraction, radiation therapists acquire a 3D megavoltage CT (MVCT) of the patient in treatment position which is subsequently registered to the patient's planning CT and based on the registration, the patient is re-positioned and treated. As outlined in the previous chapter, to ensure the target is situated in the same geometric location on a daily basis, registration should result in the overlap of the prostate volumes in the MVCT and planning CT images. This varies from traditional prostate treatment protocols where the lack of soft tissue contrast in portal images made prostate matching impossible, and without the aid of implanted fiducials, patient re-positioning was based on the matching of bony anatomy.¹¹⁻¹⁶ This change in patient positioning methodology has potential detrimental consequences to the dosimetry of critical structures. For example, consider the general scenario where a target volume has moved slightly in the direction of a critical structure. Bone matching, in combination with sufficient margins, will ensure the entire target receives the prescription dose, however, target matching would certainly lead to an increased dose to the critical structure (Figure 5-1).

Unfortunately, the dosimetric implications of using prostate matching instead of bone matching for daily image guidance have not been sufficiently investigated. The objective of this work is to quantify and compare the doses that would be delivered to the prostate, bladder, and rectum if image guidance on the Hi*Art II system was based on prostate matching or on bone matching. The

dependence of dosimetric variations on the direction of daily prostate motion will also be investigated.

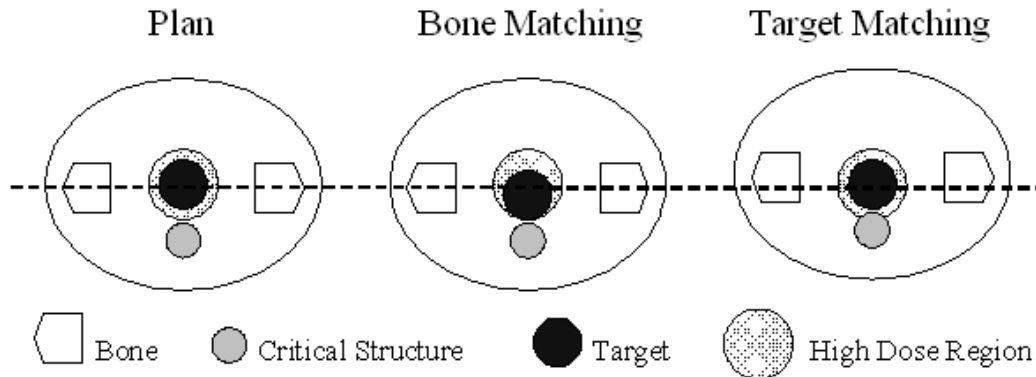


Figure 5-1. Simplified schematic demonstrating the potential increased dose to a critical structure as a result of target matching. A gap is present between the target and critical structure in the planning CT, but the target has moved towards the critical structure when the patient is treated. With appropriate margins, bone matching results in complete coverage of the target without having any of the critical structure situated in the high dose region. On the other hand, part of the critical structure receives the target dose if target matching is used for patient positioning. It should be noted that although the depicted scenario may be interpreted as the target being the prostate and the critical structure representing the rectum, this is not the intent. The diagram depicts a general scenario where the target has moved in the direction of a critical structure.

5.2 Methods and Materials

Treatment data from four research patients treated for high risk prostate cancer on the Hi*Art II unit were available for this retrospective study. The primary planning target volume (PTV), treated to 68.0 Gy over 25 fractions (2.72 Gy/fraction), was defined by margins of 7-mm posteriorly and 10-mm in all other directions around the prostate gland and seminal vesicles. Constraints for the rectum and bladder during inverse planning were that no more than 30% of the rectum volume receive 45.0 Gy (1.80 Gy/fraction) and no more than 45% of the bladder volume receive 50.0 Gy (2.00 Gy/per fraction). Patients were instructed to have a full bladder and empty rectum during simulation and each daily treatment fraction. Prior to each fraction, a pelvic MVCT was acquired and used for patient re-positioning. For our purposes, one MVCT was removed from the data set because the entire prostate was not imaged, leaving ninety-nine fractions available for this study.

As a result of daily prostate motion with respect to rigid pelvic bony anatomy, prostate matching and bone matching of daily MVCT and planning images produces two different image alignments.¹⁷ In this work, prostate matching and bone matching were performed using the same in-house developed automatic registration software used in chapter 4. For prostate matching, daily MVCT images were registered to planning CT images by optimizing the correlation coefficient metric. To ensure the overlap of the MVCT and planning CT prostate volumes, only the planning CT voxels corresponding to prostate plus a small 6.0-mm border were used in cost function calculation.¹⁸⁻²⁰ Voxels in the

border region corresponding to bone and intestinal gas were filtered via thresholding to eliminate their influence on registration. In addition, a noise reducing median filter²¹ was applied to MVCT images prior to registration. For bone matching, we used the mutual information algorithm proposed by Mattes *et al.*,²² however, only the automatically segmented planning CT voxels corresponding to bony anatomy were used to evaluate the cost function. Both the prostate and bone matching procedures rely on the Nelder-Mead simplex algorithm²³ for cost function optimization.

Following completion of bone matching and prostate matching procedures, dose distributions that would have been delivered using both image guidance strategies were evaluated with the Hi*Art II system's inherent Planned Adaptive software. The software evaluates delivered dose distributions by applying the treatment delivery sinogram to daily MVCT images, and has been demonstrated to have dosimetric accuracy comparable to that of planning CT dose calculations.¹⁰ A number of studies have been published in which the tool was used to compare planned and delivered doses,^{24,25} however, to the best of our knowledge, the software has not been used to calculate theoretical dose distributions that would have been delivered had patient positioning been performed differently.

Retrospectively, prostate, rectum, and bladder volumes were contoured by a radiation oncologist on all pre-treatment MVCT images using the Planned Adaptive software, and dose volume histograms (DVH) were evaluated for each dose distribution. Structures on each MVCT image were delineated only once

and external software was used to account for the translational shifts in the contour co-ordinates between the two matching methods. Dosimetric endpoints for DVH analysis were adopted from the tumour and sensitive structure constraints implemented during inverse planning. As such, values for D95, D45, and D30 were extracted from each prostate, bladder, and rectum DVH, respectively. In addition to absolute evaluation, the differences between dosimetric endpoints for each method were also evaluated.²⁶ As such, for comparison of prostate matching and bone matching image guidance strategies, $\Delta D95$, defined as prostate D95 for prostate matching minus prostate D95 for bone matching, was determined for each fraction. Defined analogously, bladder $\Delta D45$ and rectum $\Delta D30$ values were also evaluated. In addition, five MVCT images were selected at random and re-contoured upon which dosimetric analysis was repeated to determine the effect of intra-observer variations in structure delineation on the evaluated endpoints.

The relationship between bladder^{27,28} and rectal²⁷⁻²⁹ filling and prostate motion in the superior/inferior (SI) and anterior/posterior (AP) directions has been repeatedly documented in the literature. Bladder D45 and rectum D30 values are clearly dependent on organ volumes, and as such, endpoints were also evaluated with respect to the measured daily prostate motion. Daily prostate motion (i.e. for each fraction) was calculated from the differences between the bone matching and prostate matching alignments.

5.3 Results

5.3.1 Daily Prostate Motion

The mean (\pm standard deviation) of the prostate motion for the ninety-nine fraction cohort was 2.4 ± 1.9 mm superiorly, 0.7 ± 2.5 mm anteriorly, and 0.3 ± 0.5 mm to the left. It should be noted that the mean shift in the SI direction is noticeably different than the reported value in table 4-5. However, this difference is systematic and will be discussed in section 5.4. In addition, although motion was skewed superiorly, standard deviations are comparable with values previously reported in the literature,¹ albeit on the lower end. Statistics for each individual patient are reported in table 5-1.

5.3.2 Dose Volume Histogram Analysis

The mean (\pm standard deviation) prostate D95, bladder D45 and rectum D30 values for each matching method are given in table 5-2. Although mean prostate D95 values are identical for prostate matching and bone matching, evaluated critical structure endpoints are dependent on the matching method. Worth mentioning is the fact that the inverse planning constraints for prostate D95 were met, however, reported bladder D45 and rectum D30 values exceed their respective inverse planning constraints. In light of these observations, the percentage of fractionated bladder D45 and rectum D30 values that exceeded the constraints by differing dosimetric amounts were evaluated and appear in table 5-3. Observed bladder and rectum dosimetric endpoints correlate with the observed trends of anterior and superior prostate motion reported in the previous section.

Presumably, if the prostate has moved superiorly towards the bladder, prostate matching would increase the volume of bladder that receives the prescription dose. Similarly, anterior prostate motion would result in the prescription dose being delivered to less rectal volume. The thirteen odd numbered fraction dose volume histograms for patient 1 are plotted in figure 5-2 to demonstrate the daily variations in prostate, bladder and rectum dosimetry for each matching method.

5.3.3 Image Guidance Comparison

Histograms of the theoretical prostate ΔD_{95} , bladder ΔD_{45} , and rectum ΔD_{30} values for all ninety-nine fractions are displayed in figure 5-3. The mean (\pm standard deviation) prostate ΔD_{95} for the cohort was 0.00 ± 0.01 Gy, with values ranging from -0.02 to 0.02 Gy. Observed bladder ΔD_{45} values ranged from -0.22 to 0.52 Gy, having a mean value of 0.07 ± 0.12 Gy. Finally, the mean rectum ΔD_{30} value was -0.06 ± 0.14 Gy, with values ranging from -0.40 to 0.34 Gy. Statistics for each individual patient are reported in table 5-4. Measured bladder ΔD_{45} and rectum ΔD_{30} values are plotted as a function of prostate motion in the AP and SI directions in figure 5-4. A dependence on the direction of prostate motion is clearly evident.

Table 5-1. Prostate motion statistics for each individual patient. Negative values correspond to motion superiorly, anteriorly and to the left.

Patient	Direction	Mean \pm SD (mm)	Range (mm)
1	LR	0.0 \pm 0.4	-0.8 to 0.8
	AP	-2.3 \pm 3.2	-8.3 to 8.4
	SI	-4.1 \pm 1.6	-8.0 to -1.6
2	LR	-0.1 \pm 0.4	-1.0 to 0.7
	AP	0.0 \pm 1.5	-3.3 to 3.0
	SI	-2.1 \pm 1.2	-6.7 to -0.2
3	LR	-0.8 \pm 0.4	-1.7 to -0.3
	AP	-1.7 \pm 1.9	-5.3 to 1.9
	SI	-1.1 \pm 2.0	-4.7 to 2.8
4	LR	-0.3 \pm 0.6	-2.1 to 0.4
	AP	0.9 \pm 1.8	-2.3 to 6.5
	SI	-2.2 \pm 1.6	-5.0 to 2.4
Combined	LR	-0.3 \pm 0.5	-2.1 to 0.8
	AP	-0.7 \pm 2.5	-8.3 to 8.4
	SI	-2.4 \pm 1.9	-8.0 to 2.8

Table 5-2. Per fraction mean \pm standard deviation prostate D95, bladder D45 and rectum D30 values for all ninety-nine fractions for each matching method.

Inverse planning constraints are given in brackets.

	Bone Matching (Gy)	Prostate Matching (Gy)
Prostate D95 (≥ 2.72 Gy)	2.81 ± 0.02	2.81 ± 0.02
Bladder D45 (≤ 2.00 Gy)	2.06 ± 0.17	2.13 ± 0.21
Rectum D30 (≤ 1.80 Gy)	2.29 ± 0.22	2.23 ± 0.17

Table 5-3. Percent of fractions in which the bladder and rectum inverse planning constraints were dosimetrically exceeded, exceeded by 10% and exceeded by 25% for each matching method.

	Bone Matching (%)	Prostate Matching (%)
Bladder D45 exceeded (≥ 2.00 Gy)	59	67
Bladder D45 exceeded by 10% (≥ 2.20 Gy)	12	32
Bladder D45 exceeded by 25% (≥ 2.50 Gy)	4	7
Rectum D30 exceeded (≥ 1.80 Gy)	100	100
Rectum D30 exceeded by 10% (>1.98 Gy)	97	96
Rectum D30 exceeded by 25% (>2.25 Gy)	51	42

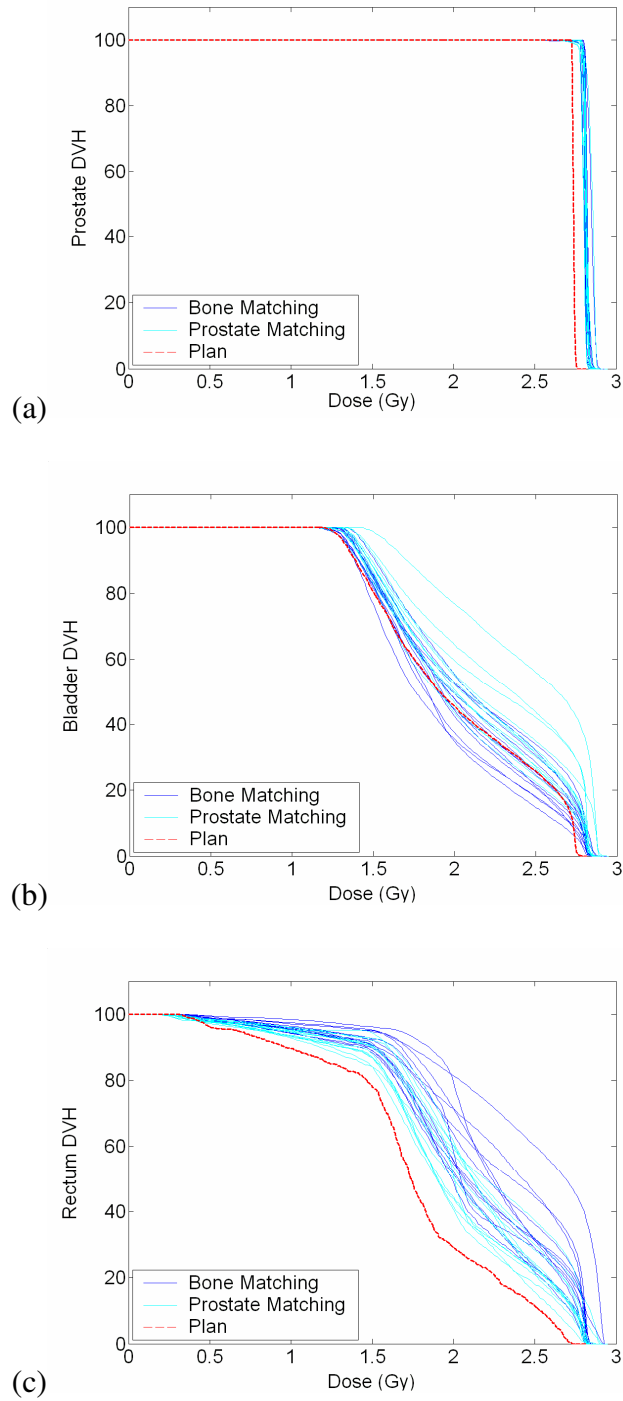


Figure 5-2. DVH comparison of prostate matching (PM) and bone matching (BM) for patient 1 odd numbered fractions (i.e. fraction 1, 3, ..., 23, 25). (a) Prostate, (b) bladder, (c) rectum.

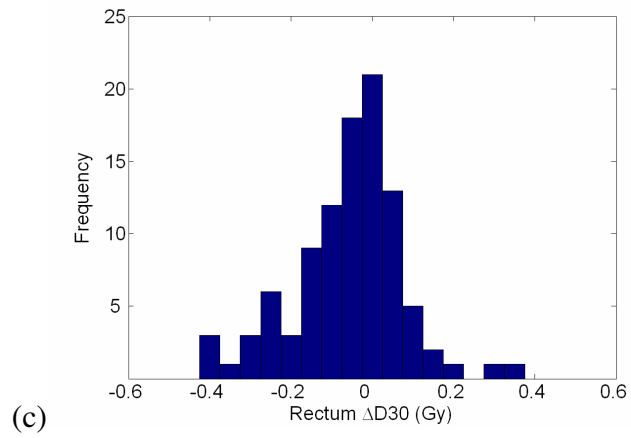
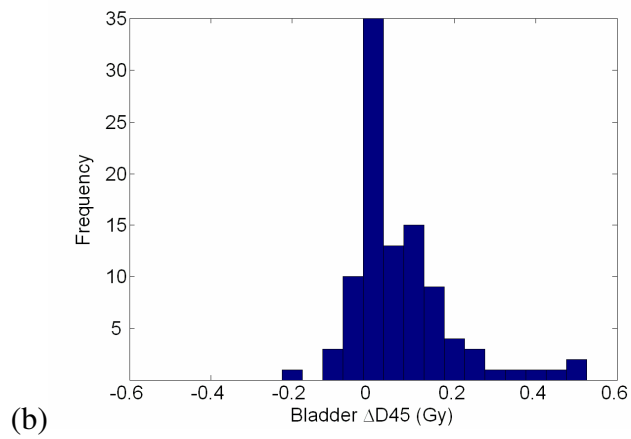
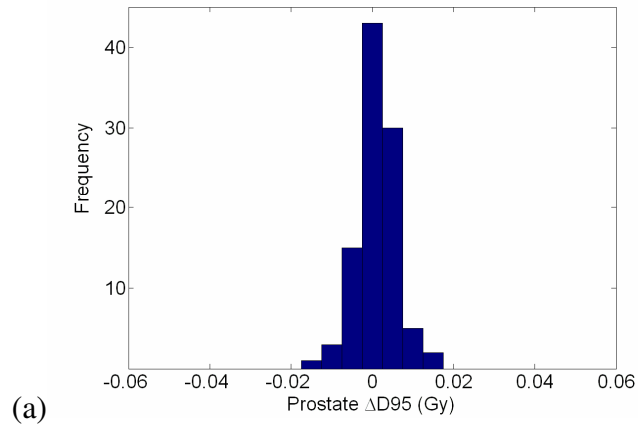


Figure 5-3. Frequency histograms of the dosimetric differences between prostate and bone matching. (a) Prostate $\Delta D95$, (b) bladder $\Delta D45$, and (c) rectum $\Delta D30$ values for all ninety-nine fractions.

Table 5-4. Individual patient statistics for prostate $\Delta D95$, bladder $\Delta D45$ and rectum $\Delta D30$. Δ denotes prostate matching minus bone matching. The combined patient values are also normalized to the inverse planning constraints (i.e. prostate: 2.72 Gy, bladder: 2.00 Gy and rectum: 1.80 Gy).

Patient	Endpoint	Standard Deviation (Gy)	Range (Gy)
1	Prostate $\Delta D95$	< 0.01	-0.01 to 0.00
	Bladder $\Delta D45$	0.16	-0.22 to 0.52
	Rectum $\Delta D30$	0.15	-0.40 to 0.32
2	Prostate $\Delta D95$	< 0.01	-0.02 to 0.01
	Bladder $\Delta D45$	0.05	-0.09 to 0.17
	Rectum $\Delta D30$	0.09	-0.26 to 0.22
3	Prostate $\Delta D95$	< 0.01	0.00 to 0.01
	Bladder $\Delta D45$	0.08	-0.08 to 0.20
	Rectum $\Delta D30$	0.10	-0.34 to 0.06
4	Prostate $\Delta D95$	< 0.01	0.00 to 0.02
	Bladder $\Delta D45$	0.04	-0.08 to 0.08
	Rectum $\Delta D30$	0.09	-0.10 to 0.34
Combined	Prostate $\Delta D95$	< 0.01 (0.2%)	-0.02 to 0.02 (-0.6 to 0.6%)
	Bladder $\Delta D45$	0.12 (6.1%)	-0.22 to 0.52 (-11.2 to 26.0%)
	Rectum $\Delta D30$	0.14 (7.5%)	-0.40 to 0.34 (-22.0 to 19.1%)

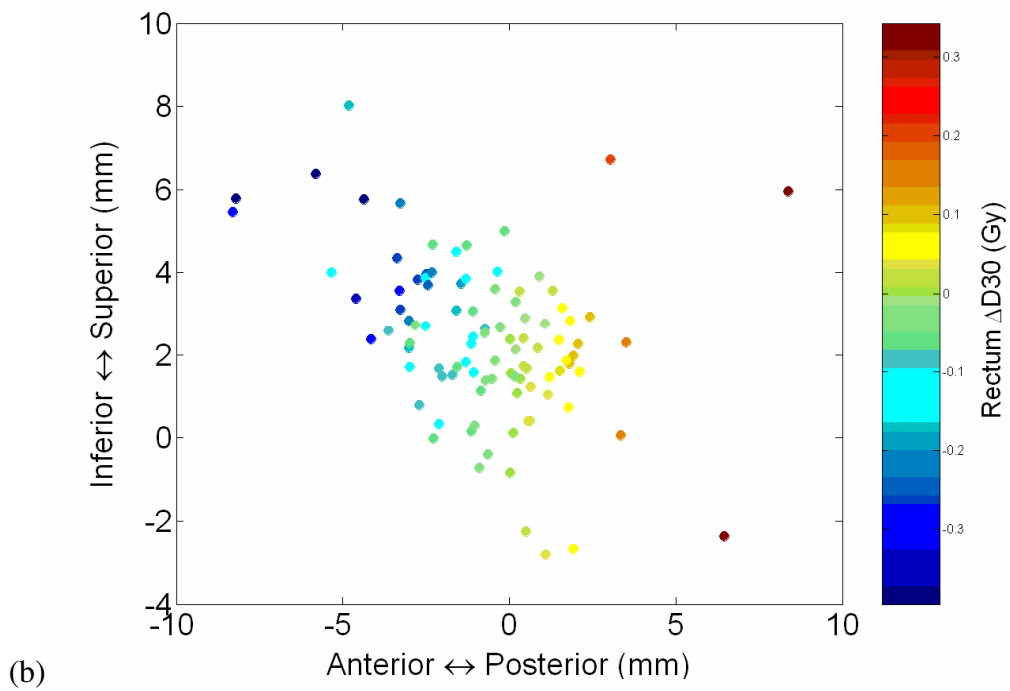
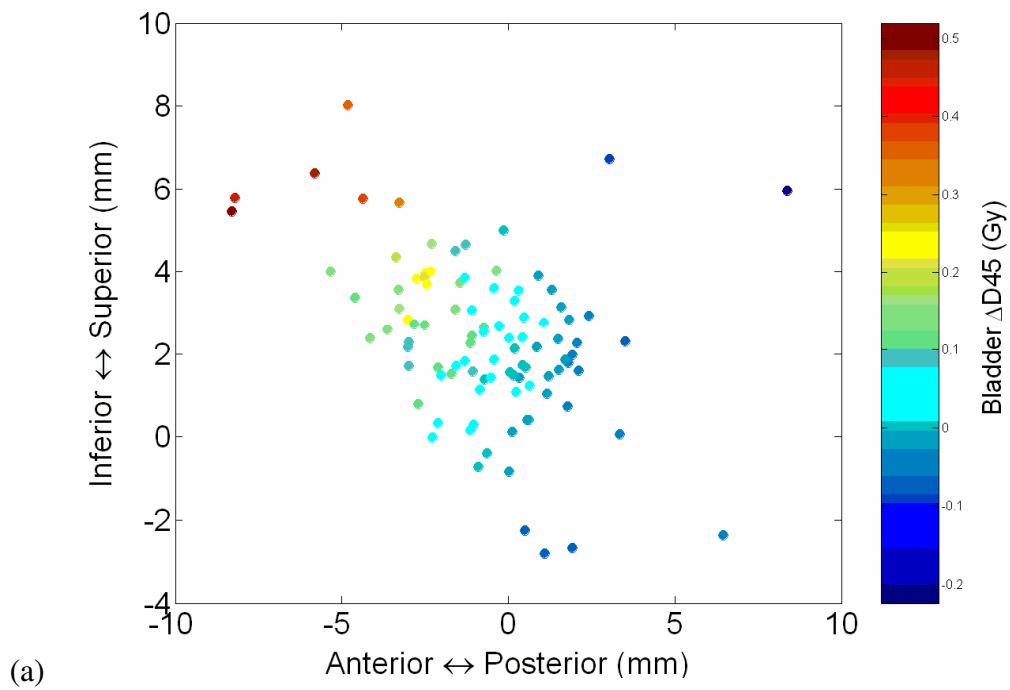


Figure 5-4. Scatter plot of per fraction (a) bladder $\Delta D45$ and (b) rectum $\Delta D30$ values (Gy) for all ninety-nine fractions as a function of prostate motion in the superior/inferior and anterior/posterior directions.

5.3.4 Contour Dependence

The absolute difference between dosimetric endpoints evaluated using original and repeat contours was calculated for each of the five re-contoured MVCT images. The mean (\pm standard deviation) absolute difference of the ten (five for each matching method) bladder D45 values was 0.03 ± 0.02 Gy. This represents $1.2 \pm 0.7\%$ of the prescription dose. Corresponding values for rectum D30 absolute differences were slightly higher at 0.07 ± 0.07 Gy or, $2.5 \pm 2.6\%$ of the prescription dose. The mean (\pm standard deviation) of the five bladder Δ D45 absolute differences was 0.01 ± 0.02 Gy or $0.3 \pm 0.6\%$ of the prescription dose. Rectum Δ D30 values were 0.04 ± 0.04 Gy or $1.4 \pm 1.2\%$. Mean and standard deviations of the absolute differences in both prostate D95 and prostate Δ D95 values were less than 0.1% of the prescription dose. Based on these observations, the reported magnitudes of prostate Δ D95, bladder Δ D45 and rectum Δ D30 values exceed the respective errors associated with intra-observer variations in contour delineation. For reference, the average value of the absolute difference between original and repeat contour volumes was 14.9 cc, 15.4 cc and 10.7 cc, for bladder, prostate and rectum, respectively. Average volumes were 147.3 cc (bladder), 48.7 cc (prostate) and 100.0 cc (rectum).

5.4 Discussion

The image guidance protocol mandated at our clinic for the treatment of high risk prostate patients on the Hi*Art II system including those analyzed in this study, is as follows. After initial automatic registration of bony anatomy in daily

MVCT and planning CT images, the alignment is manually adjusted by a radiation therapist with the goal of overlapping the prostate gland in the two images using the prostate/rectum interface at the mid-plane of the prostate as a reference. Recently, Langen *et al.*³⁰ investigated the accuracy of a manual method similar to ours and found that over 224 manual registrations performed by two radiation therapists, prostate misalignment exceeded 3 mm 24%, 33%, and 3% of the time in the AP, SI, and LR directions, respectively. Misalignment never exceeded 5 mm in any single direction. Although our work compares image matching strategies specifically, the observed alignment differences between prostate and bone matching are representative of the range of possible prostate misalignments during treatment. As such, the prostate $\Delta D95$ values observed in this study suggest that for the margins used clinically and the errors associated with the manual patient positioning method employed at our centre, delivered prostate D95 values are unaffected by observed prostate positioning errors. This suggests that daily image guidance based on prostate matching of treatment and planning CT images allows for a reduction of the 10 mm margins used for the patients included in this study. Recent work by Meijer *et al.*³¹ demonstrated that a prostate margin of 6 mm is clinically acceptable when daily image guidance is based on the alignment of implanted fiducials. Without fiducials, as is the case for the Hi*Art II patients at our centre, daily prostate positioning errors will increase³⁰ meaning a 6 mm border is insufficient. Further investigation is required to determine where within the 6 to 10 mm range the acceptable margin for prostate matching without fiducials is situated.

In relation to the two critical structures, the observed ranges of bladder $\Delta D45$ and rectum $\Delta D30$ values in combination with the fact that reported mean bladder $D45$ and rectum $D30$ values exceed inverse planning constraints, suggests that the selection of matching procedure has repercussions on the dosimetry of the critical structures during each individual fraction. However, over the entire ninety-nine fraction cohort analyzed in this study, positive and negative bladder $\Delta D45$ and rectum $\Delta D30$ values offset each other, giving rise to mean values of 2.6% and -2.2% of the prescription dose, respectively. How this fractionated trend translates when comparing matching methods based on the cumulative critical structure dosimetry over entire treatments remains unanswered. Investigating this requires accurate deformable registration to track daily anatomical variations^{32,33} and will be the focus of later chapters. However, regardless of whether or not fractionated dose differences between matching methods cancel out over prolonged treatment regimens, the fractionated analysis reported in this paper is beneficial for a number of reasons. First, the easiest way to ensure treatment protocols are satisfied over protracted treatment regimens is to ensure those same protocols are satisfied for each fraction. Furthermore, the radiobiological effect of varying daily doses differs from that associated with static daily dosimetry, regardless of whether the cumulative dosimetry is equivalent. Finally, results demonstrate that systematic trends in daily prostate motion for individual patients can lead to large discrepancies in dosimetry for prostate and bone matching. Patient 1, for example, had consistently and often significantly less bladder volume in daily treatment images as compared to

planning CT images, which contributed to a mean prostate shift of 4.1 mm superiorly over all twenty-five fractions.²⁸ This systematic prostate motion resulted in a mean bladder $\Delta D45$ of 0.20 Gy, which represents 10.0% of the inverse planning D45 constraint, suggesting that the selection of daily matching strategies can potentially have a significant effect on cumulative critical structure dosimetry as well. Whether or not these fractionated, or cumulative dose differences for that matter, have clinical repercussions requires correlation of doses and observed toxicities for large patient cohorts. This analysis is beyond the scope of this thesis; however, its discussion will be revisited in chapters 7 and 8.

Although the primary objective of this study was the comparison of dosimetry for prostate matching and bone matching registration methods, another issue requires addressing. Critical structure inverse planning constraints were often exceeded, rectum D30 in particular, regardless of the matching technique. On the surface, this may seem like a major problem, however, the discrepancies can be rationalized. First, it is a common discipline-wide practice to push inverse planning algorithms by using stringent constraints that cannot be realistically satisfied.³⁴ The radiation oncologist must then determine if the generated plan is acceptable in terms of target coverage and critical structure sparing. In fact, the mean planned rectum D30 for the four patients analyzed was 51.90 Gy or 2.08 Gy per fraction, which is larger than the 1.80 Gy per fraction inverse planning constraint. Constraint values were listed as opposed to planned values simply because they were equivalent for all four patients. Also, it must be emphasized

that planning constraints were not solely listed for comparison with bone and prostate matching dosimetry, but also to stress the relevance of the bone and prostate matching comparison. If the bone and prostate matching doses were significantly lower than the constraints, which were certainly not the case, an argument could be made that the observed bone and prostate matching dosimetric differences are irrelevant.

The second inherent problem with drawing conclusions in regards to the dosimetric differences between the two matching methods and the planning constraints is due to inter-observer variability. Planning dose volume histograms were constructed using contours delineated on the planning CT by a dosimetrist and approved by a radiation oncologist as part of the treatment planning process. On the other hand, daily MVCT contours were retrospectively drawn by a different oncologist, completely independent of the treatment planning procedure. Rasch *et al.*³⁵ demonstrated that without strict contouring guidelines, dosimetric variations due to inter-observer differences in structure delineation can be significant. Even when a standard guideline for the extent of the contoured rectum is established, differences in the mean rectum dose upwards of 10% of the prescription dose, due solely to variations in inter-observer rectum delineation, have been observed.³⁶ As an exercise, the radiation oncologist that contoured daily MVCT images was asked to contour the rectum on the four planning CT images. New dose volume histograms were constructed and the mean planned rectum D30 when using these new contour sets was 2.20 Gy per fraction.

Finally, planned doses and the doses for the two matching methods during each fraction were evaluated within completely different frames of reference. For example, the volume of the MVCT contoured rectum of patient 1 varied from 32 cc to 118 cc over the twenty-five fraction treatment due to the daily variations in bowel content. With all other factors considered equal, it suffices to say that a 32 cc rectum DVH will be considerably different than that for a 118 cc rectum. Variations in rectal volume had a demonstrable effect on dose volume histograms in work published by Mohan *et al.*³⁷ as well. They evaluated treatment dose volume histograms using contours delineated on CT images acquired immediately prior to nine daily treatments of a single prostate patient. Average rectal values for V70 (i.e. percentage of volume that receives 70 Gy), V60, V50, V40 and V30, as well as the corresponding treatment planning values were reported. A simple cubic spline interpolation of their data reveals that over the nine fractions analyzed, the treatment mean rectum D30 exceeded the planned value by approximately 22% of the prescription dose. Worth mentioning is that we may be in the midst of a methodological shift in the way that clinicians evaluate rectal doses. It has been demonstrated that some rectal toxicity data is better correlated with rectal wall doses as opposed to doses to the entire rectal volume.³⁸ The contribution of daily variation in rectal filling to the observed variance in our dosimetric endpoint (i.e. rectum D30), may have been reduced by limiting analysis to simply the rectal wall. However, it was decided that this retrospective study should be consistent with the original treatment plan and full rectal volume analysis was completed.

5.5 Conclusions

We have used the Planned Adaptive software on the Hi*Art II system to compare the doses that would have been delivered to high risk prostate patients if daily patient re-positioning was based on bone matching versus prostate matching. DVH analysis demonstrates that the difference in prostate dose for each matching technique is insignificant, and allows for potential margin reduction. However, observed ranges in the differences between critical structure dosimetry for bone and prostate matching suggest that the selection of matching method employed during patient re-positioning may have clinical repercussions. In fact, the doses delivered to the bladder and rectum were found to be highly dependent not only on the image guidance strategy, but also the direction of daily prostate motion. In particular, for prostate motion anteriorly and superiorly, bone matching decreases bladder dose whereas prostate matching decreases rectal dose. Potentially, the matching method can be selected each day based on the observed prostate motion in order to minimize dose and possible subsequent complications to the bladder and rectum.

5.6 References

1. Langen KM, Jones DTL. Organ motion and its management. *Int J Radiat Oncol Biol Phys.* 2001;50:265-278.
2. Byrne TE. A review of prostate motion with considerations for the treatment of prostate cancer. *Medical Dosimetry.* 2005;30:155-161.

3. Nederveen, AJ, Dehnad H, van der Heide UA, van Moorseelaar RJA, Hofman P, Lagendijk JJW. Comparison of megavoltage position verification for prostate irradiation based on bony anatomy and implanted fiducials. *Radiother Oncol.* 2003;68:81-88.
4. Willoughby TR, Kupelian PA, Pouliot J, Shinohara K, Aubin M, Roach M, Skrumeda LL, Balter JM, Litzenberg DW, Hadley SW, Wei JT, Sandler HM. Target localization and real-time tracking using the Calypso 4D localization system in patients with localized prostate cancer. *Int J Radiat Oncol Biol Phys.* 2006;65:528-534.
5. Chen J, Lee RJ, Handrahan D, Sause WT. Intensity-modulated radiotherapy using implanted fiducial markers with daily portal imaging: assessment of prostate organ motion. *Int J Radiat Oncol Biol Phys.* 2007;68:912-919.
6. Cheng CW, Wong J, Grimm L, Chow M, Uematsu M, Fung A. Commissioning and clinical implementation of a sliding gantry CT scanner installed in an existing treatment room and early clinical experience for precise tumor localization. *Am J Clin Oncol.* 2003;26:e28-e36.
7. Wong JR, Grimm L, Uematsu M, Oren R, Cheng CW, Merrick S, Schiff P. Image-guided radiotherapy for prostate cancer by CT-linear accelerator combination: prostate movements and dosimetric considerations. *Int J Radiat Oncol Biol Phys.* 2005;61:561-569.
8. Sorcini B, Tilikidis A. Clinical application of image-guided radiotherapy, IGRT (on the Varian OBI platform). *Cancer Radiother.* 2006;10:252-257.

9. Kupelian PA, Lee C, Langen KM, Zeidan OA, Manon RR, Willoughby TR, Meeks SL. Evaluation of image-guidance strategies in the treatment of localized prostate cancer. *Int J Radiat Oncol Biol Phys.* 2008;70:1151-1157.
10. Langen KM, Meeks SL, Poole DO, Wagner TH, Willoughby TR, Kupelian PA, Ruchala KJ, Haimerl J, Olivera GH. The use of megavoltage CT (MVCT) images for dose recomputations. *Phys Med Biol.* 2005;50:4259-4276.
11. Cionini L, Bucciolini M. Role of portal imaging in clinical radiotherapy: Florence experience. *Radiother Oncol.* 1993;29:230-236.
12. Gilhuijs KG, el-Gayed AA, van Herk M, Vijlbrief RE. An algorithm for automatic analysis of portal images: clinical evaluation for prostate treatments. *Radiother Oncol.* 1993;29:261-268.
13. Althof VG, Hoekstra CJ, te Loo HJ. Variation in prostate position relative to adjacent bony anatomy. *Int J Radiat Oncol Biol Phys.* 1996;34:709-715.
14. Bieri S, Miralbell R, Nouet P, Delorme H, Rouzaud M. Reproducibility of conformal radiation therapy in localized carcinoma of the prostate without rigid immobilization. *Radiother Oncol.* 1996;38:223-230.
15. Mubata CD, Bidmead AM, Ellingham LM, Thompson V, Dearnaley DP. Portal imaging protocol for radical dose-escalated radiotherapy treatment of prostate cancer. *Int J Radiat Oncol Biol Phys.* 1998;40:221-231.
16. Greer PB, Mortensen TM, Jose CC. Comparison of two methods for anterior-posterior isocenter localization in pelvic radiotherapy using electronic portal imaging. *Int J Radiat Oncol Biol Phys.* 1998;41:1193-1199.

17. Fiorino C, Di Muzio N, Broggi S, Cozzarini C, Maggiulli E, Alongi F, Valdagni R, Fazio F, Calandrino R. Evidence of limited motion of the prostate by carefully emptying the rectum as assessed by daily MVCT image guidance with helical tomotherapy. *Int J Radiat Oncol Biol Phys.* 2008;71:611-617.
18. Court LE, Dong L. Automatic registration of the prostate for computed-tomography-guided radiotherapy. *Med Phys.* 2003;30:2750-2757.
19. Smitsmans MHP, Wolthaus JWH, Artignan X, de Bois J, Jaffray DA, Lebesque JV, van Herk M. Automatic localization of the prostate for on-line or off-line image-guided radiotherapy. *Int J Radiat Oncol Biol Phys.* 2004;60:623-635.
20. Smitsmans MHP, de Bois J, Sonke JJ, Betgen A, Zijp LJ, Jaffray DA, JV Lebesque, van Herk M. Automatic prostate localization on cone-beam CT scans for high precision image-guided radiotherapy. *Int J Radiat Oncol Biol Phys.* 2005;63:975-984.
21. Lau YH, Braun M, Hutton BF. Non-rigid image registration using a median-filtered coarse-to-fine displacement field and a symmetric correlation ratio. *Phys Med Biol.* 2001;46:1297-1319.
22. Mattes D, Haynor DR, Vesselle H, Lewellen TK, Eubank W, PET-CT image registration in the chest using free-form deformations. *IEEE Trans Med Imag.* 2003;22:120-128.
23. Nelder JA, Mead R. A simplex method for function minimization. *Computer Journal.* 1965;7:308-313.

24. Kupelian PA, Langen KM, Zeidan OA, Meeks SL, Willoughby TR, Wagner TH, Jeswani S, Ruchala KJ, Haimerl J, Olivera GH. Daily variations in delivered doses in patients treated with radiotherapy for localized prostate cancer. *Int J Radiat Oncol Biol Phys.* 2006;66:876-882.
25. Han C, Chen YJ, Liu A, Schultheiss TE, Wong JY. Actual dose variation of parotid glands and spinal cord for nasopharyngeal cancer patients during radiotherapy. *Int J Radiat Oncol Biol Phys.* 2008;70:1256-1262.
26. Grabec D, Kragelj B. The sigmoid colon and bladder shielding in whole pelvic irradiation of prostate cancer (forward planned IMRT from Institute of Oncology Ljubljana). *Radiol Oncol.* 2009;43:56-64.
27. Roeske JC, Forman JD, Mesina CF, He T, Pelizzari CA, Fontenla E, Vijayakumar S, Chen GTY. Evaluation of changes in the size and location of the prostate, seminal vesicles, bladder, and rectum during a course of external beam radiation therapy. *Int J Radiat Oncol Biol Phys.* 1995;33:1321-1329.
28. Melian E, Mageras GS, Fuks Z, Leibel SA, Niehaus A, Lorant H, Zelefsky M, Baldwin B, Kutcher GJ. Variation in prostate position quantitation and implications for three-dimensional conformal treatment planning. *Int J Radiat Oncol Biol Phys.* 1997;38:73-81.
29. van Herk M, Bruce A, Kroes APG, Shouman T, Touw A, Lebesque JV. Quantification of organ motion during conformal radiotherapy of the prostate by three dimensional image registration. *Int J Radiat Oncol Biol Phys.* 1995;33:1311-1320.

30. Langen KM, Zhang Y, Andrews RD, Hurley ME, Meeks SL, Poole DO, Willoughby TR, Kupelian PA. Initial experience with megavoltage (MV) CT guidance for daily prostate alignments. *Int J Radiat Oncol Biol Phys.* 2005;62:1517-1524.
31. Meijer GJ, de Klerk J, Bzdusek K, van den Berg HA, Janssen R, Kaus MR, Rodrigus P, van der Toorn PP. What CTV-to-PTV margins should be applied for prostate irradiation? Four-dimensional quantitative assessment using model-based deformable image registration techniques. *Int J Radiat Oncol Biol Phys.* 2008;72:1416-1425.
32. Schaly B, Kempe JA, Bauman GS, Battista JJ, Van Dyk J. Tracking the dose distribution in radiation therapy by accounting for variable anatomy. *Phys Med Biol.* 2004;49:791-805.
33. Lu W, Olivera GH, Chen Q, Ruchala KJ, Haimerl J, Meeks SL, Langen KM, Kupelian PA. Deformable registration of the planning image (kVCT) and the daily images (MVCT) for adaptive radiation therapy. *Phys Med Biol.* 2006;51:4357-4374.
34. Hristov DH, Moftah BA, Charrois C, Parker W, Souhami L, Podgorsak EB. On the selection of optimization parameters for an inverse treatment planning replacement of a forward planning technique for prostate cancer. *J Appl Clin Med Phys.* 2002;3:200-211.
35. Rasch C, Barillot I, Remeijer P, Touw A, van Herk M, Lebesque JV. Definition of the prostate in CT and MRI: a multi-observer study. *Int J Radiat Oncol Biol Phys.* 1999;43:57-66.

36. Fiorino C, Vavassori V, Sanguineti G, Bianchi C, Cattaneo GM, Piazzolla A, Cozzarini C. Rectum contouring variability in patients treated for prostate cancer: impact on rectum dose-volume histograms and normal tissue complication probability. *Radiother Oncol.* 2002;63:249-255.
37. Mohan R, Zhang X, Wang H, Kang Y, Wang X, Liu H, Ang K, Kuban D, Dong L. Use of deformed intensity distributions for on-line modification of image-guided IMRT to account for interfractional anatomic changes. *Int J Radiat Oncol Biol Phys.* 2005;61:1258-1266.
38. Tucker SL, Dong L, Cheung R, Johnson J, Mohan R, Huang EH, Liu HH, Thames HD, Kuban D. Comparison of rectal dose-wall histogram versus dose-volume histogram for modeling the incidence of late rectal bleeding after radiotherapy. *Int J Radiat Oncol Biol Phys.* 2004;60:1589-1601.

Chapter 6: Incorporation of planning contour data into a voxel based deformable registration algorithm for prostate adaptive radiation therapy

A version of this chapter has been submitted for publication:

Rivest DRC, Riauka TA, Murtha AD, Fallone BG. Incorporation of planning contour data into a voxel based deformable registration algorithm for prostate adaptive radiation therapy. J Appl Clin Med Phys. Submitted.

6.1 Introduction

Extensive research in the field of radiotherapy over the past decade has led to its progression from so-called conventional treatments, to three-dimensional conformal radiotherapy (3DCRT), and finally to where it is today, adaptive radiotherapy (ART).¹ Although not yet fully developed and implemented, ART is based on the underlying principle that since a patient's anatomy is not static over the course of treatment, the treatment plan should not be either. Anatomical variations occurring between planning and treatment delivery, whether from set-up irregularities, physiological changes, or other clinical factors, can cause the delivered dose distribution to differ significantly from what was planned.² This could lead to underdosing of the clinical target volume (CTV) or

the delivery of therapeutic doses to organs at risk (OAR), potentially having an adverse impact on the efficacy of treatment. An essential requirement of ART is the acquisition of anatomical images over the course of treatment for comparison with the original planning CT. A number of commercially available systems allow for three-dimensional (3D) patient imaging in the treatment position on a daily basis. Examples include the cone-beam CT (CBCT) capable on-board imagers (OBI) developed by Varian (Varian Medical Systems, Palo Alto, CA)³ and Elekta (Elekta AB, Stockholm, Sweden),⁴ the Siemens Primatom CT-on-rails (Siemens Medical Systems, Concord, CA)⁵ and the Hi*Art II helical tomotherapy (TomoTherapy, Inc., Madison, WI)⁶ systems. In addition to anatomical data, on-line CT imaging provides the electron density information required for the calculation of delivered fractionated dose distributions⁷ and the potential for tracking of the accumulated dose for each volume element (voxel) in the treatment planning CT. However, anatomical variations mandate that the position of each voxel in each treatment CT be mapped to its corresponding position in the planning CT, and that mapping must then be applied to the delivered dose distribution in order to accurately compare planned and delivered doses. Accurate deformable registration establishes anatomical correspondences and the required mappings between treatment and planning images.

A number of approaches have been applied to the undertaking of deformable registration, in particular the registration of pelvic CT images. Most techniques can be classified as either feature based or voxel based. Feature based algorithms minimize the distance between corresponding surfaces or points that

have been manually or automatically delineated. A commonly cited example is the work of Schaly *et al.*⁸ in which the thin-plate spline transform (TPS)⁹ was used to deform contours drawn on multiple CT images in order to calculate the cumulative dose delivered over multiple treatment fractions. More recently, deformable registration using biomechanical finite element modeling (FEM)¹⁰ has been used to account for prostate deformation resulting from an endorectal imaging probe in CT image pairs.¹¹ Such feature based algorithms are advantageous in that they focus on individual anatomical structures of clinical importance. This idea suits the ART framework as treatment plans, and presumably adaptive plans, are evaluated based on doses delivered to regions of interest (ROI). However, they typically require time consuming human intervention and any errors introduced during contour delineation are carried over to the registration process.

On the other hand, voxel-based deformable registration algorithms tend to be automatic and are only dependent on the intensities of individual voxels in the registered images. A common approach is to base registration on models in which transformations are obtained by solving a set of partial differential equations (PDE) that minimize some energy function. The energy function must include a measure of similarity between images and often includes a regularization term to ensure the smoothness of the transformation. Foskey *et al.*¹² assumed a viscous fluid model¹³ when constructing their PDE in the registration of prostate images acquired on a CT-on-rails system and planning images. A modified version of the demons algorithm¹⁴ was proposed by Wang *et*

*al.*¹⁵ to register a pair of sequential CT images from a prostate cancer patient. The demons algorithm is based on the optical flow equation and regularization is achieved by smoothing the deformation field with a Gaussian filter following each iteration. A diffusion type PDE was used by Lu *et al.*¹⁶ to register on-line and planning CT images and later to register megavoltage CT (MVCT) images to planning images.¹⁷ A similar algorithm was used by Gao *et al.*¹⁸ to register prostate planning CT images to images from a commercial CT-LINAC system. Another class of automatic voxel based algorithms is those based on block matching.¹⁹ A vector field is generated by performing individual rigid registrations over a large number of small regularly or irregularly spaced image regions. After planning CT segmentation, Malsch *et al.*²⁰ automatically selected landmarks at borders between different tissue types to act as the image region centers for each rigid registration. Relocation vectors were input into a TPS model to deform planning images to treatment images.

An important consideration when using voxel based deformable registration is the underlying principle that these algorithms assume correspondence between image pairs. Unfortunately, in some instances, anatomical differences between imaging studies cause this assumption to break down and the lack of one-to-one correspondence needs to be considered during registration. This is of particular concern when registering pelvic images that contain differing concentrations of intestinal gas. If the treatment CT contains a region of bowel gas and there is no gas present in the same region in the planning CT, without addressing the issue, voxel based deformable registration will fail.

A number of methods have been developed recently to overcome this problem. Foskey's¹² solution to ensure correspondence was to completely eliminate all gas pockets. Gassy regions were segmented via thresholding and then shrunk to a point using a method they referred to as *deflation*. This *deflation* procedure was applied to both treatment and planning images that contained gas pockets and was carried out prior to deformable registration. Malsch *et al.*²⁰ detected gas cavities in planning images by Gaussian filtering followed by thresholding and then automatically selected pairs of landmarks at the border and centre of the cavities to be incorporated into their thin plate spline deformable model. Yang *et al.*²¹ automatically scanned images for intestinal gas voxels and set their intensities to a predetermined average value for solid bowel contents. Gao *et al.*¹⁸ incorporated planning contour information into their procedure in which tiny gas pockets were inserted into planning images prior to registration with treatment images.

Voxel based methods are advantageous in that they do not require any feature extraction, however, they tend to be computationally expensive and the transformations they produce are defined over larger regions instead of defined regions of clinical interest. Often, the contribution to the cost function of the voxels outside the clinically important ROI exceeds that of those inside. This is problematic in that the accuracy of the deformation field at an ROI may be compromised in order to produce a transformation that optimizes the cost function over the entire image. This problem may be reduced by applying a mask encompassing a limited anatomical region such as the pelvis and only registering within the cropped section,²² however unnecessary contributions to the cost

function will still be present. This is not an issue in the feature based algorithms described above in that only the ROI contribute to the cost function. Taking concepts from both classes of deformable registration algorithms, we propose an automatic voxel based deformable registration algorithm that incorporates known ROI information. Using only planning contour data, we register treatment and planning images by performing separate voxel based deformable registrations in the local neighbourhood of each individual planning ROI. Treatment image contours do not require delineation. To achieve this, we look to another class of voxel based deformable registration algorithms based on free form B-splines.²³ In their first reported medical application, Rueckert *et al.*²⁴ used cubic B-splines to model the local motion of the breast by maximizing the normalized mutual information²⁵ between serial contrast-enhanced MRI images. Since then, a number of implementations of the algorithm have been proposed for various applications.^{22,26-28}

The objective of this work is to develop an automatic algorithm for the B-spline parameterized deformable registration of on-line treatment CT images to planning CT images with the intention of applying the output transformation to delivered dose distributions in order to correct for anatomical variations when comparing planned and delivered doses.

6.2 Methods and Materials

Using similar notation as in chapter 2, let us assume we have a full three-dimensional (3D) treatment image $I(\mathbf{x}_i)$, acquired during fraction i , which we

want to register to a planning image $I(\mathbf{x}_0)$. For our purposes, the goal of image registration is to find the function \mathbf{T}_i that transforms each individual voxel in image $I(\mathbf{x}_i)$ to its corresponding position in image $I(\mathbf{x}_0)$

$$\mathbf{x}_0 = \mathbf{T}_i(\mathbf{x}_i). \quad 6.1$$

For this, we assume a collection of \mathbf{T}_i^{ROI} , each of which are only defined over each individual ROI (prostate, bladder, rectum, left femur and right femur) and are themselves a linear combination of rigid and deformable components

$$\mathbf{T}_i^{ROI}(\mathbf{x}_i) = \mathbf{T}_i^{ROI-rigid}(\mathbf{x}_i) + \mathbf{T}_i^{ROI-deform}(\mathbf{x}_i). \quad 6.2$$

In general, the treatment image $I(\mathbf{x}_i)$ may be acquired on any system capable of on-line CT imaging. For the purpose of this study however, our focus will be MVCT images acquired on a clinical Hi*Art II system (TomoTherapy Inc., Madison, WI) which have inherently reduced contrast and increased noise compared to other on-line CT modalities. This decision is partially based on availability as well as the system's built-in Planned Adaptive software which readily allows for the calculation of daily treatment dose distributions.^{2,29} Furthermore, if suitability is determined for MVCT images, our methods would presumably be useful for other on-line CT modalities that generate images of greater quality.

6.2.1 Rigid Transformation

The rigid component of each \mathbf{T}_i^{ROI} in our registration framework is the 3D Euler transform that aligns the pelvic bony anatomy in the planning and treatment images

$$\mathbf{T}_i^{ROI-rigid}(\mathbf{x}_i) = \mathbf{T}_i^{Bone}(\mathbf{x}_i). \quad 6.3$$

In an initial pre-processing procedure, bony voxels in the planning image $I(\mathbf{x}_0)$ are automatically segmented via thresholding creating an irregular domain Ω_0^{Bone} . Using only the voxels within Ω_0^{Bone} , we minimize the mean square intensity differences (MSD) between voxels in the planning and treatment images due to its large capture range.³⁰

6.2.2 Deformable Transformation

B-spline parameterization of image deformation requires the creation of a 3D rectangular mask over each ROI in the planning CT. Given a 3D contour C_0^{ROI} made up of a collection of points (x_0, y_0, z_0) that define a planning CT ROI, and a uniform user-defined margin or border b_0^{ROI} , we define $x_{\min} = \min(x_0) - b_0^{ROI}$, $x_{\max} = \max(x_0) + b_0^{ROI}$, $y_{\min} = \min(y_0) - b_0^{ROI}$, $y_{\max} = \max(y_0) + b_0^{ROI}$, $z_{\min} = \min(z_0) - b_0^{ROI}$ and $z_{\max} = \max(z_i) + b_0^{ROI}$. In our notation, x , y and z refer to the lateral left/right (LR), anterior/posterior (AP), and superior/inferior (SI) image directions, respectively. Let $\Omega_0^{ROI-deform}$ define a 3D rectangular domain in the planning CT encompassing the region

$x_{\min} \leq x \leq x_{\max}$, $y_{\min} \leq y \leq y_{\max}$ and $z_{\min} \leq z \leq z_{\max}$. Φ denotes an underlying $n_x \times n_y \times n_z$ mesh of control points $\phi_{i,j,k}$ with uniform spacing δ_x , δ_y , δ_z . The displacement field defined by the B-spline can be expressed by

$$\mathbf{T}_i^{ROI-deform}(x, y, z) = \sum_{l=0}^3 \sum_{m=0}^3 \sum_{n=0}^3 B_l(u) B_m(v) B_n(w) \phi_{i+l, j+m, k+n} \quad 6.6$$

where $i = \lfloor (x - x_{\min}) / \delta_x \rfloor - 1$, $j = \lfloor (y - y_{\min}) / \delta_y \rfloor - 1$, $k = \lfloor (z - z_{\min}) / \delta_z \rfloor - 1$,
 $u = (x - x_{\min}) / \delta_x - \lfloor (x - x_{\min}) / \delta_x \rfloor$, $v = (y - y_{\min}) / \delta_y - \lfloor (y - y_{\min}) / \delta_y \rfloor$,
 $w = (z - z_{\min}) / \delta_z - \lfloor (z - z_{\min}) / \delta_z \rfloor$ and where B_l represents the l th basis function of the B-spline

$$B_0(u) = (1 - u)^2 / 6$$

$$B_1(u) = (3u^3 - 6u^2 + 4) / 6$$

$$B_2(u) = (-3u^3 + 3u^2 + 3u + 1) / 6$$

$$B_3(u) = u^3 / 6.$$

The notation here is slightly different than that presented in chapter 2 in order to account for the separate B-spline meshes for each ROI. Based on the cost function's success in performing rigid ROI-based registration in the previous two chapters, $\mathbf{T}_i^{ROI-deform}$ is determined by finding the positions of the control points $\phi_{i,j,k}$ that optimize the well known correlation coefficient metric. For cost function evaluation, we define a region Ω_0^{ROI} that contains all voxels within the ROI including those voxels outside of the ROI that are within a distance b_0^{ROI} of its borders and only the image voxels within Ω_0^{ROI} and their overlapping voxels in

\mathbf{x}_i are used in cost function calculation. Note that Ω_0^{ROI} , which has the general shape of the ROI, is not equivalent to the rectangular $\Omega_0^{ROI-deform}$. In defining Ω_0^{ROI} for cost function evaluation instead of simply using $\Omega_0^{ROI-deform}$, we eliminate the possibility that voxels far away from the ROI will contribute to the registration cost function. Optimization is achieved using a version of the limited memory BFGS quasi-Newton optimizer proposed by Byrd *et al.*³¹

6.2.3 Prostate Motion

It has been observed repeatedly that the position of the prostate gland with respect to rigid bony anatomy can vary as a result of variations in bladder and rectal filling.^{32,33} This motion is not described by \mathbf{T}_i^{Bone} and depending on its magnitude may complicate deformable registration, resulting in an inaccurate $\mathbf{T}_i^{Prostate-deform}$. In order to account for this motion, we define a translational transformation $\mathbf{T}_i^{Prostate-trans}$ component of $\mathbf{T}_i^{Prostate}$ that accounts for the daily prostate motion in the SI, AP and LR directions. $\mathbf{T}_i^{Prostate-trans}$ is found for each treatment/planning image pair by maximizing the correlation coefficient metric using only the voxels in $\Omega_0^{Prostate}$ which consists of a border $b_0^{Prostate} = 6.0$ mm. This is the same method used in the previous two chapters.

6.2.4 Image Correspondence

To overcome the problems associated with lack of correspondence due to intestinal gas variations in planning and treatment images, we combine the

approaches of Gao *et al.*¹⁸ and Yang *et al.*²¹ The protocol for prostate treatment in our clinic is for patients to empty their rectums prior to the planning procedure and presumably before each subsequent treatment fraction. Solid or gaseous contents present in the rectum during planning may significantly compromise anatomic reproducibility during each treatment, so special care is made to ensure each patient's rectum is empty during planning CT acquisition. Although mandated, patient throughput requirements limit the ability of therapists to ensure a completely empty rectum before each daily treatment fraction. In terms of correspondence, or lack thereof, our primary concern stems from gas pockets in the treatment CT that are not present in the planning CT. When this occurs, we use the method published by Gao *et al.*¹⁸ in which correspondence is ensured by modifying the intensity of voxels in the planning rectum to mimic the insertion of small gas pockets. The approach is based on the number of gaseous voxels in the treatment and planning images on a slice by slice basis after initial bony alignment and after the treatment image has been resampled to the same resolution as the planning image. First, the number of gas voxels N_0 in each slice in the rectum planning contour C_0^{Rectum} is determined via thresholding. Using the same method, each corresponding slice in the rectangular region $\Omega_0^{\text{Rectum-deform}}$ in the treatment CT is searched to determine the number of gas voxels N_i in each treatment slice. For each slice, if N_i exceeds a user-defined threshold N_t and N_0 is less than that same threshold, that slice on the planning CT is selected for modification and a gaseous pocket is inserted, thus providing a cavity for inflated treatment rectums to deform to. The centre of the pocket is

approximately situated at the centre of the contour and the intensities of the voxels within the pocket are modified as described by Gao *et al.*¹⁸ to ensure a smooth transition between the centre of the gas pocket and the rectal wall. In the rare cases where N_0 exceeds N_t , but N_i is less than the threshold N_t , the planning CT gas pocket is filled by modifying the intensities of the gaseous voxels similar to the method proposed by Yang *et al.*²¹ Intensities are randomly selected from a Gaussian distribution defined by the automatically evaluated mean and standard deviation of the intensities of the solid rectal voxels within the entire planning CT. As was the approach when the intensity modification procedure was developed by Gao *et al.*,¹⁸ small gas pockets were assumed to have limited effect on the registration. As such, if N_0 and N_i were both less than N_t , no modification was performed. Analogously, if both values were greater than N_t , once again, no modification was performed.

In order to further simplify the model and improve the accuracy of rectum deformations, we take advantage of a finding published by Yan *et al.*³⁴ who demonstrated using biomechanical modeling that daily displacement of a patient's rectal wall is typically confined to within 1 mm in the SI direction. As such, we used a two-staged approach to rectum deformable registration. First, registration of each rectal slice was performed using our deformable model, but simplified from 3D to 2D. The 2D B-spline parameters were subsequently used to define the initial parameters of the full 3D deformable registration over $\Omega_0^{\text{Rectum-deform}}$, which although it converged after minimal iterations, was still required to model any SI motion and to ensure a smooth transformation from slice to slice. As a result, the

number of B-spline grid nodes in the SI direction, n_z , was equivalent to the number of slices in $\Omega_0^{\text{Rectum-deform}}$ for rectum registrations.

6.2.5 Registration Framework

The step by step procedure performed by the registration algorithm is as follows.

- (i) MSD based bony alignment of the treatment and planning images to acquire $\mathbf{T}_i^{\text{ROI-rigid}} = \mathbf{T}_i^{\text{Bone}}$.
- (ii) Determination of $\mathbf{T}_i^{\text{Prostate-trans}}$ to account for daily prostate motion.
- (iii) Rectum intensity modification.
- (iv) For each deformable ROI (prostate, bladder, and rectum), determine $\mathbf{T}_i^{\text{ROI-deform}}$ using our model.

The net result will be separate functions for each individual ROI,

$$\mathbf{T}_i^{\text{Prostate}} = \mathbf{T}_i^{\text{Bone}} + \mathbf{T}_i^{\text{Prostate-trans}} + \mathbf{T}_i^{\text{Prostate-deform}}$$

$$\mathbf{T}_i^{\text{Bladder}} = \mathbf{T}_i^{\text{Bone}} + \mathbf{T}_i^{\text{Bladder-deform}}$$

$$\mathbf{T}_i^{\text{Rectum}} = \mathbf{T}_i^{\text{Bone}} + \mathbf{T}_i^{\text{Rectum-deform}} \tag{6.7}$$

$$\mathbf{T}_i^{\text{LeftFemur}} = \mathbf{T}_i^{\text{Bone}}$$

$$\mathbf{T}_i^{\text{RightFemur}} = \mathbf{T}_i^{\text{Bone}}$$

each of which will only be defined in the local neighbourhood of each Ω_0^{ROI} . As evident by the equations for $\mathbf{T}_i^{\text{LeftFemur}}$ and $\mathbf{T}_i^{\text{RightFemur}}$, our model assumes that bony anatomy does not deform. It should be noted that additional ROI may be incorporated into the model and although yet to be investigated, adaptation of the

algorithm for other clinical sites is possible. Once each \mathbf{T}_i^{ROI} has been established there are two potential tactics in going forward. The first option is to create a \mathbf{T}_i defined over the entire image via interpolation of each individual \mathbf{T}_i^{ROI} . The second option is to maintain the separation of each individual \mathbf{T}_i^{ROI} , which is often the case in feature based algorithms. The objective of this work is to develop a deformable registration algorithm that establishes correspondence between treatment and planning CT images for the purpose of comparing planned and delivered doses. As previously mentioned, radiotherapy treatment plans are evaluated based on doses delivered to ROI and any adaptive radiotherapy protocol will surely follow the same framework. By deforming dose distributions using each individual \mathbf{T}_i^{ROI} , the possibility of incorporating interpolation artifacts introduced by generating \mathbf{T}_i is eliminated and more importantly, focus remains on the individual ROI. Admittedly, a practical downside of this approach is that as a result of an erroneous \mathbf{T}_i^{ROI} , an individual treatment CT voxel corresponding to one specific ROI may be incorrectly mapped to multiple planning CT ROI. Any such occurrences, however, would negatively affect validation metrics accordingly. It should also be mentioned that if the algorithm was used for other purposes requiring a complete deformed image such as diagnosis or follow-up studies, generation of a function \mathbf{T}_i would be mandatory.

6.2.6 Validation

The performance of the algorithm was quantified using forty-nine pre-treatment MVCT and planning CT pairs. The prostate, bladder, and rectum were contoured on each image by a single radiation oncologist. It should be emphasized that contours were delineated on treatment images solely for validation purposes as they are not required as part of the registration process. Transformations obtained by registration \mathbf{T}_i^{ROI} were applied to each treatment contour C_i^{ROI} in order to generate $C_i^{ROI-deform}$

$$C_i^{ROI-deform} = \mathbf{T}_i^{ROI}(C_i^{ROI}). \quad 6.8$$

Each $C_i^{ROI-deform}$ was compared to its corresponding $C_0^{ROI'}$ using the Dice similarity coefficient (DSC)³⁵ utilized in chapter 3:

$$DSC(C_0^{ROI'}, C_i^{ROI-deform}) = \frac{2 \cdot \text{Volume}(C_0^{ROI'} \cap C_i^{ROI-deform})}{\text{Volume}(C_0^{ROI'}) + \text{Volume}(C_i^{ROI-deform})} \quad 6.9$$

Note that the prime in the planning term in equation 6.9 indicates that the contour was retrospectively delineated by the same radiation oncologist that contoured the treatment images and is not the same C_0^{ROI} delineated during radiation therapy planning that drives the deformable registration. This eliminates any inter-observer variations as well as ensuring there is no bias that may or may not be present if the same planning contour that was used to drive registration was also used for validation. Possible values of the DSC range from 1 for identical contours to 0 for no contour overlap. It is generally considered that a DSC value > 0.7 is indicative of good agreement between volumes.^{10,12,36}

In addition to the volumetric analysis provided by DSC, we also evaluated two surface based metrics. For each contour point in C_0^{ROI} , we define the surface distance³⁷ as the shortest absolute Euclidean distance to $C_i^{ROI-deform}$. Mean (\bar{d}) and maximum surface distances between C_0^{ROI} and $C_i^{ROI-deform}$ were determined after each registration.

Metrics were evaluated for bladder, rectum and prostate using different combinations of $n_x \times n_y \times n_z$ B-spline mesh resolutions and contour borders b_0^{ROI} . For consistency, mesh resolutions were selected in an attempt to confine the values of the B-spline grid spacings δ_x , δ_y and δ_z within the range of 15 – 25 mm, but in some instances slight deviations did occur depending on the contour border, the size of each patient’s organs and the anatomical extent of what was imaged. This range of values has been shown to represent a suitable trade-off between optimizing the level of refinement of the transformation, while minimizing the number of degrees of freedom.^{22,27} We also investigated the usefulness of applying a noise reducing median filter (MF) to MVCT images prior to registration. After the first sixteen registrations, results were analyzed and compared, upon which registration of the remaining thirty-three image pairs was carried out using the optimal mesh resolution, filtration and border settings. Finally, select image pairs were registered globally using a standard B-spline parameterized deformable registration algorithm to quantify the benefits of performing separate registrations for each ROI.

6.3 Results

6.3.1 Dependence on Registration Settings

Registrations of the initial sixteen image pairs were conducted for various combinations of mesh resolutions, contour borders and MVCT filtration. Mean DSC and \bar{d} values for bladder, prostate and rectum are given in tables 6-1, 6-2 and 6-3, respectively. Data suggests that for all three organs, a nonzero border b_{ROI} is required, otherwise registration is significantly compromised. However, for each ROI, there also appears to be no further gain and perhaps a slight reduction in registration accuracy when the border is increased from 10 to 20 mm. In addition, unlike in the prostate matching procedure investigated in chapter 4, applying a median filter to each MVCT image prior to registration appears to have negligible effects on the validation metrics. As mentioned in appendix A, the Nelder-Mead simplex optimizer is known for sometimes erroneously converging to local minima and in chapter 4, the occurrence of inaccurate registrations was reduced because median filtration served to smooth the cost function parameter space. Here, the cost function parameter space has significantly more degrees of freedom and a different optimization strategy is employed. As a result, median filtration does not significantly improve registration. Finally, in regards to the B-spline meshes employed, the different resolutions have little effect on bladder and rectum deformation. An argument could be made that with all other settings equal, improvements in prostate registration occur when selecting a 6 x 6 x 6 mesh as opposed to a 4 x 4 x 4 mesh.

Table 6-1. Mean bladder DSC and \bar{d} metrics for the first 16 image pairs.

$n_x \times n_y \times n_z$	b_0^{ROI} (mm)	MF	DSC	\bar{d} (mm)
6 x 6 x 6	0.0	No	0.73	3.3
6 x 6 x 6	10.0	No	0.89	1.5
6 x 6 x 6	20.0	No	0.88	1.8
8 x 8 x 8	0.0	No	0.72	2.9
8 x 8 x 8	10.0	No	0.88	1.5
8 x 8 x 8	20.0	No	0.89	1.6
6 x 6 x 6	10.0	Yes	0.88	1.6

Table 6-2. Mean prostate DSC and \bar{d} metrics for the first 16 image pairs.

$n_x \times n_y \times n_z$	b_0^{ROI} (mm)	MF	DSC	\bar{d} (mm)
4 x 4 x 4	0.0	No	0.60	4.0
4 x 4 x 4	10.0	No	0.77	2.1
4 x 4 x 4	20.0	No	0.74	2.3
6 x 6 x 6	0.0	No	0.66	3.0
6 x 6 x 6	10.0	No	0.78	2.0
6 x 6 x 6	20.0	No	0.77	1.9
6 x 6 x 6	10.0	Yes	0.78	1.9

Table 6-3. Mean rectum DSC and \bar{d} metrics for the first 16 image pairs.

$n_x \times n_y$	b_0^{ROI} (mm)	MF	DSC	\bar{d} (mm)
4 x 4	0.0	No	0.65	2.1
4 x 4	10.0	No	0.69	2.0
4 x 4	20.0	No	0.67	2.2
6 x 6	0.0	No	0.67	2.0
6 x 6	10.0	No	0.69	1.9
6 x 6	20.0	No	0.67	2.1
6 x 6	10.0	Yes	0.68	1.8

6.3.2 Cohort Analysis

Based on the results of the initial sixteen registrations, mesh resolutions in each dimension were set to 6, borders were set to 10 mm and no median filtration was employed for all subsequent ROI registrations. The remainder of the forty-nine image pairs were registered and analyzed. Measured bladder, prostate and rectum DSC values after deformable registration are plotted in histogram form in figure 6-1. All but one (98%) of the bladder DSC values is greater than 0.7 and all but five (90%) exceed a value of 0.8. Corresponding percentages for prostate DSC values are 100% and 57%. Rectum values are 71% and 35%, respectively. The combined statistics for the DSC analysis of all organs are given in table 6-4. Histograms of the mean surface distances \bar{d} are depicted in figure 6-2 and statistics are tabulated in table 6-5. Maximum surface distances were also evaluated for each ROI and the median values for the forty-nine bladder, prostate

and rectum registrations were 11.2 mm, 7.1 mm and 8.4 mm, respectively. Figure 6-3 provides an illustration of a typical bladder registration while sample prostate and rectum registrations are depicted in figures 6-4 and 6-5, respectively. For reference, examples of mediocre registrations are illustrated in figure 6.6. In addition, a collection of original and deformed images were imported into Reveal-MVS (Mirada Solutions Ltd., Oxford, UK) and based on visual inspection, registrations were qualitatively deemed to correlate well with the quantitative analysis.

Table 6-4. Statistics for the bladder, prostate and rectum DSC measures (n=49).

Dice Similarity Coefficient (DSC)			
	Bladder	Prostate	Rectum
Mean	0.87	0.80	0.75
Median	0.89	0.81	0.78

Table 6-5. Statistics for the bladder, prostate and rectum \bar{d} measures (n=49).

Mean Surface Distance (mm)			
	Bladder	Prostate	Rectum
Mean	1.6	1.7	1.8
Median	1.4	1.7	1.7

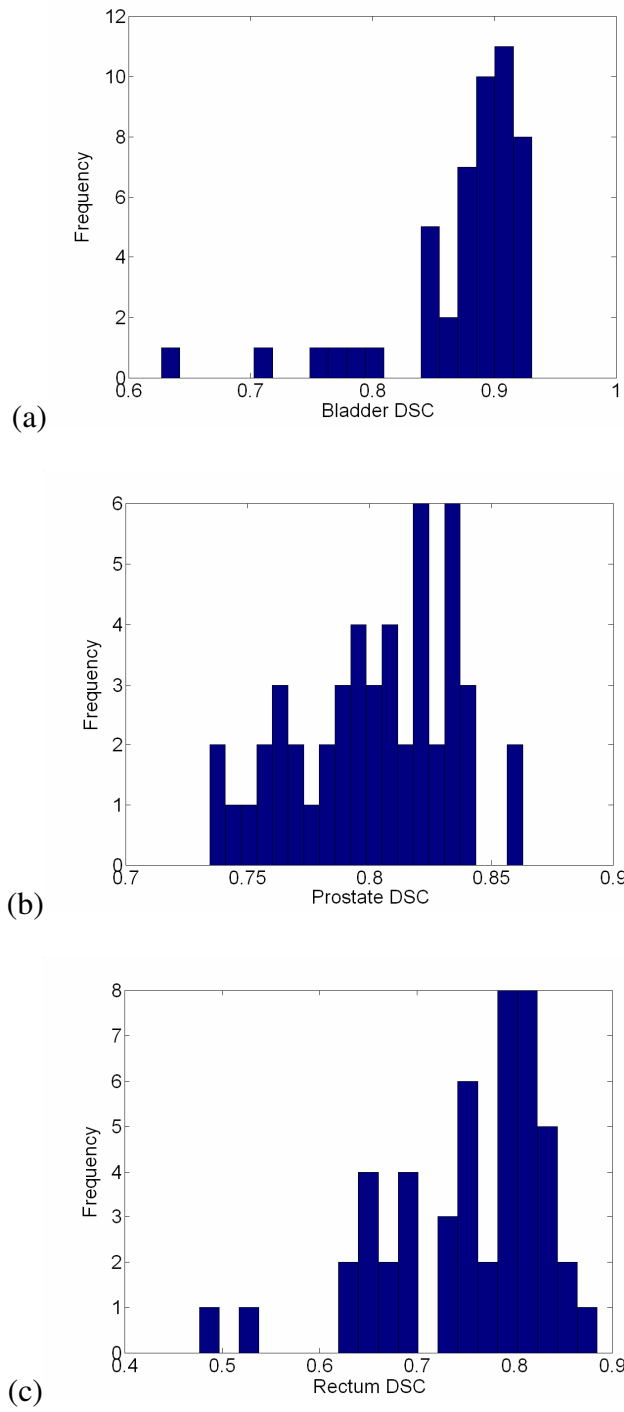


Figure 6-1. Histogram plots of 49 DSC values for (a) bladder, (b) prostate and (c) rectum.

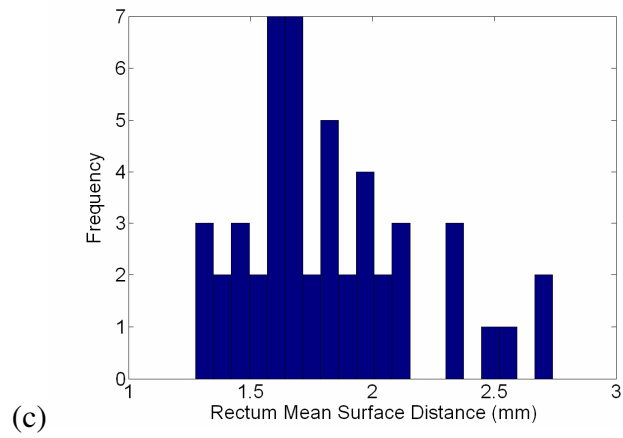
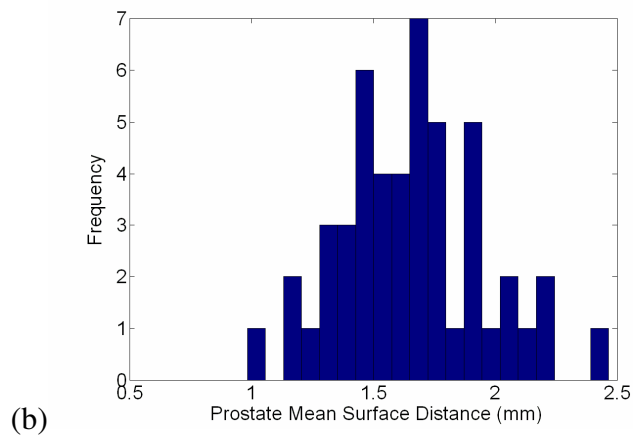
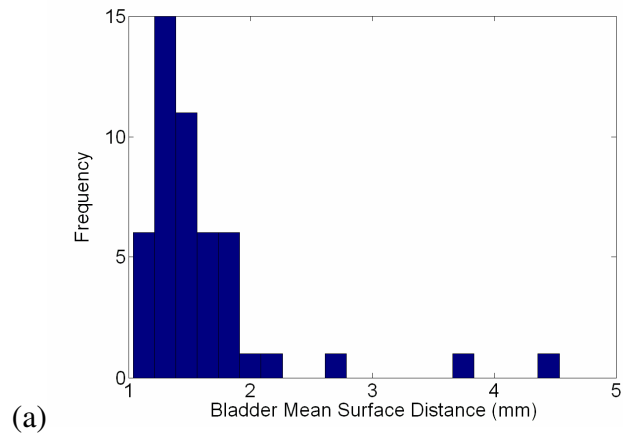


Figure 6-2. Histogram plots of 49 \bar{d} values for (a) bladder, (b) prostate and (c) rectum.

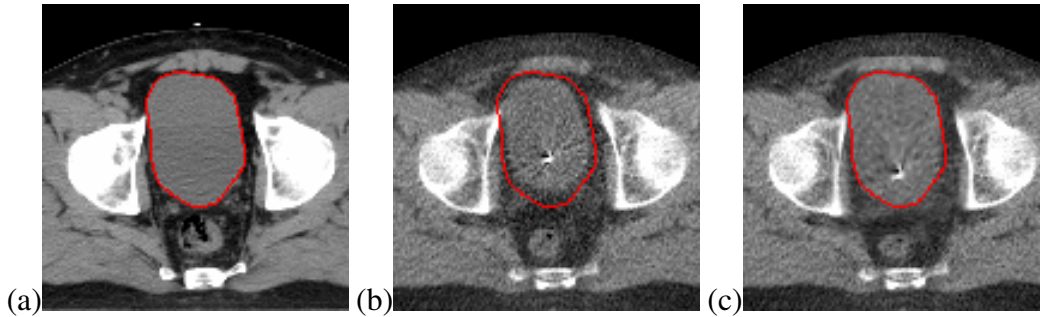


Figure 6-3. Axial slices from a selected treatment fraction demonstrating the algorithm’s bladder deformation capabilities. (a) Planning CT with the bladder contoured in red. (b) Corresponding axial MVCT slice with the planning bladder overlaid. The bladder’s size is clearly reduced during treatment as compared to planning. (c) After deformable registration, the MVCT bladder wall shows excellent alignment with the planning contour (DSC = 0.92, $\bar{d} = 1.2$ mm).

6.3.3 Comparison to Standard B-spline Registration

To demonstrate the advantages of constraining computations over $\Omega_0^{ROI-deform}$, a cohort of the most demanding image pairs were registered using a standard B-spline parameterized FFD multi-resolution deformable algorithm.^{26,27} The image pairs whose mean surface distances were amongst the ten largest bladder, prostate or rectum values after rigid alignment were included in this group. Registration was conducted over a cropped rectangular image domain $\Omega_0^{Pelvis-deform}$ containing the pelvic ROI and a three-stage strategy was employed in which the number of B-spline grid points was doubled after each resolution increase. The final grid resolution was 12 x 12 x 12, which corresponds to spacings δ_x , δ_y and δ_z of less than 20 mm. In addition, three image resolutions

were used in each B-spline mesh resolution. To be consistent with the ROI based registrations, the cost function and optimizer were unchanged and rectum intensity modification was performed prior to registration. Mean values for the mean surface distance metric for both registration strategies are given in table 6-6. The ROI based strategy leads to a 57%, 31% and 43% reduction in mean \bar{d} values for bladder, prostate and rectum, respectively.

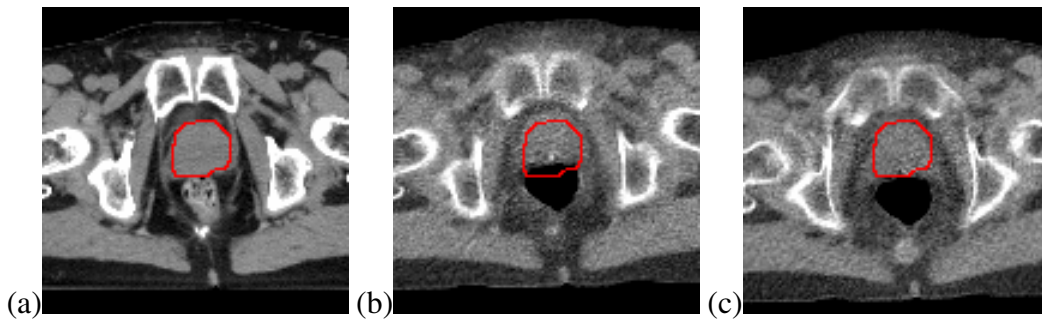


Figure 6-4. Demonstration of prostate registration in our deformable algorithm. (a) Axial slice of planning CT with planning prostate contour overlaid. An interface between the posterior border of the prostate and the anterior rectum surface is clearly visible. (b) The corresponding axial MVCT slice for a selected treatment fraction with the same planning contour shown. The prostate has shifted anteriorly with respect to its planning position to the point where its planning contour is now on top of the MVCT rectum. (c) The same axial MVCT slice after prostate translation and deformation ($DSC = 0.82$, $\bar{d} = 1.9$ mm). The borders of the prostate are not as discernible as in the planning image, but a distinct interface between the prostate contour and the rectum is visible as is the case in the planning CT.

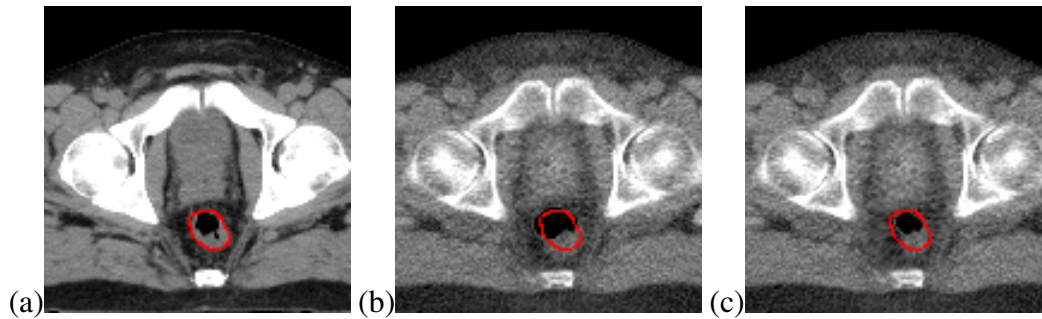


Figure 6-5. Sample rectum deformation. (a) Axial slice of the planning CT showing the rectum contoured in red. (b) After bony alignment, it is apparent in the MVCT that the rectum has changed in size and shape prior to treatment. (c) The deformed MVCT image in which the MVCT rectal volume agrees well with the planning volume ($DSC = 0.76$, $\bar{d} = 1.6$ mm).

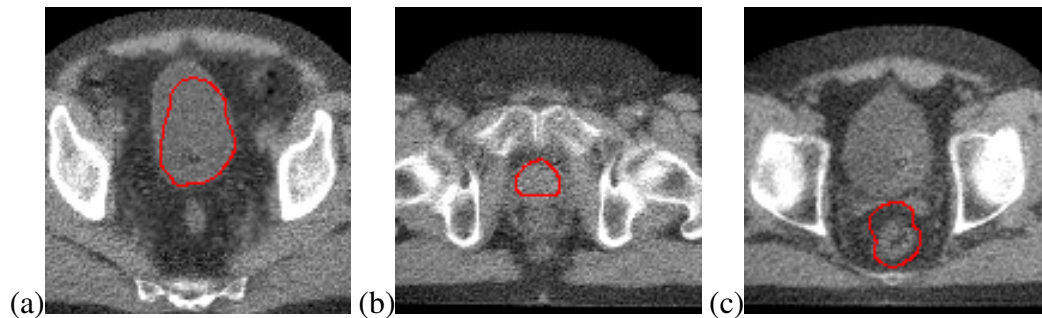


Figure 6-6. Axial slices depicting examples of mediocre bladder ($DSC = 0.63$, $\bar{d} = 3.8$ mm), prostate ($DSC = 0.73$, $\bar{d} = 2.5$ mm) and rectum ($DSC = 0.64$, $\bar{d} = 2.7$ mm) deformable registrations. Respective planning contours are overlaid on each of the deformed (a) bladder, (b) prostate and (c) rectum MVCT images.

Table 6-6. Mean \bar{d} for two registration strategies (n=10).

	Mean Surface Distance (mm)		
	Bladder	Prostate	Rectum
ROI based FFD	2.0	1.8	2.1
Standard multi-resolution FFD	4.6	2.6	3.7

6.4 Discussion

The objective of this work was to develop a deformable registration algorithm for prostate adaptive radiotherapy by incorporating known planning contour information into a voxel based deformable model. Based on the presented data, our efforts demonstrate that by incorporating planning contour data into an automatic voxel based algorithm, the combined advantages of both voxel and feature based algorithms can be realized. Focus is constrained to the clinically strategic ROI, yet no additional user intervention is required. In addition, our deformable registration algorithm can readily be incorporated into the proposed adaptive radiation therapy framework presented in chapter 2. Since the framework calls for off-line deformable registration after completion of each treatment fraction, we were able to computationally implement our registration model focusing on accuracy as opposed to temporal considerations. However, for reference, the time required for each ROI deformable registration was on the order of minutes.

Of course, incorporating contour information into deformable registration algorithms is not a new idea. Structure delineation is required for the surface

based registration algorithms such as those based on the thin plate splines (TPS) or finite element models (FEM) described in section 6.1. In multiple studies, Christensen and colleagues have segmented lungs,^{38,39} brains,^{40,41} and female pelvic organs⁴² in images prior to voxel based deformable registration. Recently, contour information was incorporated into a deformable algorithm based on the optical flow equation for registration of prostate MVCT and planning images.²¹ In all of these references, without exception, segmentation was performed on both the source and target images. Our work demonstrates that time consuming structure delineation on treatment images is not required when registering prostate CT images as long as an appropriately sized mask is applied to the neighbourhood of each planning ROI prior to registration. Comparison of our approach to the standard B-spline parameterized FFD algorithm in section 6.3.3 reveals that significant improvements in registration accuracy can be achieved by limiting the number of voxels outside the clinically strategic ROI that contribute to the optimized cost function. This effect may have even contributed to the slight deviations in the validation metrics that occurred when the border b_0^{ROI} was increased from 10 to 20 mm in section 6.3.1, although the differences were too slight to assert definitively.

Mean bladder, prostate and rectum DSC values presented in section 6.3.1 all exceed 0.7, the value repeatedly deemed in the literature to represent good agreement.^{10,12,36} It should be noted that mean prostate DSC values after accounting for simply prostate motion and after full deformable registration were approximately equivalent. This suggests that for the evaluated images, any

prostate deformation was within the uncertainties of MVCT prostate delineation. In comparison to other prostate deformable registration studies involving DSC analysis in the literature, our mean prostate value of 0.80 is nearly identical to the 0.811 value reported by Foskey *et al.*¹² when registering higher quality kVCT images acquired on a Siemens Somatom scanner. They also report an average bladder DSC of 0.82 upon registration of twenty image pairs which is less than our 0.87 value. Bladder, prostate, and rectum DSC values published by Yang *et al.*²¹ exceed our values, however, a bias was present in that their algorithm required contouring of both planning and treatment images and the same planning and treatment contours that influenced registration were also used for analysis. It must be stressed that the values obtained by other authors are purely for reference as valid algorithm comparison requires the registration of identical images. Our 0.76 mean rectum *DSC* value is lower than what was achieved for bladder and prostate deformation, however, it does exceed the 0.7 threshold. Visual analysis of rectum registrations revealed that the majority of disagreement between planning and deformed treatment contours occurred in the superior region of the rectum where extremely large positional shifts can occur from day to day. Fortunately, these regions are isolated from the CTV and as such, the limited doses they receive would have limited effect on comparative dose metrics such as DVH's, after ART dose deformation. Prostate image deformable registration references containing measurements of neither the mean surface distance metric nor a standard threshold for acceptance could be found in the literature.

The difficulties of accurately delineating structures when using contour information for deformable registration analysis, in particular for studies involving MVCT images, are understood by the authors and have been discussed elsewhere.²¹ However, by analyzing forty-nine image pairs, the influence of random contouring errors on the volumetric analysis measures employed in this study should be statistically limited in comparison to other studies involving significantly smaller cohorts. In addition, any systematic errors in contours delineated by a single radiation oncologist would ideally affect both registration approaches identically for the comparative analysis in section 6.3.3. Of course, an added benefit of our model is that MVCT contours have no influence on the actual registration, simply on its evaluation.

In this work, we assume B-spline parameterization of the deformation field, although other warping methods such as the non-parametric deformable models proposed by Lu *et al.*¹⁶ and Foskey *et al.*¹² could be implemented. Investigating the benefits of introducing planning contour data into Lu's diffusion type or Foskey's fluid flow algorithms is certainly worthy of further research. In addition, analysis was restricted to the registration of daily prostate MVCT images to planning CT images. However, as previously alluded, other on-line imaging modalities are commercially available and images from those systems could immediately be imported into our software without additional processing so long as they are in the standard DICOM format. Treatment images produced by the CT-on-rails system and to a lesser extent, kV cone beam imagers, would have improved contrast over MVCT images, potentially yielding improved results in

comparison to what we report for MVCT registration. In terms of cost functions, from our experience, we have found that the correlation coefficient performs quite admirably when registering MVCT images to kVCT images. However, other metrics such as mean square intensity differences or mutual information may be more suitable when registration is restricted to CT images acquired at similar energies.

6.5 Conclusions

We have developed a voxel based deformable registration algorithm for the registration of treatment and planning CT images for prostate radiotherapy that incorporates known planning contour data into its design. The algorithm combines the respective advantages of both voxel based and feature based methods in that it operates automatically and focuses on the clinically important ROI. Instead of performing registration over entire images, separate transformations are generated for each region of clinical importance. After rigid bony alignment, prostate motion correction and rectum intensity modification, separate deformable registrations are performed for each clinical ROI. The algorithm uses quasi-Newton techniques for correlation coefficient optimization and employs B-spline parameterization of the deformation field. Although the algorithm has been tested with MVCT images acquired on the Hi*Art II system, presumably it is suitable for any on-line CT imaging modality. In the next chapter, the algorithm will be used to correct for daily anatomical variations in the comparison of planned and delivered doses.

6.6 References

1. Yan D, Vicini F, Wong J, Martinez A. Adaptive radiation therapy. *Phys Med Biol.* 1997;42:123-132.
2. Kupelian PA, Langen KM, Zeidan OA, Meeks SL, Willoughby TR, Wagner TH, Jeswani S, Ruchala KJ, Haimerl J, Olivera GH. Daily variations in delivered doses in patients treated with radiotherapy for localized prostate cancer. *Int J Radiat Oncol Biol Phys.* 2006;66:876-882.
3. Sorcini B, Tilikidis A. Clinical application of image-guided radiotherapy, IGRT (on the Varian OBI platform). *Cancer Radiother.* 2006;10:252-257.
4. Lehmann J, Perks J, Semon S, Harse R, Purdy JA. Commissioning experience with cone-beam computed tomography for image-guided radiation therapy. *J Appl Clin Med Phys.* 2007;8:21-36.
5. Wong JR, Grimm L, Uematsu M, Oren R, Cheng CW, Merrick S, Schiff P. Image-guided radiotherapy for prostate cancer by CT-linear accelerator combination: prostate movements and dosimetric considerations. *Int J Radiat Oncol Biol Phys.* 2005;61:561-569.
6. Tome WA, Jaradat HA, Nelson IA, Ritter MA, Mehta MP. Helical tomotherapy: image guidance and adaptive dose guidance. *Front Radiat Ther Oncol.* 2007;40:162-178.
7. Langen KM, Meeks SL, Poole DO, Wagner TH, Willoughby TR, Kupelian PA, Ruchala KJ, Haimerl J, Olivera GH. The use of megavoltage CT (MVCT) images for dose recomputations. *Phys Med Biol.* 2005;50:4259-4276.

8. Schaly B, Kempe JA, Bauman GS, Battista JJ, Van Dyk J. Tracking the dose distribution in radiation therapy by accounting for variable anatomy. *Phys Med Biol.* 2004;49:791-805.
9. Bookstein FL. Principal warps: thin plate splines and the decomposition of deformations. *IEEE Trans Pattern Anal Mach Intell.* 1989;11:567-585.
10. Bharatha A, Hirose M, Hata N, Warfield SK, Ferrant M, Zou KH, Suarez-Santana E, Ruiz-Alzola J, D'Amico A, Cormack RA, Kikinis R, Jolesz FA, Tempany CMC. Evaluation of three-dimensional finite element-based deformable registration of pre- and intraoperative prostate imaging. *Med Phys.* 2001;28:2551-2560.
11. Crouch JR, Pizer SM, Chaney EL, Hu YC, Mageras GS, Zaider M. Automated finite-element analysis for deformable registration of prostate images. *IEEE Trans Med Imag.* 2007;26:1379-1390.
12. Foskey M, Davis B, Goyal L, Chang S, Chaney E, Strehl N, Tomei S, Rosenman J, Joshi S. Large deformation three-dimensional image registration in image-guided radiation therapy. *Phys Med Biol.* 2005;50:5869-5892.
13. Christensen GE, Rabbitt RD, Miller MI. Deformable templates using large deformation kinematics. *IEEE Trans Image Process.* 1996;5:1435-1447.
14. Thirion JP. Image matching as a diffusion process: an analogy with Maxwell's demons. *Med Image Anal.* 1998;2:243-260.
15. Wang H, Dong L, O'Daniel J, Mohan R, Garden AS, Ang KK, Kuban QA, Bonnen M, Chang JY, Cheung R. Validation of an accelerated 'demons'

algorithm for deformable image registration in radiation therapy. *Phys Med Biol.* 2005;50:2887-2905.

16. Lu W, Chen ML, Olivera GH, Ruchala KJ, Mackie TR. Fast free-form deformable registration via calculus of variations. *Phys Med Biol.* 2004;49:3067-3087.

17. Lu W, Olivera GH, Chen Q, Ruchala KJ, Haimerl J, Meeks SL, Langen KM, Kupelian PA. Deformable registration of the planning image (kVCT) and the daily images (MVCT) for adaptive radiation therapy. *Phys Med Biol.* 2006;51:4357-4374.

18. Gao S, Zhang L, Wang H, de Crevoisier R, Kuban DD, Mohan R, Dong L. A deformable image registration method to handle distended rectums in prostate cancer radiotherapy. *Med Phys.* 2006;33:3304-3312.

19. Lau YH, Braun M, Hutton BF. Non-rigid image registration using a median-filtered coarse-to-fine displacement field and a symmetric correlation ratio. *Phys Med Biol.* 2001;46:1297-1319.

20. Malsch U, Thieke C, Huber PE, Bendl R. An enhanced block matching algorithm for fast elastic registration in adaptive radiotherapy. *Phys Med Biol.* 2006;51:4789-4806.

21. Yang D, Chaudhari SR, Goddu SM, Pratt D, Khullar D, Deasy JO, El Naqa I. Deformable registration of abdominal kilovoltage treatment planning CT and tomotherapy daily megavoltage CT for treatment adaptation. *Med Phys.* 2009;36:329-338.

22. Murphy MJ, Wei Z, Fatyga M, Williamson, J, Anscher M, Wallace T, Weiss E. How does CT image noise affect 3D deformable image registration for image-guided radiotherapy planning? *Med Phys*. 2008;35:1145-1153.
23. Lee S, Wolberg G, Chwa KY, Shin SY. Image metamorphosis with scattered feature constraints. *IEEE Trans Vis Comp Graph*. 1996;2:337-354.
24. Rueckert D, Sonoda LI, Hayes C, Hill DLG, Leach MO, Hawkes DJ. Nonrigid registration using free-form deformations: application to breast MR images. *IEEE Trans Med Imag*. 1999;18:712-721.
25. Studholme C, Hill DLG, Hawkes DJ. An overlap invariant entropy measure of 3D medical image alignment. *Pattern Recognit*. 1998;32:71-86.
26. Mattes D, Haynor DR, Vesselle H, Lewellen TK, Eubank W, PET-CT image registration in the chest using free-form deformations. *IEEE Trans Med Imag*. 2003;22:120-128.
27. Klein S, Staring M, Pluim JPW. Evaluation of optimization methods for nonrigid medical image registration using mutual information and B-splines. *IEEE Trans. Image Process*. 2007;16:2879-2890.
28. Feng Y, Castro-Pareja C, Shekhar R, Yu C. Direct aperture deformation: an interfraction image guidance strategy. *Med Phys*. 2006;33:4490-4498.
29. Langen KM, Zhang Y, Andrews RD, Hurley ME, Meeks SL, Poole DO, Willoughby TR, Kupelian PA. Initial experience with megavoltage (MV) CT guidance for daily prostate alignments. *Int J Radiat Oncol Biol Phys*. 2005;62:1517-1524.

30. Lin X. Model-based strategies for automated segmentation of cardiac magnetic resonance images. PhD dissertation. University of Auckland, Auckland, New Zealand; 2008.
31. Byrd RH, Lu P, Nocedal J, Zhu C. A limited memory algorithm for bound constrained optimization. *SIAM J Sci Comput.* 1995;16:1190-1208.
32. Langen KM, Jones DTL. Organ motion and its management. *Int J Radiat Oncol Biol Phys.* 2001;50:265-278.
33. Byrne TE. A review of prostate motion with considerations for the treatment of prostate cancer. *Medical Dosimetry.* 2005;30:155-161.
34. Yan D, Jaffray DA, Wong JW. A model to accumulate fractionated dose in a deforming organ. *Int J Radiat Oncol Biol Phys.* 1999;44:665-675.
35. Dice LR. Measures of the amount of ecologic association between species. *Ecology.* 1945;26:297-302.
36. Zijdenbos AP, Dawant BM, Margolin RA, Palmer AC. Morphometric analysis of white matter in MR images: method and validation. *IEEE Trans Med Imag.* 1994;13:716-724.
37. Wang H, Garden AS, Zhang L, Wei X, Ahamad A, Kuban DA, Komaki R, O'Daniel J, Zhang Y, Mohan R, Dong L. Performance evaluation of automatic anatomy segmentation algorithm on repeat or four-dimensional computed tomography images using deformable image registration method. *Int J Radiat Oncol Biol Phys.* 2008;72:210-219.
38. Li B, Christensen GE, Hoffman EA, McLennan G, Reinhardt JM. Pulmonary CT image registration and warping for tracking tissue deformation during the

respiratory cycle through 3D consistent image registration. *Med Phys.* 2008;35:5575-5583.

39. Christensen GE, Song JH, Lu W, El Naqa I, Low DA. Tracking lung tissue motion and expansion/compression with inverse consistent image registration and spirometry. *Med Phys.* 2007;34:2155-2163.

40. Christensen GE, Johnson HJ, Vannier MW. Synthesizing average 3D anatomical shapes. *Neuroimage.* 2006;32:146-158.

41. Christensen GE, Johnson HJ. Consistent image registration. *IEEE Trans Med Imag.* 2001;20:568-582.

42. Christensen GE, Carlson B, Chao KSC, Yin P, Grigsby PW, Nguyen K, Dempsey JF, Lerma FA, Bae KT, Vannier MW, Williamson JF. Image-based dose planning of intracavitary brachytherapy: registration of serial-imaging studies using deformable anatomic templates. *Int J Radiat Oncol Biol Phys.* 2001;51:227-243.

Chapter 7: Accounting for daily anatomical variations in the evaluation of cumulative dosimetry

7.1 Introduction

A fundamental flaw in the preparation, planning and delivery of conventional radiation therapy is the underlying assumption of an unchanging geometric, anatomic and dosimetric system. Over a decade ago, Yan *et al.*¹ established the concept of adaptive radiation therapy (ART) by proposing that after monitoring a small number of initial fractions, treatment plans be modified to incorporate patient specific margins and dose prescriptions. Since then, ART has itself adapted to include strategies such as offline² and online³ re-optimization, dose compensation⁴ and direct aperture deformation (DAD).⁵ A necessary requirement in any advanced adaptive protocol, whether on-line or off-line, is the ability to evaluate the cumulative dosimetry of target and dose sensitive volumes, a process often referred to as dose accumulation.

Dose accumulation has three essential requirements: three-dimensional (3D) treatment imaging, dose recalculation or reconstruction and deformable image registration. Each component has been the subject of considerable research reported in the literature in recent years. A variety of in-room computed tomography (CT) imaging modalities have been designed, manufactured and implemented clinically, including CT-on-rails,⁶ cone beam CT (CBCT)^{7,8} and megavoltage CT (MVCT) imaging on helical tomotherapy.⁹ For the second requirement, preliminary dose accumulation efforts assumed the transfer of planned dose distributions onto treatment images, neglecting any effects of anatomical variations on dosimetry.¹⁰ Since then, methods have been developed to either reconstruct or recalculate the delivered dose using the information contained in treatment images. It has been demonstrated that the combination of exit fluence detection during treatment delivery and in-room CT imaging allows for the reconstruction of delivered dose distributions.¹¹ In addition, doses can accurately be calculated by applying beam parameters to treatment images in the same manner that doses are evaluated on planning CT images.^{12,13} The final requirement for dose accumulation is the deformable registration of treatment and planning images in order to track the daily motion of individual voxels in the initial planning CT.

Image registration, whether rigid or deformable, requires optimization of a cost function and as such, algorithms are often classified as either feature based or voxel based depending on cost function definition. Feature based methods minimize the distances between point landmarks or surfaces delineated on the

registered images while voxel based methods utilize the information contained in image intensity values to achieve correspondence. Prevalent feature based methods include modeling deformations with thin-plate splines¹⁴ or using finite element methods (FEM) to biomechanically deform segmented structures.¹⁰ A wide range of voxel based algorithms involving optical flow,^{15,16} fluid models,^{17,18} diffusion equations,^{19,20} block matching^{21,22} and B-splines^{23,24} have been reported in the literature. Feature based algorithms are advantageous in that they tend to focus on structures of clinical importance, whereas voxel based algorithms being significantly more computationally complex may sacrifice accuracy near critical regions of interest (ROI) in order to optimize correspondence over entire images. However, unlike automatic voxel based methods, feature extraction often requires time consuming human intervention. In the previous chapter, we developed and validated an automatic deformable registration technique that combined the benefits of both classes of registration algorithms. Known planning contour information is integrated in our model that assumes B-spline parameterization of ROI specific deformations between prostate MVCT and planning CT images.

A number of studies in which dose warping was used as a tool to simply compare planned and delivered doses in a common reference frame, as well as those involving full fledged dose accumulation, have been reported in the literature. Yan *et al.*¹⁰ tracked the dose delivered to each volume element in a single patient's rectal wall over fourteen treatment fractions using manually delineated contours and FEM based deformable registration. More recently, prostate, seminal vesicle, bladder and rectum cumulative doses delivered over ten

fractions were evaluated for nine patients using the same registration method.²⁵ Manual contouring was also required for separate studies in which a TPS deformable model was assumed when doses to multiple ROI were accumulated for one¹⁴ and five²⁶ prostate patients, respectively. Automatic fluid flow voxel based registration provided an accumulated prostate dose for a single patient in work published by Foskey *et al.*¹⁸ O'Daniel *et al.*²⁷ evaluated cumulative doses delivered to twelve head and neck patients using bi-weekly treatment images and an automatic deformable registration algorithm based on optical flow. Head and neck has also been the site of choice for the limited number of dose accumulation studies involving MVCT images^{20,28} found in the literature.

Many of the aforementioned dose accumulation studies involve only a sample of treatment fractions, a single ROI, or single patients, or require significant manual intervention. In this chapter, we present a framework for dose accumulation in prostate treatments on the High*Art II helical tomotherapy system. After establishing framework methodologies, we provide a discussion of dose warping errors and assess our dose accumulation software using a landmark based validation. Next, we compare planned and cumulatively delivered dose distributions for multiple patients at various stages over the course of treatment. Finally, we evaluate the cumulative dosimetry of two different daily image guidance strategies.

7.2 Methods and Materials

The terms dose accumulation and cumulative dose often appear in the literature in two separate contexts. Currently, researchers are developing the field of four dimensional (4D) planning in which planning CT images are acquired at multiple phases of the respiratory cycle.²⁹⁻³¹ Dose distributions evaluated at each phase are weighted based on a respiratory model and accumulated to generate a cumulative planned dose distribution. Our work focuses on the accumulated dose delivered over the course of radiation therapy treatment and although there is certainly potential for methodological overlap, they are two distinct problems. Unless otherwise noted, the terms dose accumulation and cumulative dose when used throughout this chapter will refer specifically to the latter context.

Daily pre-treatment MVCT images from four prostate patients treated on our research Hi*Art II helical tomotherapy system were available for this study. Patients 1 through 3 underwent twenty-five treatment fractions with a prescribed dose of 68 Gy (2.72 Gy per fraction) to the primary PTV which consisted of the prostate gland and seminal vesicles plus a margin 7mm posteriorly and 10mm in all other directions. The remaining patient, patient 4, was treated to 60 Gy over twenty fractions (3.00 Gy per fraction). Treatment dose distributions were calculated by applying the planned delivery to MVCT images using the High*Art II system's Planned Adaptive software.

7.2.1 Dose Accumulation

Assuming a Cartesian co-ordinate system, let \mathbf{x}_0 represent a 3D planning CT image volume in which an intensity $I_0(\mathbf{x}_0)$ and dose value $d_0(\mathbf{x}_0)$ are available for each voxelized position (x, y, z) in the image. Similarly, we define a treatment image volume \mathbf{x}_i with analogous intensity $I_i(\mathbf{x}_i)$ and dose $d_i(\mathbf{x}_i)$ representations for each treatment fraction i .

The fractionated deformed dose distribution is given by

$$d_i(\mathbf{x}_0) = d_i(\mathbf{T}_i(\mathbf{x}_i)) \quad 7.1$$

in which the transformation \mathbf{T}_i maps each treatment voxel position (x_i, y_i, z_i) to its corresponding planning voxel location (x_0, y_0, z_0) as determined by deformable registration. By performing this mapping over N_F treatment fractions, the accumulated dose

$$d_{total}(\mathbf{x}_0) = \sum_{i=1}^{N_F} d_i(\mathbf{x}_0) \quad 7.2$$

delivered over the course of treatment can be evaluated. To generate the required deformable transformation for each treatment fraction, we used the algorithm developed and validated in the previous chapter. The algorithm, which will be reviewed briefly, was incorporated into dose accumulation software developed as part of this project.

7.2.1.1 Deformable Registration

Our deformable registration algorithm consists of four separate processes, in which all steps are performed automatically upon input of planning contours

and planning and treatment images. The net result is a separate transformation \mathbf{T}_i^{ROI} for each individual ROI (left femur, right femur, prostate, bladder and rectum) instead of a single transformation \mathbf{T}_i .

Rigid alignment: Initially, rigid bony alignment of treatment and planning images is achieved through mean square intensity difference (MSD) registration using only the planning CT bony voxels segmented via thresholding in the calculation of the cost function.

Prostate localization: Next, the translation of the prostate with respect to surrounding anatomy is determined using correlation coefficient (CC) registration in which only the planning CT delineated prostate plus a small 6 mm border are included in CC evaluation. Bone and bowel gas voxels contained within the border are excluded via segmentation in order to eliminate their impact on registration convergence.

Rectum intensity modification: The third step involves the potential modification of rectum planning CT voxels in order to correct for any major differences in bowel gas concentrations between planning and treatment images. The algorithm loops through each individual slice that contains a delineated rectum contour and if the treatment slice contains a large bowel gas pocket that is not present on the corresponding slice in the planning CT, a gas pocket is inserted in the centre of the planning CT rectum to aid in achieving correspondence during deformation of the treatment CT rectum. In situations where the planning CT slice contains a gas pocket not present in the treatment CT, the pocket is filled in using appropriate intensities for solid bowel contents.

Warping of deformable ROI: In the fourth and final step, separate B-spline parameterized deformable registrations are performed in the local neighbourhoods of the planning CT delineated bladder, rectum and prostate volumes. Registration relies on quasi-Newton optimization of the correlation coefficient evaluated using only the delineated planning CT voxels plus a modifiable user-defined border for each ROI.

7.2.1.2 Dose Accumulation Software

Dose accumulation was performed using a graphical user interface (GUI) developed in Visual Basic .NET that calls C++ scripts to perform the registration and dose warping computations. The GUI consists of eleven tabs for input, registration, dose accumulation and analysis. There are three separate input tabs in which import of files for planning data (image and contours), treatment images and dose distributions (planning and treatment) are defined. Treatment information including prescription dose, number of fractions, and treatment couch shifts are also input on the dose distribution tab. Images are imported in DICOM format, while contours and dose distributions are imported in the text and binary formats output by the Hi*Art II system, respectively. Four additional tabs allow for user definition of the bone, prostate, bladder and rectum registration settings. Settings include cost function parameters such as borders and thresholds, parameters associated with optimization convergence, intensities for rectum modification, and the resolution of B-spline functions. An additional tab allows for axial viewing of planning, treatment and deformed treatment images,

each with planning contours overlaid. Based on registrations and treatment shifts, the software generates warped treatment dose distributions and delivered dose volume histograms (DVH) for each individual treatment fraction. Two output tabs provide a quantitative comparison of planned and delivered doses. Planned and delivered DVHs are plotted on the first tab, while difference maps between planned and warped treatment dose distributions are displayed on the second output tab. The final tab is for dose accumulation. It allows the user to select which treatment fractions to accumulate and upon evaluation of accumulated doses, cumulative dose difference maps and cumulative DVHs are displayed on the two output tabs. The functions provided by each of the eleven tabs are summarized in table 7-1.

7.2.2 Uncertainty in Accumulated Dose Distributions

A number of factors contribute to the uncertainty in the evaluation of each deformed treatment dose distribution $d_i(\mathbf{x}_0)$. For our purposes, we are only interested in errors inherent to the analysis and processing of treatment images in the dose accumulation framework presented in section 7.2.1. These include dose recalculation, interpolation of warped doses and inaccurate deformable transformations, each of which will be discussed briefly. Other sources of error such as improper delivery due to treatment machine failure³² or intra-fraction motion³³ have been discussed elsewhere and are beyond the scope of this thesis.

Table 7-1. Summary of the functions provided in each of the eleven tabs in the dose accumulation graphical user interface (GUI).

Tab	Function
1. Plan Data	Input of planning CT and planning contour files (prostate, bladder, rectum, left femur, right femur)
2. MVCT Data	Input of daily MVCT
3. Doses	Input of planned dose distribution, treatment dose distribution, number of fractions, prescription dose, and daily treatment shift
4. Bony Align	Rigid bony registration settings
5. Prostate Align	Translational prostate registration and deformable prostate registration settings
6. Bladder Deform	Bladder deformable registration settings
7. Rectum Deform	Rectum deformable registration settings
8. Viewer	Display of planned CT, MVCT after bony alignment and MVCT after deformable registration. Planning contour overlays allow for visual inspection of registration.
9. Cumulative	Selection of fractions to be used in dose accumulation
10. DVH	Display of planned and treatment (individual fraction or cumulative) dose volume histograms
11. Distributions	Display of difference maps between planned and cumulative treatment dose distributions.

7.2.2.1 Recalculation

All dose calculation algorithms that use electron density information obtained from CT data contain some approximations that inevitably result in limitations and uncertainties. Delivered dose distributions on the Hi*Art II system are evaluated by applying the daily delivery sinogram to each treatment MVCT image $I(\mathbf{x}_i)$ using the system's built-in Planned Adaptive software. Phantom studies have demonstrated that daily dose distributions are calculated with accuracy similar to that of initial planning CT dose calculations.¹²

7.2.2.2 Interpolation

The combined process of deforming a Cartesian voxelized dose distribution and the interpolation of deformed dose values on another rectangular voxelized grid has intrinsic limitations that introduce errors in the evaluation of $d_i(\mathbf{x}_0)$.³⁴⁻³⁶ These errors are due to the fact that interpolation strategies using nearest neighbour, linear or other higher order kernels do not conserve energy when deformed doses are interpolated. These dose interpolation errors may be significant in high dose gradient regions or at the interface between two different types of tissue. In fact, Heath *et al.*³⁵ reported interpolation based dose errors of up to 16% in the beam penumbra using a thoracic phantom. In appendix C, we demonstrate that interpolation errors should have only a marginal impact on dose accumulation in the prostate patients examined in this study.

7.2.2.3 Deformation

The final source of error in deformed dose distributions is due to irregularities in the transformation determined via deformable registration. The goal of deformable registration in dose accumulation is to determine complete anatomical correspondence between the treatment and planning images. For quantification of deformable registration errors, an ongoing area of research, a number of methods have been proposed including phantom studies,^{16,19,37,38} synthetic transformations,^{16,19,21} point landmarks^{29,30,39} and contour analysis.^{18,40,41} Ultimately, the deformable registration error itself is not important as it is the error in the deformed dose due to inaccurate registration that plays a vital role in dose accumulation, although a relationship likely exists. Unfortunately, dose inaccuracies due to deformable registration errors are not easily quantifiable. In the next section, we describe a landmark based assessment of dose deformation that is dependent on registration errors.

7.2.3 Landmark Based Assessment of Dose Warping

Anatomical correspondence as determined by deformable registration can be exploited to provide a landmark based assessment of dose warping accuracy. We begin with an individual voxel (x_i, y_i, z_i) in a treatment image $I(\mathbf{x}_i)$ that was delivered a fractionated dose $d_i(x_i, y_i, z_i)$. Upon dose deformation, the dose $d_i(x_i, y_i, z_i)$ will be mapped to the corresponding location (x_0, y_0, z_0) in the planning CT reference frame. Assuming perfect registration correspondence and no interpolation based errors, the deformed treatment dose $d_i(x_0, y_0, z_0)$ at

planning CT voxel (x_0, y_0, z_0) will be equivalent to $d_i(x_i, y_i, z_i)$. The value of $d_i(x_i, y_i, z_i)$ at visible landmarks in a treatment image volume \mathbf{x}_i can be compared to the deformed dose $d_i(x_0, y_0, z_0)$ at the corresponding landmarks identified in the planning image volume \mathbf{x}_0 to assess the accuracy of dose deformation.

Deformed dose verification was accomplished by identifying six landmarks on twenty selected treatment image volumes \mathbf{x}_i and their corresponding planning image volumes \mathbf{x}_0 . Landmarks were selected based on ease of identification and the desire to include points situated at focal features within the planned dose distribution. The first two landmarks were adapted from the methodology used by Yan *et al.*¹⁰ in which they assumed anatomical correspondence at the most anterior and posterior points on inner and outer rectal wall contours delineated in multiple CT images when biomechanically modeling rectal wall deformation. Similarly, we selected the most anterior and posterior points on the outer rectal wall at the prostate mid-plane for landmarks 1 and 2, respectively. The prostate inferior apex provided landmark 3, while landmark 4 was positioned at the most anterior point on the prostate mid-plane. The final two landmarks were selected from the set of anatomical points used by Xiong *et al.*⁴² in the validation of their bladder deformation algorithm. The junction of the left ureter and bladder wall and the junction of the right ureter and bladder wall were used as the fifth and sixth landmarks, respectively. Landmarks 1 through 4 were automatically located on radiation oncologist delineated prostate and rectum contours while landmarks 5 and 6 were visually identified by a radiologist.

Presumably, landmarks 1, 3 and 4 are situated in the high dose region adjacent to dose gradients surrounding the target volume whereas the other three landmarks are within the dose gradient region.

An intrinsic limitation of our landmark based analysis is that reported dose warping errors are dependent on uncertainties in landmark identification. In order to quantify the error contribution associated with landmark identification, each landmark position (x_i, y_i, z_i) was re-identified in five randomly selected treatment MVCT images. For each landmark, the standard deviation of the differences in $d_i(x_i, y_i, z_i)$ values from the two identification procedures for the five repeat fractions was evaluated. It should be noted that repeat identification of landmarks enables the random component of the error contribution to be estimated, however the systematic component remains unknown.

7.2.4 Comparison of Planned and Delivered Doses

Dose accumulation as described in section 7.2.1 was retrospectively performed for patients 2 and 4. Cumulatively delivered dose distributions were evaluated after one, five, ten, fifteen, twenty and twenty-five fractions and were compared to planned dose values. In addition, prostate, bladder, rectum, left femur and right femur dose volume histograms were computed for each of the aforementioned dose distributions.

7.2.5 Dosimetric Evaluation of Image Guidance Strategies

As discussed in chapter 5, prior to the clinical use of CT to monitor treatment set-up, daily image guidance was based on the matching of two-dimensional (2D) portal films or electronic portal images (EPI) with digitally reconstructed radiographs (DRR). The lack of soft tissue contrast in these 2D images meant that patient positioning was often based on the matching of rigid bony anatomy and with the target location unbeknownst to clinicians; target volumes could easily have been missed. With the advent of treatment CT imaging, daily patient positioning can now be performed by matching the target prostate volumes in treatment and planning images. If performed accurately the likelihood of underdosing the target is significantly reduced, but potentially at a cost. As demonstrated in chapter 5, if the target has moved adjacent to a critical structure the radiosensitive volume may be significantly overdosed, leading to increased toxicity. To evaluate the dosimetric differences between bone matching and prostate matching image guidance strategies, we evaluated the dose distributions that would have been delivered during each fractionated treatment if patient positioning was based on each method for all four patients. Translational bone and prostate matching shifts were determined using automatic registration software described in chapter 5. Using our dose accumulation framework we compared the cumulative doses that would have been delivered had daily positioning been based on these two strategies.

7.3 Results

7.3.1 Landmark Based Dose Warping Assessment

The dose warping accuracy at the six landmark positions was determined by evaluating the standard deviation of the differences between deformed doses $d_i(x_0, y_0, z_0)$ and delivered doses $d_i(x_i, y_i, z_i)$ for all twenty fractions. Values are normalized to the fractionated prescription dose. Standard deviations and the corresponding mean, maximum and minimum dose differences for each landmark are presented in table 7-2. Unfortunately, a number of outliers contributed to the large observed deviations for some of the landmarks. However, over the twenty fractions analyzed, the positive and negative dose discrepancies offset, resulting in the observed low mean values. This may suggest that dose accumulation errors resulting from incorrect warping are statistical in nature and as such, the accuracy of cumulative dosimetry increases as dose distributions from more and more fractions are added together. However, reported dose discrepancies are probably a result of both warping error and landmark identification error, with the respective contributions unknown. The standard deviations of the differences in $d_i(x_i, y_i, z_i)$ values for landmarks 1 through 6 after landmark re-identification were 0.2, 4.3, 0.4, 4.5, 0.9 and 4.5%, respectively.

7.3.2 Comparison of Planned and Delivered Doses

A feature of our dose accumulation software is the generation of dose difference maps evaluated after a user defined number of cumulative fractions. The delivered dose minus the planning dose in each ROI voxel is normalized to

the prescription dose and displayed as a colormap overlaid on the grayscale planning CT. A sample slice from difference maps after one, five, ten, fifteen, twenty and twenty-five fractions for patient 2 is displayed in figure 7-1. Cumulative treatment dose volume histograms after five, ten, fifteen and twenty fractions are plotted alongside their corresponding planned dose volume histograms for patient 4 in figure 7-2.

Table 7-2. Statistics for the landmark based method of determining dose warping errors. Errors were evaluated at each landmark in twenty treatment fractions and values are normalized to the fractionated prescription dose.

Landmark	σ (%)	Mean (%)	Range (%)
1. Anterior point on outer rectal wall at prostate mid-plane	2.3	-1.0	-7.1 to 2.8
2. Posterior point on outer rectal wall at prostate mid-plane	4.2	-0.1	-6.0 to 10.0
3. Prostate inferior apex	0.4	0.0	-0.8 to 0.7
4. Anterior point on prostate mid-plane	2.7	-0.7	-8.7 to 5.9
5. Junction of left ureter and bladder wall	5.2	-3.7	-16.8 to 0.8
6. Junction of right ureter and bladder wall	8.1	-1.4	-22.5 to 9.5

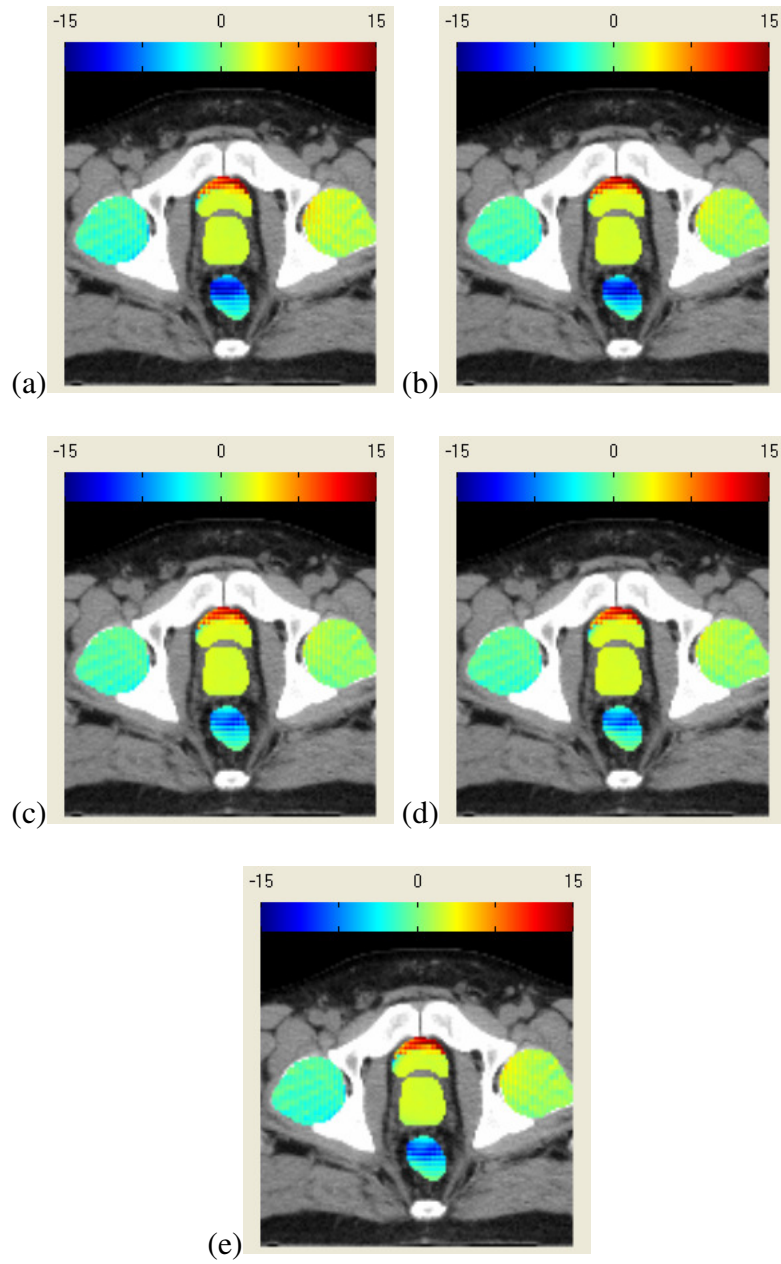


Figure 7-1. Cumulative treatment doses minus planned doses (in percent, normalized to prescription dose) for patient 2 after (a) five, (b) ten, (c) fifteen, (d) twenty and (e) twenty-five fractions.

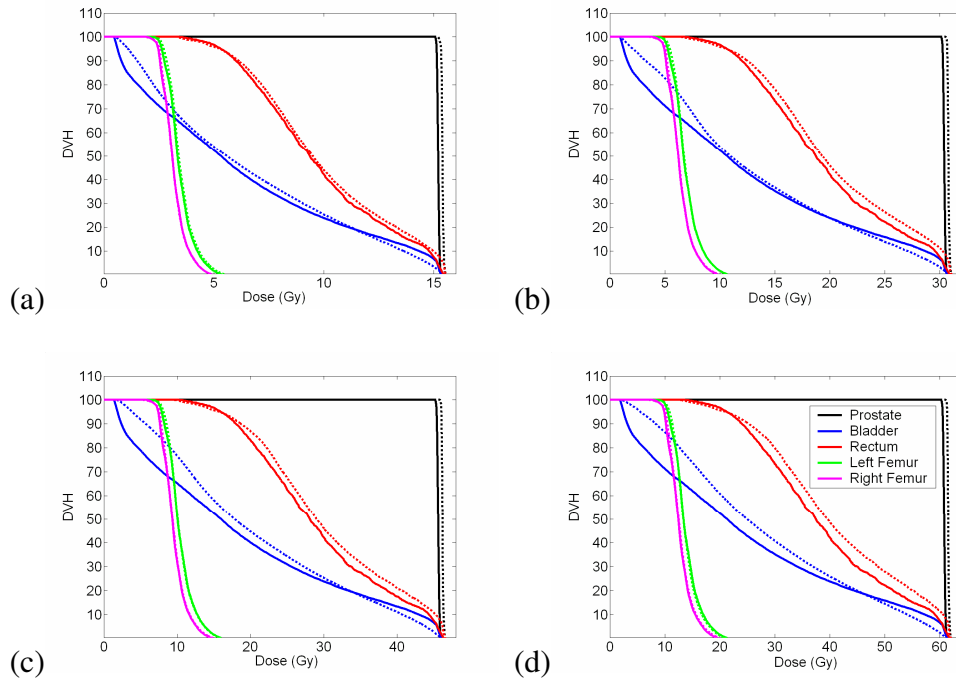


Figure 7-2. Comparison of patient 4 planned (solid) and treatment (dashed) dose volume histograms after (a) five, (b) ten, (c) fifteen and (d) twenty fractions.

A comparison of treatment and planning prostate D95 values is provided in table 7-3 for the two patients in which cumulative treatment doses were evaluated. Once again, cumulative analysis was performed after five, ten, fifteen, twenty and twenty-five fractions and interestingly, all tabulated treatment D95 values exceed those that were planned. Treatment D95 differences from corresponding planning values ranged from 1.3 to 2.7 per cent.

Endpoints used for comparison of planned and treatment bladder and rectum doses were adapted from the RTOG 0415 protocol⁴³ which mandates limits to bladder and rectum D50, D35, D25 and D15 values. We evaluated the differences between treatment and planned bladder D50 and D15 values for the two patients in table 7-4. Similarly, rectum D50 and D15 values are tabulated in

table 7-5. Treatment bladder D50 and D15 differences ranged from 3.0 to 17.9 and -4.5 to 4.2 per cent of their planned values, respectively. Corresponding rectum differences were -3.4 to 5.6 and -11.8 to 5.5 per cent.

Table 7-3. Differences between treatment and planning prostate D95 values after completion of five, ten, fifteen, twenty, and twenty-five fractions. Dose differences are expressed in percent and normalized to planned D95 values, which are also included for reference (N_F = number of fractions).

Patient	Plan D95 (Gy)	$N_F = 5$	$N_F = 10$	$N_F = 15$	$N_F = 20$	$N_F = 25$
2	68.21	2.5	2.5	2.6	2.7	1.8
4	60.53	1.3	1.4	1.4	1.4	-

Table 7-4. Differences between treatment and planning bladder D50 and D15 values after completion of five, ten, fifteen, twenty, and twenty-five fractions. Dose differences are expressed in percent and normalized to planned values, which are also included for reference.

Patient	D50/D15	Planned (Gy)	$N_F = 5$	$N_F = 10$	$N_F = 15$	$N_F = 20$	$N_F = 25$
2	D50	48.58	12.9	15.2	17.9	16.2	15.5
2	D15	66.34	3.1	4.0	4.2	4.0	3.8
4	D50	21.34	5.1	3.0	11.9	17.3	-
4	D15	51.24	-3.1	-4.5	-3.2	-3.1	-

Table 7-5. Differences between treatment and planning rectum D50 and D15 values after completion of five, ten, fifteen, twenty, and twenty-five fractions. Dose differences are expressed in percent and normalized to planned values, which are also included for reference.

Patient	D50/D15	Planned (Gy)	$N_F =$ 5	$N_F =$ 10	$N_F =$ 15	$N_F =$ 20	$N_F =$ 25
2	D50	44.49	-2.3	-3.4	-2.8	-2.0	-2.7
2	D15	59.38	-10.3	-11.8	-10.1	-9.3	-10.8
4	D50	37.50	1.4	3.1	3.2	5.6	-
4	D15	55.23	3.0	5.0	4.4	5.5	-

7.3.3 Comparison of Bone and Prostate Matching Image Guidance Strategies

Depicted in figure 7-3 are the dose volume histograms that would have been delivered had daily patient positioning of patient 4 been based on either automatic bone matching or automatic prostate matching. Once again, comparative histograms were evaluated after every five fractions. For comparison of bone and prostate matching dosimetry, we use the same methodology as in chapter 5 and introduce prostate $\Delta D95$, which is defined as D95 for prostate matching minus D95 for bone matching. Analogously, we define $\Delta D50$ and $\Delta D15$ for the bladder and rectum as well. Prostate $\Delta D95$ values are listed for all four patients in table 7-6. Bladder and rectum $\Delta D50$ and $\Delta D15$ values are given in tables 7-7 and 7-8, respectively.

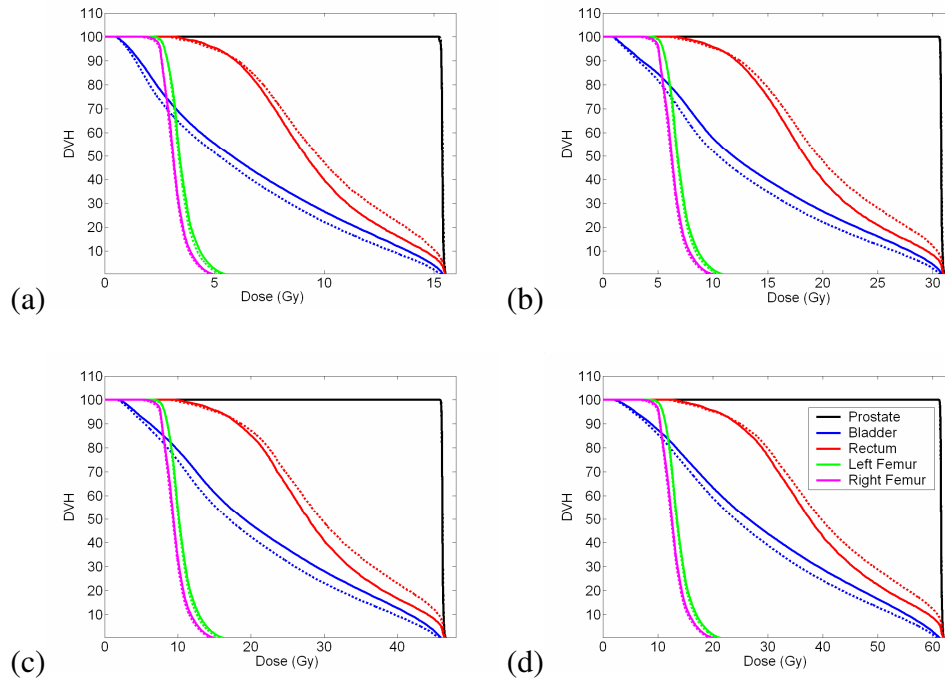


Figure 7-3. Comparison of patient 4 bone matching (solid) and prostate matching (dashed) dose volume histograms after (a) five, (b) ten, (c) fifteen and (d) twenty fractions.

Table 7-6. Prostate ΔD_{95} (expressed in percent and normalized to planned D_{95} values) at five fraction intervals.

Patient	$N_F = 5$	$N_F = 10$	$N_F = 15$	$N_F = 20$	$N_F = 25$
1	0.1	0.0	0.1	0.1	0.1
2	-0.3	-0.6	-0.5	-0.4	0.6
3	0.1	0.1	0.2	0.1	0.1
4	0.0	0.0	0.0	-0.1	-

Table 7-7. Bladder $\Delta D50$ (expressed in percent and normalized to planned D50 values) and $\Delta D15$ (expressed in percent and normalized to planned D15 values) at five fractions intervals.

Patient	D50/D15	$N_F = 5$	$N_F = 10$	$N_F = 15$	$N_F = 20$	$N_F = 25$
1	$\Delta D50$	0.4	0.5	1.1	1.2	1.1
1	$\Delta D15$	1.5	1.2	1.4	1.7	1.4
2	$\Delta D50$	2.1	3.6	4.8	3.5	2.1
2	$\Delta D15$	0.1	0.3	0.7	0.5	0.4
3	$\Delta D50$	0.0	-0.4	-0.1	-0.4	-0.6
3	$\Delta D15$	2.8	1.4	1.6	0.9	0.9
4	$\Delta D50$	-10.9	-12.5	-13.0	-11.4	-
4	$\Delta D15$	-7.4	-7.1	-7.1	-6.2	-

In chapter 5, we evaluated bone matching and prostate matching bladder D45 and rectum D30 values for a collection of individual patient fractions including all of those for patients 1 through 3. These specific endpoints were selected because constraints were set for these quantities during the inverse planning of the patients studied. Instead of the methods presented in this chapter, dose volume histograms were evaluated using contours delineated by a radiation oncologist on each treatment MVCT and without the correspondence achieved through deformable registration, cumulative analysis was not possible. However, the fractionated analysis of the previous study allows for an interesting comparison with the corresponding cumulative values evaluated in this chapter.

Using the results from the previous study, we evaluated the mean fractionated bone matching and prostate matching bladder D45 values over each patient's individual twenty-five fractions. We then compared those values to the cumulative twenty-five fraction bladder D45 values determined in this study, the results of which are presented in table 7-9. Similar analysis for rectum D30 is provided in table 7-10.

Table 7-8. Rectum $\Delta D50$ (expressed in percent and normalized to planned D50 values) and $\Delta D15$ (expressed in percent and normalized to planned D15 values) at five fractions intervals.

Patient	D50/D15	$N_F = 5$	$N_F = 10$	$N_F = 15$	$N_F = 20$	$N_F = 25$
1	$\Delta D50$	1.7	1.1	0.7	0.5	1.0
1	$\Delta D15$	0.6	-0.4	-1.3	-1.4	-1.1
2	$\Delta D50$	-1.2	-2.1	-2.8	-2.2	-1.0
2	$\Delta D15$	-2.5	-4.0	-5.4	-4.4	-2.4
3	$\Delta D50$	2.1	2.7	2.4	2.8	2.8
3	$\Delta D15$	0.1	0.7	0.7	1.0	0.9
4	$\Delta D50$	6.1	6.5	6.3	5.5	-
4	$\Delta D15$	6.5	6.9	6.7	5.7	-

7.4 Discussion

A fundamental requirement of dose accumulation software, whether used clinically or for research, is the ability to generate accurate deformed dose

distributions. A limited number of approaches have been used to determine the accuracy of dose warping in published dose accumulation studies. Unfortunately, the majority of dose accumulation articles discussed in section 7.1 either rely on deformable registration validation, mention the problem in passing or even altogether fail to address the issue of assessing the accuracy of their cumulative dose values. Schaly *et al.*⁴⁴ performed a virtual phantom study in which they assumed a linear expansion of a spherical clinical target volume (CTV) phantom and an analytical dose distribution. After contour driven TPS deformable registration, warped dose distributions were compared to their theoretical ground truth counterparts. This phantom based approach has interesting theoretical implications, but its applicability to validating dose warping required for the complex anatomical variations observed in a daily clinical setting may be limited. A unique approach was proposed by Zhong *et al.*⁴⁵ in which they linked dose warping errors to the concept of unbalanced energy,⁴⁶ a measure of the physical fidelity of the deformable registration displacement field. Their approach was applied with success to truncated pelvic CT images that included only a small region surrounding the prostate gland. Although promising, its relevancy to clinical ROI prone to significantly larger anatomical variations must be established.

In this chapter, we present a landmark based approach to quantifying the accuracy of deformed doses. The assessed deformed dose uncertainties at landmarks 1, 3 and 4, those situated in the high dose region, are all less than 3%. As expected, dose values at landmarks 2, 5 and 6 have larger uncertainties,

considering they are located in dose gradient regions. In the patients studied, dose gradients greater than 3% per mm surrounding the high dose PTV region were not uncommon. If this dose gradient value is assumed, the warped dose uncertainties at these three landmarks correspond to distances less than 3 mm. Ideally, deformed dose distribution errors that are random in nature will statistically cancel upon dose accumulation over a prolonged treatment regimen. Our results suggest this may be the case. Unfortunately, errors associated with systematic effects such as failing to account for lack of correspondence due to daily variations in bowel content may propagate throughout cumulative dose calculations. Admittedly, dose warping verification at six landmarks does not constitute a comprehensive evaluation of the dose accumulation software presented in this work. It must also be noted that our approach is potentially limited in that error analysis is based on the manual identification of landmarks, a procedure subject to human error. However, based on the validation of our deformable registration algorithm and the error analysis presented in this chapter, we have confidence in our dose accumulation software's ability to accurately calculate cumulatively delivered doses. That being said, a complete analysis requires deformable dose verification in all voxels of interest, leaving the door open for considerable amounts of further research in this area.

Accurate dose accumulation software allows for a number of potential research opportunities, two of which were presented in this paper. In comparing planned and delivered doses we demonstrated that a fractionated treatment regimen is not necessarily delivered as planned. Although cumulative prostate

D95 values differed from planned values by less than 3%, deviations were larger for the bladder and rectum. Similar observations were reported by Schaly *et al.*¹⁴ in which negative and positive treatment and planning prostate dose discrepancies ranged from -0.1 to 1.3% of the prescription dose. Corresponding bladder and rectum values were -12.9 to 31.9% and -1.9 to 22.5%, respectively. Future plans are to investigate the correlation between delivered doses and clinical endpoints such as toxicities or patient survival for statistically large patient cohorts. If correlations are established, the ultimate goal for this particular application of our dose accumulation software is treatment adaptation based on delivered dosimetry.

Table 7-9. Comparison of mean fractionated bone matching (BM) and prostate matching (PM) bladder D45 values determined previously and the cumulative bladder D45 values determined in this study. Cumulative values are divided by twenty-five to account for differences in scale. All dose values are in units of Gy.

Patient	Mean Fractionated		Cumulative / N _F	
	BM	PM	BM	PM
1	2.03	2.06	2.06	2.09
2	2.17	2.23	2.34	2.38
3	1.98	1.98	1.92	1.92

The second application of dose accumulation investigated in this work involved the dosimetric comparison of two image guidance strategies. With the

advent of treatment systems that provide on-line 3D-CT imaging and the ability to rigidly register treatment and planning images, patient set-up errors may be less of a concern than in the past. The problem now may be to select the appropriate patient positioning strategy when significant anatomical variations between planning and treatment are visibly apparent. Results suggest that patient positioning strategies have a greater effect on bladder and rectum dosimetry than that of the prostate. In the patients studied, daily patient positioning based on bone matching or prostate matching had little effect on prostate doses. In fact, as suggested by the negative ΔD_{95} values in table 7-6, in some instances cumulative D_{95} values for bone matching were greater than those for prostate matching, which intuitively does not make sense. However, all of this suggests that treatment margins are considerably greater than the observed prostate motion, and therefore 95% of the prostate volume receives an equivalent cumulative dose regardless of the patient positioning strategy. All ΔD_{95} values are within the -1 to 1% range, which is within the accuracy of dose recalculation on the Hi*Art II system's Planned Adaptive software.

Both the cumulative comparison of planned and treatment doses and the cumulative analysis of bone matching and prostate matching dosimetry also provided an opportunity to demonstrate the importance of dose accumulation in a clinical setting. Simply relying on planning dosimetry or individual fractionated treatment dosimetry does not paint an accurate picture of a prolonged fractionated treatment regimen. Based on figures 7-1 and 7-2 and tables 7-3 through 7-5, treatment and planning doses can vary significantly. Interestingly, the observed

discrepancies for patients 2 and 4 for the most part exceeded the differences between the bone and prostate dosimetric analysis for all four patients. This suggests that anatomical variations between simulation and treatment have a greater effect on treatment dosimetry than the selection of daily patient positioning strategy. Furthermore, the comparison of mean fractionated and cumulative bladder D45 and rectum D30 values in tables 7-9 and 7-10, respectively, demonstrates that treatment DVH analysis for each individual fraction is not adequate. Anatomical correspondence must be established from fraction to fraction through deformable registration, and doses must be properly accumulated. However, fractionated analysis does in all cases accurately reveal which strategy, whether bone or prostate matching, will yield the lower cumulative dose, just not the value of that dose.

Table 7-10. Comparison of mean fractionated bone matching (BM) and prostate matching (PM) rectum D30 values determined previously and the cumulative rectum D30 values determined in this study. Cumulative values are divided by twenty-five to account for differences in scale. All dose values are in units of Gy.

Patient	Mean Fractionated		Cumulative / N_F	
	BM	PM	BM	PM
1	2.17	2.17	2.14	2.14
2	2.12	2.04	1.90	1.88
3	2.29	2.32	2.58	2.62

7.5 Conclusions

We have presented a framework for automatic dose accumulation in fractionated prostate treatments delivered on the Hi*Art II helical tomotherapy system. Initially, daily treatment dose distributions are generated on the Hi*Art II system's Planned Adaptive software using the electron density information extracted from pre-treatment MVCT images. Next, in-house developed standalone software reads the planning CT, planning dose distribution and planning contour data as well as the daily pre-treatment MVCT images and treatment dose distributions. After performing automatic deformable registration of each MVCT to the planning CT, each treatment dose distribution is warped to account for daily anatomical variations and summed to generate the cumulative treatment dose distribution. A landmark based validation method was used to verify dose accumulation accuracy was clinically acceptable.

Two applications of dose accumulation were investigated. First, we compared planned and cumulative treatment doses for two prostate patients treated on the Hi*Art II helical tomotherapy system and dosimetric discrepancies were observed. Next, we evaluated the cumulative dosimetry that would have been delivered had daily patient positioning been based on prostate matching or bone matching. Analysis of four patients demonstrates that dosimetric differences between PM and BM exist; however, they are not as significant as the deviations between planned and treatment doses. Further research is required to determine the generality of this observation, however, it does suggest that limiting anatomical differences between simulation and treatment as opposed to daily

patient positioning strategy selection may play a greater role in ensuring treatments are delivered as planned. In future work, our framework will be used to investigate the correlation between delivered doses and clinical endpoints such as toxicities and patient survival for statistically large patient cohorts. Established correlations will solidify the argument for adaptive radiation therapy.

7.6 References

1. Yan D, Vicini F, Wong J, Martinez A. Adaptive radiation therapy. *Phys Med Biol.* 1997;42:123-132.
2. Wu C, Jeraj R, Olivera GH, Mackie TR. Re-optimization in adaptive radiotherapy. *Phys Med Biol.* 2002;47:3181-3195.
3. Wu QJ, Thongphiew D, Wang Z, Mathayomchan B, Chankong V, Yoo S, Lee WR, FF Yin. On-line re-optimization of prostate IMRT plans for adaptive radiation therapy. *Phys Med Biol.* 2008;53:673-691.
4. Wu Q, Liang J, Yan D. Application of dose compensation in image-guided radiotherapy of prostate cancer. *Phys Med Biol.* 2006;51:1405-1419.
5. Feng Y, Castro-Pareja C, Shekhar R, Yu C. Direct aperture deformation: an interfraction image guidance strategy. *Med Phys.* 2006;33:4490-4498.
6. Wong JR, Grimm L, Uematsu M, Oren R, Cheng CW, Merrick S, Schiff P. Image-guided radiotherapy for prostate cancer by CT-linear accelerator combination: prostate movements and dosimetric considerations. *Int J Radiat Oncol Biol Phys.* 2005;61:561-569.

7. Sorcini B, Tilikidis A. Clinical application of image-guided radiotherapy, IGRT (on the Varian OBI platform). *Cancer Radiother.* 2006;10:252-257.
8. Lehmann J, Perks J, Semon S, Harse R, Purdy JA. Commissioning experience with cone-beam computed tomography for image-guided radiation therapy. *J Appl Clin Med Phys.* 2007;8:21-36.
9. Tome WA, Jaradat HA, Nelson IA, Ritter MA, Mehta MP. Helical tomotherapy: image guidance and adaptive dose guidance. *Front Radiat Ther Oncol.* 2007;40:162-178.
10. Yan D, Jaffray DA, Wong JW. A model to accumulate fractionated dose in a deforming organ. *Int J Radiat Oncol Biol Phys.* 1999;44:665-675.
11. Kapatoes JM, Olivera GH, Ruchala KJ, Smilowitz JB, Reckwerdt PJ, Mackie TR. A feasible method for clinical delivery verification and dose reconstruction in tomotherapy. *Med Phys.* 2001;28:528-542.
12. Langen KM, Meeks SL, Poole DO, Wagner TH, Willoughby TR, Kupelian PA, Ruchala KJ, Haimerl J, Olivera GH. The use of megavoltage CT (MVCT) images for dose recomputations. *Phys Med Biol.* 2005;50:4259-4276.
13. Yang Y, Schreibmann E, Li T, Wang C, Xing L. Evaluation of on-board kV cone beam CT (CBCT)-based dose calculation. *Phys Med Biol.* 2007;52:685-705.
14. Schaly B, Kempe JA, Bauman GS, Battista JJ, Van Dyk J. Tracking the dose distribution in radiation therapy by accounting for variable anatomy. *Phys Med Biol.* 2004;49:791-805.
15. Thirion JP. Image matching as a diffusion process: an analogy with Maxwell's demons. *Med Image Anal.* 1998;2:243-260.

16. Wang H, Dong L, O'Daniel J, Mohan R, Garden AS, Ang KK, Kuban QA, Bonnen M, Chang JY, Cheung R. Validation of an accelerated 'demons' algorithm for deformable image registration in radiation therapy. *Phys Med Biol.* 2005;50:2887-2905.
17. Christensen GE, Rabbitt RD, Miller MI. Deformable templates using large deformation kinematics. *IEEE Trans Image Process.* 1996;5:1435-1447.
18. Foskey M, Davis B, Goyal L, Chang S, Chaney E, Strehl N, Tomei S, Rosenman J, Joshi S. Large deformation three-dimensional image registration in image-guided radiation therapy. *Phys Med Biol.* 2005;50:5869-5892.
19. Lu W, Chen ML, Olivera GH, Ruchala KJ, Mackie TR. Fast free-form deformable registration via calculus of variations. *Phys Med Biol.* 2004;49:3067-3087.
20. Lu W, Olivera GH, Chen Q, Ruchala KJ, Haimerl J, Meeks SL, Langen KM, Kupelian PA. Deformable registration of the planning image (kVCT) and the daily images (MVCT) for adaptive radiation therapy. *Phys Med Biol.* 2006;51:4357-4374.
21. Lau YH, Braun M, Hutton BF. Non-rigid image registration using a median-filtered coarse-to-fine displacement field and a symmetric correlation ratio. *Phys Med Biol.* 2001;46:1297-1319.
22. Malsch U, Thieke C, Huber PE, Bendl R. An enhanced block matching algorithm for fast elastic registration in adaptive radiotherapy. *Phys Med Biol.* 2006;51:4789-4806.

23. Rueckert D, Sonoda LI, Hayes C, Hill DLG, Leach MO, Hawkes DJ. Nonrigid registration using free-form deformations: application to breast MR images. *IEEE Trans Med Imag.* 1999;18:712-721.
24. Mattes D, Haynor DR, Vesselle H, Lewellen TK, Eubank W, PET-CT image registration in the chest using free-form deformations. *IEEE Trans Med Imag.* 2003;22:120-128.
25. Schulze D, Liang J, Yan D, Zhang T. Comparison of various online IGRT strategies: the benefits of online treatment plan re-optimization. *Radiother Oncol.* 2009;90:367-376.
26. Song WY, Wong E, Bauman GS, Battista JJ, Van Dyk J. Dosimetric evaluation of daily rigid and nonrigid geometric correction strategies during on-line image-guided radiation therapy (IGRT) of prostate cancer. *Med Phys.* 2007;34:352-365.
27. O'Daniel JC, Garden AS, Schwartz DL, Wang H, Ang KK, Ahamad A, Rosenthal DI, Morrison WH, Asper JA, Zhang L, Tung SM, Mohan R, Dong L. Parotid gland dose in intensity-modulated radiotherapy for head and neck cancer: is what you plan what you get? *Int J Radiat Oncol Biol Phys.* 2007;69:1290-1296.
28. Lee C, Langen KM, Lu W, Haimerl J, Schnarr E, Ruchala KJ, Olivera GH, Meeks SL, Kupelian PA, Shellenberger TD, Manon RR. Assessment of parotid gland dose changes during head and neck cancer radiotherapy using daily megavoltage computed tomography and deformable image registration. *Int J Radiat Oncol Biol Phys.* 2008;71:1563-1571.

29. Rietzel E, Chen GTY. Deformable registration of 4D computed tomography data. *Med Phys.* 2006;33:4423-4430.
30. Heath E, Collins DL, Keall PJ, Dong L, Seuntjens J. Quantification of accuracy of the automated nonlinear image matching and anatomical labeling (ANIMAL) nonlinear registration algorithm for 4D CT images of lung. *Med Phys.* 2007;34:4409-4421.
31. Rosu M, Balter JM, Chetty IJ, Kessler ML, McShan DL, Balter P, Ten Haken RK. How extensive of a 4D dataset is needed to estimate cumulative dose distribution plan evaluation metrics in conformal lung therapy? *Med Phys.* 2007;34:233-245.
32. Rangel A, Dunscombe P. Tolerances on MLC leaf position accuracy for IMRT delivery with a dynamic MLC. *Med Phys.* 2009;36:3304-3309.
33. Langen KM, Lu W, Willoughby TR, Chauhan B, Meeks SL, Kupelian PA, Olivera G. Dosimetric effect of prostate motion during helical tomotherapy. *Int J Radiat Oncol Biol Phys.* 2009;74:1134-1142.
34. Rosu M, Chetty IJ, Balter JM, Kessler ML, McShan DL, Ten Haken RK. Dose reconstruction in deforming lung anatomy: dose grid size effects and clinical implications. *Med Phys.* 2005;32:2487-2495.
35. Heath E, Seuntjens J. A direct voxel tracking method for four-dimensional Monte Carlo dose calculations in deforming anatomy. *Med Phys.* 2006;33:434-445.
36. Siebers JV, Zhong H. An energy transfer method for 4D Monte Carlo dose calculation. *Med Phys.* 2008;35:4096-4105.

37. Lian J, Xing L, Hunjan S, Dumoulin C, Levin J, Lo A, Watkins R, Rohling K, Giaquinto R, Kim D, Spielman D, Daniel B. Mapping of the prostate in endorectal coil-based MRI/MRSI and CT: a deformable registration and validation study. *Med Phys.* 2004;31:3087-3094.
38. Crouch JR, Pizer SM, Chaney EL, Hu YC, Mageras GS, Zaider M. Automated finite-element analysis for deformable registration of prostate images. *IEEE Trans Med Imag.* 2007;26:1379-1390.
39. Brock KK, Sharpe MB, Dawson LA, Kim SM, Jaffray DA. Accuracy of finite element model-based multi-organ deformable image registration. *Med Phys.* 2005;32:1647-1659.
40. Bharatha A, Hirose M, Hata N, Warfield SK, Ferrant M, Zou KH, Suarez-Santana E, Ruiz-Alzola J, D'Amico A, Cormack RA, Kikinis R, Jolesz FA, Tempany CMC. Evaluation of three-dimensional finite element-based deformable registration of pre- and intraoperative prostate imaging. *Med Phys.* 2001;28:2551-2560.
41. Venugopal N, McCurdy B, Hnatov A, Dubey A. A feasibility study to investigate the use of thin-plate splines to account for prostate deformation. *Phys Med Biol.* 2005;50:2871-2885.
42. Xiong L, Viswanathan A, Stewart AJ, Haker S, Tempany CM, Chin LM, Cormack RA. Deformable structure registration of bladder through surface mapping. *Med Phys.* 2006;33:1848-1856.

43. RTOG. RTOG 0415: a phase III randomized study of hypofractionated 3D-CRT/IMRT versus conventionally fractionated 3D-CRT/IMRT in patients with favorable-risk prostate cancer. Philadelphia (PA): RTOG; 2009.
44. Schaly B, Bauman GS, Battista JJ, Van Dyk J. Validation of contour-driven thin-plate splines for tracking fraction-to-fraction changes in anatomy and radiation therapy dose mapping. *Phys Med Biol.* 2005;50:459-475.
45. Zhong H, Weiss E, Siebers JV. Assessment of dose reconstruction errors in image-guided radiation therapy. *Phys Med Biol.* 2008;53:719-736.
46. Zhong H, Peters T, Siebers JV. FEM-based evaluation of deformable image registration for radiation therapy. *Phys Med Biol.* 2007;52:4721-4738.

Chapter 8: Conclusions and future work

The contents of this thesis can be divided into three separate components: deformable image registration validation, rigid registration based daily patient positioning and deformable image registration in dose accumulation. General conclusions and potential areas of future research will be summarized for each of the three sections.

8.1 Deformable Image Registration Validation

Deformable image registration has numerous applications in the treatment of cancer and will continue to play a vital role in radiation therapy for many years. As a result, we can expect the arrival of a number of commercial systems in the marketplace in the upcoming years. The capabilities of these systems must be independently assessed prior to clinical use and we have provided an initial

framework. Taking a four component approach, we developed a protocol for the assessment of commercial deformable registration systems and applied it to the Reveal-MVS system. Using a qualitative phantom study, relative validation based on similarity measures, synthetic image based intra-modality assessment and contour based inter-modality validation, it was demonstrated that the Reveal-MVS system is better suited for applications in which images differ by global anatomic differences as opposed to smaller local ones. Perhaps the most important conclusion, however, is that deformable registration and deformable registration validation can be enhanced by focusing on individual applications as opposed to taking a universal approach. Future work will focus on the refinement of absolute validation methods. This includes expanding the protocol to include application specific metrics for additional uses of deformable registration in radiation therapy as well as determining minimum quantitative benchmarks for each application and each metric.

8.2 Rigid Registration Based Daily Patient Positioning

The advent of treatment modalities with on-line 3D CT imaging capabilities allows for highly accurate daily patient positioning. Instead of using external markers or low contrast 2D images, patients can be re-positioned prior to each treatment fraction based on the registration of 3D pre-treatment and planning CT images, significantly increasing the likelihood that the target will be in the intended location on a daily basis. In chapter 4, we quantified the prostate positioning errors that would have occurred if daily patient positioning of helical

tomotherapy patients was based on the rigid registration of the entire treatment and planning CT images or simply the bony anatomy. Results clearly demonstrate that given the choice of mutual information based automatic image matching (IM) or bone matching (BM); the latter will yield greater prostate positioning accuracy. However, with accurate rigid registration of treatment and planning images, bony structure based patient set-up errors should be less of a concern. The problem now is to select the patient positioning strategy when significant anatomical variations between planning and treatment are visibly apparent. In chapter 5, we compared the dosimetric consequences of daily patient positioning of helical tomotherapy patients based on automatic bone matching and automatic prostate matching (PM) and demonstrated that depending on the daily inter-fraction prostate motion, situating the target in the same location on a daily basis may result in increased dose to the surrounding critical structures. Future work will focus on the further development of fast, automated and accurate registration based methods of aligning the target volumes in treatment and planning images. Treatment images include those acquired on helical tomotherapy or linear accelerators with on-board CT imagers, as well as a novel integrated linac-MR system in development at our clinic.¹

8.3 Deformable Registration and Dose Accumulation

On-line 3D treatment imaging not only allows for daily image guidance, images acquired with the patient in treatment position, in combination with deformable registration and dose calculation tools, can be used to account for

daily anatomical variations in the evaluation of cumulative treatment dosimetry. In chapters 6 and 7, we developed a framework and the required software for accurate dose accumulation in prostate adaptive radiation therapy. By incorporating known planning contour data and focusing on only the local neighbourhood of each region of interest, we demonstrated that accurate deformable registration of treatment and planning CT images can be achieved without the aid of any additional manual intervention. Our deformable registration algorithm was then integrated into software designed specifically for dose accumulation in prostate adaptive radiation therapy. In using the software to compare planned and cumulative treatment doses, as well as evaluating the cumulative dosimetry of the aforementioned bone matching and prostate matching image guidance strategies, we concluded that for the patients investigated, daily anatomical variations play a greater role in treatment dosimetry than does the selection of approaches to automated registration based patient positioning. Areas of future research include the refinement of our deformable registration algorithm by identifying and addressing its subtle limitations, development of techniques for the improved assessment of accumulated dose errors, as well as evaluating the cumulative treatment dosimetry for significantly larger patient cohorts. Ideally, a direct relationship between treatment dosimetry and clinical endpoints will be established, confirming the need for adaptive radiation therapy.

8.4 References

1. Fallone BG, Murray B, Rathee S, Stanescu T, Steciw S, Vidakovic S, Blosser E, Tymofichuk D. First MR images obtained during megavoltage photon irradiation from a prototype integrated linac-MR system. *Med Phys.* 2009;36:2084-2088.

Appendix A: Optimization algorithms

Function optimization is a generic computational problem with numerous applications, not solely limited to image registration. In general, given a function f that depends on one or more independent variables, the objective of optimization is to find the value of the variables whereby f is a minimum. If maximization of f is required, one typically finds the minimum of $-f$. Optimization algorithms generally fall into two classes depending on whether or not derivatives or the gradient of f are evaluated.¹ If f is a function of more than one variable, the derivative is a vector quantity referred to as the gradient. Algorithms involving gradient calculation tend to be more powerful than those relying simply on the evaluation of f , however, their benefits do not always compensate for the additional computational requirements of derivative calculation.¹ In this thesis, a non-gradient based algorithm was used for rigid

registration cost function optimization, while the increased complexity of deformable registration was approached with a gradient based method. The remainder of this appendix will be a discussion of both the non-gradient based Nelder-Mead simplex² and the gradient based limited memory Broyden-Fletcher-Goldfarb-Shanno with simple bounds (L-BFGS-B)³ optimizers.

A.1 Nelder-Mead Simplex

Suppose f is a function of N independent variables where $N > 1$. We define a simplex, a geometrical figure in N dimensions consisting of $N + 1$ vertices or points ($P_i = P_0, P_1, \dots, P_N$) at user defined initial locations. Note that in the case of $N = 2$, a simplex is simply a triangle. Optimization commences with the evaluation of f at each vertex P_i , of which the values are denoted by f_i . We then denote f_h as the maximum value of f_i and f_l as the minimum value in the set. At each stage or iteration in the optimization process, the location of P_h (i.e. P_i corresponding to f_h) is replaced by a new point determined by a series of *reflection*, *contraction* and *expansion* operations. The first step in each iteration is a *reflection*, whereby P_h is reflected through the opposite face of the simplex to a point P^* , conserving the simplex's volume in the process. Depending on the value at P^* (i.e. f^*) in relation to f_h and f_l , the simplex may undergo either an *expansion* in the direction of the *reflection*, a *contraction* towards the minimum, or the next iteration begins with the new simplex. Through a strategic series of these operations, the simplex eventually contracts itself around a minimum. In

our implementation, the optimization procedure terminates when the simplex diameter is smaller in magnitude than a tolerance $dtol$ and the difference in cost function values at the corners of the simplex is fractionally smaller than another tolerance $ftol$. The Nelder-Mead simplex algorithm has been used in numerous image registration applications with considerable success;⁴ however, it requires mention that it is not uncommon for the optimizer to incorrectly converge to false local minima.¹

A.2 Limited Memory Broyden-Fletcher-Goldfarb-Shanno with Simple Bounds

The L-BFGS-B optimizer is based on the well known Broyden-Fletcher-Goldfarb-Shanno (BFGS)¹ updating scheme for function optimization. The optimizer's underlying principles will be introduced, the BFGS updating scheme will be given and finally, the limited memory and simple bounds aspects of the algorithm will be discussed. Let us assume that f is dependent on a set of N variables, which will be denoted by \mathbf{z} and our goal is to iteratively find the \mathbf{z} that minimizes f . If we start with an initial point \mathbf{z}_k , the function can be approximated near that point by its second order Taylor series

$$f(\mathbf{z}) \approx f(\mathbf{z}_k) + (\mathbf{z} - \mathbf{z}_k) \cdot \nabla f(\mathbf{z}_k) + \frac{1}{2} (\mathbf{z} - \mathbf{z}_k) \cdot \mathbf{A} \cdot (\mathbf{z} - \mathbf{z}_k), \quad \text{A.1}$$

where ∇f is the gradient matrix and \mathbf{A} is the second order partial derivative matrix of f . \mathbf{A} is often referred to as the Hessian matrix. The gradient of A.1 is easily evaluated and given by

$$\nabla f(\mathbf{z}) = \nabla f(\mathbf{z}_k) + \mathbf{A} \cdot (\mathbf{z} - \mathbf{z}_k). \quad \text{A.2}$$

When $f(\mathbf{z})$ is at a minimum, its gradient $\nabla f(\mathbf{z})$ will equal zero. Setting A.2 equal to zero and rearranging, we obtain the equation for Newton's method of line minimizations

$$\mathbf{z} = \mathbf{z}_k - \mathbf{A}^{-1} \cdot \nabla f(\mathbf{z}_k), \quad \text{A.3}$$

in which $-\mathbf{A}^{-1} \cdot \nabla f(\mathbf{z}_k)$ defines the direction of descent. In general, more sophisticated line minimization procedures may be employed; however, the direction of descent $-\mathbf{A}^{-1} \cdot \nabla f(\mathbf{z}_k)$ will remain consistent. For simplicity we will continue the discussion assuming Newton's method.

Unfortunately, the Hessian of a function, and consequently its inverse, are not always available. The BFGS updating scheme overcomes this problem by iteratively finding a good approximation of the inverse Hessian \mathbf{A}^{-1} , which we will denote by $\mathbf{H} \approx \mathbf{A}^{-1}$. Taking an iterative approach, A.3 can be re-written as

$$\mathbf{z}_{k+1} = \mathbf{z}_k - \mathbf{H}_{k+1} \cdot \nabla f(\mathbf{z}_k), \quad \text{A.4}$$

where \mathbf{z}_{k+1} is the next iterative point and \mathbf{H}_{k+1} is the newest approximation of the inverse Hessian matrix. Typically, the initial \mathbf{H}_0 matrix is assumed to be the unity matrix and during each iteration, a new inverse Hessian approximation is obtained using the BFGS updating scheme:

$$\begin{aligned}
\mathbf{H}_{k+1} = \mathbf{H}_k &+ \frac{(\mathbf{z}_{k+1} - \mathbf{z}_k) \otimes (\mathbf{z}_{k+1} - \mathbf{z}_k)}{(\mathbf{z}_{k+1} - \mathbf{z}_k) \cdot (\nabla f_{k+1} - \nabla f_k)} \\
&- \frac{[\mathbf{H}_k \cdot (\nabla f_{k+1} - \nabla f_k)] \otimes [\mathbf{H}_k \cdot (\nabla f_{k+1} - \nabla f_k)]}{(\nabla f_{k+1} - \nabla f_k) \cdot \mathbf{H}_k \cdot (\nabla f_{k+1} - \nabla f_k)} \\
&+ [(\nabla f_{k+1} - \nabla f_k) \cdot \mathbf{H}_k \cdot (\nabla f_{k+1} - \nabla f_k)] \mathbf{u} \otimes \mathbf{u}
\end{aligned} \tag{A.5}$$

where

$$\mathbf{u} = \frac{(\mathbf{z}_{k+1} - \mathbf{z}_k)}{(\mathbf{z}_{k+1} - \mathbf{z}_k) \cdot (\nabla f_{k+1} - \nabla f_k)} - \frac{\mathbf{H}_k \cdot (\nabla f_{k+1} - \nabla f_k)}{(\nabla f_{k+1} - \nabla f_k) \cdot \mathbf{H}_k \cdot (\nabla f_{k+1} - \nabla f_k)}.$$

In A.5, \otimes denotes the outer product of two vectors. In addition, we use the abbreviated notation $\nabla f_k = \nabla f(\mathbf{z}_k)$ and $\nabla f_{k+1} = \nabla f(\mathbf{z}_{k+1})$. The mathematical proof is beyond the scope of this thesis,⁵ however, by using the BFGS updating scheme in A.5, a sequence of matrices \mathbf{H}_k is constructed with the property¹

$$\lim_{k \rightarrow \infty} \mathbf{H}_k = \mathbf{A}^{-1}. \tag{A.6}$$

In the case of large N , the amount of memory required to store an $N \times N$ matrix \mathbf{H}_k , as well as the time required to process it, can be considerable. To overcome this problem, the L-BFGS-B optimizer uses a limited memory approach⁶ in that it never explicitly evaluates or stores the inverse Hessian. Instead, the optimizer stores a small number, denoted by m , of \mathbf{z}_k and $\nabla f(\mathbf{z}_k)$ updates or correction pairs. These correction pairs are used to construct limited memory matrices that are used to implicitly perform operations involving the inverse Hessian. Another feature of the L-BFGS-B algorithm is that it allows for constraint optimization. The variables \mathbf{z} are subject to the simple bound constraints $\mathbf{l} \leq \mathbf{z} \leq \mathbf{u}$ where the vectors \mathbf{l} and \mathbf{u} represent the lower and upper

bounds on the variables, respectively. In our implementation, the algorithm terminates when one of two conditions occur. The first stopping condition occurs if the reduction in the cost function from one iteration to the next is fractionally smaller than a user defined percentage (*factr*) of the computer precision. The algorithm will also terminate if the norm of the gradient vector becomes smaller than some tolerance *pgtol*.

A.3 References

1. Press WH, Teukolsky SA, Vetterling WT, Flannery BP. Numerical recipes in C: the art of scientific computing. 2nd ed. Cambridge (UK): Cambridge University Press; 1992.
2. Nelder JA, Mead R. A simplex method for function minimization. Computer Journal. 1965;7:308-313.
3. Byrd RH, Lu P, Nocedal J, Zhu C. A limited memory algorithm for bound constrained optimization. SIAM J Sci Comput. 1995;16:1190-1208.
4. Maes F, Vandermeulen D, Suetens P. Comparative evaluation of multiresolution optimization strategies for multimodality image registration by maximization of mutual information. Med Imag Anal. 1999;3:373-386.
5. Polak E. Computational methods in optimization. New York (NY): Academic Press; 1971.
6. Byrd RH, Nocedal J, Schnabel RB. Representations of quasi-Newton matrices and their use in limited memory methods. Math Programming. 1994;63:129-156.

Appendix B: Relative evaluation of Reveal-MVS deformable registration settings

Table B-1. Rankings of the deformable registration setting combinations used on Reveal-MVS when registering PET/CT images. Rankings are based on post-registration normalized mutual information (NMI) values for each patient (P) as well as the mean value for all five patients. Also listed are the mean NMI values for each setting.

	P1	P2	P3	P4	P5	All	NMI
Medium-Fast-Coarse	25	27	27	30	25	26	1.1295
Medium-Fast-Fine	13	18	22	20	18	19	1.1311
Medium-Fast-Medium	18	22	21	24	24	22	1.1300
Medium-Medium-Coarse	26	24	30	31	23	24	1.1296
Medium-Medium-Fine	12	7	11	16	10	10	1.1322
Medium-Medium-Medium	21	19	9	19	13	20	1.1310
Medium-Slow-Coarse	27	23	28	29	22	23	1.1296
Medium-Slow-Fine	11	8	10	14	9	9	1.1322
Medium-Slow-Medium	19	17	12	18	14	18	1.1311
None-Fast-Coarse	22	25	36	25	26	27	1.1293
None-Fast-Fine	5	14	19	17	11	11	1.1320
None-Fast-Medium	14	20	20	8	21	17	1.1312
None-Medium-Coarse	16	10	13	11	19	13	1.1316
None-Medium-Fine	2	2	4	1	3	2	1.1347
None-Medium-Medium	9	9	5	6	8	8	1.1331
None-Slow-Coarse	17	12	14	12	17	14	1.1315
None-Slow-Fine	4	4	2	10	1	3	1.1345

None-Slow-Medium	7	11	3	3	5	6	1.1334
Soft-Fast-Coarse	23	26	31	26	27	25	1.1295
Soft-Fast-Fine	6	16	17	15	12	12	1.1319
Soft-Fast-Medium	15	21	18	7	20	16	1.1313
Soft-Medium-Coarse	24	13	15	27	16	21	1.1307
Soft-Medium-Fine	3	1	7	2	4	4	1.1344
Soft-Medium-Medium	10	5	8	4	7	7	1.1332
Soft-Slow-Coarse	20	15	16	13	15	15	1.1313
Soft-Slow-Fine	1	3	1	9	2	1	1.1347
Soft-Slow-Medium	8	6	6	5	6	5	1.1334
Stiff-Fast-Coarse	30	28	23	21	28	28	1.1287
Stiff-Fast-Fine	32	36	29	34	31	33	1.1275
Stiff-Fast-Medium	31	31	26	28	30	30	1.1281
Stiff-Medium-Coarse	29	29	25	23	29	29	1.1286
Stiff-Medium-Fine	35	35	35	35	35	35	1.1272
Stiff-Medium-Medium	33	32	32	32	33	32	1.1278
Stiff-Slow-Coarse	28	30	24	22	36	36	1.1254
Stiff-Slow-Fine	34	34	34	36	32	34	1.1272
Stiff-Slow-Medium	36	33	33	33	34	31	1.1278

Table B-2. Rankings of the deformable registration setting combinations used on Reveal-MVS when registering PET/CT images. Rankings are based on post-registration symmetric correlation ratio (SCR) values for each patient (P) as well as the mean value for all five patients. Also listed are the mean SCR values for each setting.

	P1	P2	P3	P4	P5	All	SCR
Medium-Fast-Coarse	16	24	23	30	23	21	1.2099
Medium-Fast-Fine	9	17	36	10	16	18	1.2140
Medium-Fast-Medium	25	25	32	25	22	26	1.2093
Medium-Medium-Coarse	18	22	25	32	25	23	1.2097
Medium-Medium-Fine	6	6	12	8	8	6	1.2211
Medium-Medium-Medium	22	18	14	17	13	19	1.2135
Medium-Slow-Coarse	17	21	26	31	24	22	1.2098
Medium-Slow-Fine	5	7	6	7	7	5	1.2219
Medium-Slow-Medium	21	19	10	14	14	17	1.2140
None-Fast-Coarse	19	27	35	27	27	29	1.2081
None-Fast-Fine	7	3	15	12	11	7	1.2206
None-Fast-Medium	30	20	33	23	21	20	1.2101
None-Medium-Coarse	26	14	7	2	19	14	1.2161
None-Medium-Fine	2	2	3	9	3	3	1.2332
None-Medium-Medium	13	12	9	18	10	11	1.2176
None-Slow-Coarse	23	10	16	3	15	15	1.2159
None-Slow-Fine	4	5	1	6	1	2	1.2342

None-Slow-Medium	10	16	4	24	5	8	1.2192
Soft-Fast-Coarse	20	26	30	28	26	28	1.2087
Soft-Fast-Fine	8	8	28	13	12	10	1.2180
Soft-Fast-Medium	24	23	29	34	20	24	1.2096
Soft-Medium-Coarse	15	11	13	29	18	16	1.2143
Soft-Medium-Fine	3	1	5	4	4	14	1.2327
Soft-Medium-Medium	12	15	11	26	9	13	1.2166
Soft-Slow-Coarse	14	9	17	1	17	12	1.2168
Soft-Slow-Fine	1	4	2	5	2	1	1.2349
Soft-Slow-Medium	11	13	8	22	6	9	1.2182
Stiff-Fast-Coarse	27	28	20	11	28	25	1.2093
Stiff-Fast-Fine	34	35	27	35	33	33	1.2029
Stiff-Fast-Medium	31	31	21	19	30	30	1.2077
Stiff-Medium-Coarse	29	29	18	16	29	27	1.2091
Stiff-Medium-Fine	35	36	31	33	35	34	1.2024
Stiff-Medium-Medium	32	32	22	21	31	31	1.2067
Stiff-Slow-Coarse	28	30	19	15	36	36	1.1920
Stiff-Slow-Fine	36	34	34	36	34	35	1.2021
Stiff-Slow-Medium	33	33	24	20	32	32	1.2063

Table B-3. Rankings of the deformable registration setting combinations used on Reveal-MVS when registering longitudinal PET images. Rankings are based on post-registration normalized mutual information (NMI) values for each patient (P) as well as the mean value for all five patients. Also listed are the mean NMI values for each setting.

	P1	P2	P3	P4	P5	All	NMI
Medium-Fast-Coarse	27	26	25	27	25	27	1.2891
Medium-Fast-Fine	14	7	15	18	14	15	1.2983
Medium-Fast-Medium	21	14	19	24	18	20	1.2954
Medium-Medium-Coarse	26	22	26	26	27	26	1.2894
Medium-Medium-Fine	8	3	14	11	6	12	1.3004
Medium-Medium-Medium	20	10	16	21	17	18	1.2959
Medium-Slow-Coarse	25	24	27	25	26	25	1.2894
Medium-Slow-Fine	7	4	13	14	5	11	1.3004
Medium-Slow-Medium	19	11	18	23	16	17	1.2959
None-Fast-Coarse	16	25	21	20	22	23	1.2945
None-Fast-Fine	5	21	9	5	13	6	1.3022
None-Fast-Medium	10	23	11	16	12	13	1.2989
None-Medium-Coarse	17	15	20	15	24	16	1.2959
None-Medium-Fine	2	1	2	1	2	1	1.3070
None-Medium-Medium	11	9	6	9	9	8	1.3010
None-Slow-Coarse	22	18	17	12	21	19	1.2956
None-Slow-Fine	1	6	1	2	4	3	1.3063

None-Slow-Medium	9	13	4	7	7	7	1.3016
Soft-Fast-Coarse	18	27	24	22	19	24	1.2943
Soft-Fast-Fine	6	17	7	6	8	5	1.3024
Soft-Fast-Medium	15	20	12	13	15	14	1.2984
Soft-Medium-Coarse	24	16	23	19	23	22	1.2948
Soft-Medium-Fine	3	2	5	3	1	2	1.3068
Soft-Medium-Medium	12	8	10	8	10	9	1.3007
Soft-Slow-Coarse	23	19	22	17	20	21	1.2949
Soft-Slow-Fine	4	5	3	4	3	4	1.3051
Soft-Slow-Medium	13	12	8	10	11	10	1.3004
Stiff-Fast-Coarse	34	35	35	34	34	34	1.2815
Stiff-Fast-Fine	30	28	36	30	30	30	1.2847
Stiff-Fast-Medium	33	33	31	33	33	33	1.2832
Stiff-Medium-Coarse	35	34	33	35	36	35	1.2814
Stiff-Medium-Fine	28	29	32	28	29	29	1.2850
Stiff-Medium-Medium	32	32	29	31	32	32	1.2833
Stiff-Slow-Coarse	36	36	34	36	35	36	1.2809
Stiff-Slow-Fine	29	30	30	29	28	28	1.2850
Stiff-Slow-Medium	31	31	28	32	31	31	1.2834

Table B-4. Rankings of the deformable registration setting combinations used on Reveal-MVS when registering longitudinal PET images. Rankings are based on post-registration symmetric correlation ratio (SCR) values for each patient (P) as well as the mean value for all five patients. Also listed are the mean SCR values for each setting.

	P1	P2	P3	P4	P5	All	SCR
Medium-Fast-Coarse	26	24	25	26	26	27	1.6686
Medium-Fast-Fine	9	20	21	20	23	15	1.6947
Medium-Fast-Medium	18	16	12	22	27	20	1.6867
Medium-Medium-Coarse	25	23	26	25	25	26	1.6688
Medium-Medium-Fine	7	5	20	17	10	13	1.7003
Medium-Medium-Medium	17	12	23	23	22	21	1.6860
Medium-Slow-Coarse	24	22	27	27	24	25	1.6694
Medium-Slow-Fine	8	10	18	21	7	14	1.6988
Medium-Slow-Medium	16	13	24	24	18	23	1.6851
None-Fast-Coarse	20	17	8	15	9	16	1.6938
None-Fast-Fine	3	26	14	7	2	4	1.7446
None-Fast-Medium	10	27	2	11	15	8	1.7227
None-Medium-Coarse	23	11	16	14	20	19	1.6895
None-Medium-Fine	1	1	10	2	4	1	1.7577
None-Medium-Medium	12	6	5	10	17	10	1.7199
None-Slow-Coarse	21	15	17	13	14	18	1.6897
None-Slow-Fine	2	4	6	4	5	2	1.7570

None-Slow-Medium	11	9	1	5	11	6	1.7343
Soft-Fast-Coarse	19	18	13	16	8	17	1.6908
Soft-Fast-Fine	6	25	15	6	1	7	1.7311
Soft-Fast-Medium	15	21	3	12	21	11	1.7191
Soft-Medium-Coarse	27	14	22	18	19	24	1.6833
Soft-Medium-Fine	4	2	11	3	3	3	1.7464
Soft-Medium-Medium	13	7	7	9	16	12	1.7157
Soft-Slow-Coarse	22	19	19	19	13	22	1.6851
Soft-Slow-Fine	5	3	9	1	6	5	1.7430
Soft-Slow-Medium	14	8	4	8	12	9	1.7206
Stiff-Fast-Coarse	34	35	30	28	28	35	1.6483
Stiff-Fast-Fine	30	29	36	35	29	30	1.6523
Stiff-Fast-Medium	33	32	35	36	34	33	1.6504
Stiff-Medium-Coarse	36	34	29	34	31	34	1.6491
Stiff-Medium-Fine	28	28	33	30	30	28	1.6547
Stiff-Medium-Medium	31	33	32	32	35	31	1.6520
Stiff-Slow-Coarse	35	36	28	33	32	36	1.6475
Stiff-Slow-Fine	29	30	34	29	33	29	1.6541
Stiff-Slow-Medium	32	31	31	31	36	32	1.6519

Table B-5. Rankings of the deformable registration setting combinations used on Reveal-MVS when registering longitudinal PET images. Rankings are based on post-registration correlation coefficient (CC) values for each patient (P) as well as the mean value for all five patients. Also listed are the mean CC values for each setting.

	P1	P2	P3	P4	P5	All	CC
Medium-Fast-Coarse	23	27	25	25	27	27	0.8136
Medium-Fast-Fine	10	9	20	20	23	15	0.8226
Medium-Fast-Medium	18	22	12	21	26	20	0.8194
Medium-Medium-Coarse	21	26	26	26	25	26	0.8136
Medium-Medium-Fine	7	15	21	19	10	13	0.8237
Medium-Medium-Medium	17	24	23	23	22	21	0.8188
Medium-Slow-Coarse	20	25	27	27	24	25	0.8138
Medium-Slow-Fine	8	13	18	22	7	14	0.8232
Medium-Slow-Medium	16	23	24	24	18	22	0.8186
None-Fast-Coarse	22	1	9	15	9	16	0.8216
None-Fast-Fine	3	14	15	9	2	3	0.8404
None-Fast-Medium	9	20	2	11	13	8	0.8323
None-Medium-Coarse	26	4	16	14	21	19	0.8196
None-Medium-Fine	1	19	10	2	4	2	0.8436
None-Medium-Medium	12	18	5	10	15	11	0.8298
None-Slow-Coarse	24	3	17	13	16	18	0.8199
None-Slow-Fine	2	7	7	3	5	1	0.8438

None-Slow-Medium	11	12	1	5	12	7	0.8344
Soft-Fast-Coarse	19	2	13	16	8	17	0.8208
Soft-Fast-Fine	6	10	14	8	1	6	0.8350
Soft-Fast-Medium	15	21	3	12	19	9	0.8304
Soft-Medium-Coarse	29	8	22	17	20	24	0.8177
Soft-Medium-Fine	4	16	11	4	3	4	0.8394
Soft-Medium-Medium	13	17	6	7	17	12	0.8283
Soft-Slow-Coarse	25	5	19	18	14	23	0.8185
Soft-Slow-Fine	5	6	8	1	6	5	0.8384
Soft-Slow-Medium	14	11	4	6	11	10	0.8301
Stiff-Fast-Coarse	36	35	30	33	28	35	0.8083
Stiff-Fast-Fine	30	30	36	32	31	32	0.8090
Stiff-Fast-Medium	33	32	35	34	34	33	0.8086
Stiff-Medium-Coarse	34	34	29	36	29	34	0.8084
Stiff-Medium-Fine	27	28	33	29	32	29	0.8098
Stiff-Medium-Medium	32	33	32	31	35	31	0.8091
Stiff-Slow-Coarse	35	36	28	35	30	36	0.8082
Stiff-Slow-Fine	28	29	34	28	33	28	0.8098
Stiff-Slow-Medium	31	31	31	30	36	30	0.8091

Table B-6. Rankings of the deformable registration setting combinations used on Reveal-MVS when registering longitudinal thoracic CT images. Rankings are based on post-registration normalized mutual information (NMI) values for each patient (P) as well as the mean value for all five patients. Also listed are the mean NMI values for each setting.

	P1	P2	P3	P4	P5	All	NMI
Medium-Fast-Coarse	32	33	31	31	32	33	1.2128
Medium-Fast-Fine	5	11	19	14	20	12	1.2184
Medium-Fast-Medium	15	13	17	16	18	16	1.2180
Medium-Medium-Coarse	33	32	32	26	23	32	1.2132
Medium-Medium-Fine	10	7	14	9	6	6	1.2192
Medium-Medium-Medium	16	21	10	19	15	20	1.2176
Medium-Slow-Coarse	31	30	33	30	25	31	1.2133
Medium-Slow-Fine	4	5	3	6	4	4	1.2202
Medium-Slow-Medium	18	14	7	20	12	13	1.2182
None-Fast-Coarse	25	28	22	33	30	29	1.2140
None-Fast-Fine	3	10	21	13	16	10	1.2187
None-Fast-Medium	11	16	16	18	19	19	1.2176
None-Medium-Coarse	29	24	28	25	24	26	1.2147
None-Medium-Fine	13	9	12	11	7	9	1.2191
None-Medium-Medium	21	23	5	22	14	18	1.2178
None-Slow-Coarse	27	25	30	27	27	27	1.2146
None-Slow-Fine	9	3	1	8	3	2	1.2203

None-Slow-Medium	17	17	9	24	9	15	1.2180
Soft-Fast-Coarse	26	29	24	32	29	30	1.2140
Soft-Fast-Fine	7	12	20	15	17	11	1.2186
Soft-Fast-Medium	14	18	18	17	22	21	1.2175
Soft-Medium-Coarse	30	19	26	28	21	25	1.2148
Soft-Medium-Fine	12	8	13	10	8	8	1.2191
Soft-Medium-Medium	20	22	6	21	11	17	1.2178
Soft-Slow-Coarse	28	20	29	29	26	28	1.2145
Soft-Slow-Fine	8	2	2	7	2	3	1.2203
Soft-Slow-Medium	19	15	8	23	10	14	1.2180
Stiff-Fast-Coarse	34	36	34	36	36	36	1.2024
Stiff-Fast-Fine	6	6	11	12	13	7	1.2191
Stiff-Fast-Medium	24	31	23	1	33	24	1.2150
Stiff-Medium-Coarse	36	35	35	35	35	35	1.2026
Stiff-Medium-Fine	2	4	15	4	5	5	1.2198
Stiff-Medium-Medium	23	27	25	2	28	22	1.2157
Stiff-Slow-Coarse	35	34	36	34	34	34	1.2028
Stiff-Slow-Fine	1	1	4	3	1	1	1.2208
Stiff-Slow-Medium	22	26	27	5	31	23	1.2156

Table B-7. Rankings of the deformable registration setting combinations used on Reveal-MVS when registering longitudinal thoracic CT images. Rankings are based on post-registration symmetric correlation ratio (SCR) values for each patient (P) as well as the mean value for all five patients. Also listed are the mean SCR values for each setting.

	P1	P2	P3	P4	P5	All	SCR
Medium-Fast-Coarse	31	32	33	31	32	33	1.7767
Medium-Fast-Fine	11	11	19	11	18	12	1.7960
Medium-Fast-Medium	15	13	16	4	19	14	1.7947
Medium-Medium-Coarse	30	29	32	29	22	32	1.7781
Medium-Medium-Fine	6	7	14	22	3	9	1.7978
Medium-Medium-Medium	14	23	10	21	16	21	1.7920
Medium-Slow-Coarse	29	28	31	30	25	31	1.7791
Medium-Slow-Fine	3	4	3	16	6	4	1.8019
Medium-Slow-Medium	19	17	7	12	17	13	1.7951
None-Fast-Coarse	24	26	28	33	31	26	1.7823
None-Fast-Fine	9	10	21	9	15	10	1.7965
None-Fast-Medium	12	14	17	3	20	17	1.7932
None-Medium-Coarse	25	22	26	26	26	23	1.7858
None-Medium-Fine	8	9	12	24	4	8	1.7978
None-Medium-Medium	21	25	5	20	13	20	1.7927
None-Slow-Coarse	32	21	30	25	29	25	1.7840
None-Slow-Fine	5	2	1	18	8	3	1.8023

None-Slow-Medium	17	20	9	15	10	16	1.7943
Soft-Fast-Coarse	26	27	27	32	30	29	1.7819
Soft-Fast-Fine	10	12	20	13	14	11	1.7963
Soft-Fast-Medium	13	15	18	2	21	19	1.7929
Soft-Medium-Coarse	28	16	25	27	23	22	1.7858
Soft-Medium-Fine	7	8	13	23	5	7	1.7978
Soft-Medium-Medium	20	24	6	19	12	18	1.7929
Soft-Slow-Coarse	33	18	29	28	27	24	1.7844
Soft-Slow-Fine	4	1	2	17	7	2	1.8023
Soft-Slow-Medium	18	19	8	14	11	15	1.7944
Stiff-Fast-Coarse	34	36	34	36	36	36	1.7363
Stiff-Fast-Fine	16	6	11	7	9	6	1.7979
Stiff-Fast-Medium	27	33	22	1	33	30	1.7798
Stiff-Medium-Coarse	36	35	35	35	35	35	1.7375
Stiff-Medium-Fine	2	5	15	10	1	5	1.7996
Stiff-Medium-Medium	23	31	24	6	24	28	1.7821
Stiff-Slow-Coarse	35	34	36	34	34	34	1.7381
Stiff-Slow-Fine	1	3	4	8	2	1	1.8028
Stiff-Slow-Medium	22	30	23	5	28	21	1.7821

Table B-8. Rankings of the deformable registration setting combinations used on Reveal-MVS when registering longitudinal thoracic CT images. Rankings are based on post-registration correlation coefficient (CC) values for each patient (P) as well as the mean value for all five patients. Also listed are the mean CC values for each setting.

	P1	P2	P3	P4	P5	All	CC
Medium-Fast-Coarse	30	30	32	31	32	33	0.8901
Medium-Fast-Fine	11	8	19	17	22	12	0.8951
Medium-Fast-Medium	16	13	15	4	16	13	0.8944
Medium-Medium-Coarse	29	29	33	29	20	32	0.8904
Medium-Medium-Fine	6	10	14	18	3	9	0.8954
Medium-Medium-Medium	15	23	10	12	11	19	0.8936
Medium-Slow-Coarse	28	28	31	30	25	30	0.8907
Medium-Slow-Fine	3	3	3	19	13	4	0.8964
Medium-Slow-Medium	18	19	5	7	12	14	0.8942
None-Fast-Coarse	23	26	24	33	31	26	0.8916
None-Fast-Fine	9	7	21	16	19	10	0.8952
None-Fast-Medium	12	15	16	3	17	17	0.8941
None-Medium-Coarse	26	20	27	26	24	23	0.8924
None-Medium-Fine	8	12	12	21	5	8	0.8954
None-Medium-Medium	21	25	8	10	8	20	0.8934
None-Slow-Coarse	32	18	30	25	28	25	0.8917
None-Slow-Fine	5	2	1	24	15	3	0.8965

None-Slow-Medium	17	22	7	11	9	16	0.8940
Soft-Fast-Coarse	25	27	23	32	30	29	0.8914
Soft-Fast-Fine	10	9	20	22	18	11	0.8951
Soft-Fast-Medium	14	16	17	2	21	19	0.8940
Soft-Medium-Coarse	31	14	25	27	23	22	0.8922
Soft-Medium-Fine	7	11	13	20	4	7	0.8954
Soft-Medium-Medium	20	24	9	8	7	18	0.8935
Soft-Slow-Coarse	33	17	29	28	27	24	0.8918
Soft-Slow-Fine	4	1	2	23	14	2	0.8965
Soft-Slow-Medium	19	21	6	9	10	15	0.8940
Stiff-Fast-Coarse	34	36	34	36	36	36	0.8796
Stiff-Fast-Fine	13	6	11	13	6	6	0.8956
Stiff-Fast-Medium	27	33	22	1	33	30	0.8906
Stiff-Medium-Coarse	36	35	35	35	35	35	0.8800
Stiff-Medium-Fine	2	5	18	15	1	5	0.8957
Stiff-Medium-Medium	24	32	28	5	26	28	0.8910
Stiff-Slow-Coarse	35	34	36	34	34	34	0.8802
Stiff-Slow-Fine	1	4	4	14	2	1	0.8965
Stiff-Slow-Medium	22	31	26	6	29	27	0.8910

Table B-9. Rankings of the deformable registration setting combinations used on Reveal-MVS when registering male pelvic MRI images to planning CT images. Rankings are based on post-registration normalized mutual information (NMI) values for each patient (P) as well as the mean value for all five patients. Also listed are the mean NMI values for each setting.

	P1	P2	P3	P4	P5	All	NMI
Medium-Fast-Coarse	26	16	25	1	3	21	1.1126
Medium-Fast-Fine	24	11	24	17	33	26	1.1102
Medium-Fast-Medium	15	29	27	13	12	22	1.1123
Medium-Medium-Coarse	28	13	22	34	15	27	1.1097
Medium-Medium-Fine	11	5	10	18	23	19	1.1129
Medium-Medium-Medium	21	23	14	9	4	15	1.1132
Medium-Slow-Coarse	25	30	18	21	11	24	1.1106
Medium-Slow-Fine	7	7	5	12	25	17	1.1130
Medium-Slow-Medium	18	32	12	5	1	10	1.1136
None-Fast-Coarse	22	14	8	2	21	2	1.1139
None-Fast-Fine	1	9	28	16	27	6	1.1138
None-Fast-Medium	2	28	17	19	17	1	1.1143
None-Medium-Coarse	14	19	4	35	9	20	1.1128
None-Medium-Fine	5	3	16	23	18	14	1.1132
None-Medium-Medium	12	18	21	22	8	16	1.1130
None-Slow-Coarse	17	35	2	6	10	13	1.1132
None-Slow-Fine	4	22	7	10	19	9	1.1136

None-Slow-Medium	10	24	20	7	7	11	1.1135
Soft-Fast-Coarse	23	15	11	3	14	5	1.1138
Soft-Fast-Fine	20	10	26	27	31	25	1.1104
Soft-Fast-Medium	3	2	13	20	16	4	1.1138
Soft-Medium-Coarse	16	26	9	36	13	23	1.1121
Soft-Medium-Fine	6	4	15	24	22	18	1.1129
Soft-Medium-Medium	13	20	1	14	6	3	1.1138
Soft-Slow-Coarse	19	33	3	4	5	8	1.1136
Soft-Slow-Fine	9	21	6	11	20	12	1.1132
Soft-Slow-Medium	8	25	19	8	2	7	1.1137
Stiff-Fast-Coarse	32	36	34	33	32	32	1.1056
Stiff-Fast-Fine	36	17	33	26	36	34	1.1053
Stiff-Fast-Medium	34	1	23	29	28	30	1.1075
Stiff-Medium-Coarse	33	34	32	32	34	33	1.1054
Stiff-Medium-Fine	30	12	31	30	26	29	1.1083
Stiff-Medium-Medium	35	6	29	28	29	31	1.1070
Stiff-Slow-Coarse	27	31	36	31	35	36	1.1031
Stiff-Slow-Fine	31	27	30	25	24	28	1.1084
Stiff-Slow-Medium	29	8	35	15	30	35	1.1049

Table B-10. Rankings of the deformable registration setting combinations used on Reveal-MVS when registering male pelvic MRI images to planning CT images. Rankings are based on post-registration symmetric correlation ratio (SCR) values for each patient (P) as well as the mean value for all five patients. Also listed are the mean SCR values for each setting.

	P1	P2	P3	P4	P5	All	SCR
Medium-Fast-Coarse	27	28	24	26	16	27	1.4291
Medium-Fast-Fine	22	16	25	13	31	23	1.4391
Medium-Fast-Medium	19	33	21	18	8	17	1.4587
Medium-Medium-Coarse	26	25	17	34	18	26	1.4297
Medium-Medium-Fine	9	6	5	7	24	13	1.4651
Medium-Medium-Medium	11	5	23	9	4	10	1.4668
Medium-Slow-Coarse	25	24	19	23	17	24	1.4379
Medium-Slow-Fine	8	4	2	4	22	7	1.4681
Medium-Slow-Medium	12	29	14	3	1	5	1.4693
None-Fast-Coarse	20	31	20	30	14	20	1.4511
None-Fast-Fine	23	14	26	11	27	22	1.4418
None-Fast-Medium	18	32	10	21	10	16	1.4603
None-Medium-Coarse	15	11	9	35	12	18	1.4569
None-Medium-Fine	3	9	11	10	15	6	1.4685
None-Medium-Medium	7	1	22	17	6	12	1.4662
None-Slow-Coarse	13	27	4	8	7	8	1.4674
None-Slow-Fine	1	23	8	1	19	4	1.4715

None-Slow-Medium	4	13	13	5	3	1	1.4727
Soft-Fast-Coarse	21	30	15	29	20	21	1.4501
Soft-Fast-Fine	24	15	27	16	28	25	1.4367
Soft-Fast-Medium	17	17	6	22	11	15	1.4629
Soft-Medium-Coarse	14	18	16	36	9	19	1.4558
Soft-Medium-Fine	2	7	12	12	23	11	1.4664
Soft-Medium-Medium	6	2	1	15	5	2	1.4718
Soft-Slow-Coarse	16	26	3	19	13	14	1.4630
Soft-Slow-Fine	10	22	7	2	21	9	1.4668
Soft-Slow-Medium	5	20	18	6	2	3	1.4717
Stiff-Fast-Coarse	30	36	34	33	34	34	1.3639
Stiff-Fast-Fine	32	19	32	27	29	32	1.3877
Stiff-Fast-Medium	34	8	28	24	30	30	1.3942
Stiff-Medium-Coarse	31	35	33	31	35	33	1.3714
Stiff-Medium-Fine	29	10	29	25	26	29	1.4130
Stiff-Medium-Medium	35	12	30	28	32	31	1.3880
Stiff-Slow-Coarse	33	34	36	32	36	36	1.3340
Stiff-Slow-Fine	28	21	31	14	25	28	1.4166
Stiff-Slow-Medium	36	3	35	20	33	35	1.3607

Table B-11. Rankings of the deformable registration setting combinations used on Reveal-MVS when registering male pelvic MVCT images to planning CT images. Rankings are based on post-registration normalized mutual information (NMI) values for each patient (P) as well as the mean value for all five patients. Also listed are the mean NMI values for each setting.

	P1	P2	P3	P4	P5	All	NMI
Medium-Fast-Coarse	9	7	6	20	6	5	1.1523
Medium-Fast-Fine	36	30	35	23	24	33	1.1429
Medium-Fast-Medium	27	15	12	7	15	16	1.1509
Medium-Medium-Coarse	1	10	10	15	18	9	1.1518
Medium-Medium-Fine	33	28	29	25	25	30	1.1435
Medium-Medium-Medium	19	13	17	1	13	14	1.1513
Medium-Slow-Coarse	4	4	3	18	11	2	1.1526
Medium-Slow-Fine	23	31	21	14	23	26	1.1443
Medium-Slow-Medium	17	21	4	4	7	11	1.1517
None-Fast-Coarse	8	8	9	24	9	8	1.1518
None-Fast-Fine	34	27	34	19	19	31	1.1434
None-Fast-Medium	28	22	15	9	17	18	1.1501
None-Medium-Coarse	3	5	18	13	5	6	1.1520
None-Medium-Fine	32	26	27	26	27	29	1.1436
None-Medium-Medium	20	14	13	3	14	13	1.1513
None-Slow-Coarse	6	12	1	22	2	4	1.1524
None-Slow-Fine	25	32	20	11	21	25	1.1444

None-Slow-Medium	16	20	5	6	8	10	1.1517
Soft-Fast-Coarse	10	9	11	21	4	7	1.1518
Soft-Fast-Fine	35	29	33	17	20	32	1.1433
Soft-Fast-Medium	24	23	16	8	16	17	1.1503
Soft-Medium-Coarse	2	6	8	10	3	3	1.1524
Soft-Medium-Fine	31	25	28	27	26	28	1.1437
Soft-Medium-Medium	21	18	14	2	12	15	1.1510
Soft-Slow-Coarse	5	11	2	16	1	1	1.1527
Soft-Slow-Fine	26	33	19	12	22	27	1.1442
Soft-Slow-Medium	15	19	7	5	10	12	1.1516
Stiff-Fast-Coarse	13	2	23	35	33	20	1.1488
Stiff-Fast-Fine	29	34	36	29	34	36	1.1401
Stiff-Fast-Medium	11	17	22	30	29	22	1.1482
Stiff-Medium-Coarse	7	1	25	33	31	19	1.1491
Stiff-Medium-Fine	30	35	31	36	36	35	1.1406
Stiff-Medium-Medium	18	24	30	31	30	24	1.1471
Stiff-Slow-Coarse	14	3	24	34	32	21	1.1487
Stiff-Slow-Fine	22	36	32	28	35	34	1.1410
Stiff-Slow-Medium	12	16	26	32	28	23	1.1478

Table B-12. Rankings of the deformable registration setting combinations used on Reveal-MVS when registering male pelvic MVCT images to planning CT images. Rankings are based on post-registration symmetric correlation ratio (SCR) values for each patient (P) as well as the mean value for all five patients. Also listed are the mean SCR values for each setting.

	P1	P2	P3	P4	P5	All	SCR
Medium-Fast-Coarse	2	7	3	14	7	3	1.8030
Medium-Fast-Fine	36	27	36	33	25	26	1.7157
Medium-Fast-Medium	25	15	20	7	14	17	1.7884
Medium-Medium-Coarse	1	11	2	12	2	1	1.8040
Medium-Medium-Fine	34	29	33	32	30	30	1.7096
Medium-Medium-Medium	26	13	19	1	10	12	1.7920
Medium-Slow-Coarse	7	6	1	13	1	2	1.8035
Medium-Slow-Fine	17	34	29	27	35	34	1.7028
Medium-Slow-Medium	20	21	7	2	11	8	1.7941
None-Fast-Coarse	6	8	14	18	13	7	1.7941
None-Fast-Fine	31	26	34	29	26	25	1.7163
None-Fast-Medium	30	22	22	9	17	23	1.7834
None-Medium-Coarse	5	4	24	11	6	11	1.7926
None-Medium-Fine	35	31	31	30	33	32	1.7047
None-Medium-Medium	27	14	16	3	9	10	1.7927
None-Slow-Coarse	9	12	4	16	4	5	1.8003
None-Slow-Fine	19	35	28	25	34	36	1.7017

None-Slow-Medium	16	19	15	6	16	14	1.7904
Soft-Fast-Coarse	3	9	21	17	12	9	1.7936
Soft-Fast-Fine	32	28	35	28	28	28	1.7141
Soft-Fast-Medium	29	23	23	8	18	24	1.7830
Soft-Medium-Coarse	4	5	13	10	5	6	1.7988
Soft-Medium-Fine	33	32	32	31	32	33	1.7037
Soft-Medium-Medium	28	17	17	4	8	13	1.7914
Soft-Slow-Coarse	8	10	5	15	3	4	1.8003
Soft-Slow-Fine	18	36	27	26	31	35	1.7022
Soft-Slow-Medium	14	18	18	5	15	15	1.7903
Stiff-Fast-Coarse	23	2	10	24	24	22	1.7844
Stiff-Fast-Fine	22	25	30	36	36	29	1.7138
Stiff-Fast-Medium	12	16	6	19	20	16	1.7898
Stiff-Medium-Coarse	15	1	12	22	22	19	1.7856
Stiff-Medium-Fine	21	30	25	35	29	27	1.7141
Stiff-Medium-Medium	10	24	11	20	21	21	1.7845
Stiff-Slow-Coarse	24	3	9	23	23	20	1.7846
Stiff-Slow-Fine	13	33	26	34	27	31	1.7080
Stiff-Slow-Medium	11	20	8	21	19	18	1.7874

Table B-13. Rankings of the deformable registration setting combinations used on Reveal-MVS when registering male pelvic MVCT images to planning CT images. Rankings are based on post-registration correlation coefficient (CC) values for each patient (P) as well as the mean value for all five patients. Also listed are the mean CC values for each setting.

	P1	P2	P3	P4	P5	All	CC
Medium-Fast-Coarse	3	17	3	12	4	1	0.8282
Medium-Fast-Fine	30	28	36	32	25	30	0.8235
Medium-Fast-Medium	33	10	16	9	15	20	0.8267
Medium-Medium-Coarse	5	24	1	17	8	5	0.8280
Medium-Medium-Fine	34	29	31	33	31	34	0.8233
Medium-Medium-Medium	18	2	14	4	12	11	0.8277
Medium-Slow-Coarse	10	23	2	13	3	4	0.8280
Medium-Slow-Fine	24	34	28	27	35	32	0.8234
Medium-Slow-Medium	13	7	9	1	13	6	0.8279
None-Fast-Coarse	9	19	12	18	9	15	0.8276
None-Fast-Fine	28	25	34	29	28	28	0.8236
None-Fast-Medium	35	11	22	8	20	23	0.8265
None-Medium-Coarse	8	15	24	11	7	18	0.8273
None-Medium-Fine	32	31	32	30	34	36	0.8231
None-Medium-Medium	17	3	19	5	11	14	0.8276
None-Slow-Coarse	12	13	4	16	2	3	0.8280
None-Slow-Fine	23	35	27	25	36	33	0.8233

None-Slow-Medium	15	8	15	2	16	17	0.8275
Soft-Fast-Coarse	6	18	21	15	6	13	0.8276
Soft-Fast-Fine	29	26	35	28	29	29	0.8235
Soft-Fast-Medium	36	12	23	7	21	24	0.8264
Soft-Medium-Coarse	7	16	17	10	5	10	0.8277
Soft-Medium-Fine	31	32	33	31	33	35	0.8231
Soft-Medium-Medium	19	1	20	6	10	12	0.8276
Soft-Slow-Coarse	11	14	5	14	1	2	0.8280
Soft-Slow-Fine	22	36	26	26	32	31	0.8234
Soft-Slow-Medium	14	6	18	3	14	16	0.8275
Stiff-Fast-Coarse	21	21	11	24	24	21	0.8266
Stiff-Fast-Fine	25	27	30	36	30	26	0.8237
Stiff-Fast-Medium	2	9	6	20	17	8	0.8278
Stiff-Medium-Coarse	16	22	13	22	22	19	0.8267
Stiff-Medium-Fine	27	30	25	34	26	25	0.8239
Stiff-Medium-Medium	4	5	8	19	19	9	0.8277
Stiff-Slow-Coarse	26	20	10	23	23	22	0.8265
Stiff-Slow-Fine	20	33	29	35	27	27	0.8236
Stiff-Slow-Medium	1	4	7	21	18	7	0.8278

Appendix C: Interpolation based dose warping errors in prostate MVCT studies

Consider that as a result of anatomical deformations, the biological contents of a single voxel $\mathbf{x}_0(\mu)$ in a patient's planning CT completely occupy two adjacent voxels $\mathbf{x}_i(\mu)$ and $\mathbf{x}_i(\nu)$ in a fractionated treatment CT. Assuming that deformable registration accurately determines the transformation \mathbf{T}_i and that the volume of each voxel is identical, the linearly interpolated delivered dose in $\mathbf{x}_0(\mu)$ will be

$$d_i(\mathbf{x}_0(\mu)) = \frac{1}{2} [d_i(\mathbf{x}_i(\mu)) + d_i(\mathbf{x}_i(\nu))] = \frac{1}{2} \left[\frac{E(\mathbf{x}_i(\mu))}{M(\mathbf{x}_i(\mu))} + \frac{E(\mathbf{x}_i(\nu))}{M(\mathbf{x}_i(\nu))} \right] \quad \text{C.1}$$

where E and M are operators for energy absorbed and mass, respectively. However, conservation of mass and conservation of energy dictate that the true fractionated dose delivered to $\mathbf{x}_0(\mu)$ is

$$d_i^{True}(\mathbf{x}_0(\mu)) = \left[\frac{E(\mathbf{x}_i(\mu)) + E(\mathbf{x}_i(\nu))}{M(\mathbf{x}_i(\mu)) + M(\mathbf{x}_i(\nu))} \right] \quad \text{C.2}$$

As a result, interpolation yields an erroneous value for the deformed dose $d_i(\mathbf{x}_0(\mu))$, with the error given by

$$\begin{aligned} \delta d_i(\mathbf{x}_0(\mu)) &= d_i(\mathbf{x}_0(\mu)) - d_i^{True}(\mathbf{x}_0(\mu)) \\ &= \frac{1}{2} \left[\frac{M(\mathbf{x}_i(\nu)) - M(\mathbf{x}_i(\mu))}{M(\mathbf{x}_i(\nu)) + M(\mathbf{x}_i(\mu))} \right] [d_i(\mathbf{x}_i(\mu)) - d_i(\mathbf{x}_i(\nu))] \quad \text{C.3} \end{aligned}$$

The equation for $\delta d_i(\mathbf{x}_0(\mu))$, which was previously derived by Siebers *et al.*,¹ will now be expressed in terms of MVCT voxel intensities. Upon denoting mass in terms of volume and physical density and assuming a linear relationship² between physical density and MVCT voxel intensity (i.e. $\rho = sI + I_0$), further simplification yields

$$\delta d_i(\mathbf{x}_0(\mu)) = \frac{1}{2} \left[\frac{I(\mathbf{x}_i(\nu)) - I(\mathbf{x}_i(\mu))}{I(\mathbf{x}_i(\nu)) + I(\mathbf{x}_i(\mu)) + 2I_0 / s} \right] [d_i(\mathbf{x}_i(\mu)) - d_i(\mathbf{x}_i(\nu))]. \quad \text{C.4}$$

The above equation demonstrates that the interpolation based error in the dose delivered to voxel $\mathbf{x}_0(\mu)$ is independent of voxel volume, but more importantly, its value is nil if either the dose or intensity of the adjacent voxels in the treatment image are equivalent.

The above equation for interpolation based dose warping errors is of course an oversimplification, as internal anatomical variations within a patient are more complex than having two volumes of tissue deforming into one. However, by substituting clinically relevant combinations of dose and intensity values, we can estimate approximately the interpolation based errors present in the results

reported in chapter 7. For the patients included in chapter 7, the dose falloff surrounding the high dose PTV was greatest in the inferior direction where maximum gradient values of 10% (of the prescription dose) per 3 mm (superior/inferior voxel spacing) were commonplace. An MVCT image was selected at random and the prostate, bladder, rectal wall, and any intestinal gas were contoured by a radiation oncologist. A histogram of the voxel intensities for each structure was fit to a Gaussian and fitted centre values for the prostate, bladder, rectal wall, and intestinal gas were 51, 24, 31 and -471, respectively. Assuming a 10% dose gradient, and appropriate dose and intensity values, the value of $\delta l_i(\mathbf{x}_0(\mu))$ at various tissue interfaces and dose regions was evaluated and is listed in table C-1. Based on the tabulated values, interpolation based dose accumulation errors when evaluating the cumulative dosimetry of Hi*Art II helical tomotherapy prostate patients may only be non-negligible at interfaces between intestinal gas and the rectal wall that are situated in high dose gradient regions.

Table C-1. Interpolation based dose warping error ($\delta d_i(\mathbf{x}_0(\mu))$) when adjacent treatment image voxels $\mathbf{x}_i(\mu)$ and $\mathbf{x}_i(\nu)$ deform into one planning CT voxel. A 10% dose gradient is assumed. The unit for dose values is percentage of prescription dose.

Interface	Dose	$I(\mathbf{x}_i(\mu))$	$I(\mathbf{x}_i(\nu))$	$d_i(\mathbf{x}_i(\mu))$	$d_i(\mathbf{x}_i(\nu))$	$\delta d_i(\mathbf{x}_0(\mu))$
Region						
Prostate/	High	51	24	100	90	<0.1
Rectal Wall						
Prostate/	High	51	31	100	90	<0.1
Bladder						
Rectal Wall/	High	31	-471	100	90	1.8
Intestinal gas						
Rectal Wall/	Low	31	-471	40	50	1.8
Intestinal gas						

C.1 References

1. Siebers JV, Zhong H. An energy transfer method for 4D Monte Carlo dose calculation. *Med Phys.* 2008;35:4096-4105.
2. Langen KM, Meeks SL, Poole DO, Wagner TH, Willoughby TR, Kupelian PA, Ruchala KJ, Haimerl J, Olivera GH. The use of megavoltage CT (MVCT) images for dose recomputations. *Phys Med Biol.* 2005;50:4259-4276.